THESIS FOR THE DEGREE OF DOCTOR OF PHILOSOPHY

Operation, Monitoring, and Protection of Future Power Systems

Advanced Congestion Forecast and Dynamic State Estimation Applications

Ankur Srivastava

CHALMERS
UNIVERSITY OF TECHNOLOGY

Division of Electric Power Engineering
Department of Electrical Engineering
Chalmers University of Technology
Gothenburg, Sweden, 2022

Operation, Monitoring, and Protection of Future Power Systems
Advanced Congestion Forecast and Dynamic State Estimation Applications

Ankur Srivastava

ISBN 978-91-7905-714-5
Doktorsavhandlingar vid Chalmers tekniska högskola
Ny serie nr 5180
ISSN 0346-718X

This thesis has been prepared using LaTeX.

Division of Electric Power Engineering
Department of Electrical Engineering
Chalmers University of Technology
SE-412 96 Gothenburg, Sweden
Phone: +46 (0)31 772 1000
www.chalmers.se

Printed by Chalmers Reproservice
Gothenburg, Sweden, 2022

To the Almighty, my parents, Deepanjali, Sweden and India

Operation, Monitoring, and Protection of Future Power Systems: Advanced Congestion Forecast and Dynamic State Estimation Applications

Ankur Srivastava
Division of Electric Power Engineering
Department of Electrical Engineering
Chalmers University of Technology, Sweden

Abstract

The electrical power systems are undergoing drastic changes such as increasing levels of renewable energy sources, energy storage, electrification of energy-efficient loads such as heat pumps and electric vehicles, demand-side resources, etc., in the last decade, and more changes will be followed in the near future. The emergence of digitalization and advanced communication in the case of distribution systems to enhance the performance of the electricity infrastructure also adds further complexities. These changes pose challenges such as increased levels of network congestion, voltage variations, protection mis-operations, increased needs for real-time monitoring, and improved planning practices of the system operators. These challenges will require the development of new paradigms to operate the power grids securely, safely, and economically.
This thesis attempted to address those challenges and had the following main contributions:

- First, the thesis started by presenting a comprehensive assessment framework to address the distribution system operators' future-readiness and help the distribution system operators to determine the current status of their network infrastructures, business models, and policies and thus identify the pathways for the required developments for the smooth transition towards future intelligent distribution grids.
- Second, the thesis presents an advanced congestion forecast tool that would support the distribution system operators to forecast and visualize network congestion and voltage variations issues for multiple forecasting horizons ranging from close-to-real time to a day-ahead. The tool is based on a probabilistic power flow that incorporates forecasts of solar photovoltaic production and electricity demand, combined with advanced load models and different operating modes of solar photovoltaic inverters. The tool has been integrated to an existing industrial graded distribution management system via an IoT platform Codex Smart Edge of Atos Worldgrid. The results from case studies demonstrated that the tool performs satisfactorily for both small and large networks and can visualise the cumulative probabilities of network congestion and voltage variations for a variety of forecast horizons as desired by the distribution system operator.
- Third, a dynamic state estimation-based protection scheme for the transmission lines which does not require complicated relay settings and coordination has been demonstrated using an experimental setup at Chalmers power system laboratory. The scheme makes use of the real-time measurements provided by advanced sensors which are developed by Smart State Technology, The Netherlands. The experimental validations of the scheme have been performed under different fault types and conditions, e.g., unbalanced faults, three-phase faults, high impedance faults, hidden failures,

inductive load conditions, etc. The results have shown that the scheme performs adequately in both normal and fault conditions and thus the scheme would work for transmission line protection by avoiding relay coordination and settings issues.

- Finally, the thesis presents a decentralized dynamic state estimation method for estimating the dynamic states of a transmission line in real-time. This method utilizes the sampled measurements from the local end of a transmission line, and thereafter dynamic state estimation is performed by employing an unscented Kalman filter. The advantage of the method is that the remote end state variables of a transmission line can be estimated using only the local end variables and, hence, the need for communication infrastructure is eliminated. Furthermore, an exact nonlinear model of the transmission line is utilized and the dynamic state estimation of one transmission line is independent of the other lines. These features in turn result in reduced complexity, higher accuracy, and easier implementation of the decentralized estimator. The method is envisioned to have potential applications in transmission line monitoring, control, and protection.

Keywords: Congestion forecast, distribution system operator, dynamic state estimation, energy transition, experimental validation, future distribution systems, future-readiness, phasor measurement unit, photovoltaics, power system protection, probabilistic power flow, renewable energy, smart grid solutions.

Acknowledgments

This work has been carried out at the Division of Electric Power Engineering, Department of Electrical Engineering, Chalmers University of Technology, Gothenburg, Sweden. The financial support for this work is provided by the UNITED-GRID project which has been funded by the European Community's Horizon 2020 Framework Programme under grant agreement no. 773717 and the FlexiGrid project which has been funded by the European Community's Horizon 2020 Framework Programme under grant agreement no. 864048, which is gratefully acknowledged.

I want to begin by expressing my sincere gratitude to my supervisor Associate Prof. Tuan Le for giving me the opportunity to pursue my Ph.D. studies at Chalmers. I still remember our first physical meeting on November 1^{st}, 2017 (the day when I commenced my Ph.D. journey) where you introduced me to Sweden, Chalmers, and the Ph.D. project. Out of all the information you gave me that day, I clearly remember you mentioned the "*Open-door policy*". At the end of five years, I can say that whenever I knocked on your office door during these years, I never returned disappointed. I have learned a lot from you including research, teaching, and writing skills. I will definitely miss the enthusiastic discussions we had on the whiteboard in your office and also your assistance with the IEEE TPWRD paper. Alike many Ph.D. students, I also faced low times in the Ph.D. journey, but your motivational words and advice during these challenging times will always be remembered and deserves the highest recognition. Your support during the Covid Pandemic was exceptional.

I also want to thank my co-supervisor Dr. David Steen for his support and encouragement during my entire Ph.D. studies. Your assistance with the technical work and accomplishing tasks despite your hectic schedule deserves the highest appreciation. You always insisted on "*planning*" whether it was tasks, courses, teaching, etc., which I think helped me a lot during these years, and due to that everything went smoothly.

I am greatly indebted to my Ph.D. examiner Prof. Ola Carlson for his guidance, support, and encouragement during this research work. I want to recall some of your words from the interview for this Ph.D. position. Towards the end of the interview, you said to me "*We have long and dark winters in Sweden*", and like many others, I also thought about what's new in that, even in India, winters are darker than summers and nights are longer than a day. But after seeing five "*long and dark winters in Sweden*", I understood how meaningful was that sentence.

I want to specially acknowledge Sweden as a whole. On a lighter note, despite all the learning, you taught me the importance of the sun. You are the best host I can imagine. There is so much to learn in Sweden whether it is closeness to nature, sustainability, recyclability, ethics, neutrality, and more importantly respecting every individual. I would humbly accept that I have learned a lot of new things and developed new habits during these five years.

I would appreciate the support extended by Prof. Massimo Bongiorno and Prof. Yuriy Serdyuk in their role as the division and unit heads, respectively.

Now coming to my wonderful colleagues, I would start by acknowledging Ali Fotouhi who was my office mate for almost three years. I always felt very comfortable discussing any professional or personal things with you and obviously, you always gave an honest opinion and the best suggestions. Your humbleness and readiness to help deserve the highest recognition. I am unable to recall any occasion when I asked you for help or favour and you

said no. I firmly believe that I am fortunate to have you as my friend and office mate during these years.

I also want to mention another very dear friend and colleague Rabindra Mohanty. There is so much to learn from you as a person both technically and otherwise. I cherish our technical discussions related to power systems (especially protection). Your support and help with all other things are extraordinary and will always be remembered.

I am thankful to Kyriaki Antoniadou-Plytaria for being a friend in happiness and distress. You were always ready to help me to any extent for which I admire you the most.

I cannot miss writing about my intelligent and smart friend who is also now the latest Ph.D. degree recipient Hannes Hagmar for your support and friendship. It was a pleasure sharing an office with you during the starting years of my Ph.D. I will especially remember our badminton matches and I wish one day I could beat you in all the matches in a day.

My thankful regards go to another dear friend Georgios Mademlis for being so nice and friendly. I really enjoy our discussions and this is why (if I am not wrong) I have visited most of the places in Gothenburg such as lakes, cafeterias, castles, shopping stores, etc. with you.

I would like to distinctively acknowledge Christos Agathokleous for his friendship and the fun time we had together.

I am grateful to my current office mates Evelina Wikner and Tatiana Santos Andrade for being nice and friendly toward me. Thank you, Evelina, for being patient to answer some of my silly questions and wrong pronunciation of Swedish words. Tatiana, I will always remember how we greeted each other every morning by asking "How's life", even though we knew that nothing much had changed.

I am greatly indebted to Maryam Mohiti, Mohammadreza Mazidi, Mostafa Kermani, Rahmatollah Khezri, Luca Boscaglia, Dimitrios Sagris, Vineetha Puttaraj, Mohammadreza Safaritirtashi, Michela Diana, and Rohini Sharma for your friendship and the nice time we spent together.

I am obliged to Annie Grundevik, Sara Fogelström, Ioannis Bouloumpasis, Anna Wallin, Hanna Youn, Gustavo Pinares, Nima Mirzaei Alavijeh, Junfei Tang, and all other colleagues at the division for providing a pleasant working environment. I want to note my appreciation to colleagues in E2 Ph.D. Council.

My thankful regards go to Dennis Bijwaard and Omar Mansour from Smart State Technology, The Netherlands, and Dr. Abhinav Kumar Singh from the University of Southampton, UK, for their cooperation and support in this research work. Also, I express my sincere thanks to Joni Rossi, Jacqueline Plette, Tran The Hoang, Quoc Tuan Tran, Ulrika Wahlström, Henrik Forsgren, Lucile Lemius, and all other colleagues involved in the EU project UNITED-GRID. Special recognition goes to Frida Barrett who is involved in the FlexiGrid project.

I would thank my friends Shrey Sharma, Tanushree Sahu, Milagros Navarro Navia, Agin Vyas, and Verena Steub for their affection and companionship all these years.

I would also humbly acknowledge my previous mentors Prof. Sydulu Maheswarapu and Prof. Saikat Chakrabarti for their continuous guidance, encouragement, and support.

This acknowledgment would not be completed without mentioning my wife and soulmate Deepanjali Khare. I am blessed to have you as my life partner. I am thankful to you for the support and motivation you gave me and for always believing in me.

Finally, this would not have been possible without the support, encouragement, and

blessings of my parents, Veena Srivastava and Umapati Ram Srivastava. Thank you for always being by my side.

Ankur Srivastava
Gothenburg, Sweden
October 2022

List of Abbreviations

ADC	Analog to Digital Converters
ADMS	Advanced Distribution Management System
AdvSens	Advanced Sensors
AMI	Advanced Metering Infrastructure
ANN	Artificial Neural Network
AQCF	Algebraic Quadratic Companion Form
BESS	Battery Energy Storage Systems
BFS	Backward-forward Sweep
CCVT	Coupling Capacitor Voltage Transformer
CL	Confidence Level
CM	Colour-map
CP	Cumulative Probability
CT	Current Transformer
DAE	Differential and Algebraic Equations
DER	Distributed Energy Resources
DG	Distributed Generation
DMS	Distribution Management Systems
DSE	Dynamic State Estimation
DSEBP	Dynamic State Estimation based Protection
DSEBPS	Dynamic State Estimation based Protection Scheme
DSO	Distribution System Operator
DSP	Digital Signal Processing
EHV	Extra High Voltage
EKF	Extended Kalman Filter
EMS	Energy Management Systems
ESS	Energy Storage Systems
ETIP	European Technology and Innovation Platforms
EU	European Union
EV	Electric Vehicles
GPS	Global Positioning System
HHT	Hilbert–Huang Transform

HV	High Voltage
HVDC	High Voltage Direct Current
ICT	Information and Communication Technologies
IEA	International Energy Agency
IoT	Internet of Things
IRENA	International Renewable Energy Agency
KCL	Kirchhoff's Current Law
KVL	Kirchhoff's Voltage Law
LV	Low Voltage
MC	Model Calculation
MCS	Monte-Carlo Simulation
MG	Microgrid
ML	Machine Learning
MR	Microprocessor Relay
MU	Merging Units
MV	Medium Voltage
NERC	North American Electric Reliability Corporation
OCP	Open-Cross Platform
PCC	Point of Common Coupling
PDF	Probability Density Function
PEV	Plug-in Electric Vehicles
PMU	Phasor Measurement Unit
PPF	Probabilistic Power Flow
PPS	Pulse Per Second
PV	Photovoltaics
PVPS	Photovoltaic Power Systems Programme
QI	Quadratic Integration
REP	Renewable Energy Production
RES	Renewable Energy Sources
RSQ	Research Questions
SA	Surge Arrestor
SBC	Single-board Computer
SC	Sample Collection
SCADA	Supervisory Control and Data Acquisition

SE	State Estimation
SNET	Smart Networks for Energy Transition
SRA	SmartGrids Strategic Research Agenda
SVM	Support Vector Machine
SW	Sliding Window
TB	Toolbox
TRL	Technology Readiness Level
TSO	Transmission System Operator
UGS	UNITED-GRID Solution
UK	United Kingdom
UKF	Unscented Kalman Filter
USB	Universal Serial Bus
VT	Voltage Transformer
WLS	Weighted Least Square
WT	Wavelet Transform

List of Nomenclature

${A_r}^{(p)}$	Current injection at node r for p^{th} iteration
α	Smoothing factor
br	Total number of branches
χ^2	Chi-squares function
constant-pf	Constant power factor mode of PV-inverter
constant-V	Voltage-reactive power mode of PV-inverter
C, C_1, C_2	Constant matrices
C_A, C_B, C_C	Capacitances of phase A, B, C
C_{AA}, C_{BB}, C_{CC}	Self-capacitances of phase A, B, C
C_{AB}, C_{BC}, C_{CA}	Mutual-capacitances between phase A, B, C
C_J	Capacitance of a transmission line
η	Measurement error vector
E_1, E_2, E_3, E_4, E_5	Constant quantities
F_1, F_2, F_3, F_4, F_5	Constant quantities
G_A, G_B, G_C	Conductance of phase A, B, C
H	Jacobian matrix
h	Component health
${I_q}^{(p)}$	Current in branch q for p^{th} iteration
${I_{rQ}}^{(p)}$	Reactive current injection at node r for p^{th} iteration
i_J	Sampled value of sending end current
i_j	Sampled value of receiving end current
i_A, i_B, i_C	Sampled values of sending end currents of phase A, B, C
i_a, i_b, i_c	Sampled values of receiving end currents of phase A, B, C
i_{dA}, i_{dB}, i_{dC}	Currents in series branches of phase A, B, C
J	Original objective function of state estimation
J^f	New objective function of state estimation
kWp	Kilowatt peak
k	Integration time step
K_{P_P}	Constant representing P proportion for active power load
K_{Q_P}	Constant representing P proportion for reactive power load
K_{P_I}	Constant representing I proportion for active power load

K_{Q_I}	Constant representing I proportion for reactive power load
K_{P_Z}	Constant representing Z proportion for active power load
K_{Q_Z}	Constant representing Z proportion for reactive power load
L_A, L_B, L_C	Reactances of phase A, B, C
L_{AA}, L_{BB}, L_{CC}	Self-reactances of phase A, B, C
L_{AB}, L_{BC}, L_{CA}	Mutual-inductances between phase A, B, C
L_J	Inductance of a transmission line
μ	Mean for PV and load forecast
m	Number of measurements
M_1, M_2, ..., M_6	Constant quantities
$m - n$	Degrees of freedom
n	Number of state variables
N	Total number of nodes
p	Probability of estimation confidence
P	Active power
P_x	Estimated covariance
P_0	Rated active power
P_v	Process noise covariance matrix
P_w	Measurement noise covariance matrix
P_{xv}	Cross-correlation between the x and v
P_{inj}	Active power injection
P-Q	Load nodes
P-V	Generator nodes
Q	Reactive power, Covariance matrix for process noise
Q_0	Rated reactive power
Q_{inj}	Reactive power injection
Q_{rL}	Total reactive power load at node r
${Q_{rR}}^{(p)}$	Total reactive power requirement at node r for p^{th} iteration
R	Measurement weight matrix, Covariance matrix for measurement noise
R_A, R_B, R_C	Resistances of phase A, B, C
R_{AA}, R_{BB}, R_{CC}	Self-resistances of phase A, B, C
R_{AB}, R_{BC}, R_{CA}	Mutual-resistances between phase A, B, C
R_J	Resistance of a transmission line
R_1, R_2, S_1, S_2	Constant matrices

S_{rated}	Rated apparent power
S_r	Apparent power load at node r
σ	Standard deviation for PV and load forecast
$\sigma_1^2, \sigma_2^2, \ldots, \sigma_m^2$	Error associated with different measurements
$\sigma_{V_{wA}}, \sigma_{V_{wB}}, \sigma_{V_{wC}}$	Standard deviation of pseudo-process noise
$\sigma_{I_{wA}}, \sigma_{I_{wB}}, \sigma_{I_{wC}}$	Standard deviation of measurement noise
t	Total number of branches connected at node n
t, $t-k$	Time instants
T	Sampling time
u	Pseudo inputs
V	Voltage
V_0	Rated voltage
$V_r{}^{(s)}$	Specified voltage value at node r
$\Delta V_r{}^{(p)}$	Voltage magnitude mismatch at node r for p^{th} iteration
$V_r{}^{(p-1)}$	Voltage of node r for $(p-1)^{\text{th}}$ iteration
v_J	Sampled value of sending end voltage
v_j	Sampled value of receiving end voltage
v_A, v_B, v_C	Sampled values of sending end voltages of phase A, B, C
v_a, v_b, v_c	Sampled values of receiving end voltages of phase A, B, C
V_{wA}, V_{wB}, V_{wC}	Pseudo process noise
V_{yA}, V_{yB}, V_{yC}	Measured values of inputs
v	Process noise
w	Measurement noise
X	Augmented state vector
x	State vector
χ	Sigma points
Y_r	Admittance at node r
$y(t)$	Considered function
z	Measurement vector
ZIP load	Combination of Z, I, and P load
Z_q	Impedance of branch q
Z	Real and constant impedance matrix

Contents

CHAPTER 1

Introduction

This chapter discusses the background of the presented research work along with the research questions identified and addressed in the thesis. Furthermore, the aim and scope of the thesis along with the main contributions of the research work are presented together with the resulting scientific publications.

1.1 Background and Motivation

With the growing concern about global warming and climate change, the universal focus has been on the transition toward low-carbon energy systems. Among the various trends associated with this transition, the replacement of conventional fossil fuel-based power generation with renewable energy sources (RESs) has been the major technological shift in the last decades. The other trends include the use of demand response resources, energy storage systems (ESSs), electric vehicles (EVs), and information and communication technologies (ICT) in distribution systems. The inclusion of these trends and technologies into today's power systems leads them towards the future's power systems. Along with the power systems, the distribution systems are also witnessing drastic changes and transitioning toward the future's intelligent distribution systems. Some of these changes bring several challenges to the power systems such as high uncertainty associated with renewable generation which makes the real-time balance of generation and load more difficult, reduced system resiliency due to lower system inertia, issues associated with the electrification of the transportation sector (i.e., an increasing number of EVs), protection and control challenges, etc. [1].

Sweden has also been instrumental in its efforts, both in RES installation and sales of EVs. Between 2018 - 2019 and 2019 - 2020, Sweden saw an approximately 70% and 50%

increment in the number of grid-connected solar photovoltaic (PV) systems, respectively. These increments have led to the total installed solar PV capacity in Sweden to 698 MW by 2019 (which comprises approximately 1.5% to 2% of the total installed electricity generation capacity) and 1090 MW by 2020 (which comprises approximately 2.5% of the total installed electricity generation capacity) [2], [3]. The installed wind power capacity in Sweden has increased from 241 MW to 8984 MW during 2000-2019 [4], [5]. With regard to EVs, Sweden has been the third most advanced market worldwide in terms of sales, while its sales share has been 6.3% in 2017, 8% in 2018, 30% in 2020, and 43% in 2021 [6]–[9].

Distribution systems are also one of the main focus areas and will play a new role as a market facilitator to integrate a large share of RES. They will become more complex as a cyber-physical ecosystem which would require an integrated paradigm for energy management and control systems based on various data resources. With the customers playing a central role in enabling integrated and flexible solutions that contribute significantly to reducing uncertainty from stochastic renewables and distributed energy resources (DERs), distribution system operators (DSOs) are envisioned as a crucial entity to enable a successful energy transition by providing a high-quality service to all customers. This will require a stronger linkage between competitive technologies and services for distribution systems in a fast-evolving energy market. A synergy between power technology research and energy market development, if developed properly, will lay a foundation for intelligent distribution systems.

The European Technology and Innovation Platforms (ETIPs) through Smart Networks for Energy Transition (SNET) had come up with Vision 2050 [10], where it is mentioned that the security of the energy supply in Europe is guaranteed by minimizing the fossil-fuel imports which are achieved by increasing share of wind, solar PV, hydro, and biomass as main sources of renewable based power generation, energy efficiency policies, and producing low-carbon fuels within Europe. The reliability and resilience of the whole European, regional, and local systems are guaranteed by [10]:

- Integrated Energy Systems, where the electrical energy systems are the backbone, designed and operated to avert or reduce the contingencies effects, with black-start capabilities activated within a few minutes for local and regional systems.
- Consideration of risk (weather and other hazards) assessment and mitigation measures in the planning and operation of the system.
- Fully inter-operable and networked sub-systems leading to seamless operation and facilitating the optimal coupling of all energy carriers.
- Integration of peer-to-peer transactions with the centrally- and locally-controlled electricity systems.

The integration of RES into the electric distribution systems increases the complexity of the operation, control, and protection of the system. These trends are expected to continue in the future as RES, mainly solar and wind, are becoming the cheapest source of power generation in the last decade in most parts of the world [11], [12]. The International Energy Agency (IEA) through Photovoltaic Power Systems Programme (PVPS) presented in the 2017 annual report that solar PV is now the fastest-growing energy technology [13]. According to their 2022 report [14], an estimated 175 GW PV capacity is installed worldwide in 2021, which raises the cumulative installed PV capacity to 942 GW at the end of 2021. There have been similar trends in EV sales, the sales of EVs have doubled in 2021 to a

record number of 6.6 million EVs, while the global stock of EVs has now crossed the mark of 16.5 million vehicles which is triple the number in 2018 [9].

These new market actors and technologies in distribution systems bring several problems for the DSOs such as uncertainty associated with renewable energy production which makes it difficult for the operators to balance the real-time generation and load. Another problem is related to network congestions and voltage issues due to the high penetration of RES and more uncertain loads. Further, the large-scale integration of renewables might lead to the failure of various existing protection schemes/methods due to phenomena such as bi-directional power flow, fault current limitation, etc. The increasing growth rate of EVs could be challenging for the DSOs to flatten the load curve or avoid peak load. Also, the increased participation of customers in the intra-day or day-ahead electricity market for demand response, flexibility provisions, selling of excessive generation, etc. The concept of peer-to-peer transactions would add further complexity to the system. Cyber-security which is associated with the integration of ICT into the systems has also been one of the concerns.

1.2 Research Questions

With the background and motivation related to the future power systems presented in Section 1.1 along with the challenges identified in Section 2.1 and extensive state-of-the-art review in Section 2.2, the following research questions (RSQ) have been identified and addressed in this thesis:

- **RSQ-1**: How can the DSOs evaluate their future-readiness along with the associated key indicators in order to prepare themselves for a smoother transition toward future intelligent distribution systems?
- **RSQ-2**: How can the network congestion be forecasted and visualized in distribution systems along with key factors and relevant indicators with high penetration of RES and more uncertain load for maintaining reliable, economical, and efficient operation?
- **RSQ-3**: What are the advantages and limitations associated with the protection scheme based on advanced measurement technologies and dynamic state estimation as compared to the existing schemes for the protection of transmission lines?
- **RSQ-4**: How can a decentralized, accurate and easily implementable dynamic state estimation method be developed for the transmission lines which consider their nonlinear dynamics and does not employ linearization techniques?

1.3 Aim and Scope of the Thesis

The aim of this thesis is the development and validation of advanced support tools and methods for system operators in the context of their transition from today's power systems towards the future's power systems. The development of a future-readiness assessment framework would assist the DSOs in system planning by assessing their current status and preparedness for future transition, the development of advanced congestion forecast tool will support the DSOs in system operation by forecasting the network congestion and voltage issues, the implementation and experimental validation of the DSE based protection scheme

to offer the system operator a novel protection scheme that can handle the existing challenges and limitations with conventional protection schemes and support them in operating their network more reliably and securely, and finally development of a decentralized dynamic state estimation method for transmission lines to assist the system operator in monitoring aspects by accurately tracking the operating point and have potential applications in transmission line monitoring, control, and protection.

The scope and limitations of the advanced support tools and methods developed and validated in this thesis are as follows:

- The development of the future-readiness assessment framework presents the assessment results for three DSOs in Europe which could be seen as examples for the other DSOs. However, these assessment results cannot be generalized to other DSOs in Europe.
- Concerning the advanced congestion forecast tool, it is assumed that the test systems studied in the thesis are balanced, PV production and load forecast data to be provided by the respective services, and, test system data and preferences provided by the DSOs. The current version of the tool uses the BFS method for obtaining the power flow results which is one of the best solutions for radial distribution systems but in the case of meshed/closed loop systems, different methods (such as Newton-Raphson, etc.) should be employed.
- Regarding the experimental validation of the DSE-based protection scheme, the validation is carried out using a scaled-down model of a simple power system. Some of the results might differ when the scheme is employed in the real power system. Further, communications play an important role in this scheme which is assumed to be available uninterruptedly and without latency.
- With regard to the development of the decentralized DSE of transmission lines, the method does not require communications to evaluate the operating conditions of a transmission line locally but it requires communications when the operating states are needed to be sent to a central control center for other applications.

1.4 Main Contributions

The main contribution of this thesis could be outlined as follows:

- The development of a **future-readiness assessment framework** contributes to addressing the challenges associated with the **planning** of future power systems as the DSOs can assess the current status and future-readiness of their network. In the development of the framework, a set of key indicators are identified which would have major impacts on the DSOs in the future and then present their assessment based on inputs from the DSOs. The output from this framework along with the description of the plausible scenarios would serve as an input for identifying the policy recommendations, pathways development, and finally a transition plan for the DSO along with the identification of vital areas of development on which they should focus for a smoother transition towards the future distribution systems.
- An **advanced congestion forecast tool** with visualisation capability contributes to addressing the **operational** challenges in future power systems by forecasting

network congestion and voltage issues in distribution systems with a high penetration of renewables. To incorporate the uncertainties in the distribution systems, the probabilistic power flow framework has been utilised with PV production and load forecast as inputs. In addition, advanced load models and operating modes of photovoltaic inverters have been incorporated into the tool. Node voltages, branches, and transformers loading levels are chosen as indicators for forecasting network congestion. Cumulative probability-based contour plots and colour-map are proposed as part of the tool's visualization functionality to inform the DSO of the location and severity of congestion in the network as well as in specific components. The proposed advanced congestion forecast tool will assist the DSO in daily congestion management and network planning, depending on the forecast horizons. In short forecast horizons, the DSO will be enabled with timely congestion management by employing market and tariff-based flexibility solutions. It would result in enhancement of the system's resilience, mitigation of equipment ageing due to overloading, reducing the high additional congestion cost, and other economic benefits, while long-term forecast horizons (e.g., several months or years ahead) will allow the DSO to procure flexibility for avoiding costly grid reinforcement. The visualization platform provided by the tool will facilitate the effective supervision of the desired network operation via an on-time and user-friendly indication of the expected network congestions. Therefore, the implementation of the developed tool will result in reduced cost for grid reinforcement and purchasing flexibility resources for the DSOs.

- The implementation and experimental validation of a **dynamic state estimation based protection scheme** (DSEBPS) for a transmission line along with the practical application of advanced sensors at Chalmers power system laboratory contribute to addressing the **protection** challenges in future power systems. The scheme performs dynamic state estimation with high-frequency measurements provided by the sensors, assesses the operating condition (i.e., health) of the transmission line in real-time, and thereby determines the tripping signal whenever a fault is detected. The validation was carried out in two steps, first with simulation studies and then with the experimental implementation using a physical scaled-down model of a power system consisting of transmission lines, transformers, and loads. The lack of coordination and the absence of complex relay settings in DSEBPS could result in a significant reduction in misoperations due to incorrect relay settings (which is one of the major causes of misoperations).
- The development of an **unscented Kalman filter (UKF) based DSE method** for transmission lines contributes to addressing the **monitoring** aspects in future power systems by estimating the remote end state variables with reduced complexity, higher accuracy, and easier implementation of the decentralized estimator. The main advantages associated with the proposed method are the ease of measurement of all the signals required by the state estimation algorithm (i.e., voltage and current at the local end) using PMUs/MUs, high accuracy and speed of estimation as the estimation model does not require any approximations or linearizations and the exact nonlinear dynamics of the transmission line are captured, no communication infrastructure is required and thus any communication failure, latency, packet loss, etc., will not have any impact on the quality of estimation, no inter-dependency between transmission lines as the estimation process for a transmission line is independent of the other line

which keeps any estimation errors remain segregated and thus makes them easier to identify, and estimation works with flat start or zero initial values which means that the estimation accuracy does not depend on the accuracy of initialization.

1.5 Thesis Outline

The remaining thesis is organized as follows:

- **Chapter 2** presents the challenges behind the development of the developed tools and methods and the extensive review of the state-of-the-art associated with them.
- **Chapter 3** presents a future-readiness assessment framework for the DSOs with the identification and evaluation of key indicators associated with the transition. The comparative assessment between the three distribution system operators (from France, The Netherlands, and Sweden) participating in the UNITED-GRID project is presented. The analysis of different future scenarios for electricity production in Sweden is presented. The impact of the regulations on future intelligent distribution systems is identified and presented. Finally, the pathways which could lead the DSOs to make a smoother transition toward the future are presented.
- **Chapter 4** explains the advanced congestion forecast tool which would assist the DSOs by forecasting congestion in their networks. Various case studies with two real distribution systems i.e, 7-bus feeder and 141-bus system have been performed and their results are presented. Further, the process details of seamless integration of the tool in the existing distribution management systems of the DSOs via an IoT platform Codex Smart Edge of Atos Worldgrid are presented.
- **Chapter 5** details the concept and modelling of a DSE-based protection scheme for a transmission line. Further, the simulation results for different fault types and conditions are presented and discussed.
- **Chapter 6** presents the details of the experimental setup associated with the validation of the dynamic state estimation based protection scheme at Chalmers power system laboratory supported by advanced measurement technologies developed by Smart State Technology. The detailed experimental validation results of different case studies are presented. A discussion on the performance of the scheme under special operating conditions is also presented. The advantages associated with the open platform and aspects related to the real-world application of the scheme are explained. Finally, a discussion related to the processing time of the scheme during the experimental validation is presented.
- **Chapter 7** presents the introduction and development of the unscented Kalman filter-based decentralized dynamic state estimation method for transmission lines. The simulation results with realistic parameters of a transmission line with a nominal voltage of 345 kV are presented and discussed.
- **Chapter 8** concludes the thesis, presents the recommendations for utilization of research results, and identifies the plan for future research work.

1.6 List of Publications

The peer-reviewed publications originating from this thesis are:

Journal Publications

[A] **A. Srivastava**, L. A. Tuan, D. Steen, O. Carlson, O. Mansour, D. Bijwaard, "Transmission line protection using dynamic state estimation and advanced sensors: Experimental validation," *in Early Access, IEEE Transactions on Power Delivery*, 2022. **DOI**: https://doi.org/10.1109/tpwrd.2022.3184479.

[B] **A. Srivastava**, D. Steen, L. A. Tuan, O. Carlson, I. Bouloumpasis, Q. T. Tran, L. Lemius, "Development of a DSO support tool for congestion forecast," *IET Generation, Transmission & Distribution*, vol. 15, no. 23, pp. 3345-3359, Aug. 2021. **DOI**: https://doi.org/10.1049/gtd2.12266.

[C] J. Rossi, **A. Srivastava**, T. T. Hoang, Q. T. Tran, M. Warneryd, "Pathways for the development of future intelligent distribution grids," *Energy Policy*, vol. 169, Oct. 2022. **DOI**: https://doi.org/10.1016/j.enpol.2022.113140.

[D] **A. Srivastava**, L. A. Tuan, D. Steen, O. Carlson, O. Mansour, D. Bijwaard, "Dynamic State Estimation based Transmission Line Protection Scheme: Extended Experimental Validation with Different Fault Types and Conditions," *in Revision, International Journal of Electrical Power & Energy Systems*, June 2022.

Conference Proceedings Publications

[E] **A. Srivastava**, D. Steen, L. A. Tuan, O. Carlson, "A congestion forecast framework for distribution systems with high penetration of PVs and PEVs," in *Proc. IEEE Milan PowerTech*, 2019, pp. 1–6. **DOI**: https://doi.org/10.1109/PTC.2019.8810871.

[F] **A. Srivastava**, D. Steen, L. A. Tuan, O. Carlson, *et. al.*, "A DSO support framework for assessment of future-readiness of distribution systems: technical, market, and policy perspectives," in *Proc. CIRED* 25^{th} *International Conference and Exhibition on Electricity Distribution*, Madrid, 2019. **DOI**: http://dx.doi.org/10.34890/832.

[G] K. A. Plytaria, **A. Srivastava**, M. A. F. Ghazvini, L. A. Tuan, D. Steen, O. Carlson, "Chalmers campus as a testbed for intelligent grids and local energy systems," in *Proc. IEEE International Conference on Smart Energy Systems and Technologies (SEST)*, Porto, 2019, pp. 1-6. **DOI**: https://doi.org/10.1109/SEST.2019.8849014.

[H] J. Rossi, **A. Srivastava**, D. Steen, L. A. Tuan, "Study of the European regulatory framework for smart grid solutions in future distribution systems," in *Proc. CIRED 2020 Workshop*, Berlin, 2020. **DOI**: https://doi.org/10.1049/oap-cired.2021.0230.

[I] **A. Srivastava**, R. Mohanty, M. A. F. Ghazvini, L. A. Tuan, D. Steen, O. Carlson, "A review on challenges and solutions in microgrid protection," in *Proc. IEEE Madrid PowerTech*, 2021, pp. 1–6. **DOI**: https://doi.org/10.1109/PowerTech46648.2021.9495090.

Other publication by the author, not included in this thesis, is:

[J] **A. Srivastava**, S. Chakrabarti, J. Soares, S. N. Singh, "An Optimization-Based Topology Error Detection Method for Power System State Estimation," *Electric Power Systems Research*, vol. 209, August 2022. **DOI**: https://doi.org/10.1016/j.epsr.2022.107914.

CHAPTER 2

Challenges and State-of-the-Art

This chapter presents the challenges to identify the research questions in this thesis. Further, the detailed state-of-the-art for these research questions is presented to highlight the contribution of the work presented in this thesis. The content presented in this chapter is partially based on the work published in Paper A, B, C, D, E, F, G, and I.

2.1 Challenges

This section discusses the challenges associated with the future-readiness assessment, network congestion problems, microgrid protection, transmission line protection, and transmission line monitoring.

2.1.1 Future-readiness Assessment

After the transformational era of deregulation in the power industry and growing concern towards global warming, electrical distribution systems are becoming more complex, hosting new market actors along with emerging technologies, e.g., distributed renewable generation, ESSs, EVs, demand resources, and ICT. The new market actors and technologies in distribution systems bring several challenges for the DSOs such as uncertainty associated with renewable energy production, network congestion, etc. Another challenge is associated with the growth rate for EVs. Increased participation of customers in the intra-day or day-ahead electricity market and the future concept of peer-to-peer transactions would add further

complexity to the system. Cyber-security which is associated with the integration of ICT into the systems has also been one of the concerns.

All distribution systems are either going through this paradigm shift or will go through it in the future and thus, would be posed with challenges in managing their day-to-day operation and control strategies. DSOs need to prepare for a transition path from today's passive systems to future intelligent distribution systems by making a strategic investment in network infrastructure, upgrading monitoring and control systems, introducing novel business models, and making policy and regulation changes to enable the active participation of market actors in the overall network management. Hence, DSOs need an assessment framework to evaluate their future-readiness and consecutively identify development gaps for plausible future scenarios and eventually make themselves ready.

2.1.2 Network Congestion

Global warming concern leads the transition from fossil fuels to RES for the generation of electricity. The European Green Deal envisions Europe to be climate-neutral by 2050 through maximizing the deployment of renewables and fully decarbonizing the energy supply [15]. The International Renewable Energy Agency (IRENA) and European Commission in their REmap analysis in [16] have identified that the European Union has the potential to generate 50% of the total electricity generation from renewables by 2030. Under this scenario, wind power would account for 21% (783 TWh) and solar PV for 8% (281 TWh) of the total generation. Similar trends for increasing renewables share could be seen for other countries as well.

Across the globe, multiple incidents related to network congestion are reported in [17]–[19] due to the higher penetration of RES. A study on congestion events in the distribution systems caused due to RES in Germany is presented in [20]. The study further presents that due to increasing RES penetration the total amount of energy curtailment in 2014 was the same as the aggregated amount from 2009 to 2013 and it is growing further. It mentions that the German Federal Network Agency reported that the majority of this curtailment (92.2%) was on the distribution grid side as most of the RES is connected here. The work presented in [21] shows how the battery energy storage systems (BESS) could aggravate the network congestion issues. It occurs when BESS starts charging as soon as the surplus power (after self-consumption) is available, leading to a full charge before the peak PV production occurs during the day. Thus, during the peak PV production, the power is being fed into the grid and which causes network congestion.

Due to the anticipated increased penetration of RES in distribution systems and more uncertain loads such as heat pumps, electric vehicles, etc., the DSOs are expected to face increasing component congestion and voltage variation issues in their networks [22]. In addition to such operational problems, the DSOs are also likely to face issues such as loss of life of the network components (transformers, distribution lines, and cables), the need for grid reinforcement and/or flexibility services, RES generation curtailments due to network constraints, generation scheduling [23], [24], etc. A study presented in [25] has estimated that Sweden, Germany, and the UK with their current grid capacity can supply 24%, 60%, and, 21% respectively, of the annual net electricity consumption from residential solar PV. Thus, if the PV generation exceeds the anticipated amount then it could lead to operational challenges like network congestion etc, as mentioned before.

2.1.3 Microgrid Protection

Microgrids (MGs) may have bidirectional power flow, wide operational range, etc. and can operate as a controlled entity both in grid-connected and islanded modes. MG can be classified into radial and ring-type networks. From a protection point of view, the power flow in a radial network is unidirectional, while in the case of a ring network it could be bidirectional. In the case of radial systems with distributed generation (DG) interconnection downstream, the power flow could also be bidirectional. Thus, the MG protection schemes developed for ring networks are also suitable for radial networks. The main challenges which drive the need to revisit the conventional protection schemes include the following:

- High penetration of RES may lead to reverse power flow or bi-directional power flow, which causes relay coordination problems and failures in the conventional protection schemes with no directional element [26]–[28]. Due to the presence of multiple DGs, loads will be fed by DGs which are close to their locations. This violates the assumption that the distribution systems are radial and the fault current is unidirectional. Thus, the conventional overcurrent protection schemes might fail to operate and are required to be direction sensitive as in the case of multi-source systems.
- Changes in the mode of operation of MGs from grid-connected to islanded mode and vice-versa could have a substantial impact on the short-circuit level due to a change in equivalent impedance [29], [30].
- Fault current limitations by the converter-based DGs could lead to undetected fault, voltage and frequency problems during islanding, etc. Due to the converter capacity limitation of DGs, they contribute limited fault current during fault conditions which makes it difficult for the conventional overcurrent relays to detect the fault and in some cases, it takes more time to respond. Regarding the voltage and frequency problems, if the microgrid gets islanded due to a fault then its voltage and frequency cannot be controlled by the grid. In the case of small embedded DGs, the voltage control problem is more significant in case of absence of any voltage control equipment. Further, the voltage level increases and frequency remains unstable leading to power quality issues for consumers [31], [32].

2.1.4 Transmission Line Protection

Protection against undesirable events is one of the important functions in power system operation. It is also important from the perspective of system reliability, continuity of power supply, and personnel safety. North American Electric Reliability Corporation (NERC) has reported that approximately 10% of protection operations are misoperations that lead to interruptions [33]. Across NERC from 2012 to 2014, 31% of misoperations occurred due to incorrect settings, 19% due to relay failures, and 13% due to communication failures which in total accounts for 63% of the total misoperations [33]. Further, the unusual fault current and voltage characteristics from inverter-interfaced renewable resources also bring challenges to conventional protection schemes [29], [34].

The conventional schemes employed for the protection of extra-high voltage (EHV) and high voltage (HV) transmission lines include e.g., distance, pilot relaying, directional overcurrent, line differential, etc. The preferred (trend of) scheme for the EHV and HV level

transmission lines is line differential protection along with distance protection. Sometimes, the teleprotection schemes such as Permissive Overreach Protection, Permissive Underreach Protection, Blocking Overreach Protection, and Accelerated Underreach Protection with line differential and distance protection. Further, the automatic reclosing function is also used for all the EHV and HV transmission lines to be in compliance with national grid codes [35].There are some limitations associated with these protection schemes which might lead to misoperation. The work presented in [36] has identified the limitations of these protection schemes and also the protection gaps which exist in transmission systems. A few highlights related to the limitations of the conventional protection schemes employed in transmission systems are,

- Distance and directional overcurrent schemes require complex coordination and the simultaneous tripping of both ends is not possible.
- Both pilot relaying and line differential schemes require communication infrastructure and its failure could lead to misoperation [36].
- Although differential protection is successfully implemented and working in transmission systems, there still exist protection gaps such as relay desensitization due to capacitive currents in long transmission lines [37], detection of high impedance faults (especially in long transmission lines), and failure in case of communication loss.

The following additional challenges also exist in the transmission line protection domain:

- Most of the existing line distance protection and line differential protection solution are based on phasor-domain calculations. Normally, their speed is around one power frequency cycle. In order to accelerate the speed, time-domain protection solutions are required which have higher speed and take less than half power frequency cycle such that all the demands are met in dependability.
- Schemes with good reliability are required for special applications such as line distance protection for series compensated lines, multi-circuit lines, etc.
- The existing line distance protection faces new challenges with increasing RES being connected to the conventional grid, especially with grid-connected wind and PV farms as the voltage and current might have large distortions and harmonics during fault conditions.

2.1.5 Transmission Line Monitoring

Climate change and global warming concerns have led to a transition from fossil fuel-based power generation to sustainable and environment-friendly renewables-based generation. Simultaneously, with the increase in electrification and load demand, the transmission system components are operated close to their operating limits. These changes (along with several other changes) pose the following main challenges related to the operation of the transmission systems [38]–[40]:

- Renewable energy sources (RES) are characterized as stochastic, intermittent, non-synchronous, and power electronics interfaced. These characteristics make their operation and control more challenging, particularly, it is difficult to accurately track the system operating point.

- Due to increasing RES penetration and electrification of different energy sectors, the prediction of power flow patterns in transmission systems is an uphill task as compared to centralized fossil fuel-based power generation.
- The operation closer to the operating limit of components could stress the transmission systems which could also lead to partial power demand failure or blackouts.

Traditionally, such issues were handled using the control and monitoring tools available with the energy management systems (EMSs). However, such tools have become inadequate mainly due to the slow update rate of SCADA systems within EMSs, and results based on steady-state models do not capture the fast system dynamics. The large-scale deployment of phasor measurement units (PMUs) in the last decades addressed some of the issues associated with fast capturing of system dynamics and the evaluation of online dynamic security assessment [41]. Most of these works are based on dynamic state estimation (DSE) which is essential for time-critical operation, monitoring, and control of transitioning power systems [42]. There have also been some observable solutions that use artificial intelligence and machine learning techniques together with modern communication technology and GPS-based time synchronization, for online stability monitoring. At the same time, transmission lines, which are one of the important components in transmission systems, also require proper control and estimation mechanisms for real-time condition monitoring, fault location, and protection.

2.2 State-of-the-Art

This section presents an extensive review of the state-of-the-art related to tools and methods which are developed and validated in this thesis.

2.2.1 Future-Readiness Assessment Framework

With regards to the challenges identified in Section 2.1.1, the researchers working in various fields have taken up research problems similar to future-readiness assessment framework by proposing different versions of assessment frameworks. For instance, in [43]–[45], a performance indicators-based framework has been proposed for evaluating the performance of engineering faculty, proactive performance monitoring scheme, and, the performance of technological audit at the firm's level, respectively. In [46], a framework is developed for the classification of smart city performance indicators and then identifies technologies and actions needed for city management and planning toward urban growth. In [47], a big data framework has been developed for the assessment of electric power data quality. A framework has been used in [48], where DSO controls have been assessed in the non-binding transactive energy market. Although several questions are raised in [49], which relate to market and policy perspectives for flexibility use to DSO in order to manage embedded microgrids and islanded power systems, still a well-developed assessment framework for evaluating the future-readiness of DSOs is required.

Based on the challenges identified in Section 2.1.1 and above state-of-the-art review, **RSQ-1** related to the evaluation of future-readiness of the DSOs has been identified and presented in Section 1.2.

2.2.2 Advanced Congestion Forecast Tool

With regards to the challenges identified in Section 2.1.2, there has been extensive ongoing research for congestion management in distribution systems. For instance, in [50], a real-time congestion management method based on the flexibility services from electric vehicles and heat pumps is proposed. The method expects that the DSO has the ability to forecast network congestion. The need for such forecasts is also emphasized in [51], which mentions that with regard to market-based congestion management models relying on flexibility, forecasting the volume of congestion would require load forecasting and state estimation of the distribution system. In [52], a distributed optimization-based dynamic tariff method is proposed for congestion management, which requires the inputs of the congestion forecast, but the method and the characteristics of such a congestion forecast are not presented in detail. Similarly, a multi-objective congestion management approach is proposed in [53] which utilizes the generation rescheduling and load shedding along with the inclusion of voltage-dependent load models.

The current practices related to solving the network congestion problem in Sweden mostly involve grid reinforcements, although the distribution systems have been relatively well-dimensioned here. Due to the relatively long process for grid reinforcements as compared to the rapid evolution of distributed generation and load, the problem of network congestion within distribution systems has become a critical and emerging issue in the very near future.

Most of these works have either mentioned the need for the congestion forecast or have simply assumed that the DSOs have the capability to forecast the congestion. From these discussions, it is evident that there is an emerging interest in a solution for a fast and accurate congestion forecast which can forecast congestion in different time horizons. An accurate congestion forecast would allow the DSOs to efficiently manage the network congestion by employing their desired congestion management methods.

A few research works have addressed the congestion forecast issue, e.g. [54], in which a probabilistic method is developed for detecting and ranking the congested lines to help network operators. A congestion forecast framework is proposed in [55], which considers only snapshot data of system uncertainties with limited visualization of network congestion. However, what is expected to be primarily needed by the DSOs in the coming years is a compact tool that can forecast network congestion on different timescales and has interactive visualization capabilities. Further, the inclusion of other operating conditions such as PV-inverter operating modes and load models within such congestion forecast tool would be an enhancement for the DSOs.

The probabilistic approach is widely accepted for modelling uncertainties. Several research works have used this approach for different applications. As in [56], a probabilistic algorithm is developed to evaluate the capacity of power reserve for a system with high PV penetration. The authors in [57] used it for the evaluation of the maximum integration limits for distributed generations with voltage constraints. A simplified version of the backward-forward sweep (BFS) method, which employs a Gaussian mixture distribution, is proposed to solve probabilistic power flow (PPF) more efficiently to be used for the planning of LV networks in [58]. Similarly, a new probabilistic method is proposed in [59], which is based on quasi-static time-series analysis in combination with the golden section search algorithm to prevent reverse power flow in distribution systems due to PV integration. The impact of uncertainty associated with DERs is analyzed in [60], and the benefits of installing microgrids to address such challenges are also demonstrated. Thus, the probabilistic approach is utilized for

addressing several research problems in the distribution systems; however, most of the existing works have not addressed the research problem associated with the forecasting of network congestion.

On the commercial side, among the available solution's for the advanced distribution management system (ADMS) such as Network Manager by Hitachi ABB [61], Spectrum Power^{TM} by Siemens [62], EcoStruxure^{TM} by Schneider Electric [63], etc., provide functionalities such as DERs production forecast, demand forecast, state estimation, load flow, protection, etc. In general, most ADMS solutions have several advanced functionalities which are associated with the evolution of distribution systems. However, the congestion forecasting functionality especially on short-term forecast horizons or near real-time is not explicitly included or addressed in these ADMS solutions. In the case of long-term forecast horizons (such as over years) such functionalities are available since the 1980s through the network information systems and later through ADMS but they are mainly used for planning purposes.

Today, the DSOs are not equipped with congestion forecast tools, at least at an operational level. However, some DSOs may have already invested in research approaches to develop similar tools, driven by the expected increased congestion incidents. Thus, keeping in mind today's and future need of the DSO, a novel congestion forecast tool is required which can accurately forecast the congestion levels in their network.

Based on the challenges identified in Section 2.1.2 and above state-of-the-art review, **RSQ-2** related to the development of congestion forecast tool for distribution systems has been identified and presented in Section 1.2.

2.2.3 Challenges and Solutions in Microgrid Protection

With regards to the challenges identified in Section 2.1.3, there is ongoing research to address these protection challenges in MG. Some researchers have proposed new methods that are based on traditional protection principles such as adaptive overcurrent, directional overcurrent, Undervoltage, fault loop impedance, and sequence component. Simultaneously, in the era of the evolution of new techniques such as machine learning (ML), data-mining, the Internet of things, synchrophasors, multi-agents, etc., researchers are also utilizing these promising techniques in addressing the protection challenges in MG. Some research works in [31], [32], [64], [65] have presented a review of the protection schemes in MG. However, still, a categorical review of MG protection schemes based on traditional protection principles and special techniques is missing.

To address the aforementioned gap, this work presents a categorical review of various traditional protection principles based schemes proposed for MG. Also, a comprehensive review of protection schemes that applies special techniques in addressing the challenges, is presented in the chapter. A comparative assessment with general advantages, areas of improvement, and potential applications for the different protection categories are also presented to summarize the review work.

2.2.3.1 MG Protection Schemes based on Traditional Protection Principles

This section reviews the MG protection schemes for both grid-connected and islanded modes of operation, which are developed based on traditional protection principles.

Due to the protection challenges as discussed in Section 2.1.3, the conventional protection schemes are required to be re-designed for MG. The relay protection settings would be different and depend on the operating mode of MG. There are also adaptive protection schemes that are suitable for both grid-connected and islanded operating modes. These protection challenges in an MG are addressed through the following protection schemes. The schematic of a grid-connected MG with different components is presented in Figure 2.1.

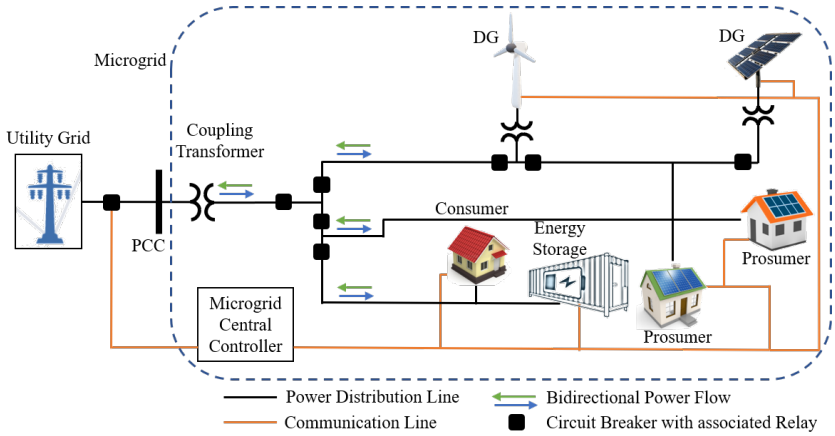

Figure 2.1: Schematics of intelligent microgrid with different components.

Protection Schemes for Grid-connected Microgrid

- *Current-based Protection Schemes*: Current-based protection schemes includes overcurrent, differential, current-only directional principles. An adaptive phase current-based protection method is proposed in [26]. The effect of the high penetration of DGs on relay coordination is explored first. Subsequently, fault detection is performed using the current contribution information from all the sources, including the main grid. The faulted section is identified by the pre-calculation of the Thevenin equivalent impedance of each source for different fault types.

  A protection strategy is presented in [66] where the MG is not disconnected from the main grid in case of an MG fault. The overcurrent relay performs correctly and selectively clears the fault due to the large fault current supplied by the grid. For a fault on the grid side, the MG gets disconnected and operates in an islanded mode. In case, if a fault occurs within the MG in islanded mode, it is considered a second fault, resulting in the disconnection of the MG DGs (after a certain time delay) to avoid any undesirable situation.

  In grid-connected mode, directional overcurrent relay distinguishes the forward and reverse direction faults. For proper coordination, a definite time delay is added in the

reverse mode. The negative sequence component of current is incorporated in the directional unit to detect unbalanced faults in MG [67].

- *Voltage-based Protection Schemes*: The three-phase balanced faults do not contain negative and zero-sequence components and thus an Undervoltage relay accompanied by a directional element can be used for protection during the balanced fault [29]. Also, a definite time delay is utilized for coordinated operation in forward and reverse direction of fault [67].
- *Both Voltage and Current based Protection Schemes*: Protection principles based on impedance, reactance, and the directional unit use both voltage and current for the protection decision. Usually, impedance-based protection schemes are deployed for transmission level, but being free from fault calculations, they also find applications in MG protection. An impedance-based protection scheme for MG is discussed in [30]. However, its performance in a system with multiple tapped feeders is not reliable due to the current in-feed.

Protection Schemes for Grid-disconnected (Islanded) Microgrid

The subsection discusses the protection schemes where the MG is islanded from the main grid due to any reason.

A comprehensive digital protection scheme is proposed in [68] for MGs operating in both grid-connected and islanded modes. The current differential technique is used for line protection, while overcurrent, Undervoltage, and negative sequence-based protection functions are used for DG and point of common coupling (PCC) protection.

A dynamic adaptive overcurrent relay is presented in [69] for the protection of MG in islanded mode. The relay changes the pickup current settings by using the DG status.

A symmetrical component-based protection scheme is proposed in [70], where the fault is detected by obtaining the positive-sequence impedance of the line. Thereafter, the correct faulted section is identified by comparing the upstream and downstream positive sequence impedance during fault and pre-fault conditions.

An integrated impedance angle (computed from positive sequence voltage and current phasors) based protection scheme is presented in [71] for MGs in islanded operation. An internal fault is confirmed when the angle is in the range of -5° to -90°; otherwise, it is treated as an external fault.

The rate of change of voltage phase angle of a bus with respect to PCC is used for fault detection in [72]. The method uses a PMU with IEEE C37.118.1 standard for angle estimation and the rate of angle difference between two buses is an indicator of fault identification.

The sum of the phase and neutral currents are used in [73] to detect the fault in MG, where the entire MG is divided into several protection zones, and a circuit breaker is connected between the zones to isolate the minimum part during a fault.

Islanded (Stand-alone) Microgrid Protection Schemes

This subsection discusses the protection schemes when the MG operates in islanded mode only.

A protection scheme based on inverter-control and microprocessor-relay (MR) settings is proposed in [74]. The scheme injects a percentage of the fifth harmonic into the fault

current using software current control to support MR in accurately identifying the fault. The inverter is also protected against short-circuit faults by limiting currents using hardware hysteresis and software current control.

An adaptive overcurrent protection scheme is proposed in [75] utilizing programmable microprocessor-based intelligent electronic devices. These devices communicate among themselves and with a central controller to make a decision.

An active protection method based on differential protection and injection of off-nominal frequency during fault conditions through the inverter-based DG control is proposed in [76] for islanded MG.

A new time-domain model for inverter-interfaced DG is proposed to investigate the protection issues in islanded MG [77]. The protection issues in islanded MG completely fed by DG or have very high DG penetration are addressed in [78].

Anti-Islanding Protection Schemes

Unintentional islanding of an MG is a concern as it causes safety hazards for personnel and damage to equipment due to out-of-phase tripping [79]. The anti-islanding requirement in DG is adopted to avoid such severe issues and hence the DG must be disconnected from the network followed by islanding.

The anti-islanding protection is broadly classified into three categories as active, passive, and hybrid detection strategies [80]. Active strategies amplify the small perturbation generated in frequency, phase angle, and harmonics during the disturbance. Passive strategies are based on under/overvoltage and under/over-frequency at the PCC. Hybrid strategies are based on the exploitation of the strength of both passive and active strategies where passive detection is used first. Thereafter, perturbations are injected for enabling the active methods.

2.2.3.2 Special Techniques Based Protection Schemes

This section reviews the protection schemes which employ special techniques in protection design for MG operating in both grid-connected and islanded modes.

Setting-less Protection Schemes

Setting-less protection is a novel approach based on dynamic state estimation. The proposed method has the potential to address the existing protection gaps and also improve zone protection [36].

The concept of setting-less protection also referred to as dynamic state estimation based protection (DSEBP), is derived from differential protection and can be regarded as its generalization. DSEBP utilizes the voltage and current measurements from inside and the terminals of the protection zone, speed and torque measurements in case of rotating devices, or other internal measurements (such as thermal measurements).

DSEBP does the dynamic modelling of physical laws for protection zone such as Kirchhoff's current and voltage, thermodynamics, and motion law which should be obeyed by all the measurements. Thus, in the absence of any internal fault in the protection zone, all the physical laws should be satisfied by the measurements, while vice-versa in case of any internal fault, leading to a clear, secure, and reliable identification of the internal faults [36].

DSEBP can also be applied for MG protection to address the various challenges. A DSEBP scheme is proposed in [81] for all the MG components. The work demonstrates the application and advantages of this scheme for MG circuits by comparing the performance with the traditional protection techniques. A distributed dynamic state estimation is used to achieve adaptive grid protection in [82]. Further, DSEBP is used to design a centralized protection scheme for MG in [27].

Synchrophasor Assisted Protection Schemes

The last decade has seen an enormous rise in the number of PMU installations i.e., several thousand PMUs are installed in the power systems. However, their application in the protection is limited mainly due to associated errors and reliability of GPS clocks, etc. A few of the research works employing the synchrophasor technology are presented.

The integrated impedance angle based protection scheme is proposed in [71] which uses PMU retrieved positive sequence voltage and currents from both ends of the lines to detect the fault type, location, and resistance. The scheme is robust in distinguishing the critical issues from the faults, and thus it could be a potential candidate for developing centralized protection schemes for MG.

An effective, fast, and reliable fault detection scheme is proposed in [72] for different operating conditions of MG. The method detects the faults by monitoring the absolute value of the rate of angle difference of the phase voltage between the PCC and the bus closest to the faulted line by using PMUs.

A MG protection scheme based on the positive-sequence component with the capability of single-phase tripping is developed in [70]. It employs PMUs and microprocessor-relay based on a digital communication platform to enable the protection of MGs in looped and radial configurations under both operating modes.

Travelling Wave based Protection Schemes

The implementation of the travelling wave-based protection scheme requires communication. In practice, polarity-based direction detection schemes are used in transmission systems. The single-ended travelling wave-based protection scheme is still not employed in AC power systems.

The single-phase-to-ground fault is detected by a novel travelling wave-based protection scheme proposed in [83]. The method determines the fault direction by comparing the polarities of current and voltage travelling waves, which are measured immediately when the fault occurs.

The initial current travelling wave-based protection scheme is introduced in [84] with specific logic for meshed networks and feeders with single-end measurement. The proposed scheme is based on mathematical morphology technology and a simplified polarity detection method.

A travelling wave theory-based protection algorithm for medium voltage lines is presented in [85]. The algorithm determines the fault direction by analyzing the differential equations, which describe the behavior of fault-induced current waves. The neural network-based classifiers are used to distinguish between internal and external faults. This approach only requires local measurements of current. Information exchange is not required as frequently

as compared to other protection schemes, and thus it could be implemented using fewer communication links. These characteristics make it a reliable and low-cost solution for the protection of the MGs. The shortcomings of [85] are resolved in [86] by using both voltage and current measurements. The main advantage is the use of physical considerations compared to the data-driven ML algorithm previously used.

Machine Learning based Protection Schemes

A reliable adaptive protection scheme based on ML techniques is presented in [87]. The scheme first uses Pearson correlation coefficients from data-mining to analyze uncertain elements and then a hybrid artificial neural network and support vector machine (SVM) model for MG state recognition based on big data streams. Finally, the proposed scheme determines the adaptive protection settings and network reconfigurations.

A new method based on a semi-supervised ML technique with the co-training of decision tree and k-nearest neighbour is proposed in [88] for the fault classification in MG. It provides better performance as compared to previous supervised ML techniques due to the use of both labeled and unlabeled data for building and training the classifier model.

A MG protection scheme proposed in [89] is based on the Hilbert–Huang transform (HHT) and ML techniques. The scheme initially extracts the differential features from specific current signals using HHT, which are then fed as input to the three different ML models, i.e., Naive Bayes classifier, SVM, and extreme learning machine, for the detection and classification of MG faults.

A protection scheme based on a sparse auto encoder and deep neural network is proposed in [90] to clearly distinguish array and symmetrical line faults for PV-integrated MG. The proposed scheme has added features like fault detection and classification, section identification, and mode detection.

ML algorithms based adaptive protection scheme for MG in both grid-connected and islanded modes is proposed in [91]. The work shows that relay measurements could be used to obtain detection features for ML-based prediction models to detect faults accurately.

A supervised ML method using principal component analysis to extract features is proposed in [92] for fault detection.

A MG protection scheme based on wavelet transform (WT) and deep neural networks is proposed in [93]. The scheme samples and prepossesses the current signals using discrete WT for the extraction of statistical features. The fault detection is done by giving these features as inputs to deep neural networks for training and testing.

Wavelet Transform based Protection Schemes

A wavelet transformation is a signal processing method that is often used for travelling wave abstraction from different frequency bands.

A combined WT and decision tree-based MG protection scheme is proposed in [94]. The effective features such as deviation in energy and entropy, etc., are calculated by obtaining and prepossessing the current signals through WT. After the feature extraction, training and validation of the decision tree are performed. Finally, the fault classification is done by the inclusion of both wavelet-based and current signal features.

A protection scheme based on WT and ensemble of the SVM classifier is proposed in [95]. It provides the standard deviation of coefficients obtained by the feature extraction process of WT as inputs ensemble of SVM for training.

An adaptive distance protection scheme is proposed in [96] for inverter-based DG composed MG based on complex WT. The scheme generates the relay command and setting by coordination optimization model using an ant colony algorithm.

Multi-agents based Protection Schemes

A multi-agents based differential protection scheme with variable tripping time is proposed in [97]. The agents have their primary, backup, and bus protection layers, which are used for primary and backup protection.

A protection scheme based on a Q-learning algorithm and multi-agent systems is proposed in [98]. The agents are trained using the Q-learning algorithm for fault identification and clearance. Further, the agents communicate with each other using decentralized blockchain-based connections.

A protection scheme is proposed in [99] using resilient intelligent agents. The voltage and current measurements are used for fault detection. The components act as agents and communicate the decision to upper control levels and neighbouring components for performance enhancement.

A multi-agents based MG protection scheme is proposed in [100] where the MG components like DGs, relays, PCC, and controllers act as agents. The scheme uses adaptive protection where the pre-contingency decentralized adaptive protection interacts with the MG central controller to adapt the new protection settings in post-contingency conditions.

A MG protection scheme for fault detection, clearing, and localization, along with the restoration method based on a communication-assisted multi-agents system, is proposed in [101]. The agents are present at the end and middle of each section and compare the phase angles of current signals from both sides to produce the relay decision.

A scheme using a co-simulation platform based on a multi-agent system is proposed in [102]. It utilizes a supercapacitor bank for resiliency enhancement and does not require different settings with the change in MG configuration.

Data-Mining based Protection Schemes

A data-mining patterns and classification algorithms based fault detection method in MG is proposed in [103]. Two different classifiers, i.e., random forest and K-nearest neighbours, are used to distinguish the fault features with no-fault conditions which are obtained by wavelet packet transform.

A comprehensive data-mining based differential protection scheme is proposed in [104]. The voltage and current signals during the fault are prepossessed to estimate the sensitive features. After that, the differential features are computed from these features which are further used to build a decision tree-based data-mining model to obtain the final relay output.

2.2.3.3 Remarks and Discussions

The following can be summarized from the review of protection schemes for MGs:

- The challenge associated with the bi-directional power flow including the sympathetic tripping and protection blinding is addressed in [27], [28], [30], [64]–[68], [71]–[73], [78], [79], [81], [86], [90].
- The challenge associated with the change in the mode of operation is addressed in [27], [30], [64], [65], [67]–[75], [77], [79]–[81], [84], [86]–[91], [93], [94], [97], [102]–[104].
- The challenge associated with the fault current limitation is addressed in [27], [30], [67], [68], [70], [73]–[80], [96].

The review further suggests that the time-domain and communication-assisted protection schemes could be feasible solutions for achieving fast relay operation in future low-inertia MGs. However, in the case of time-domain schemes, issues such as low signal strength of travelling wave for a certain fault inception instant and switch-on-to-fault (unavailability of pre-fault data) in superimposed component, while communication failure and cyber-attack in case of communication-assisted schemes, could be possible areas of developments. The research gaps identified from the review can be summarized as follows:

i) How can cost-efficient communication-assisted protection be designed which is robust to communication delay and link failures?

ii) How can the field and practical validations are enhanced for special techniques-based protection schemes?

iii) How can the data and latency issues be handled for synchrophasor-based protection schemes?

The parameters such as speed, sensitivity, and reliability are important to be considered in designing a protection scheme for future low-inertia MGs.

2.2.4 Dynamic State Estimation based Protection Scheme for Transmission Lines

With regards to the challenges identified in Section 2.1.4, DSE-based protection is one of the possible solutions to address the challenges which exist in transmission line protection as it adapts to the operating conditions of the system in real-time and provides better visibility of the system status [105]. A feasibility study for such a protection scheme is presented in [106]. The study is further supported by its application for fault detection in a transmission line and capacitor bank. The detailed concept of this scheme along with its capabilities to improve zone protection, detection, and self-healing against hidden failures are discussed in [36]. The DSE-based protection is based on a generalized concept and has been applied to the protection of series compensated transmission line [39], transmission line fault classification [107], and several other components.

The more recent application of the DSE-based protection scheme includes the development of centralized substation protection in [108]. A microgrid protection scheme is developed using synchrophasor-based state estimation (SE) in [109]. A DSE-enabled protection scheme is proposed in [110] for large synchronous generators during out-of-step conditions. A novel fault location method utilizing DSE and gradient descent is proposed in [111] for transmission lines in modular multilevel converter-HVDC grids. A wide-area backup protection scheme is

proposed in [112] which employs cubature Kalman filter-based DSE along with a few PMU measurements for acquiring full network observability. Despite the application of the different DSE versions in designing the protection scheme for power systems and their components, most of the research works have presented the simulation results and validation with the hardware-in-the-loop test. Therefore, validation of this scheme in a real environment is needed for technology advancement before it can actually be employed in power systems. The task force paper on DSE-based protection also identifies the practical implementation as a key research area in the future [113]. DSE-based protection requires real-time measurements as the input. With the advent of PMU technology in the 1980s and development thereafter, it has evolved as one of the reliable solutions for real-time measurements. PMU finds huge applications in the monitoring, operation, and protection of power systems. However, most commercial PMUs have little scope for third-party users to modify and develop their control algorithms. In this context, an affordable measurement solution (advanced sensors) with a scalable and modular design, web interface feature, secure edge computing, and development in an open platform developed by Smart State Technology is used. This solution could be deployed at all voltage levels for further enhancement of the grid's monitoring, operation, and protection.

Based on the challenges identified in Section 2.1.4 and above state-of-the-art review, **RSQ-3** related to implementation and validation of a protection scheme based on advanced measurement technologies and DSE has been identified and presented in Section 1.2.

2.2.5 Decentralized Dynamic State Estimation of Transmission Lines

With regards to the challenges identified in Section 2.1.5, DSE can be one of the potential solutions to meet such requirements. Proper metering infrastructure based on PMUs and merging units (MUs) is one of the main requirements in such applications [38]. The potential of DSE in the transmission line protection is explored in [36], [39], [114]–[117]. However, these works make grossly inaccurate approximations in both the modelling and the identification stages, because of which the speed and accuracy of transmission line estimation and protection are adversely affected. For instance, [39], [116], [117] use quadratic approximation in the dynamic modelling, while for state estimation, the weighted least squares (WLS) method is employed in [116], [117], an improved version of WLS in [115], and Lagrangian multipliers in [39]. However, all these estimation methods are based on algorithms traditionally used in static state estimation (SSE) and, hence, do not adequately capture the system dynamics, as required by DSE. An ensemble Kalman filter-based DSE method is presented in [118] which overcomes some of the limitations of WLS, however, it does not consider the second-order time derivative terms which leads to reduced estimation accuracy. In addition to these limitations, [36], [39], [114], [115] require remote end measurements to perform DSE which clearly emphasizes the need for communication. Hence, such methods along with conventional protection schemes such as the differential, distance, and pilot relaying could maloperate in case of communication failures leading to misoperation.

Based on the challenges identified in Section 2.1.5 and above state-of-the-art review, **RSQ-4** related to the development of an accurate DSE method for transmission lines has been identified and presented in Section 1.2.

CHAPTER 3

Study of Future-readiness Assessment Framework, Electricity Production Scenarios, Impact of Regulations, and Pathways for the DSOs

This chapter presents the work conducted on the development of a DSO support framework for assessing the future-readiness of distribution systems, analysis of future scenarios for electricity production, the impact of regulations on the future intelligent distribution systems, and finally the pathways for the DSOs to make a smoother transition towards the future. The content presented in this chapter is based on the work published in Paper C, F, and H.

3.1 Future-readiness Assessment Framework

3.1.1 Description

The framework for distribution systems assessment consists of two steps, i.e., the selection of key indicators and their assessment. The overall methodology for assessment framework is shown in Figure 3.1 [119], [120].

The first step is to identify the key indicators which impact this transition. Although, the most relevant advancements are related to technical requirements for the DSOs, the available market structures, policies, and regulations are also instrumental. The market and policy aspects will have a potential impact on the DSOs but are not directly controlled by them. Thus, all these aspects are interrelated, and their exclusion may limit the possible

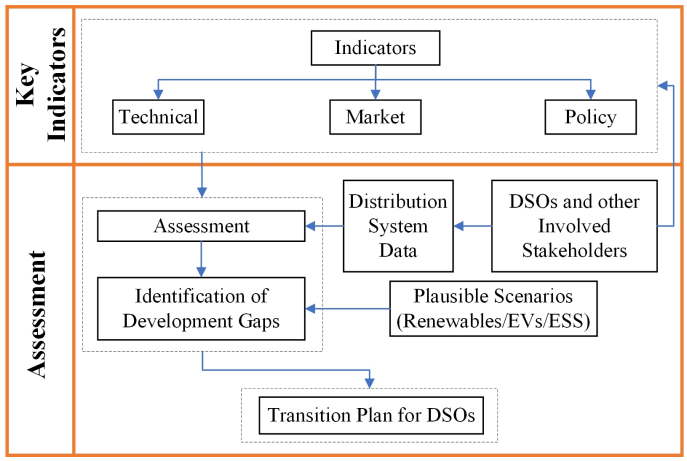

Figure 3.1: Overall methodology for future-readiness assessment framework.

advancement in one direction or reduce the possible benefit in another. As a result, the indicators are classified as technical, market, and policy. The description of these indicators and their sub-indicators is presented as follows:

3.1.1.1 Technical Indicators

These indicators mainly address the technical aspects associated with the production and distribution of electricity. The selection of indicators is motivated by the issues addressed in ETIPs-SNET SRA 2035 [121] and inputs from the partner DSOs involved in the UNITED-GRID project. The following technical indicators are identified:

(a) *Distributed Energy Resources*: It covers the aspects such as the amount of distributed renewable energy production (REP) and associated forecasting, EVs integration, heat pumps, and district heating along with its availability for flexibility, and energy storage systems.

(b) *Level of Monitoring and Control*: It covers the advancement level of the DSOs with respect to monitoring and control, e.g., smart meters, advanced metering infrastructure (AMIs), and supervisory control and data acquisition (SCADA).

(c) *System Status*: It covers the present infrastructure situation and operational data of the system such as loading profile and levels, existing system capacity, system configuration, quality and reliability of supply, and participation in frequency control.

(d) *Cyber-physical Description*: It covers the cyber-physical characteristics such as systematic architecture, structural framework for fidelity models, and systems integration. It has gained importance as ICT system security has been one of the focus areas for the DSOs.

3.1.1.2 Market Indicators

These indicators mainly address services and markets, tariffs, financial aspects, and business models. In addition to the financial and market context set up by the DSO itself, it is important to consider how external actors/stakeholders could influence the DSOs. To capture the external influences, some indicators are related to available services from external stakeholders such as electricity retailers and service providers. The following market indicators are identified:

(a) *Markets and Services*: It refers to the available markets organized by the DSO or by other actors where end-users could provide their services.

(b) *Tariffs*: It refers to the evaluation of the electricity charges for the end-user. The tariff is divided into grid tariff and retail electricity pricing.

(c) *Business Models*: It refers to the available business models provided by the DSOs or other actors.

3.1.1.3 Policy Indicators

These indicators mainly address the regulation and policy aspects. They become a relevant indicator, especially in the era of changing role of the DSOs. Traditionally, the DSOs are highly regulated entities driven by national and European authorities because they act as natural monopolies (to have numerous competing structures would make no sense), while new policies are being drafted which will have a significant impact on the DSOs, their absence may hinder possible technology advancements. The following policy indicators are identified:

(a) *Level of Unbundling*: It refers to the implementation of the unbundling. The most relevant existing European policy in this regard is the third energy package [122], which has been enacted to improve the functioning of the internal energy market and resolve structural problems.

(b) *Roll-out of Smart Meters*: It refers to a cost-benefit analysis for the roll-out of smart meters and policies supporting them. It is one of the most relevant indicators for the DSOs in the energy transition, as mentioned in the third energy package [122].

(c) *Network Codes*: It refers to finding the key barriers for the DSOs in the implementation of existing network codes, which are legally binding European implementing regulations supporting the integration of national and regional electricity markets into a unified internal European market. It gains relevance as it is feared sometimes that current codes do not account for the more diverse, flexible, and active role that the DSOs need to take up in the future.

(d) *Impact of Winter Package on the DSOs Tasks*: It refers to the effect of policy aspects of the winter package [123], on different tasks of the DSOs. The package includes both non-legislative initiatives as well as legislative proposals. They include new rules on European Union (EU) electricity market design and a proposal for a directive on common rules for the internal electricity market and a proposal for a regulation on the internal electricity market. Many of the new principles focus on empowering consumers and the importance of the internal market.

(e) *Impact of New Network Codes and Guidelines*: It refers to the expected effects of new network codes and guidelines as mentioned in the winter package [122]. The package not just proposes a new set of network codes and guidelines but also specifies the way the DSOs will be involved in their development.

(f) *National/Regional Policies on DERs*: It refers to identifying other national policies that can have an impact on the distribution systems, for instance, incentives for certain types of renewable energy or legislation/lack of legislation on aggregators.

The second step is to assess the current status, i.e., future-readiness of the DSOs. The qualitative assessment is done based on the DSOs' response to the proposed indicators. The DSOs along with other involved stakeholders will provide inputs in the form of system data, market/business models, regulatory policies, etc. The output of the proposed assessment framework would serve as an input for the identification of the development gaps, i.e., the progress needed, within each area, i.e., technical, market, or policy, for the transition toward future intelligent distribution systems. Finally, with the identified development gaps and plausible scenarios (Renewables/EVs/ESSs, etc.), a suggestion for the DSO transition plan will be delivered.

3.1.2 Case Studies

The proposed framework has been used to assess the current status of three distribution systems in Sweden, France, and the Netherlands. The presented case studies could be used as an example of how to use the framework and how the results may look like. The DSOs included in the case study are:

(a) *Göteborg Energi (Sweden)*: Göteborg Energi is a Swedish municipality owned energy company. The grid has nearly 262 000 customers and 4.4 TWh of annual energy consumption.

(b) *Sorea (France)*: Sorea is a small distribution network company in France. It is active in electricity production and distribution and operates its grid mainly with hydro- and PV-based production. The grid has nearly 14 000 customers and 140 GWh of annual energy consumption.

(c) *Enexis (The Netherlands)*: Enexis is a Dutch DSO supplying electricity to around 2.8 million customers. The annual energy consumption is 34.5 TWh. Their distribution system covers both urban and rural areas.

The three involved DSOs have filled the proposed indicators list and the assessment has been done based on their responses. A comparative assessment with the proposed indicators of the three DSOs is presented in Table 3.1. Although the three DSOs have relatively different sizes and numbers of customers (hence power demand), as well as different market rules and policies at the national level, it would be beneficial for them as well as for other DSOs in Europe to look at the comparative assessment between them. This may also act as a motivation for a transition towards future intelligent distribution systems.

Table 3.1: Comparative Assessment of the three European DSOs

Indicators Name	**Comparative Assessment**
Distributed Energy Resources	Limited local renewable energy production in all the DSOs. The EVs demand is not high in all the networks, but the infrastructure is being built. Only Enexis has a small amount of energy storage provisions. Although, none of the networks has provision for flexibility today.
Level of Monitoring and Control	The level assessed by AMIs and automation systems varies from high (Göteborg Energi and Enexis) to low (Sorea).
System Status	The power distribution is mainly done by underground cables in all the DSOs. Also, all have a high level of reliability of supply, while frequency control is done at the transmission system operator (TSO) level.
Cyber-Physical Description	As of today, not much information is available for Göteborg Energi and Sorea. But Enexis has implemented some standards for improved risk and security management.
Markets and Services	Currently, not much information is available for Sorea and Enexis, whereas Göteborg Energi has some advanced provisions for competitive electricity prices that are available through different market mechanisms.
Tariffs	Grid tariffs are mainly based on fixed costs with provisions of subscribed power and energy charge in case of all three DSOs.
Business Models	Currently, not much information is available for Göteborg Energi, while Sorea and Enexis have feed-in tariff models available for PV- and hydro-power.
Level of Unbundling	The level of unbundling varies from partial unbundling (Sorea) to total unbundling (Göteborg Energi and Enexis).
Roll-out of Smart Meters	Roll-out varied from currently 100% in Göteborg Energi to expected 72% by 2020 in Enexis and expected 100% by 2024 in Sorea.
Network Codes	Currently, not much information is available for Göteborg Energi and Enexis, while Sorea is aligning themselves to achieve objectives.
Impact of Winter Package on the DSO Tasks	Currently, not much information is available for Sorea and Enexis, while Göteborg Energi has possibilities of new tariffs being introduced at a local level.
National/Regional Policies on DERs	All DSOs are committed to the national legislation for the reduction in greenhouse gas emissions, increased renewable generation, energy savings, advanced metering, and setup of local energy storage and communities.

The investigated DSOs have shown diversity in terms of technology, policy, and market readiness. The DSOs need to be prepared themselves for the following:

- Needs for investments in flexibilities
- Needs for advanced forecasting and monitoring

- Needs for advanced system automation and protection
- Needs for incentives schemes and business models
- Needs for changes in the role of the DSOs which can own and/or procure certain resources and services

3.2 Future Scenarios for Electricity Production in Sweden

In the transition towards the future intelligent distribution systems, analysis of well-developed and thought-out future scenarios could be extremely helpful to make this transition smoother and predict the possible challenges before the DSOs. These future scenarios would also provide inputs to future-readiness assessment framework for the identification of development gaps and further assist in the development of a transition plan for the DSOs as presented in Figure 3.1.

In this context, four future scenarios have been studied from IVA's (Royal Swedish Academy of Engineering Sciences) project Electricity Crossroads for the electricity production in Sweden during 2030-2050, which is based on the gross energy potential available from different energy sources [124]. The economical or environmental aspects are not considered in the gross energy potential. For these four future scenarios, a different combination of fossil-free electricity generation is considered. The details of the electricity production from IVA's Electricity Crossroads scenarios are presented in Table 3.2 [125].

Table 3.2: IVA's Electricity Crossroads scenarios electricity production in Sweden during 2030-2050

Scenarios	**Hydro** (TWh)	**Wind** (TWh)	**Solar** (TWh)	**Bioenergy** (TWh)	**Nuclear** (TWh)
More Solar and Wind	65	55	15	25	0
More Bioenergy	65	40	5	50	0
New Nuclear Power	65	20	5	20	50
More Hydro Power	85	35	5	35	0

The key observations from these scenarios can be presented below:

(a) In *Scenario 1 - More solar and wind*, almost 50% of the total annual energy consumption will come from variable energy resources. But due to the higher share of variable energy resources, there must be some technical supplementary measures in place to accommodate the associated uncertainty.

(b) In *Scenario 2 - More Bioenergy*, it has the capability to make Sweden self-sufficient in terms of the need for both power and energy. But this alternative has an associated risk that involves huge investment costs due to the absence of biomass competition in large-scale bio-energy solutions.

(c) In *Scenario 3 - New Nuclear Power*, there is no significant investment need in the development of new systems. Although, the technology development and the experience gained internationally should be taken into consideration to choose the best alternative among the available technologies.

(d) In *Scenario 4 - More Hydro Power*, the share of hydropower will be increased which has the capability to make Sweden self-sufficient in terms of the need for both power and energy. There is an additional advantage to hydropower being a flexible energy source.

The analyzed future scenarios show the challenges associated with the different sources of electricity production in Sweden. These can be further translated to challenges that the DSOs might face in near future.

This work is motivated by these challenges that the DSOs will face in near future due to several complexities as discussed above.

3.3 Impact of Regulations on Future Intelligent Distribution Systems

The work presented in this section is done in collaboration with RISE, Sweden [126]. The main results from the work are presented here, while the details of the work can be found in [127].

There will be a significant impact on the role of the DSOs in Europe due to climate change goals, changing market frameworks, and technological innovations. The nature and scale of these challenges are strongly driven by the European vision and strategies on climate and energy.

An extensive review of new policy priority areas within the energy and climate framework and electricity market design, and subsequent discussions with three partner DSOs (from Sweden, France, and The Netherlands) are done. Based on them, the following five priority barriers are identified which can hinder distribution grid innovation and the implementation of advanced smart grid solutions developed for distribution systems:

(a) *Impact of Recent Developments in EU Climate Strategies on the DSOs*: The global and European visions and strategies for reaching binding climate goals result in policies and regulations that set up a process for member states to decarbonize the power sector. This requires large investments and a major transition by all stakeholders, particularly at the distribution level. However, not all DSOs have sufficiently explored innovative solutions or developed their own long-term strategies for adapting to the expected transformation of the energy sector.

(b) *The Future Role Versus the Income Regulation of the DSOs*: Distribution systems are considered as non-competitive natural monopolies with regulated incomes that are collected via network tariffs, implying low financial risks for the DSOs but also low incentives for innovation. Moreover, recent and expected future regulations on operational cost reduction might result in a tightening of the authorized income space for the DSOs, who are concerned that with additional flexibility requirements on top of the traditional DSOs' tasks, the affordability of the energy supply will be impeded

and could be a major economic barrier in the maintenance and development of their grid.

(c) *A New Active Role for the DSO in the Electricity Markets*: A transformation of the traditional DSO business model is required so that the DSO becomes a neutral market facilitator that coordinates the impact of flexibility operations on its network, irrespective of the flexibility model and the chosen technology. The core concern is that the necessary regulatory framework for smart management and the incentives toward the DSOs for innovation are not in place yet. It is difficult for the DSO to take up the new role as a market facilitator since there are no real markets for grid services yet and there are limited opportunities available in terms of differentiated components in the distribution tariffs.

(d) *Ownership of Storage Devices and Incentivizing the Use of Storage Services*: The storage services should be market-based and competitive which puts strong restrictions on the ownership and management of storage units by the DSOs. The DSOs can be enabled and incentivized to use services from energy storage and some exceptions are allowed. However, these exemptions could be short-term if an alternative solution turns up in the market. As long as a real service market does not exist, this is perceived as a regulatory gap with large uncertainties that hamper the needed investments in storage.

(e) *Legally Processing and using Personal Data from Intelligent Metering*: Smart meters will play an important role in the new market design by facilitating consumers in managing their consumption patterns through flexibility. The DSOs can only access personal data from smart meters if that is necessary to perform other legal obligations and they should not go beyond the purpose for which these data have been collected. This implies minimizing processing activities and defining specific monitoring accuracies. In some cases, such data protection challenges have slowed down the roll-out and deployment of smart meters.

3.4 Pathways for the DSOs

The work presented in this section is done in collaboration with RISE, Sweden [126]. The main results from the work are presented here, while the details of the work can be found in [128].

To cope with the barriers as described in Section 3.3, it was recognised that solutions need to be developed at several levels, in order to support the DSOs in the transition from today's passive distribution grids to the future's active and intelligent distribution grids. Ambitious decarbonisation goals and new regulatory frameworks demand a new role for the DSOs, but how to put this into practice in daily business had not been clearly defined. From the DSOs, it will not only require accelerated investment in innovation and digitalisation, but also upgrading internal processes and tools, and a shift in the cultural mindset.

To achieve this, the pathways are developed in close cooperation with three demonstration sites that are related to three DSOs: Göteborg Energi (Sweden), Sorea (France), and Enexis (the Netherlands). The description of the developed pathways is as follows:

(a) *Investment decision for advanced solutions*: The need for investments in grid technology and ICT solutions will depend on the current status and future-readiness of the DSOs and the end-user acceptance. Several tools are developed to support the DSOs' decision-making in investments for grid modernisation that enable automation and control of the network. The following steps are required to be carried out to make a decision on investment in advanced solutions:

- Assess the current status and future-readiness
- Implement smart solutions
- Validate end-user acceptance

(b) *Investigation and adoption of new business models*: In the context of multi-market players and multi-vector ecosystems, the current business models which rely mainly on charging consumer consumption to compensate for the investment, operation, and management expenses will appear to be insufficient soon. With the mass deployment of AMI and improvement in ICT infrastructure for IoT, it is expected that the future distribution grids will be more flexible in operation and enable new solutions such as advanced optimisation, coordinated protection, etc. These tools contribute to the improvement of the quality of service and securely hosting more RES. It also allows the implementation of new business models, offering advanced network services aiming at lower distribution cost, enhanced reliability, satisfactory power quality, available access service, and market facilitation services. The following two business models are developed and proposed which support the transformation from asset providing to offering advanced network services aiming at lower distribution cost, satisfactory reliability and power quality, available access service, and market facilitation services:

- The DSO as a service provider
- The DSO as a market platform operator and market maker

(c) *Adaptation to future system logic*: The DSO transition process from a passive distribution grid operator to an active distribution grid manager is highly complex. As discussed in Section 3.3, the DSOs not only need to take into account new regulations but also adapt their planning processes and make new business plans. They also need an internal adaptation to manage the uncertain future at a much faster pace than expected and to react to those changes so that the true value of the investments and changes can be concretised in the long term. Due to the large differences between the DSOs in Europe in terms of size, organisation, and technical characteristics, it is an individual process where individual methods need to be developed to achieve a preferable scenario, including milestones and critical resources. The following ways could be used to guide the DSOs through the transition process:

- Use transition workshop approach
- Review new roles and functions
- Review collaboration and competencies requirements

3.5 Summary

This chapter has presented a future-readiness assessment framework with a list of technical, market, and policy indicators for the DSOs, to assess their current status and future-readiness.

For the demonstration of the use of the developed framework, case studies for the DSOs in Sweden, France, and the Netherlands have been carried out. A comparative assessment between the DSOs is also presented along with the identification of areas of preparedness required for the transition. The key takeaways from the case studies are that the DSOs currently have a limited amount of renewable energy production in their grids, but the share will be increased. Thus, the DSOs need investments in flexibilities, advanced forecasting and monitoring, system automation and protection, incentive schemes and business models, etc. Further, some future scenarios for electricity production in Sweden are presented which provides insight into the possible challenges for the DSOs in the near future. Additionally, the DSOs will be impacted in terms of innovation and applying smart grid solutions such as advanced tools developed in this thesis, by the new regulations for the distribution systems. In this regard, five priority barriers are identified after an extensive review of new policy priority areas and discussions with the DSOs in Sweden, France, and the Netherlands. Finally, the chapter presents a set of pathways that support the DSOs in three European countries in the transition towards future intelligent distribution grids, and it can also be seen as a solution for other DSOs in Europe. These pathways lead to a conclusion that the DSOs should not only accelerate investments in innovation and implement novel business models but they should also view their role as an enabling partner for the energy transition to realise greater value for the future electricity grid.

CHAPTER 4

Advanced Congestion Forecast Tool

This chapter presents the work conducted on the development of an advanced congestion forecast tool that would assist DSOs by forecasting the congestion levels in their networks. The detailed methodology and modelling are presented followed by the case studies carried out on a part of the real distribution network of Sorea in France and the 141-bus distribution network of the Caracas metropolitan area. Further the details and results of the tool integration to an existing industrial graded distribution management system via an IoT platform Codex Smart Edge of Atos Worldgrid are presented. The content presented in this chapter is based on the work published in Paper B and E.

4.1 Advanced Congestion Forecast Tool Description

This section presents an overall description and features of the proposed congestion forecast tool including the inputs, visualization of forecast results and discusses the possible applications of the tool from the DSOs perspective. The modelling of the probabilistic power flow framework and other associated elements are discussed in Section 4.2 [129].

4.1.1 Inputs

The various inputs required for the advanced congestion forecast tool are as follows:

4.1.1.1 System Data

It includes the network parameters, branches ampacity, and transformers rated capacity. It can be provided in different data formats as separate input files by the DSO. For the

integration of the tool with the distribution management system (DMS) of the DSO, it can be provided through existing SCADA/DMS. Also, the updated network configuration is provided by the DSO in real-time as an input to the tool. In case of network reconfiguration, the tool needs to be re-run with the new network topology over all the forecast horizons because as the network configuration changes, the power flow results would change which will have an impact on the congestion forecast results.

4.1.1.2 Forecast of PV Production and Load Demand

It includes the forecasts of PV production and load, and load model parameters. The forecast errors are also provided as inputs to the tool and should be made available to the DSO through the PV production and load forecasts services.

4.1.1.3 DSO Preferences

It includes the number of Monte-Carlo simulations (MCS), node voltage limits, PV-inverter operating modes, and tolerance limits. These preferences are set as a default value but can be altered by the DSO.

The flow chart of the advanced congestion forecast tool along with the preferences is presented in Figure 4.1.

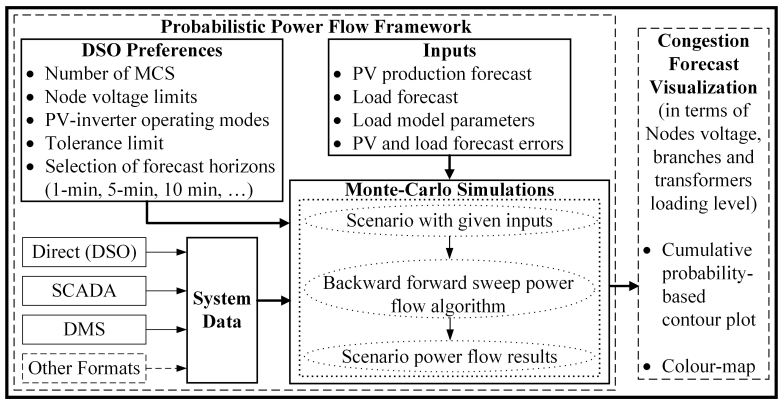

Figure 4.1: Flow chart of the advanced congestion forecast tool.

4.1.2 Visualization of Congestion Forecast Results

The congestion forecast visualization helps the DSO in identifying the exact location and severity of congestion and assists them in taking suitable mitigating actions such as market participation, flexibility procurement, etc. The main features of the congestion forecast visualization are:

4.1.2.1 Congestion Forecast Indicators

The following indicators are proposed for congestion forecast visualization:

- Cumulative Probability-based Contour Plot: Cumulative probability (CP) denotes the probability of a variable reaching a level equal to or greater than a threshold. Here, the CP's are calculated with the desired threshold for all the chosen congestion indicators such as nodes voltage and components overloading. They are used for contour plots, which help the DSO in understanding the congestion severity in a specific node and component.
- Colour-map: Colour-map (CM) is the colour-based representation of the network, indicating the severity and the exact location of the congestion.

4.1.2.2 Congestion Forecast Horizons Selection

With the proposed advanced congestion forecast tool, network congestion forecast can be made with various forecasting horizons depending on the needs and operation strategies of the DSO on how they tackle the possible congestion in their network in different time-frames. The details of the possible forecast horizons, along with the selection reasoning, are presented in Table 4.1. For instance, 5-min ahead forecast horizon value is selected by taking the average of five forecast values between 0^{th} and 5^{th} minute. It should be noted that these time-horizons can be customized by the DSO. The possible congestion management strategies with various time-horizons which can be taken by the DSO are shown in Figure 4.2.

Table 4.1: Congestion Forecast Horizons with Selection Reasoning

Sl. No.	Forecast Horizons	Reason for Selection	Forecast Value Selection
1	1-min ahead	Evaluate real-time congestion status	Next minute (0^{th}-1^{st}) forecasted value
2	5-min, 10-min and 15-min ahead	Identify congestion forecast in close to real-time conditions	Average of the forecasted values for 0^{th}-5^{th}, 5^{th}-10^{th}, and 10^{th}-15^{th} minute
3	30-min, 45-min and 60-min ahead	Set up a close to real-time congestion management plan	Average of the forecasted values for 15^{th}-30^{th}, 30^{th}-45^{th}, and 45^{th}-60^{th} minute
4	2-hour, 3-hour, ... 24-hour ahead	Set up an intra-day congestion management plan	Peak value among the average of forecasted values for four 15-min time slots between 1^{st}-2^{nd}, 2^{nd}-3^{rd}, ... and 23^{rd}-24^{th} hour

4.2 Modelling

This section presents the modelling approach associated with the different components in the advanced congestion forecast tool.

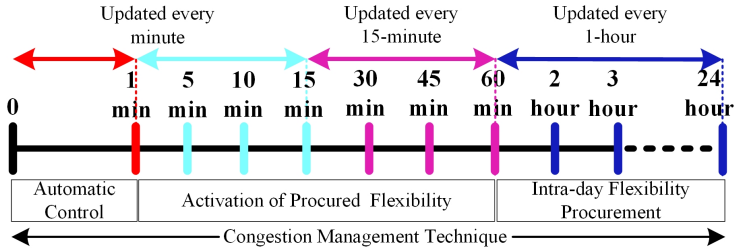

Figure 4.2: Strategic selection of forecast horizons along with the respective congestion management strategies.

4.2.1 PV Production and Load Forecasts

The PV production and load forecasts are provided by one of the UNITED-GRID project partners CEA in France [130]. The details of the work can be found in [129]. The PV production forecast is done with a very short time horizon i.e., a minute ahead, by employing machine learning techniques that use sky images and fine modelling of the cloud cover motion and the built-in combination with the on-site all-sky imager, while the load forecast is done in relatively long time horizon i.e., one hour, through an artificial neural network (ANN) model.

4.2.2 Load Modelling

This subsection presents the details of the inclusion of load models into the tool. Usually, the constant power load model is considered where the loads are assumed to remain independent of the system voltage. The active and reactive load characteristics for a combination of constant power (P), constant current (I), and constant impedance (Z), called as *ZIP* load model, can be expressed as a function of voltage:

$$P = P_0 \left[k_{P_P} + k_{P_I} \left(\frac{V}{V_0} \right) + k_{P_Z} \left(\frac{V}{V_0} \right)^2 \right] \tag{4.1}$$

$$Q = Q_0 \left[k_{Q_P} + k_{Q_I} \left(\frac{V}{V_0} \right) + k_{Q_Z} \left(\frac{V}{V_0} \right)^2 \right] \tag{4.2}$$

where V_0 represents the nominal voltage, k_{P_P} and k_{Q_P} are constants representing the proportion of P load, k_{P_I} and k_{Q_I} are constants representing the proportion of I load, k_{P_Z} and k_{Q_Z} are constants representing the proportion of Z load, for active and reactive power load, respectively. The different load model parameters are considered in this work and presented in Table 4.2.

The following steps are iterated to include the load models in the probabilistic power flow calculation [131]:

Step 1: Initial values of voltage at all the system nodes are taken as one p.u.

Step 2: Calculate load values with the inclusion of load models.

Step 3: Calculate branch currents and new node voltages.

Step 4: Update the values of both active and reactive loads with new node voltages.

4.2.3 Operating Modes of PV-inverter

Due to increased DERs penetration, there are stricter requirements for DERs interconnection with the distribution grid when compared previously. Some of these interconnection requirements are mentioned in the recent IEEE standard on the interconnection and interoperability of DERs [132]. The two most common operating modes of PV-inverter are constant power factor and voltage-reactive power. In this work, it is assumed that PV-inverter operates in both modes. These modes are incorporated into the tool to mimic the interconnection requirements as follows:

4.2.3.1 Constant Power Factor Mode (constant-pf)

In this mode, all the nodes except the slack node are modelled as P-Q nodes. The PV production at all the nodes is modelled as a negative load and with a constant power factor. The step-wise formulation of the BFS algorithm in this mode for p^{th} iteration, is as follows:

(a) A flat voltage profile is taken for all nodes except the slack node, which is kept constant.

(b) Calculate current injection at node r, as:

$$A_r{}^{(p)} = \left[\frac{S_r}{V_r{}^{(p-1)}}\right]^* - Y_r V_r{}^{(p-1)} \quad \forall\, r = 1, 2, \ldots, N \tag{4.3}$$

(c) Calculate branch currents (in branch q) in the backward direction starting from the last node, as:

$$I_q{}^{(p)} = A_n{}^{(p)} + \sum_{h=1}^{t} I_h{}^{(p)} \qquad \forall\, q = br, \ldots, 2, 1 \tag{4.4}$$

(d) Update node voltages (at node n) in the forward direction starting from the slack node, as:

$$V_n{}^{(p)} = V_m{}^{(p)} - Z_q I_q{}^{(p)} \qquad \forall\, q = 1, 2, \ldots, br \tag{4.5}$$

where N, br, t, and Z_q represent the total number of nodes, total number of branches, total number of branches connected at node n and the impedance of branch q, respectively.

These steps are iterated until convergence is reached.

4.2.3.2 Voltage-Reactive Power Mode (constant-V)

In this mode, the PV production nodes are modelled as P-V nodes and load nodes are modelled as P-Q nodes. A compensation method is used for the elimination of voltage

mismatches from their specified values at P-V nodes [133]. The step-wise formulation of voltage mismatch compensation in addition to the BFS algorithm for k P-V nodes in the system and p^{th} iteration are as follows:

(a) Calculate voltage magnitude mismatch at r^{th} node, as:

$$\Delta {V_r}^{(p)} = \left|{V_r}^{(s)}\right| - \left|{V_r}^{(p)}\right| \quad \forall\, r = 1, 2, \ldots, k \tag{4.6}$$

(b) Calculate the reactive current injection at r^{th} node, as:

$$ {I_{rQ}}^{(p)} = j \left| {Z_r}^{-1} \Delta V_r^{(p)} \right| \quad \forall\, r = 1, 2, \ldots, k \tag{4.7}$$

(c) Calculate the total reactive power requirement Q_{rR} at r^{th} node, as:

$$\begin{aligned} {Q_{rR}}^{(p)} &= {Q_r}^{(p)} + Q_{rL} \\ {Q_r}^{(p)} &= \text{Im}[V_r {I'_{rQ}}^{*}]^{(p)} \quad \forall\, r = 1, 2, \ldots, k \end{aligned} \tag{4.8}$$

(d) Check whether the calculated Q_{rR} $(= Q_{inj})$ satisfies:

$$ {P_{inj}}^2 + {Q_{inj}}^2 \leq {S_{rated}}^2 \quad \forall\, r = 1, 2, \ldots, k \tag{4.9}$$

Otherwise, calculate the new value of P_{inj} and Q_{inj} [55].

where ${V_r}^{(s)}$, Z, Q_{kL} and I'_{kQ} represents the specified voltage value at node r, a real and constant impedance matrix, reactive power load at node k, and the sum of the required reactive current and load current injection.

These steps are iterated until the voltage mismatches for all P-V nodes reach within the tolerance limit.

It shall be noted that currently, the tool employs the BFS method to solve the power flow algorithm. BFS method is a highly efficient method with fast convergence characteristics for radial networks. It is the best choice for distribution systems as they are inherently designed in a radial structure. However, due to the transitional changes in the distribution systems, their radial design is no longer guaranteed. The distribution systems now host more DG, more frequent topology changes occur due to the advanced automation, etc., under which the BFS method might not converge. In such cases, some of the well-known power flow algorithms for meshed networks such as the Newton-Raphson method, etc., could be conveniently incorporated into the tool.

4.2.4 Probabilistic Power Flow Method

The probabilistic approach is used to model the uncertainties in the proposed advanced congestion forecast tool. MCS is employed to run a large number of scenarios to incorporate PV production and load forecasts in the system. BFS method is used for solving the power flow algorithm. This work considers Gaussian probability density function (PDF) for generating MCS values using the values obtained from PV production and load forecasts [60], as described by (4.10):

$$PDF = \frac{1}{\sqrt{2\pi\sigma^2}} e^{-} \frac{(x-\mu)^2}{2\sigma^2} \tag{4.10}$$

where mean (μ) is the value of PV production and load forecasts, while standard deviation (σ) depends on forecast type and horizon.

4.2.5 Results of Congestion Forecast

The congestion results are extracted from the power flow results of MCS presented in Section 4.2.4. To visualize the congestion forecast results, the following indicators are chosen:

Node Voltage

It refers to the node voltage and deviation from its nominal value.

Branch Loading

It refers to the loading of a branch relative to its rated ampacity.

Transformer Loading

It refers to the loading of a transformer relative to its rated capacity.

4.3 Case Studies Description

4.3.1 7-bus Feeder of Sorea's Distribution System in France

The considered system, as shown in Figure 4.3, has a radial structure with seven nodes, including both medium- and low-voltage (MV and LV) nodes, five branches, and one MV-LV transformer (20/0.4 kV). The ampacity of all branches is assumed to be 350 Amperes, while the rated capacity of the transformer is 250 kVA. Presently, the system has two PV installations at nodes 5 and 7 with a maximum capacity of 74 kWp and 82 kWp (kilowatt peak), respectively. A camera-based acquisition system is installed at node 6 to be used for the PV production forecast. The network parameters are provided by the UNITED-GRID [134] project partner Sorea and presented in Appendix B.

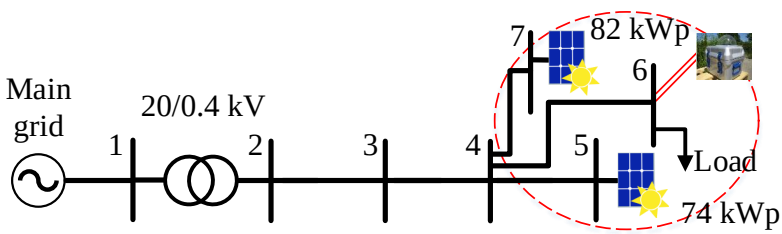

Figure 4.3: Single-line diagram of a part of Sorea's distribution system.

Other input data for the congestion forecast includes:

i) A near-real-time (one minute-ahead) PV production forecast data provided by the UNITED-GRID project partner CEA which is explained in [129].

ii) Load forecasting data is also provided by CEA which is based on ANN and is explained in [129].

The PV production and load forecasts data used in this case study are for 11$^{\text{th}}$ October 2018, as shown in Figure 4.4. It can be seen that the PV production for each installation is forecasted to vary between 0 to 40.91 kW, while the load is forecasted to vary between 0 to 7.8 kW.

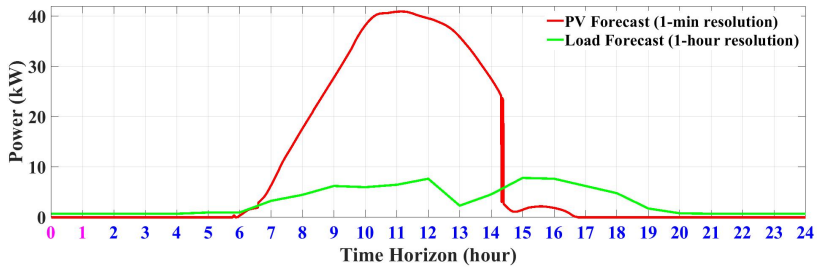

Figure 4.4: The PV production and load forecasts profile at 00:00 hours on 11$^{\text{th}}$ October 2018 over the next 24-hours for Sorea's site in France.

4.3.2 141-bus Distribution System of Caracas Metropolitan Area

The considered system is a real distribution system in the metropolitan area of Caracas [135]. The system has a nominal voltage of 12.47 kV with 140 branches and 84 load buses. The system has been modified to include PV installations at all the load buses. The same PV production profile (without affecting the generality of the results), as shown in Figure 4.4, is considered at all the PV nodes. For a realistic load scenario, the feeders in the considered system are randomly divided into residential, commercial, and industrial areas. Further, the hourly load profiles at different nodes for these areas are presented in Figure 4.5, which are obtained from the real load data of a local DSO in Sweden. The single-line diagram for the 141-bus distribution system is shown in Figure 4.6. The branches' ampacity is assumed to be 1500 Amperes.

To analyze the impact of load models on the congestion forecast accuracy, different cases are studied, which are presented in Table 4.2. These cases include constant P load, constant Z load, an equal proportion of ZIP load, and load model for a typical residential feeder. The coefficients of the load model for a residential feeder have been obtained using the real measurement data provided by a DSO in Sweden. The data include time-series measurement of active power (P), reactive power (Q), and voltage (V) from customers connected to a residential feeder [136]. From the data, the coefficients for the load model are obtained through a standard linear regression using least squares fit techniques. Subsequently, P and

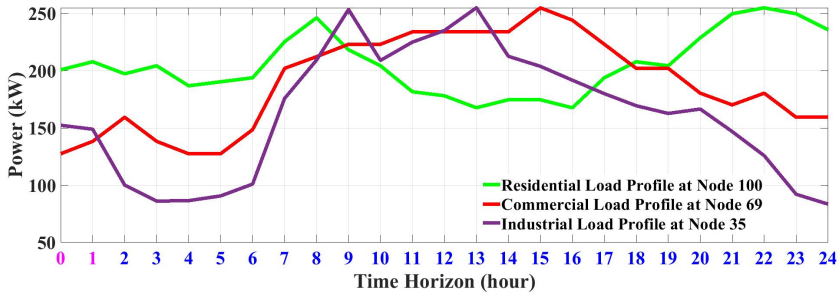

Figure 4.5: Residential, commercial, and industrial load profiles used in the 141-bus distribution system.

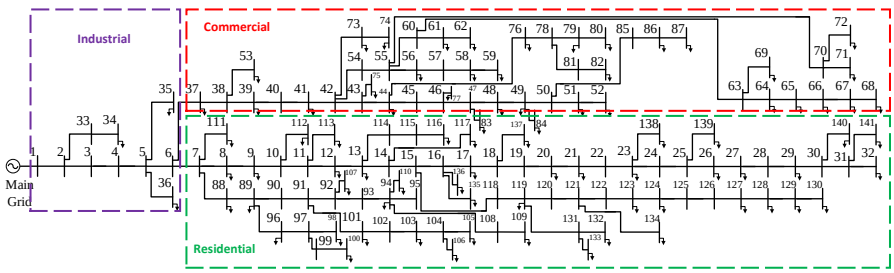

Figure 4.6: Single-line diagram of the 141-bus real distribution system in the metropolitan area of Caracas with PV installations.

Table 4.2: Load Model Parameters for Different Cases

Sl. No.	Load Type	Active Power Coefficients			Reactive Power Coefficients		
		k_{P_P}	k_{P_i}	k_{P_z}	k_{Q_P}	k_{Q_i}	k_{Q_z}
1	Constant Power	1	0	0	1	0	0
2	Residential Feeder	0.10	0.85	0.05	0.00	0.65	0.35
3	Constant Impedance	0	0	1	0	0	1
4	Equal Proportion of ZIP load	0.33	0.33	0.33	0.33	0.33	0.33

Q are represented as a function of voltage V using a polynomial model structure, as given by (4.1) and (4.2).

As explained in Section 4.1.2.2, the congestion forecast is performed continuously on a

Table 4.3: PV Production and Load Forecasts Errors over Different Forecast Horizons (in %)

Forecast Error	Forecast Type	Forecast Horizons				
		1-min ahead	5-min, 10-min and 15-min ahead	30-min, 45-min and 60-min ahead	2-hour, 3-hour, ... 6-hour ahead	7-hour, 8-hour, ... 24-hour ahead
Case 1	PV	1.0	3.0	5.0	8.0	10.0
	Load	5.0	5.0	5.0	5.0	8.0
Case 2	PV	1.5	4.0	6.0	9.0	12.0
	Load	6.0	6.0	6.0	6.0	10.0

rolling horizon. The PV production and load forecasts errors depend on the forecast horizon, and hence different errors are considered, as shown in Table 4.3. The PV production and forecast errors are considered zero during the evening and night hours.

The proposed advanced congestion forecast tool has been implemented using MATLAB R2019b and Python. The number of MCS is considered 10 000 [60], and the power flow convergence criterion is taken as 0.00001 p.u.

4.4 Results and Discussions

4.4.1 7-bus Feeder of Sorea's Distribution System in France

The visualization of the congestion forecast over a day is presented through both CP-based contour plots and colour-map. The simulation is done with PV production and load forecasts data for 00:00 hours of 11^{th} October 2018 under a constant-pf mode of PV-inverter.

4.4.1.1 Cumulative Probability-based Contour Plot

To illustrate the results of the congestion forecast, the CP for the voltage at node 5 is shown in Figure 4.7. The contour plot shows the difference over various forecast horizons. The CP for node voltage deviation remains low (green area) from 1-min to 7-hour ahead and then starts increasing (towards yellow area) until 13-hour ahead and subsequently starts decreasing. For the 13-hour ahead, the CP for node voltage to be above 1.04 p.u. is 0.7 (or 70% of the times). The colour bar in the contour plot represents the severity of congestion.

It is evident from Figure 4.7 that the network is subjected to different congestion levels over the considered forecast horizons. These changes in the congestion levels occur mainly due to varying PV production and load demand during the day. This simulation uses the forecasted data for an entire day, starting from 00:00 hour. As the sun rises, PV production increases, reaching its peak value around noon and decreasing after that. Thus, mainly the higher PV production level leads to an increase in the node voltages and vice-versa, while the load has a negligible effect due to the small proportion.

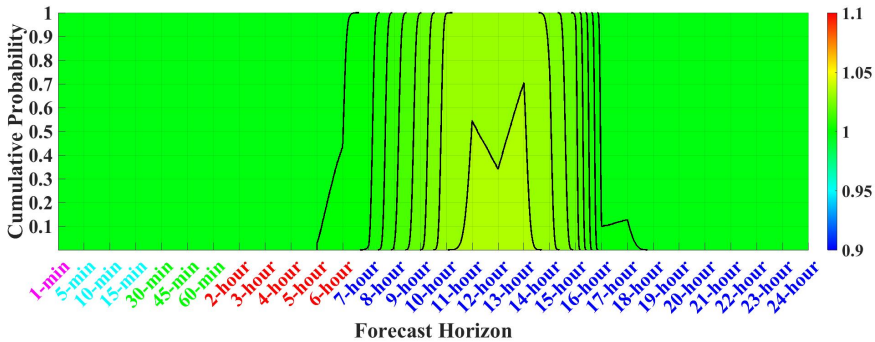

Figure 4.7: CP-based contour plot for visualization of the congestion forecast at node 5, simulated with a constant-pf mode for Sorea's 7-bus system.

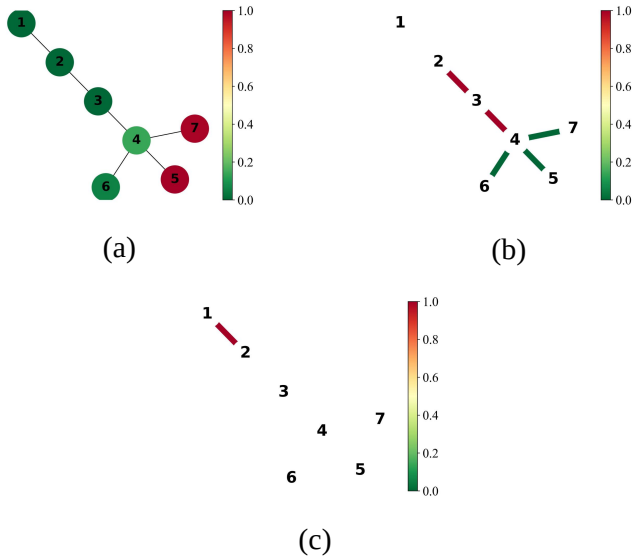

Figure 4.8: Colour-map visualizing congestion forecast for 13-hour ahead simulated with a constant-pf mode for Sorea's 7-bus system, (a) Node voltages, (b) branches loading, (c) transformer loading.

4.4.1.2 Colour-map

The colour-map is useful in evaluating the overall picture and the exact locations of the network congestion. The colourbar here represents the CP for congestion. For illustration purposes, the congestion threshold for the node voltage is taken as 1.03 p.u., for branches and transformer loading as 0.5 and 0.3 p.u., respectively. The DSOs can specify their thresholds as desired.

It can be seen from Figure 4.8(a) that for 13-hour ahead forecast, nodes 5 and 7 have high CP for voltage deviation; node 4 has medium CP, while the rest nodes have low CP for voltage deviation. Similarly, Figure 4.8(b) shows that branches $2-3$ and $3-4$ have high CP for congestion, and the rest of the branches have low CP for congestion. Furthermore, Figure 4.8(c) shows that the transformer has a high CP for overloading. Due to the space limits, the colour-map for only one time horizon is presented here, while the animated version of colour-map over different forecast horizons can be found at [137].

4.4.2 141-bus Distribution System of Caracas Metropolitan Area

4.4.2.1 Visualization of Congestion Forecast over a Day

To visualize the congestion forecast over a day, the simulation is carried out with a constant-pf mode using the PV production and load forecasts profile, as shown in Figure 4.4 and Figure 4.5, respectively. To illustrate the functionalities of the proposed tool, three different scenarios are considered, i.e., with no PV production, 50% of the PV production forecast, and 100% of the PV production forecast. With this tool, the node voltage and branches loading can be forecasted at all the system nodes and branches. Although, in this work, node 141 is chosen as it is one of the weakest nodes in terms of voltage variation, and branch $3-4$ is chosen as it is one of the most loaded branches in the network.

- Scenario 1: No PV production
  This scenario can be treated as a base case i.e., same as the original system without the consideration of any PV production. The CP-based contour plots for the voltage at node 141 and branch $3-4$ are presented in Figure 4.9. It can be seen from Figure 4.9(a) that in the absence of any PV production, the node voltage remains below 1 p.u. as only the conventional loads are present in the system. It can also be observed that in the beginning (for initial forecast horizons) which are the mid-night hours, the contour plot remains green (close to 1 p.u.) and eventually starts turning towards blue as the morning hours approach and load starts increasing. Similarly, from Figure 4.9(b), it can be seen that the loading level of branch $3-4$ largely remains around 50% during the initial forecast horizons and then increases to around 60% from 7-hour ahead until 22-hour ahead due to increased load demand during the day. Thus, it is clearly visible from CP-based contour plots (Figure 4.9) that the network is subjected to a different level of congestion over the considered forecast horizons. This scenario showcases the ability of the proposed tool to interactively forecast the under and overvoltage problems in the network.

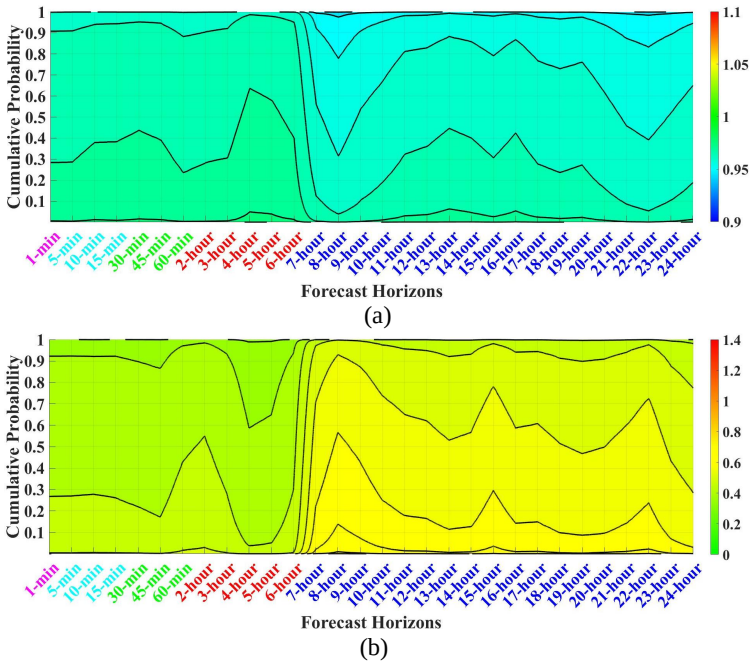

Figure 4.9: CP-based contour plots for visualization of congestion forecast simulated with a constant-pf mode for the 141-bus distribution system with no PV production, (a) The voltage at node 141, (b) the loading level of branch 3–4.

- Scenario 2: 50% of the PV production forecast
  In this scenario, the system has been modified to include PV installations at all the load buses. The same PV production profile (without affecting the generality of the results), as shown in Figure 4.4, is considered at all the load buses. Although the PV production at each bus is taken as 50% of the forecasted value and thus it varies between 0 to 204.5 kW. The CP-based contour plots for the voltage at node 141 and branch $3-4$ are presented in Figure 4.10. It can be seen from Figure 4.10(a) that for 12-hour ahead, the CP for voltage to be above 1.05 p.u. at node 141 is approximately 0.95. Similarly, from Figure 4.10(b), for 12-hour ahead the CP for loading level of branch $3-4$ to be above 0.5 p.u. is approximately 0.35. Figure 4.10(b) presents an interesting observation, that the loading level of branch $3-4$ from 12-hour ahead until 17-hour ahead forecast horizons, is lesser as compared to the loading level obtained from the scenario without any PV production. This occurs because the PV production supplies the load locally which relieves congestion in the network or leads to reduced branch loading. Thus, the CP-based contour plots (Figure 4.10) show that the network is subjected to an assorting level of congestion over the considered forecast horizons mainly due to varying PV production and load demand during the day.

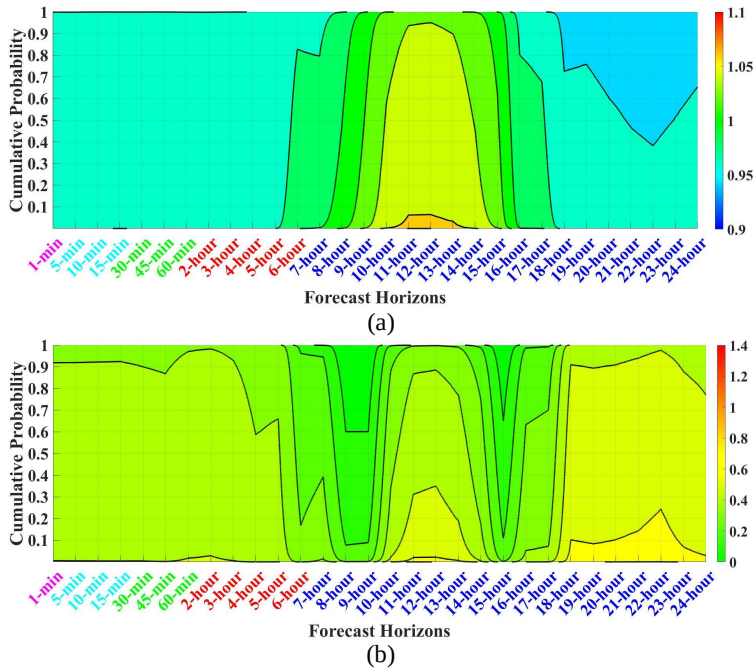

Figure 4.10: CP-based contour plots for visualization of congestion forecast simulated with a constant-pf mode for the 141-bus distribution system considering the PV installations with 50% of the PV production forecast, (a) The voltage at node 141, (b) the loading level of branch 3–4.

- Scenario 3: 100% of the PV production forecast
  In this scenario, the system has been modified to include PV installations at all the load buses. The same PV production profile (without affecting the generality of the results), as shown in Figure 4.4, is considered at all the PV nodes varying between 0 to 409.1 kW. The CP-based contour plots for the voltage at node 141 and branch $3-4$ are presented in Figure 4.11. It can be seen from Figure 4.11(a) that for 12-hour ahead, the CP for voltage to be above 1.1 p.u. at node 141 is approximately 0.85. Similarly, from Figure 4.11(b), for both 11-hour and 12-hour ahead the CP for loading level of branch $3-4$ to be above 1 p.u. is approximately 1. Thus, it is clearly visible from CP-based contour plots (Figure 4.11) that the network is subjected to a different level of congestion over the considered forecast horizons. These changes in the congestion levels occur mainly due to varying PV production and load demand during the day.

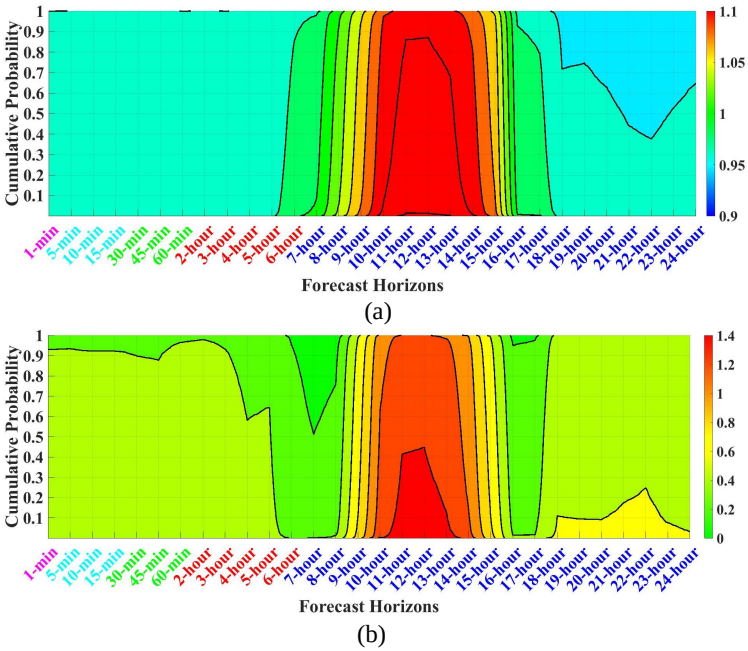

Figure 4.11: CP-based contour plots for visualization of congestion forecast simulated with a constant-pf mode for the 141-bus distribution system considering PV installations with 100% of the PV production forecast, (a) The voltage at node 141, (b) the loading level of branch 3–4.

4.4.2.2 Impact of Load Models on Congestion Forecast Results

To assess the impact of load models, four simulations with different load model parameters are carried out. The load model parameters for these simulations are presented in Table 4.2. The simulations consider the PV installations at all the load buses with the same PV production profile as shown in Figure 4.4, varying between 0 to 409.1 kW. The CP for voltage at node 141 and loading level of branch $3-4$ for 13-hour ahead (maximum PV production) with different load models are shown in Figure 4.12.

It can be seen from Figure 4.12(a) that the node voltage deviation is highest with load model 1 (P). This can be explained using the "voltage drop" equation of a simple network. Assuming an increase in the PV production at a node, there will be an increase in the node voltage, and this change will not be affected by the constant power load (the consumed power will not change regardless of the change in voltage), while the node voltage deviation is lowest with load model 3 (Z) because the increase in PV production will lead to a rise in voltage initially. As the load is a constant-impedance load, the consumed power will increase with increased voltage, which leads to a higher line current and reduced node voltage. Hence, the node voltage deviation is lowest with load model 3 (Z) and highest with load model 1 (P). Further, with load models 2 and 3 (residential feeder and constant impedance), the node voltage is higher with load model 2 because the voltage deviation will be higher in

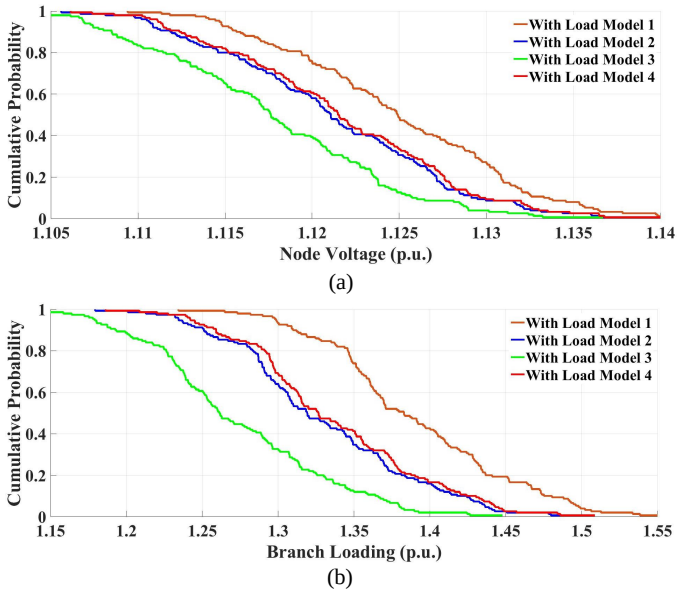

Figure 4.12: CP-based congestion indicators showing the impact of load models on congestion forecast for 13-hour ahead for the 141-bus distribution system, (a) The voltage at node 141, (b) the loading level of branch 3–4.

constant current load ($P \propto V$) than in constant impedance load ($P \propto V^2$), as the voltage is proportional to the power in I load, while it is proportional to the square root of power in Z load. Similar explanations can be applied for branch loading with the different load models as shown in Figure 4.12(b). The results have shown that it is important to have good load models to have a more accurate congestion forecast, i.e., not over- or under-estimate the network's congestion levels.

4.4.2.3 Influence of Operating Modes of PV-Inverter on Congestion Forecast Results

To assess the impact of the operating modes of PV-inverter, the simulations are done with constant-pf and constant-V modes of operation. The simulations consider the PV installations at all the load buses with the same PV production profile as shown in Figure 4.4, varying between 0 and 143.2 kW. The CP for voltage at node 141 and loading level of branch $3-4$ under the two modes of operation are presented in Figure 4.13 and Figure 4.14.

For 12-hour ahead, the CP for node voltage to be above 1.04 p.u. in constant-pf mode is 0.6 (Figure 4.13(a)), while in a constant-V mode, it is 0 (Figure 4.13(b)). Similarly, for 12-hour ahead, the CP for branch loading to be above 0.8 p.u. in constant-V mode (Figure 4.14(b)) is approximately 0.2, while it is almost 0 in constant-pf mode (Figure 4.14(a)).

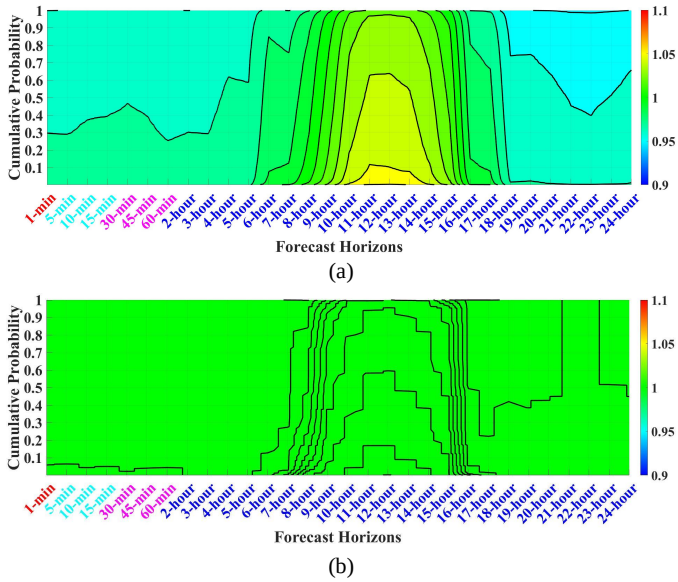

Figure 4.13: CP-based contour plots showing the influence of operating modes of PV-inverter on the congestion forecast for the 141-bus distribution system, (a) The voltage at node 141 with constant-pf mode, (b) the voltage at node 141 with constant-V mode.

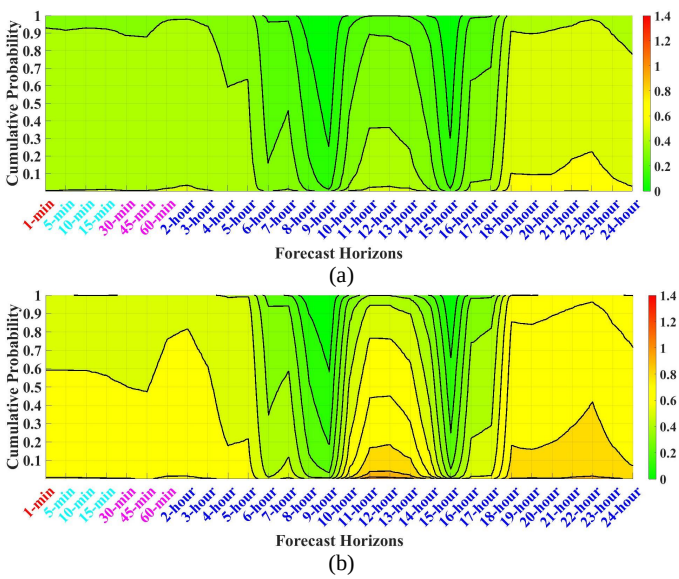

Figure 4.14: CP-based contour plots showing the influence of operating modes of PV-inverter on the congestion forecast for the 141-bus distribution system, (a) The loading level of branch 3–4 with constant-pf mode, (b) the loading level of branch 3–4 with constant-V mode.

It is evident from the results that in a constant-V mode, the CP for nodes voltage has decreased but simultaneously the loading level of branches has increased. The reason for the reduced voltage deviation is due to the consideration of $P-V$ nodes. In a constant-V mode, the voltage is maintained at a specified value through reactive power compensation by injection of higher reactive current, which leads to higher current and MVA loading in associated branches and transformers. Thus, the PV-inverter operating mode is an important aspect to be considered in the advanced congestion forecast tool.

4.5 Scalability and Accuracy of Proposed Tool

The scalability of the proposed tool when applied to a large distribution system, is an important feature, which is considered during tool development. The tool is applied to a 7-bus feeder of Sorea due to the availability of the physical solution for PV production and load forecasts. Further, the tool is applied to the 141-bus real distribution system to evaluate the scalability. The computational time (for all time horizons) for the two case studies in a constant-pf mode of operation is presented in Table 4.4. These results are obtained with MATLAB (R2019b version) and the computer configuration as Intel(R) Core(TM) i7-7700K CPU @4.20-GHz processor and 48 GB RAM.

Table 4.4: Computational Time For Advanced Congestion Forecast Tool with Different Test Systems (in seconds)

Sl. No.	**Number of MCS**	**Sorea's 7-bus system**		141**-bus system**	
		Tolerance Limit		Tolerance Limit	
		0.001 p.u.	0.00001 p.u.	0.001 p.u.	0.00001 p.u.
1	100	0.93	1.01	5.98	7.60
2	1000	3.89	4.50	58.34	75.04
3	10000	39.81	46.23	1239.13	1411.29

The computational time of the algorithm depends on the number of MCS and the tolerance limit. The higher number of MCS and stricter tolerance limits would lead to a more accurate determination of the CP for congestion indicators which is the backbone for contour plots and colour-map. It can be seen from Table 4.4 that the computational time increases with the increase in the number of MCS and stricter tolerance limits. Thus, it is a trade-off situation between computational time and accuracy for the DSO. Like in the 141-bus system, with the given computer configuration, the most optimal solution appears as 1000 MCS and 0.001 p.u. tolerance limit.

Another important aspect is the accuracy of the congestion forecast, which mainly depends on the PV production and load forecasts accuracy. The lesser PV production and load forecasts error would lead to more accurate scenarios generation through MCS, and thus, the results of the congestion forecast will be more accurate. To validate this aspect, two congestion forecast simulations are performed with different forecast errors of PV production and load. The PV production and load forecasts error used in these two simulations are shown in Table 4.3. For each congestion forecast, the mean and standard deviation for the normal distribution is calculated for node voltages and branch loading levels. The standard

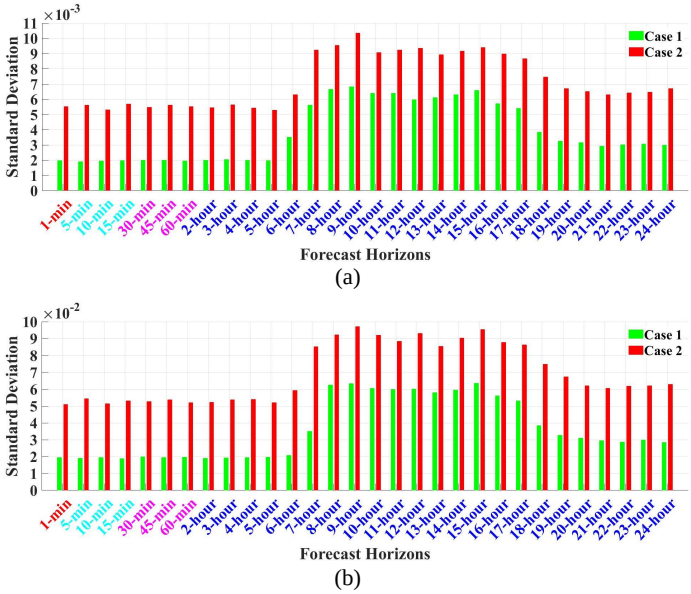

Figure 4.15: Standard deviation of congestion indicators simulated with different forecast errors for the 141-bus distribution system, (a) The node voltage at node 141, (b) the loading level of branch 3–4.

deviation for the voltage at node 141 and the loading level of branch $3-4$, are presented in Figure 4.15.

It can be seen from Figure 4.15 that higher PV production and load forecasts error lead to a higher standard deviation of node voltages (Figure 4.15(a)) and branch loading (Figure 4.15(b)) as the forecast errors considered in Case 1 are lower as compared to Case 2. However, there is no substantial difference in the mean value of node voltages and branch loading in the two simulations as the same mean (μ) obtained from PV production and load forecasts is used in the Gaussian PDF for generating MCS in the two simulations.

4.6 Integration and Demonstration with Existing Distribution Management System

The work presented in this subsection is carried out in collaboration with one of the UNITED-GRID project partner Atos Worldgrid in France [138].

The integration and demonstration of the advanced congestion forecast tool are done using the Codex Smart Edge solution of Atos Worldgrid, which is an adaptable software solution used to set up an IoT and edge computing infrastructure [138]. The main motivations behind

the integration and demonstration of the tool are validation on real test sites, compliance with the industrial standards, and reduced launch time to market. The integration and demonstration are performed for the 7-bus feeder of Sorea's distribution system in France as presented in Section 4.3.1. The solution which enables an integration of the advanced congestion forecast tool is referred to as the UNITED-GRID solution (UGS). In this work, UGS refers to only the advanced congestion forecast tool, while within the UNITED-GRID project it hosts several other tools as well. The functional diagram for the tool integration and demonstration with the existing DMS of the DSO is presented in Figure 4.16. The PV production and load forecasts solution as presented in Section 4.2.1 are also integrated with the UGS which provides inputs to the advanced congestion forecast tool.

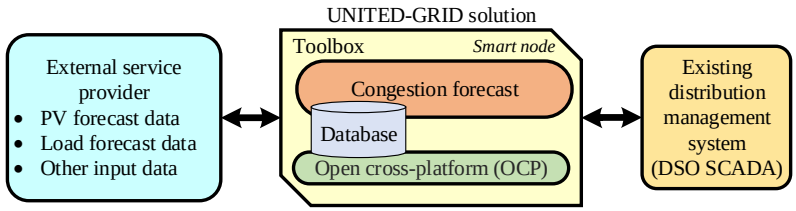

Figure 4.16: Functional diagram for tool integration and demonstration with the DSO SCADA.

The description of the involved actors in the architecture of UGS is as follows.

- External service provider refers to the external data sources such as PV production forecast, load forecast, and other input data.
- Toolbox (TB) executes and supervises the implementation of the advanced congestion forecast tool and the associated graphical interface along with the data management.
- Open cross-platform (OCP) collects and provides the data from/to the different actors. It also ensures the connectivity between the TB and external service providers, as well as the connectivity between the different instantiation of the UGS. The OCP also ensures data sharing and storing within the UGS.
- DSO SCADA platform refers to the existing SCADA system of the DSO.

The UGS dashboard login page for Sorea's demonstration site is shown in Figure 4.17. DSOs can connect through their account and get access to the UGS Dashboard.

The synoptic visualization as presented in Figure 4.18 is based on the cumulative probability of the associated congestion indicators i.e., nodes voltage or component's loading level. The colour code which has been assigned for the synoptic visualization of the congestion indicators is presented in Table 4.5. Figure 4.18(a) represents an example of the synoptic visualization for all the nodes' voltage where all the nodes are shown in red colour which indicates that the CP_{node} for a threshold voltage level (chosen by the DSO) is greater than 0.9 (or 90% of the times). Similar synoptic visualization is presented in Figure 4.18(b) for branches and transformer. In the component visualization, the threshold is selected in terms of percentage loading of the component, for instance, 60% or 80%.

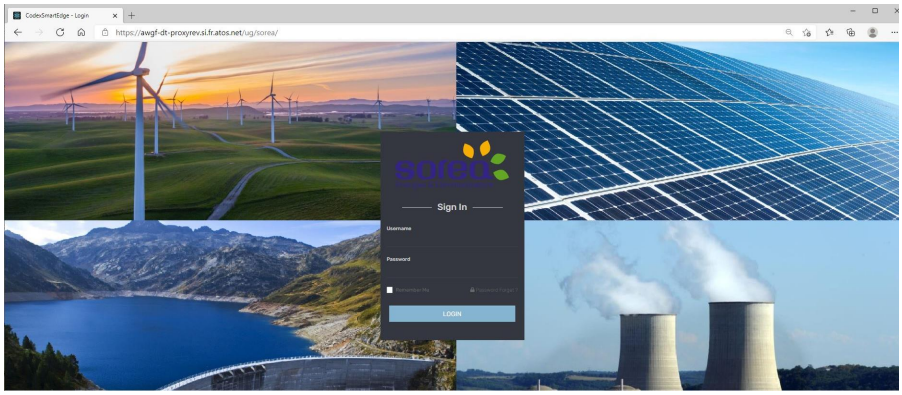

Figure 4.17: Dashboard login page for Sorea's demonstration site in France.

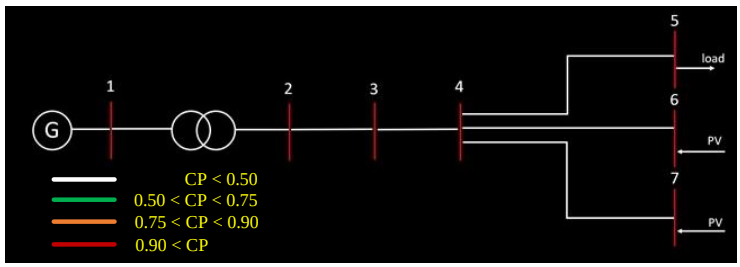

(a)

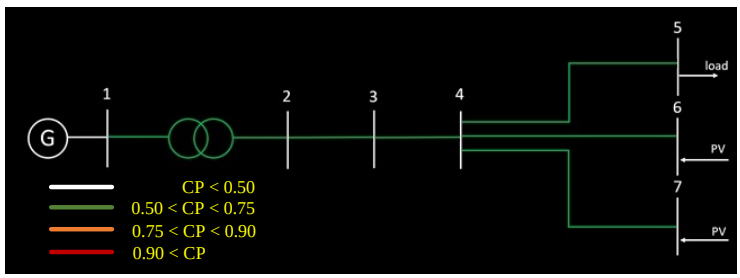

(b)

Figure 4.18: An example of synoptic visualization for 7-bus feeder of Sorea's distribution system using the Codex Smart Edge platform, (a) Nodes voltage, (b) component's loading.

The synoptic visualization presents the implementation of the colourmap (presented in Section 4.4.1.2) within the UGS. The synoptic visualization presents an overall picture

Table 4.5: Colour coding for the synoptic visualization

Cumulative probability	Colour
$CP_{\text{node/component}} < 0.5$	White
$0.5 < CP_{\text{node/component}} < 0.75$	Green
$0.75 < CP_{\text{node/component}} < 0.9$	Orange
$CP_{\text{node/component}} > 0.9$	Red

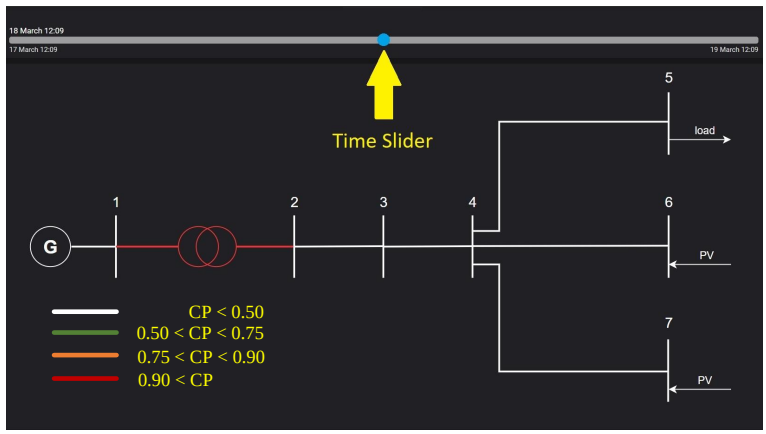

Figure 4.19: A snapshot of the synoptic visualization for 7-bus feeder of Sorea's distribution system using the Codex Smart Edge platform.

of the network before the DSO. Once the system operator identifies the exact location of the congestion, then that specific node/component could be selected (in the synoptic visualization) which will open the contour plot (presented in Section 4.4.1.1). Thus, the synoptic visualization helps the operator to understand the overall as well as component-specific network congestion picture. Further, the time slider empowers the system operator to select the desired forecast horizon for taking corresponding preventive action (discussed in Section 4.1.2.2).

Further, a snapshot of the synoptic visualization of the advanced congestion forecast tool for the 7-bus feeder of Sorea's distribution system is presented in Figure 4.19. It also shows a time slider through which the DSO can select a desired congestion forecast horizon (specific date and time). By moving the time slider, the synoptic is updated and then the operator can visualize the congestion forecast for the desired horizons (both historical and future). As can be seen from Figure 4.19, for the selected horizon, the transformer connected between $1-2$ is coloured as red which signifies that $CP_{\text{transformer}}$ must be greater than 0.9 for the threshold percentage loading which is set as 40% of transformer rated capacity. However, the branches are coloured as white signifying that CP_{branch} of the branches must be less than 0.5 for the threshold percentage loading which is set as 80% of branch ampacity. It is important to highlight that these threshold limits are chosen such that network congestion can be visualized with the present limited amount of PV production at Sorea's site. However,

the DSO can choose or vary these threshold limits according to their network conditions as mentioned in Section 4.1.

4.7 Summary

This chapter presents a tool to assist the DSO to forecast the congestion levels in their networks as per the preferences specified by the DSO. The tool is implemented using the probabilistic power flow model which employs the backward-forward sweep algorithm. The PV production forecast obtained by capturing the fast movement of clouds and the load forecast obtained through an artificial neural network is provided as inputs to the advanced congestion forecast tool. The tool can present the cumulative probability-based contour plots and colour-maps of the network which visualize the network loading conditions for the DSO and make it easy for the DSO to take necessary preventive or corrective actions. The tool has also incorporated various important factors such as PV production and load forecasts accuracy, load models, and PV-inverter operating modes, which can impact the accuracy of network congestion and their simulation results are presented in the chapter. The scalability of the proposed tool is studied by applying it to a large-size distribution system. The tool performs satisfactorily in forecasting network congestion for various time-horizons with acceptable calculation time and accuracy for a relatively large network. The tool has been integrated via an IoT platform Codex Smart Edge of Atos Worldgrid to be ready for market exploitation for real-world applications. The tool will be used by the DSOs to support their daily congestion management tasks and better utilize their grids and thus reducing the need for expensive network reinforcement. The electricity consumers will also be benefitted from the tool as the distribution network will be operated more securely and eventually incur lesser network congestion costs.

CHAPTER 5

Transmission Line Protection using Dynamic State Estimation: Concept, Modelling, and Simulation

This chapter presents the introduction and modelling aspects of a dynamic state estimation based protection scheme. Further, simulation results are presented in detail with different fault types and conditions. The content presented in this chapter is based on the work presented in Paper A.

5.1 Dynamic State Estimation based Protection Scheme

5.1.1 Background

Power system protection has evolved from the era of electromechanical relays to the present era of sophisticated microprocessor-based relays. There are various types of protection schemes such as over-current, distance, differential, etc., which are proposed over time and offer their advantages and disadvantages. The main factors contributing to the mis-operations of the present protection schemes are:

- Higher complexity and sophistication of protection schemes
- Protection based on limited system information
- Failure to operate properly during the occurrence of hidden failures in the system

NERC presented the performance statistics in the protection systems as shown in Figure 5.1. The figure presents that almost 50% of mis-operations are caused either due to incorrect setting errors or relay failures.

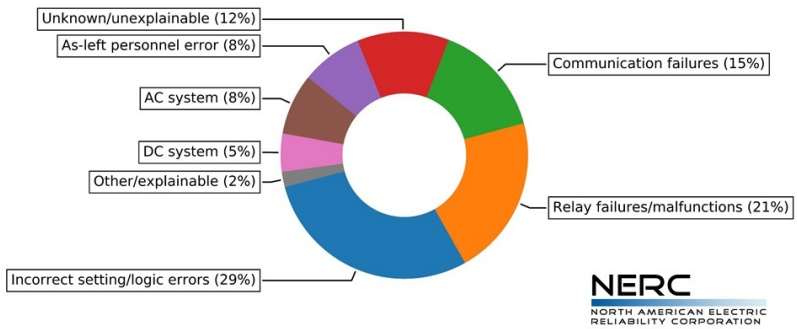

Figure 5.1: Performance Statistics in Protection Systems from NERC [33].

DSE-based protection is one of the possible solutions to these challenges as it adapts to the operating conditions of the system in real-time and provides better visibility of the system status [105]. A feasibility study for such a protection scheme is presented in [106]. The main advantages associated with this scheme are the absence of complex relay settings and lack of coordination which could lead to a substantial reduction in misoperations due to incorrect relay settings (which is one of the major causes of misoperations). The limitations and scope for further developments associated with DSE-based protection are presented in Chapter 8.

5.1.2 Brief Introduction

A dynamic state estimation-based protection scheme (DSEBPS) can be regarded as the generalization of differential protection, which is equipped with dynamic state estimation (DSE). The generalization of the differential protection can be related to the continuous observation of the currents and the terminal voltages of the component. The basic concept used in this scheme is the obeying of all physical laws including Kirchhoff's voltage and current laws, by the transmission line. If any of these laws are violated by the transmission line, then it confirms the faulty condition. The biggest advantage associated with this scheme is the simplification of the protection settings and elimination of the coordination with other components [106], [114].

DSEBPS uses DSE which performs the dynamic modelling of all physical laws that the transmission line should satisfy. The dynamic model is constantly observed by DSE and any violations of laws (abnormality) are apprehended. The analog signals such as voltage, current, etc., and digital signals such as circuit breakers, etc., are measured from the transmission line. DSE utilizes these measurements along with the dynamic model and estimates the operating states of the transmission line. After estimating the states, the Chi-square test is

performed to examine the consistency of the estimates with the measurements or goodness of fit between the dynamic model and measurements. The goodness of fit can be interpreted to determine the transmission line health and obtain the confidence level. The high confidence level indicates normal operation, while a low level indicates abnormal operation [36].

5.1.3 Problem Formulation

A generic π-model for a transmission line has been adapted from the model of distribution line which is developed in [139] by using the transmission line parameters. The motivation to choose a π-model instead of a distributed model is due to the physical availability of the π-model at Chalmers laboratory. Also, the length of the line section considered in the case study is 150 km which is less than 200 km generally above which the distributed model is employed. The mathematical problem formulation is divided into the following subsections:

5.1.3.1 Dynamic Model

The transmission line dynamic model is obtained through the algebraic quadratic companion form (AQCF) and quadratic integration (QI) method. The schematic of a three-phase transmission line is presented in Figure 5.2. The resistances and reactances of each phases are represented as (R_A, R_B, R_C) and (L_A, L_B, L_C), respectively. The shunt capacitances for each phase are represented as (C_A, C_B, C_C). The sending end currents represented as (i_A, i_B, i_C), receiving end currents as (i_a, i_b, i_c), and receiving end voltages as (v_a, v_b, v_c), are considered as the measurements, while the sending end voltages (v_A, v_B, v_C) and series branch currents (i_{dA}, i_{dB}, i_{dC}) are considered as the estimated variables. The selection of the measurements and estimated variables in this work is done on an arbitrarily basis except for the series branch currents (i_{dA}, i_{dB}, i_{dC}) due to their physical unavailability in the laboratory setup. Any set of quantities could be chosen as measurements and estimated variables such that with a given selection of quantities, the state estimation remains an over-determined problem. (G_A, G_B, G_C) are used for stability purposes in numerical integration and are not a part of the physical line model. They help in avoiding the expansion of round-off errors or

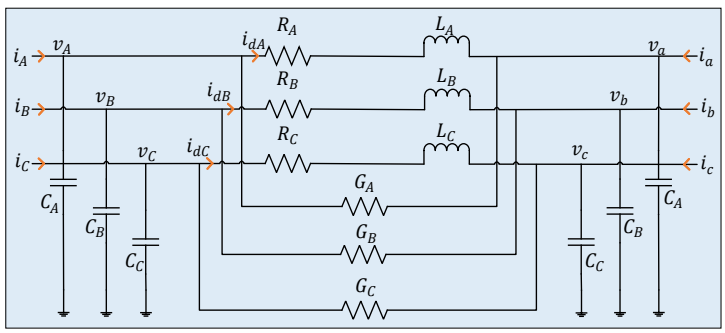

Figure 5.2: Schematic of a three-phase transmission line.

fluctuations in input data which could lead to a substantial deviation of the final answer when numerical integration is applied in differential equations [140]. The model equations for the A-phase can be written as [141]:

$$v_a = v_A - R_A i_{dA} - L_A \frac{di_{dA}}{dt} \tag{5.1}$$

$$i_A + G_A v_a = i_{dA} + G_A v_A + C_A \frac{dv_A}{dt} \tag{5.2}$$

$$i_a - G_A v_a - C_A \frac{dv_a}{dt} = -i_{dA} - G_A v_A \tag{5.3}$$

Equations (5.1)−(5.3) along with B and C phase equations can be condensed into the following form:

$$R_1 z + R_2 \frac{dz}{dt} = S_1 x + S_2 \frac{dx}{dt} \tag{5.4}$$

where z is the measurement vector and given as $[i_A\ i_B\ i_C\ i_a\ i_b\ i_c\ v_a\ v_b\ v_c]$, x is the state vector and given as $[v_A\ v_B\ v_C\ i_{dA}\ i_{dB}\ i_{dC}]$, and R_1, R_2, S_1, and S_2 are constant matrices made up of line parameters value. If mutual coupling between the different phases is considered, then equations (5.1)−(5.3) and subsequently R_1, R_2, S_1, and S_2 matrices should be updated accordingly. It should be noted that the ground path is not incorporated in the transmission line model as the type of grounding and its configuration is outside the protection zone of a transmission line and thus it shall not have an impact on DSEBPS.

QI method is used to simplify the differential equations which are involved in the formulation. In QI method, for one integration interval, the function varies quadratically and this leads to higher accuracy as compared to other methods compared to the trapezoidal method where the function varies linearly throughout. The application of QI method in (5.4) over the time intervals $[t-k, t-k/2]$ and $[t-k, t]$, leads to the following equation:

$$H_1 \begin{bmatrix} z\,(t) \\ z\left(t-\dfrac{k}{2}\right) \end{bmatrix} = H_2 \begin{bmatrix} x\,(t) \\ x\left(t-\dfrac{k}{2}\right) \end{bmatrix} - H_3\left[z\,(t-k)\right] - H_4\left[x\,(t-k)\right] \tag{5.5}$$

where k is one-time step of QI method, and H_1, H_2, H_3, and H_4 are the coefficient matrices defined as follows.

$$H_1 = \begin{bmatrix} \dfrac{k}{6}R_1 + R_2 & \dfrac{2k}{3}R_1 \\ -\dfrac{k}{24}R_1 & \dfrac{k}{3}R_1 + R_2 \end{bmatrix}, H_2 = \begin{bmatrix} \dfrac{k}{6}S_1 + S_2 & \dfrac{2k}{3}S_1 \\ -\dfrac{k}{24}S_1 & \dfrac{k}{3}S_1 + S_2 \end{bmatrix}$$

$$H_3 = \begin{bmatrix} \dfrac{k}{6}R_1 - R_2 \\ \dfrac{5k}{24}R_1 - R_2 \end{bmatrix}, H_4 = \begin{bmatrix} -\dfrac{k}{6}S_1 + S_2 \\ -\dfrac{5k}{24}S_1 + S_2 \end{bmatrix}$$

Restructuring (5.5), leads to the standard form of the state estimator and can be given as:

$$\begin{bmatrix} z\,(t) \\ z\left(t-\dfrac{k}{2}\right) \end{bmatrix} = H \begin{bmatrix} x\,(t) \\ x\left(t-\dfrac{k}{2}\right) \end{bmatrix} + C \tag{5.6}$$

where $H = H_1^{-1}H_2$, $C = -C_1\left[z\left(t-k\right)\right] - C_2\left[x\left(t-k\right)\right], C_1 = H_1^{-1}H_3$, $C_2 = H_1^{-1}H_4$.

The details of QI method and AQCF model are presented in Appendix A.1 and Appendix A.2, respectively.

5.1.3.2 State Estimation Algorithm

The most common approach for the solution of state estimation (SE) i.e., the weighted least square (WLS) algorithm is used to solve the SE problem. The linear version of the WLS algorithm can be stated as:

$$z = Hx + \eta \tag{5.7}$$

where z represents the measurement vector consisting of voltages and currents, H represents the Jacobian matrix, x represents the state vector and η represents the measurement error vector.

The objective function of SE can be defined as the minimization of the following function:

$$\begin{aligned} J &= \left(z - H\hat{x}\right)^T R^{-1}\left(z - H\hat{x}\right) \\ J &= \eta^T R^{-1}\eta \end{aligned} \tag{5.8}$$

In the above equation, $\hat{x}$ is the WLS estimate, R^{-1} is the diagonal weight matrix and defined as $diag\left(\sigma_1^2, \sigma_2^2, \sigma_3^2, \ldots., \sigma_m^2\right)$, and σ_i represents the standard deviation of each measurement i.

The expression for the WLS estimate comes out as:

$$\hat{x} = \left(H^T R^{-1} H\right)^{-1}\left(H^T R^{-1} z\right) \tag{5.9}$$

5.1.3.3 Chi-square Test

The following steps are performed for the Chi-square test using the WLS SE algorithm:

- Calculate the SE objective function J using (5.8).
- Checkup with the Chi-square distribution table to quantify the confidence level which requires the degree of freedom (d) and SE objective function J, as inputs. The degree of freedom is calculated as $d = m - n$, where m is the number of measurements and n is the number of state variables.

5.1.3.4 Confidence Level

The confidence level (h) in the transmission line health is evaluated based on the goodness of fit between the dynamic model and measurements obtained from the Chi-square test as below:

$$h = 1 - p_{[\chi^2 \leqslant J]} \tag{5.10}$$

where, $p_{[\chi^2 \leqslant J]}$ is the probability of the χ^2 distribution for $\chi^2 \leqslant J$ and is obtained from the Chi-square test.

5.1.3.5 Threshold Value and Low Pass Filter

A threshold value is selected for the objective function such that the confidence level remains high during normal operating conditions. It is required as there exists a slight mismatch

between the measurements and their estimated values during the normal operating conditions and thus the objective function is evaluated as non-zero finite values. The threshold for the objective function is selected based on the range of objective function obtained during steady-state conditions with due consideration of measurement uncertainties as well as possible variation in system configurations. In addition to the threshold value, a low pass filter as presented in (5.11) is employed for smoothing and avoiding any unreasonable spike (could be bad data) in the objective function curve.

$$J^f_{new} = (\alpha \times J) + [(1-\alpha) \times J^f_{previous}] \tag{5.11}$$

where, J and J^f are original and new objective functions, respectively, and α is the smoothing factor ranging between 0 and 1. Based on the experience from case studies performed with simulation by using different values of α, it is taken as 0.001, while from case studies performed with experimental validation, it is taken as 0.09. The objective function presented in all the following case studies in this work includes the threshold value and application of a low pass filter. In general, the threshold value that could work for most of the cases could be achieved by simulating the most credible fault cases e.g., maximum fault current, and then verifying that it should work with other cases e.g., minimum fault current considering the weakest source and highest fault impedance and also external faults. It should also be verified that the threshold level should not trigger the trip signal in high load conditions, as well as for external faults, current transformers (CTs) and voltage transformers (VTs)/coupling capacitor voltage transformers (CCVTs) errors, and/or saturation. From the experience of simulations with different faults studied in this work for a 150-km long transmission line with an operating voltage of 400 kV (scaled-down model) and maximum measurement uncertainties in the range between 0.02% and 0.03%, the threshold value shall range between 2.0e6 and 2.5e6, while from the experience of validations the threshold value ranges between 30e3 to 40e3.

5.1.3.6 Trip Signal

The consistency of the objective function is used to obtain the confidence level which in turn is used to generate the trip signal. In order to generate the trip signal, the confidence level signal should be low. The objective function is observed for three consecutive samples to be above a threshold value and then the confidence level signal goes low. The motivation to observe the objective function for three consecutive samples is to obtain enhanced reliability of the protection decision. All the confidence level results in the case studies performed with simulations are obtained by considering three consecutive samples.

5.2 Case Study

5.2.1 Description

The case study considered for the simulation of DSEBPS consists of a transformer, six π-sections of a transmission line (each π-section corresponds to 150 km of a 400 kV line), and a resistive load which is a physical setup available at Chalmers power system laboratory. One of the motivations to choose this test system is more π-sections which increase the

length of the transmission line and help to reduce the fault current. The parameters and the values of the components which are considered in the simulation are presented in Table 5.1.

Table 5.1: Parameters and the Values of the Simulation Components

Parameter		Value
Nominal grid voltage		400 V
Nominal grid frequency		50 Hz
Each π -section	Series resistance	0.052 Ω
	Series inductance	3.033 mH
	Shunt capacitance	46 μF
Resistive load		9 kW

5.2.2 Simulation Setup

The simulation for the case study is performed in MATLAB Simulink (R2020b version). The single-line diagram of the network is presented in Figure 5.3. As shown in Figure 5.3, the simulation network consists of six π-sections which are connected to the main grid at one end and 9 kW resistive load at the other end.

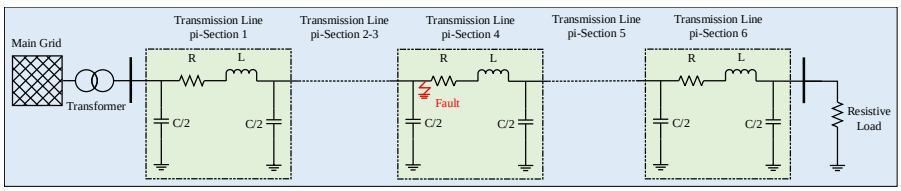

Figure 5.3: Single-line diagram of the simulation setup for a fault.

For DSEBPS, the sending end currents (i_A, i_B, i_C), receiving end currents (i_a, i_b, i_c), and receiving end voltages (v_a, v_b, v_c) are taken as the measurements, while the sending end voltages (v_A, v_B, v_C) and series branch currents (i_{dA}, i_{dB}, i_{dC}) are taken as the estimated variables, as shown in Figure 5.2. This selection is done on an arbitrarily basis except for the series branch currents (i_{dA}, i_{dB}, i_{dC}) due to their physical unavailability in the laboratory setup. In the case of a meshed network, the selection should be made such that SE remains an over-determined problem. The estimated values of the measurements are calculated back through the estimated variables so that a comparison could be made between the measurements and their estimated values. The comparison between the measurements and their estimated values is used for the calculation of the SE objective function. Additionally, as the measured values of the estimated variables are not available, they cannot be compared and hence not presented in the plots.

The transmission line is modelled using the lumped (π-model) instead of the distributed model. The corrections due to distributed model are more significant with the increased line length (more than 200 km). The lumped model is preferred in this work as the series

branch currents (i_{dA}, i_{dB}, i_{dC}) could not be calculated in a distributed model. However, the impact of distributed parameters on DSEBPS will be very limited in the present case study due to the short line length.

5.3 Simulation Results

5.3.1 Three-phase Fault with Resistive Load

The simulation is run for 0.15 seconds and the measurement sampling rate is taken as 1e-6 seconds. The sampling rate corresponds to the rate at which a continuous signal is discretized to generate sampled values. The sampling rate of 1e-6 seconds translates to a sampling frequency of 1000 kHz or 1 MHz. The single-line diagram of the network is presented in Figure 5.4. A temporary (self-clearing) three-phase fault is created for 40 milliseconds initiated at 0.04 seconds and cleared at 0.08 seconds. The simulated measurements from Simulink are saved into the workspace and are provided as inputs to the script of the DSE-based protection scheme executed in MATLAB. The simulated measurements are compared with their estimated values calculated using the estimated variables. The three-phase simulated measurements along with their estimated values are presented in Figure 5.5.

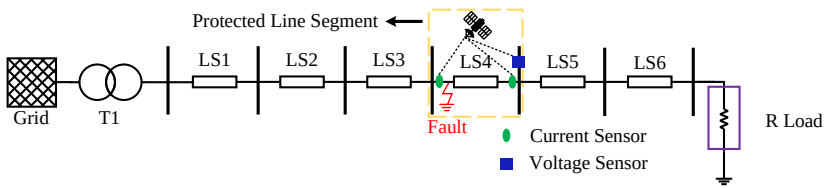

Figure 5.4: Single-line diagram of the simulation setup with resistive load.

It can be seen from Figure 5.5 that during the normal operating conditions from 0 to 0.04 seconds the simulated measurements and their estimated values are in concurrence, while when the fault occurs (between 0.04 and 0.08 seconds), the simulated measurements and their estimated values have substantial differences. The reason behind the inconsistency is due to the consideration of steady values of system parameters (e.g. constant frequency as 50 Hz) during the fault conditions. The system returns to normal conditions soon after the fault is cleared. The original objective function, filtered objective function, and confidence level are presented in Figure 5.6. A threshold value of 2.22e6 is used to set the objective function to zero during normal conditions based on the explanation provided in Section 5.1.3.

Figure 5.6 shows that values of the filtered objective function are low during the normal conditions (0 to 0.04 seconds), while they rise substantially high during the fault condition (0.04 to 0.08 seconds). Based on the objective function, the Chi-square test is performed which gives a high confidence level (indicating goodness of fit between the dynamic model and measurements) during the normal condition. During the fault conditions, the high values of objective function lead to a low confidence level. Based on the low confidence level a trip signal is generated and sent to the circuit breakers. Additionally, a separate case study

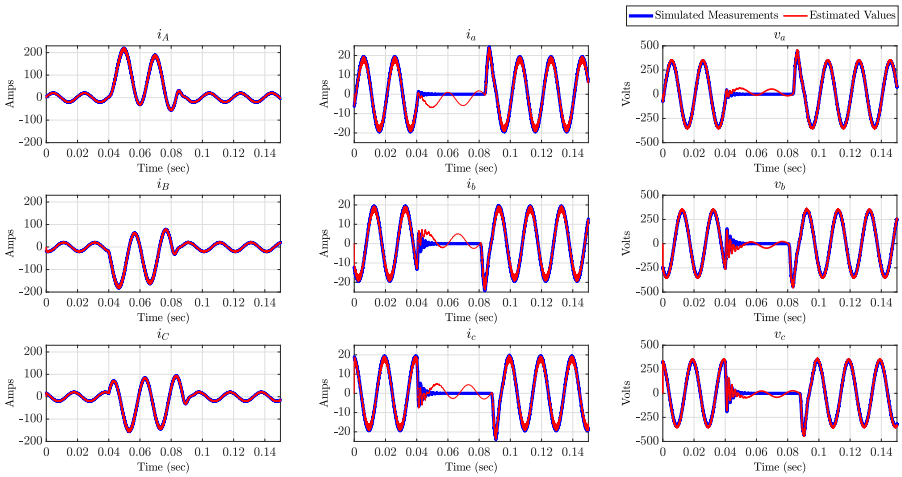

Figure 5.5: MATLAB Simulink results in terms of simulated measurements and their estimated values of the sending end currents (i_A, i_B, i_C), receiving end currents (i_a, i_b, i_c), and receiving end voltages (v_a, v_b, v_c) for a three-phase fault with resistive load.

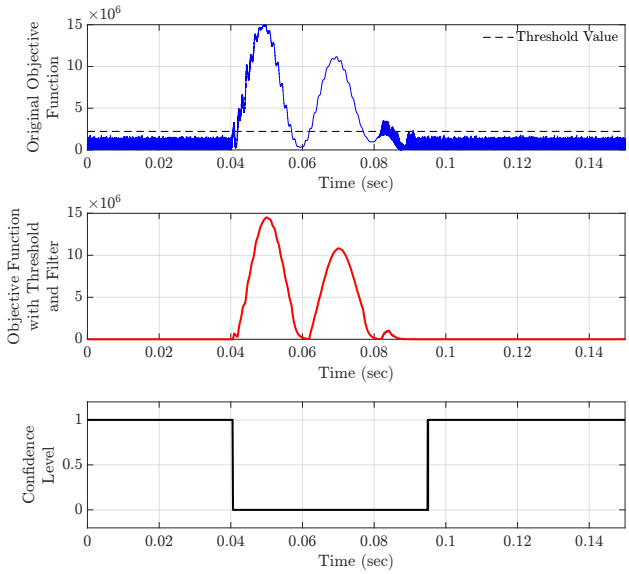

Figure 5.6: MATLAB Simulink results in terms of the original objective function, objective function with threshold and filter, and confidence level for a three-phase fault with resistive load.

with the inclusion of CTs and CCVTs was performed which showed that their transient response does not have an impact on the DSEBPS performance. In this case study, the fault was created very close to the CCVTs location leading to transients. DSEBPS performed as intended under this condition as well and the trip signal was generated successfully.

5.3.2 Three-phase Fault with Inductive Load

In order to test DSEBPS under inductive load conditions, the same test setup as explained in Section 5.2 using the MATLAB software. The single-line diagram of the network is presented in Figure 5.7. A three-phase fault is created for 40 milliseconds initiated at 0.04 seconds and cleared at 0.08 seconds.

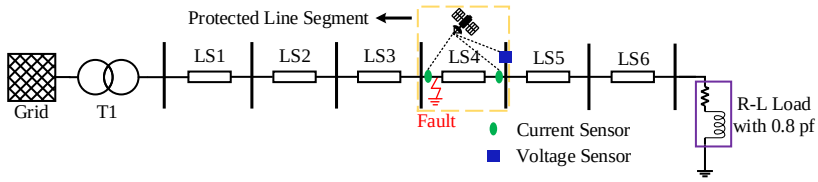

Figure 5.7: Single-line diagram of the simulation setup with R-L load of pf 0.8.

It can be seen from Figure 5.8 that both the sending and receiving end currents have increased, while the receiving end voltages have reduced, during the fault. The state

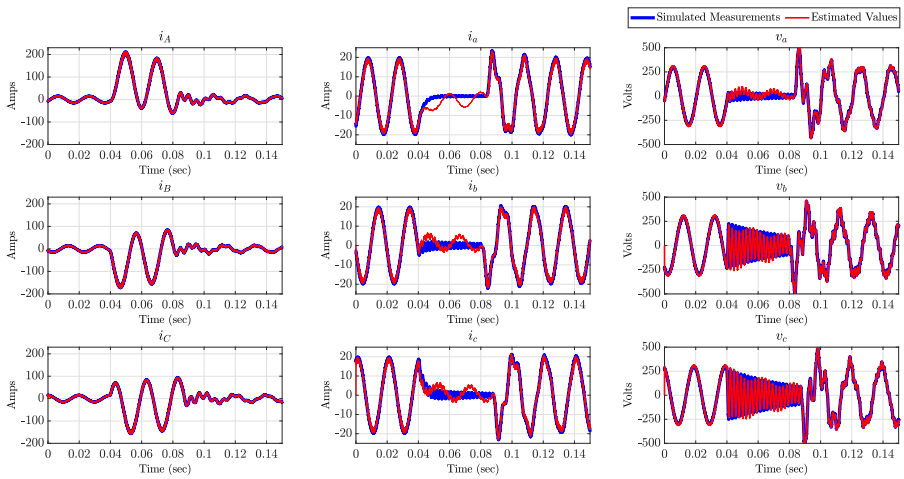

Figure 5.8: MATLAB Simulink results in terms of simulated measurements and their estimated values of the sending end currents (i_A, i_B, i_C), receiving end currents (i_a, i_b, i_c), and receiving end voltages (v_a, v_b, v_c) for a three-phase fault with R-L load of pf 0.8.

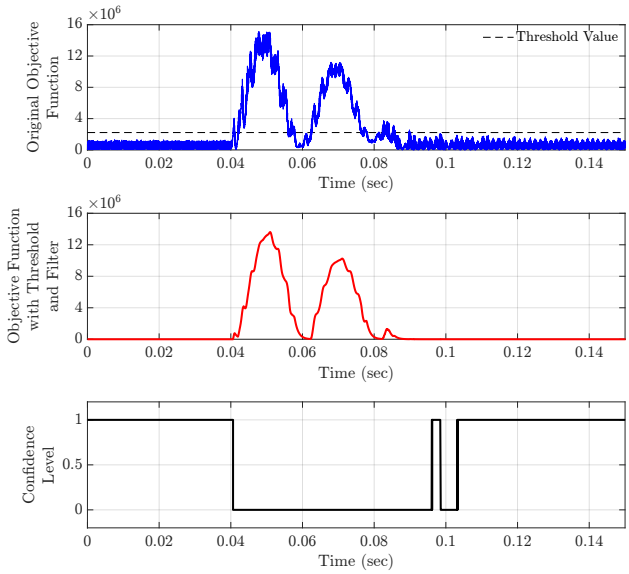

Figure 5.9: MATLAB Simulink results in terms of the original objective function, objective function with threshold and filter, and confidence level for a three-phase fault with R-L load of pf 0.8.

estimation objective function (with threshold and filter) and confidence level are presented in Figure 5.9. The same threshold value of 2.22e6 is used to set the objective function to zero during normal conditions. Figure 5.9 shows that values of state estimation objective function are low during the normal conditions (0 to 0.04 seconds), while they rise substantially high during the fault condition (0.04 to 0.08 seconds).

Based on the state estimation objective function, the Chi-square test is performed which gives a high confidence level (indicating goodness of fit between the dynamic model and measurements) during the normal condition, while during the fault conditions, the high values of objective function lead to a low confidence level. Based on the low confidence level a trip signal is generated and sent to the circuit breakers. The main changes can be observed in the current and voltage signals which show sluggish response as compared with the resistive load but it does not have an impact on the confidence level and trip signal generation. Thus, it can be concluded that DSEBPS works as intended with inductive load conditions.

5.3.3 High Impedance Fault

A high impedance fault could be described as the one where the fault impedance is high and that leads to reduced fault current, sometimes close to or less than normal loading current. DSEBPS is examined with the same test setup as explained in Section 5.2 using the MATLAB software by creating a three-phase fault with equivalent fault impedance of 20 Ω

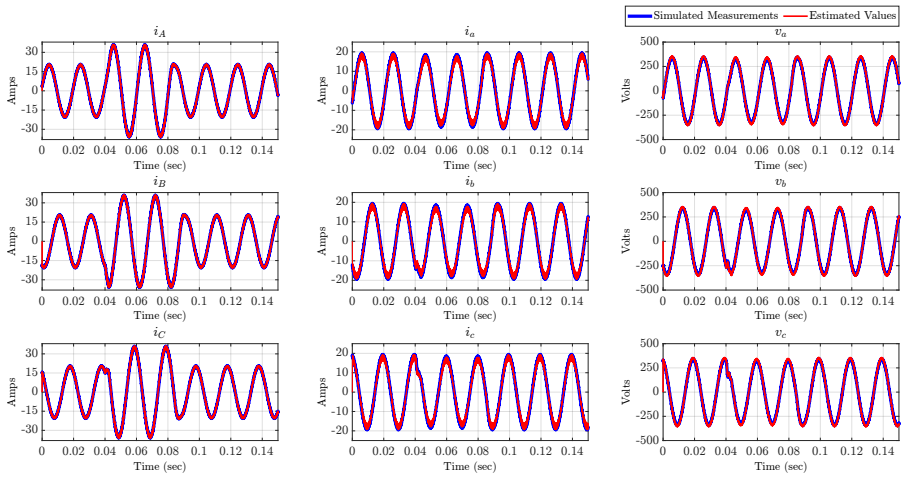

Figure 5.10: MATLAB Simulink results in terms of simulated measurements and their estimated values of the sending end currents (i_A, i_B, i_C), receiving end currents (i_a, i_b, i_c), and receiving end voltages (v_a, v_b, v_c) for a high impedance fault.

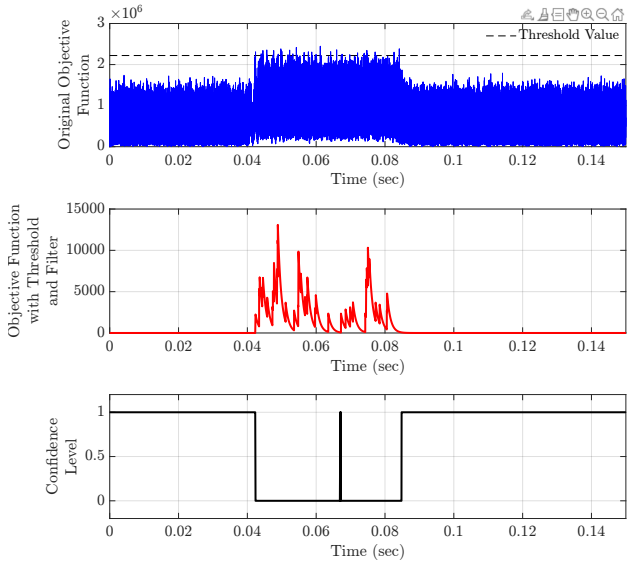

Figure 5.11: MATLAB Simulink results in terms of the original objective function, objective function with threshold and filter, and confidence level for a high impedance fault.

for 40 milliseconds initiated at 0.04 seconds and cleared at 0.08 seconds. The simulations were also carried out with various other values of equivalent fault impedances such as 15 Ω, 5 Ω, 1 Ω, and 0.1 Ω. These case studies showed that during the fault conditions the sending end currents reach a higher peak, while the receiving end currents and receiving end voltages increase with the increase in equivalent fault impedance.

The sending end current, receiving end current, and receiving end voltage with 20 Ω fault impedance are presented in Figure 5.10. It can be seen from Figure 5.10 that the receiving end voltages and receiving end currents during fault conditions are in the same range as normal operating conditions. In the case of sending end currents, a small transient (peak value of around 35 Amperes) could be seen due to the addition of a small fault current component along with load current. Despite the absence of a large fault current (due to high fault impedance) and transients, a non-conformity exists between the simulated measurements and their estimated values. Due to this non-conformity between the simulated measurements and their estimated values, the objective function sees a spike (smaller as compared to a zero impedance fault), while keeping the same threshold value (i.e., 2.22e6). As the objective function goes high, correspondingly the confidence level goes low (i.e., 0), as can be observed in Figure 5.11. It is important to mention here that the objective function presented in Figure 5.11 is with the application of filter (and threshold) which brings the peak value around 1e4. Thus, a trip signal is generated during fault and sent to the breakers.

5.3.4 External Fault

An external fault is one that occurs outside the protection zone and the protection scheme should identify it as an external fault such that a trip signal should not be issued. DSEBPS

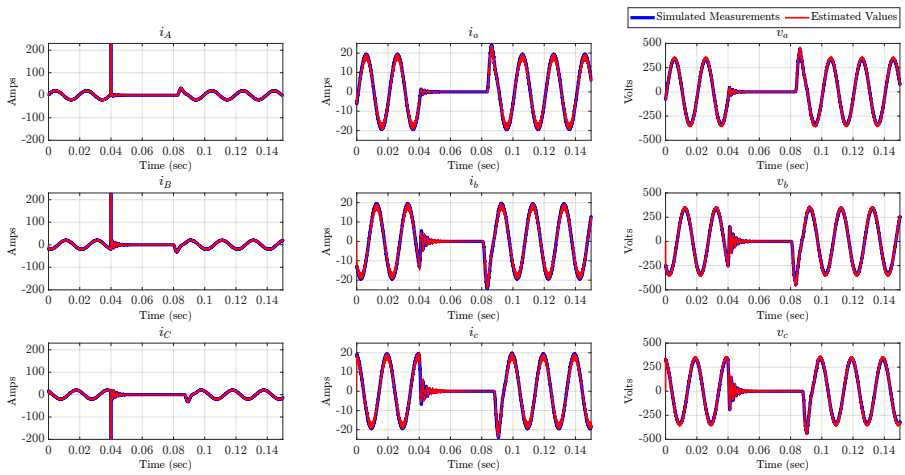

Figure 5.12: MATLAB Simulink results in terms of simulated measurements and their estimated values of the sending end currents (i_A, i_B, i_C), receiving end currents (i_a, i_b, i_c), and receiving end voltages (v_a, v_b, v_c) for an external fault.

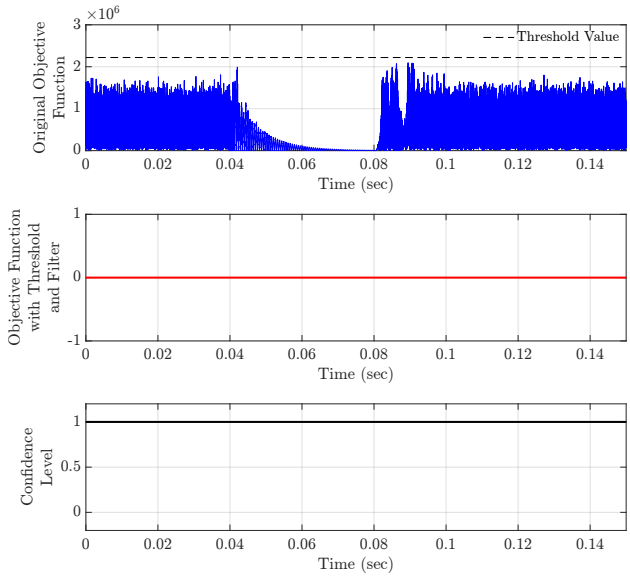

Figure 5.13: MATLAB Simulink results in terms of the original objective function, objective function with threshold and filter, and confidence level for an external fault.

is examined with the same test setup as explained in Section 5.2 by creating a three-phase external fault (just outside the protected transmission line) for 40 milliseconds initiated at 0.04 seconds and cleared at 0.08 seconds.

Figure 5.12 shows that the transients occur in the simulated measurements of sending end currents, receiving end voltages, and receiving end currents due to an external fault. Despite the transients in the simulated measurements, the estimated values are in concurrence with the measurements. Due to this concurrency between the simulated measurements and their estimated values, the objective function remains below the set threshold value and hence the confidence level remains high (i.e., 1) as can be observed in Figure 5.13, and hence a trip signal is not generated in case of an external fault (which is intended). Thus, DSEBPS discriminates against the external fault and does not issue a trip signal.

5.3.5 Fault Current Fed from Both Ends

In the case of meshed network, the fault current is fed from both ends of the transmission line. DSEBPS is examined with the same test setup as explained in Section 5.2 by adding a generator on the receiving end. A three-phase fault is created for 40 milliseconds initiated at 0.04 seconds and cleared at 0.08 seconds.

Figure 5.14 shows that the measurements and the estimated values of receiving end current (i_a, i_b, i_c) goes high during the fault conditions, unlike the previous fault due to consideration of a fault current fed from both ends. The contribution of the receiving end generator

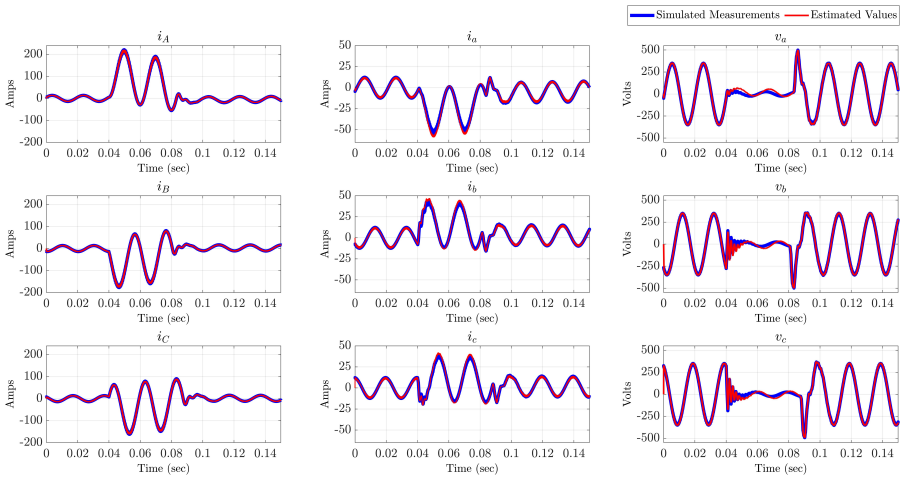

Figure 5.14: MATLAB Simulink results in terms of simulated measurements and their estimated values of the sending end currents (i_A, i_B, i_C), receiving end currents (i_a, i_b, i_c), and receiving end voltages (v_a, v_b, v_c) for a fault current fed from both ends.

depends on the rating of the generator. In the case of the receiving end voltages (v_a, v_b, v_c), it reduces during the fault but not until zero unlike the fault current fed from one end. Further, it can be seen from Figure 5.15 that as soon as the three-phase fault occurs at 0.04 seconds, the objective function goes high and subsequently the confidence level goes low (i.e., 0). Thus, a fault in the meshed network is successfully detected by DSEBPS.

5.3.6 Evolving faults

The evolving faults can be apprehended in two different ways, whose impact on DSEBPS can be explained as follows:

1. Evolving faults could be considered as the faults which are initially external faults and eventually turn into internal faults as explained in [142]. In this case, DSEBPS would not detect the external fault even if it is just outside the protection zone. As soon as the fault becomes an internal fault, it would be detected by DSEBPS. The simulation results for an external fault are presented in Section 5.3.4.
2. Another view of the evolving faults as those faults that in the beginning start as low-intensity faults (such as high impedance faults) and eventually develop into low impedance faults. The concept figure for such evolving faults is presented in Figure 5.16. In Figure 5.16, a high impedance fault (with 15 Ω) is simulated for 20 milliseconds initiated at 0.04 seconds and cleared at 0.06 seconds, followed by a medium impedance fault (with 3 Ω) is simulated for 20 milliseconds initiated at 0.06 seconds and cleared at 0.08 seconds, and finally, a low impedance fault (with 0.0001 Ω) is simulated for 20 milliseconds initiated at 0.08 seconds and cleared at 0.1 seconds.

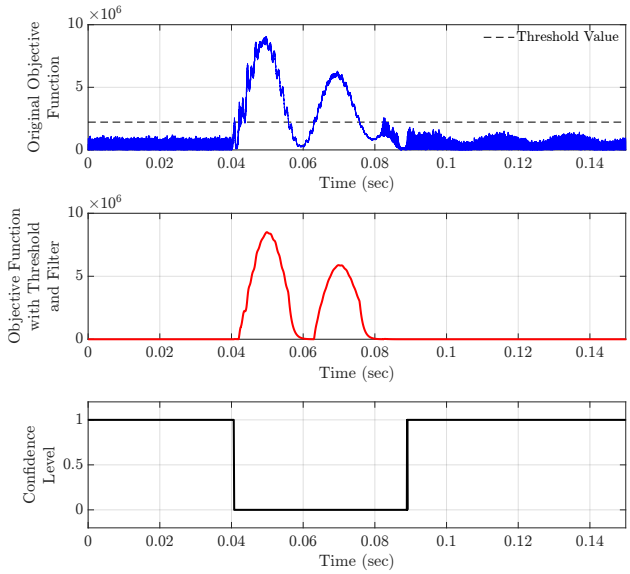

Figure 5.15: MATLAB Simulink results in terms of the original objective function, objective function with threshold and filter, and confidence level for a fault current fed from both ends.

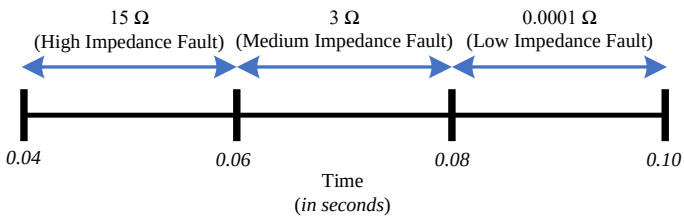

Figure 5.16: Concept figure for the evolving faults.

Although in this simulation study, the switching of fault type is done every 20 milliseconds, however, it could be longer in reality. Also, a three-phase fault is considered here in the simulation, while it could be a single-line-to-ground fault in beginning and then become a double-line-to-ground or three-phase fault. The objective here is to show that DSEBPS works as intended in this situation and the time duration between switching different faults and type of fault will not impact the results of DSEBPS.

DSEBPS is examined with the same test setup as explained in Section 5.2 using the MATLAB software by creating a fault scenario as shown in Figure 5.16. It

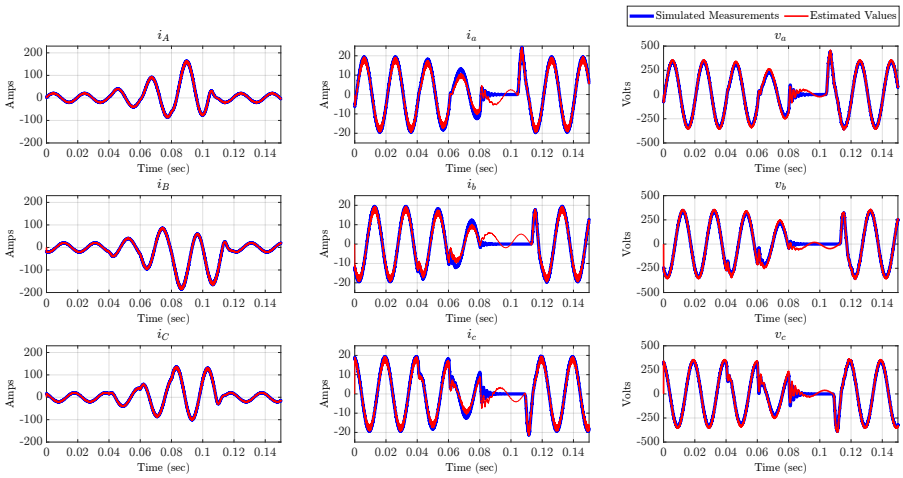

Figure 5.17: MATLAB Simulink results in terms of simulated measurements and their estimated values of the sending end currents (i_A, i_B, i_C), receiving end currents (i_a, i_b, i_c), and receiving end voltages (v_a, v_b, v_c) for an evolving fault.

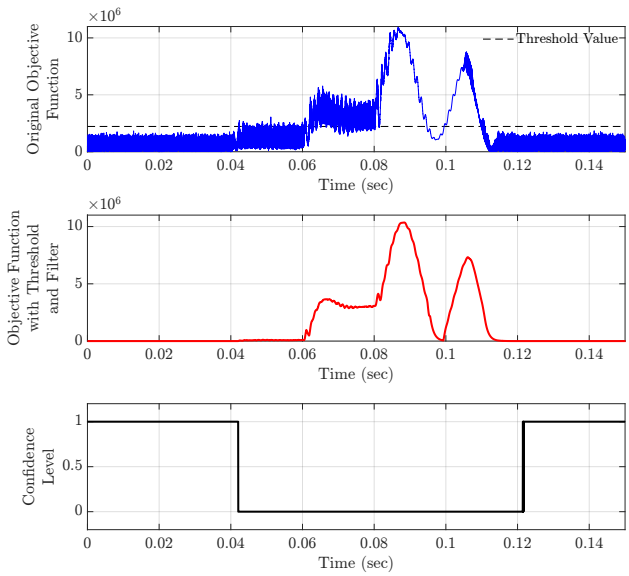

Figure 5.18: MATLAB Simulink results in terms of the original objective function, objective function with threshold and filter, and confidence level in case of an evolving fault.

can be seen from Figure 5.17 that there are small transients in fault voltages and currents every time there is fault switching. DSEBPS detects the high impedance fault despite the absence of large transients, as seen in Figure 5.18. The same threshold value (i.e., 2.22e6) is used for the objective function. As the objective function goes high, correspondingly the confidence level goes low (i.e., 0), as can be observed in Figure 5.18. It should be noted here that as the considered fault is a high impedance fault initially, therefore the corresponding increase in the objective function (with filter and threshold) is lesser as compared to a low impedance fault. Since the objective function plot is of the scale of 1e6, therefore the increase in objective function during the high impedance fault is not clearly visible, although the confidence level goes down. Thus, a trip signal is generated and sent to the breakers. The fault condition is detected much before it becomes a low impedance fault as can be seen from Figure 5.18. Thus, DSEBPS works reliably in case of an evolving fault.

5.3.7 Infeed Condition

Infeed condition could occur in a two-terminal transmission line and hence a new case study analyzing the performance of DSEBPS during the infeed condition is performed. The dynamic model of the transmission line has been modified to incorporate the changes caused due to the infeed condition in the present model. In this regard, the same test setup is chosen as explained in Section 5.2 but with the inclusion of the tapping point in the middle of the transmission line. This setup requires more measurements (including phase currents at the tapped point) as compared to the original case study. Eventually, the trip signal decision is taken based on the results obtained with all these measurements and not based on dividing the transmission line into smaller sections. The single-phase representation of the considered system is presented in Figure 5.19.

The dynamic modelling of the transmission line under this condition along with the application of the quadratic integration method is explained in Appendix A.4. The transmission line has three phases A, B, and C. The resistances and reactances of the transmission line before the tapping point are represented as R_A, R_B, R_C, and L_A, L_B, L_C, respectively. The shunt capacitances of the transmission line before the tapping point are represented as C_A, C_B, C_C. The resistances and reactances of the transmission line after the tapping point are represented as R_{A1}, R_{B1}, R_{C1}, and L_{A1}, L_{B1}, L_{C1}, respectively. The shunt capacitances of the transmission line before the tapping point are represented as C_{A1}, C_{B1}, C_{C1}. Also,

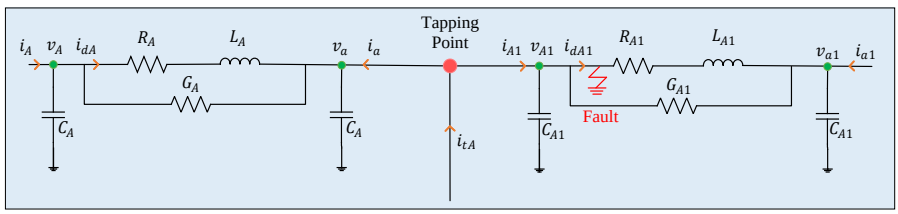

Figure 5.19: Single phase representation of the transmission line in the case of the infeed condition.

G_A, G_B, G_C, G_{A1}, G_{B1}, G_{C1} are considered for the numerical stabilization purpose and may not be essentially part of actual system. The sending end voltages and currents before the tapping point are represented as v_A, v_B, v_C, and i_A, i_B, i_C, respectively. The receiving end voltages and currents before the tapping point are represented as v_a, v_b, v_c, and i_a, i_b, i_c, respectively. Also, i_{dA}, i_{dB}, i_{dC}, are the currents in the series branch before the tapping point. The sending end voltages and currents after the tapping point are represented as v_{A1}, v_{B1}, v_{C1}, and i_{A1}, i_{B1}, i_{C1}, respectively. The receiving end voltages and currents after the tapping point are represented as v_{a1}, v_{b1}, v_{c1}, and i_{a1}, i_{b1}, i_{c1}, respectively. Also, i_{dA1}, i_{dB1}, i_{dC1}, are the currents in the series branch after the tapping point.

To examine the performance of DSEBPS during infeed conditions, a balanced three-phase fault with a fault impedance of 1 Ω is created after the tapping point for 40 milliseconds initiated at 0.04 seconds and cleared at 0.08 seconds (as shown in Figure 5.19). The simulation results in terms of measured and estimated values of sending end currents before the tapping point (i_A, i_B, i_C), receiving end currents before the tapping point (i_a, i_b, i_c), and receiving end voltages before the tapping point (v_a, v_b, v_c), sending end currents after the tapping point (i_{A1}, i_{B1}, i_{C1}), receiving end currents after the tapping point (i_{a1}, i_{b1}, i_{c1}), and receiving end voltages after the tapping point (v_{a1}, v_{b1}, v_{c1}), and tapped branch currents (i_{tA}, i_{tB}, i_{tC}) are presented in Figure 5.21. The simulation results in terms of the original objective function, filtered objective function, and confidence level are presented in Figure 5.20. All the plots in Figure 5.21 show that during the normal operating conditions (from 0.04 seconds until 0.08

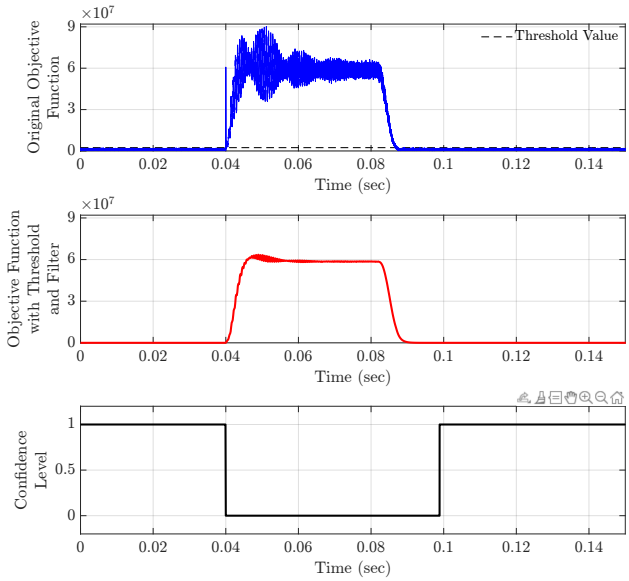

Figure 5.20: MATLAB Simulink results in terms of the original objective function, objective function with threshold and filter, and confidence level during the infeed condition in a transmission line.

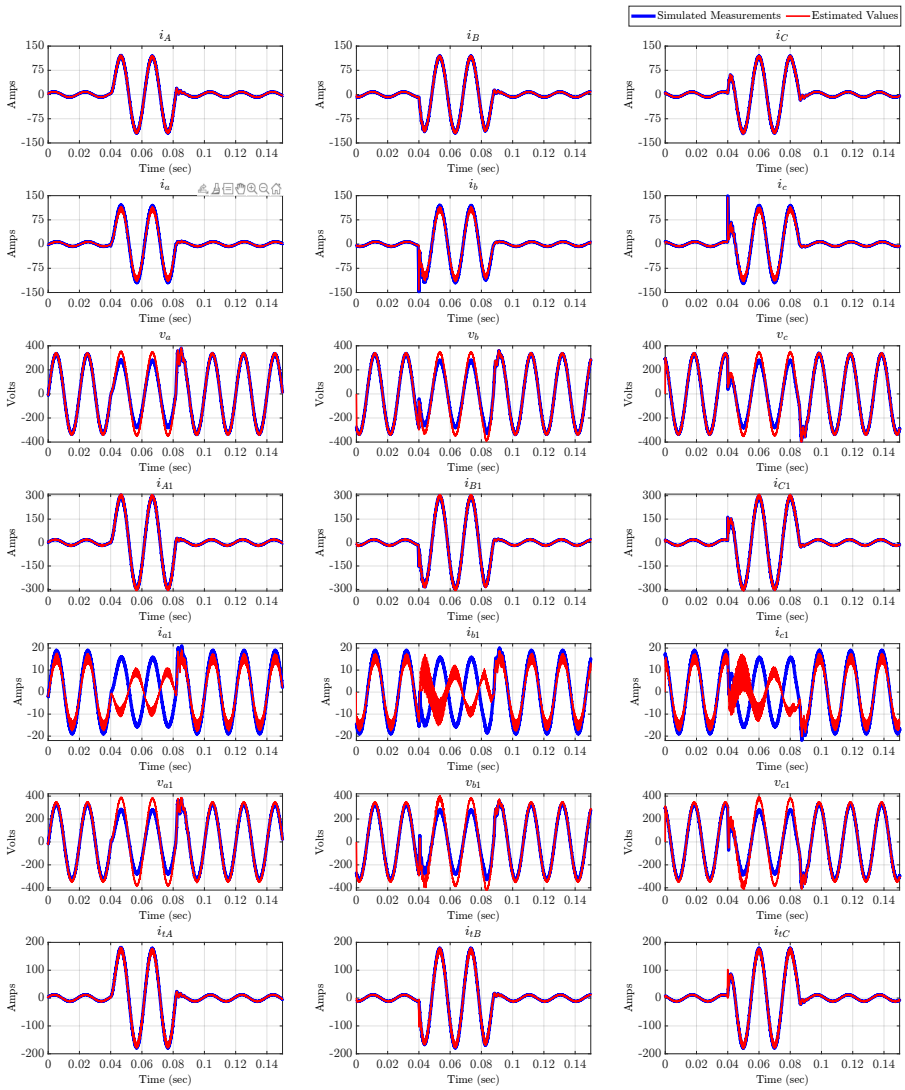

Figure 5.21: MATLAB Simulink results in terms of simulated measurements and their estimated values during the infeed condition in a transmission line.

seconds) the measured and estimated values are in concurrence with each other due to the correct modelling of the transmission line during the infeed condition.

Thereafter, a three-phase fault is created (at sending end of the transmission line after

the tapping point) for 40 milliseconds at 0.04 seconds. It can be seen from Figure 5.21 that during the fault the sending end currents after the tapping point and receiving end currents before the tapping point go very high and reaches a peak value of up to 300 Amperes and 150 Amperes, respectively. In the case of the receiving end voltages after the tapping point, it reduces a little during the fault. Further, it can be seen from Figure 5.20 that as soon as the three-phase fault occurs at 0.04 seconds, the objective function goes high, and subsequently, the confidence level goes low (i.e., 0). Thus, this case study proves that DSEBPS performs as intended during infeed conditions.

5.3.8 Transmission Line Parameter's Uncertainty

There is uncertainty associated with transmission line parameters which could have an impact on DSE accuracy or any other type of SE, which uses line parameters as inputs. The line parameters could vary ranging between 1% and 20% [143]. Based on this range, a case study is performed where all line parameters (resistances, inductances, and capacitances) are varied ±10%. The same test setup as explained in Section 5.2 is employed by creating a three-phase fault for 40 milliseconds initiated at 0.04 seconds and cleared at 0.08 seconds. To compare the results, the newly obtained objective function is plotted with the objective function obtained with the original line parameters, as shown in Figure 5.22.

It can be seen from Figure 5.22 that due to uncertainties the main change is visible in the peaks of the objective function. The difference in peaks shows a higher mismatch between the measurements and their estimated values due to uncertainties introduced in the transmission line parameters. However, it does not impact the results of DSEBPS as minimal changes are observed in the objective function immediately after the fault initiation (around 0.04 seconds).

Thus, it can generally be concluded based on the simulation studies that DSEBPS has robust performance and works satisfactorily under inductive conditions, high impedance fault,

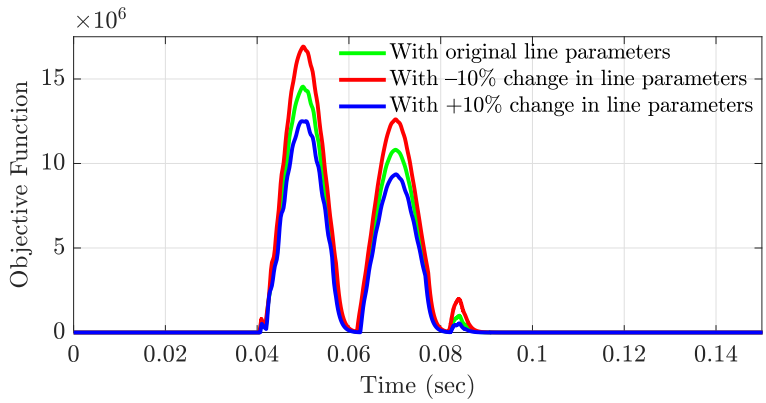

Figure 5.22: A plot of the objective function with different values of transmission line parameters accuracy.

and external fault. Further, DSEBPS works also with limited uncertainty in transmission line parameters.

5.4 Summary

This chapter presented the details of DSEBPS along with simulation results for a transmission line. Firstly, the general concept of DSEBPS is presented followed by the modelling of the transmission line using the quadratic integration method and AQCF model. Thereafter, the state estimation algorithm, Chi-squares test, component health, and protection logic are presented. The simulation results have shown that DSEBPS successfully detects the fault conditions and produces a trip signal under various types of faults and conditions performed in this chapter. The obtained results affirm that the scheme does not require any relay settings except the threshold value required for the objective function. The dependability and security of DSEBPS can be further enhanced by performing for several other types of internal and external faults in combination with other possible abnormal conditions such as switching operation transients, line energization, etc.

CHAPTER 6

Transmission Line Protection using Dynamic State Estimation: Experimental Setup and Validation

This chapter presents the work conducted on the implementation and experimental validation of a dynamic state estimation based protection scheme using advanced measurement technologies developed by Smart State Technology at Chalmers power system laboratory. The details of the fault detection time during the experimental validation are also presented. The content presented in this chapter is based on the work presented in Paper A and D.

6.1 Advanced Measurement Technologies

Advanced sensors (AdvSens) have been continuously developed by Smart State Technology [144].

6.1.1 Features

AdvSens provide high-quality (both synchrophasor and sampled) measurements of the grid. They are capable of providing high-speed sampling with a low signal-to-noise ratio. They also have a wide signal measurement range which suits different substation configurations and network cable ratings. The analog to digital converters (ADC) sampling system, which is locked to global positioning system (GPS) time, generates both phase and magnitude information. Each sensor contains an ARM-based single-board computer (SBC) with embedded Linux and is capable to process and communicate real-time data. The system

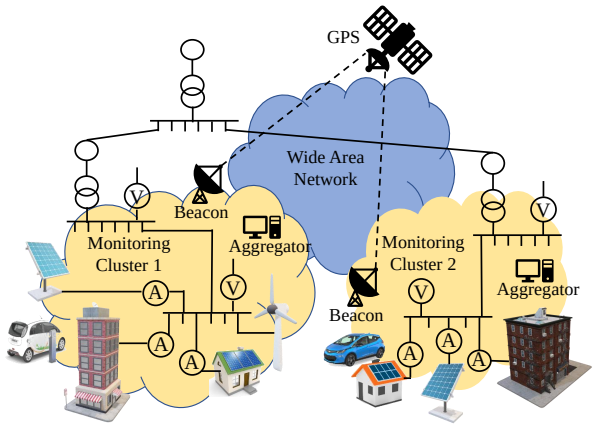

Figure 6.1: An illustrative picture for grid monitoring with AdvSens.

hosts an open development platform for algorithms and application development. A graphical illustration of such a setup is presented in Figure 6.1 which shows that AdvSens can be deployed in multiple parts of the electrical network and provide synchronized measurements within and across network clusters. The real-time measurements from AdvSens could be used to perform all kinds of distributed calculations such as power flow calculation, state estimation, etc.

6.1.2 System Architecture

The system architecture of AdvSens consists of a time beacon transmitter, voltage and current sensors, embedded computer, and data aggregation units (referred to as smart nodes). Figure 6.2 presents the architecture of AdvSens.

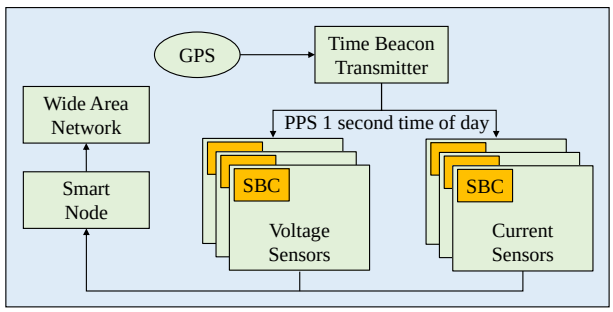

Figure 6.2: The architecture of AdvSens.

6.1.2.1 Time Beacon Transmitter

Its function is to broadcast wired or wireless-time information, based on the GPS received pulse per second (PPS) signal and time of day NMEA messages, to a cluster of AdvSens. AdvSens use this time information to synchronize their sampling system and obtain synchronized measurements of voltage and current signals which are then digitized, processed, and transmitted to smart nodes. It allows a cluster of AdvSens to discipline their ADC with the received 1 second PPS signal and synchronize their measurements. Thus, it acts as a grandmaster clock for the cluster of AdvSens to have global synchronized measurements.

6.1.2.2 Voltage and Current Sensors

There are two types of AdvSens i.e., voltage and current sensors. The voltage sensors can have a measurement range up to 800 V (230 V nominal) and make use of signal transformers, while the current sensors make use of split-core CTs and have a measurement range up to 400 A.

6.1.2.3 Embedded Computer

The embedded SBC in AdvSens is an ARM-based low power and low-cost processing platform. The SBC runs Linux as an operating system and contains drivers for receiving the synchronized ADC samples and hosts the open platform software architecture for the creation and processing of measurements. It is typically done with software digital signal processors (DSPs) that are written in C++ or Python. The open platform (explained in Section 6.8.1) contains mechanisms for semi real-time communication (via ZeroMQ messaging [145]). It can be done locally between various DSPs within AdvSens or globally between DSPs running on distributed AdvSens or smart nodes. Besides the DSP mechanism for measurement processing, AdvSens also have an embedded database (historian) for the long recording of measurements and results. A picture of the printed circuit board of the voltage sensor is presented in Figure 6.3.

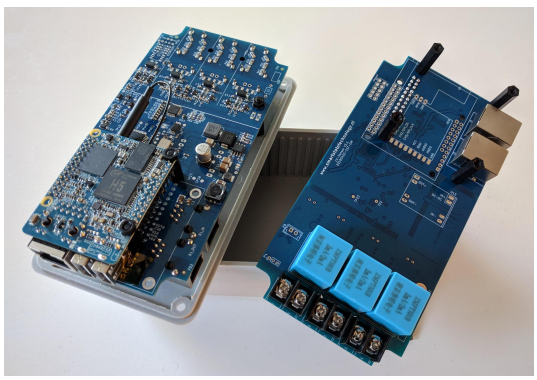

Figure 6.3: A picture of the printed circuit board of the voltage sensor.

6.1.2.4 Smart Nodes

Smart nodes are the data aggregators of the system, which hosts the transmission line dynamic model. They collect the measurement data from AdvSens and can perform calculations. Smart nodes also host the open platform of AdvSens such that real-time data processing and communication could take place and can optionally host a real-time database and dashboards like Grafana.

6.1.3 Calibration and Accuracy

The raw ADC samples may suffer from inaccuracies due to component tolerances and the non-linearity of the signal transducers. Also, the measured ADC counts are required to be converted to signal values. The sensor calibration DSP converts the ADC counts to accurate signal values. For accurate conversion, the calibration DSP uses a table that maps measurement ADC counts to actual signal values. The table stores various calibration points to cover the full measurement range of AdvSens including the measurement regions where AdvSens may exhibit non-linearity (typically in the initial low measurement region and in the saturation region of the transducer CTs). During run-time, the calibration DSP searches the region of the acquired ADC counts in the table and converts it to signal value using linear interpolation. The higher number of points in the non-linear region would ensure that AdvSens follows the measurement characteristic curve, and errors will remain below their specified value. The calibration table is created for each AdvSens by taking measurement ADC-counts (from the sensor) and actual signal measurements from a higher accuracy measurement device and then storing those results in the calibration table.

6.2 Experimental Validation of DSEBPS Using Experimental Setup

This section explains the application of AdvSens, description of the laboratory, details of the experimental setup, implementation of the scheme, data flow process, obtained results and discussion, and comparison with the simulation results.

6.2.1 Application of AdvSens

AdvSens provides the real-time sampled measurements which serve as input to DSEBPS. The accuracy and sampling frequency of the measurements are important requirements for timely and accurate detection of the fault condition. The high-frequency sampled measurements are required to capture any dynamical change in the transmission line. The motivation to choose sampled measurements over phasors is that the phasors are updated at a lower frequency (usually around 50 to 100 frames per second for a 50 Hz system and 60 to 120 frames per second for a 60 Hz system) when compared to sampled measurements. With reduced updating time of phasors, the accuracy to capture any transient event reduces. The sampled measurements are provided at a sampling rate of 4 kHz. By evaluating case studies with different data acquisition rates, the rates ranging between 2 kHz to 5 kHz are found to be feasible in terms of performance. The acquisition rates less than 2 kHz could

negatively impact the capturing of real-time picture of a transmission line due to low refresh rate, while the acquisition rates more than 5 kHz gets limited due to the increased need for computation. The measurement vector includes the voltages and currents from the terminals of the transmission line and is represented as z in (5.7).

6.2.2 Laboratory Description

The Chalmers power system laboratory hosts an experimental setup of an accurate scaled-down model of a simple power system. It consists of a synchronous generator driven by a DC motor, two transformers, six π-sections of a transmission line, and loads. Each π-section in the setup corresponds to 150 km of a 400 kV line. The whole setup operates at a nominal voltage of 400 V with a nominal grid frequency of 50 Hz. The parameters of each π-section in the setup are presented in Table 5.1.

6.2.3 Experimental Setup

A physical setup available at the Chalmers power system laboratory consisting of six π-sections of transmission line, transformers, synchronous generator, and loads, is considered in this work. The setup is an accurate scaled-down model of a power system where each π-section represents 150-km of a 400 kV transmission line. The per-phase parameters for each π-section are as follows: resistance 0.052 Ω, inductance 3.033 mH, and capacitance 46 μF. The synchronous generator has a rated three-phase voltage of 400 V and is driven by an 85 kW DC motor (which functions as a prime mover). The setup is connected to a three-phase 400 V (L-L), 50 Hz distribution grid on the grid end. The setup also contains two three-phase transformers, one on the generator end which has a YD11 connection with Y-connection on the transmission line side and D-connection on the generator side. The other transformer is on the grid end which has a DYn11 connection with D-connection on the grid side and Yn-connection on the transmission line side. The entire setup is solidly grounded through a copper strip for safety purposes. Various types of loads could be connected with the setup at different locations. The laboratory has a provision to create temporary (auto clearing) faults using a timer and push button. Advanced sensors used in the experimental setup measure sending end currents (i_A, i_B, i_C), receiving end currents (i_a, i_b, i_c), and receiving end voltages (v_a, v_b, v_c). The current sensors employ split-core current transformers (CTs) of the measurement class with a current range from normal operating current to maximum fault current, while the voltage measuring AdvSens directly measures the voltages without using the VTs/CCVTs. The voltage sensors directly measure the voltage without employing the voltage transformers. The picture of the experimental setup used in this work is shown in Figure 6.4.

6.2.4 Implementation

The implementation diagram of DSEBPS with the experimental setup is shown in Figure 6.5. AdvSens are installed at the transmission line, which provides the GPS-synchronized real-time sampled measurements and received in a smart node through an Ethernet cable (as a communication channel). The smart node used in this setup is a laptop whose configuration is presented in Table 6.1. The smart node processes the measurements along with the transmission line dynamic model to perform the DSE. The state estimates are obtained

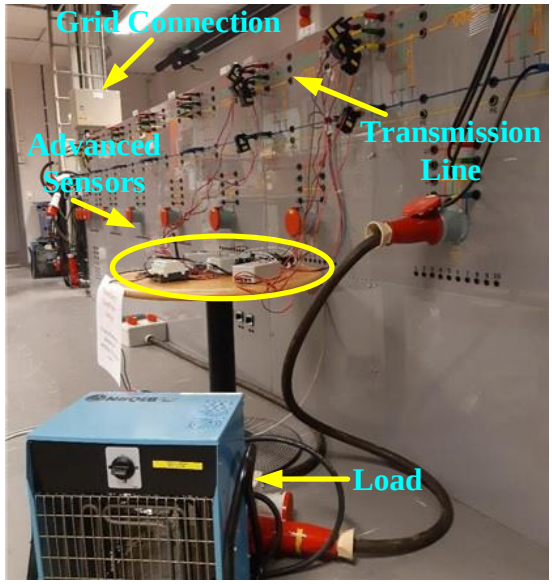

Figure 6.4: Picture of the experimental setup at Chalmers power system laboratory.

through DSE and then the Chi-square test is performed to obtain the goodness of fit between the dynamic model and measurements. The health condition is then derived based on the results of the Chi-square test which provides the confidence level and helps design the protection logic whether to generate a trip signal or not. It is important to mention here that the experimental setup is an open-loop system which means that DSEBPS only detects the fault but does not clear it using the generated trip signal in this experimental setup. Rather, the fault is cleared by the auto-clearing mechanism which is provided in the setup. Due to this fact, the confidence level signal in the results of all the case studies shows high confidence once the fault is cleared.

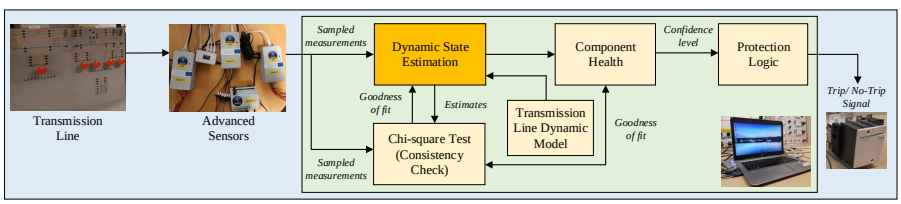

Figure 6.5: Implementation diagram of DSEBPS with experimental setup at Chalmers power system laboratory.

Table 6.1: Configuration Details of the Smart Node

Component	Configuration Details
Memory	15.5 GiB
Processor	IntelR CoreTM i7-6600U CPU @ 2.60 GHz × 4
Graphics	IntelR HD Graphics 520 (Skylake GT2)
Disk	503 GB
Ubuntu Version	Ubuntu 18.04.3 LTS
Python3 packages	Mainly NumPy (1.16.4) and SciPy (0.19.1)

6.2.5 Data Flow Process

The data flow process diagram for the experimental setup is presented in Figure 6.6, which explains the process of data flow from the measurement point until the trip signal. The setup executes two different digital signal processes, the first performs DSE and Chi-square test (abbreviated as D_1) and the second performs the confidence level calculation (D_2). Also, three real-time data plots are shown, the first plots the measurements and their estimated values (R_1), the second plots the objective function (R_2), and the third plots the confidence level (R_3).

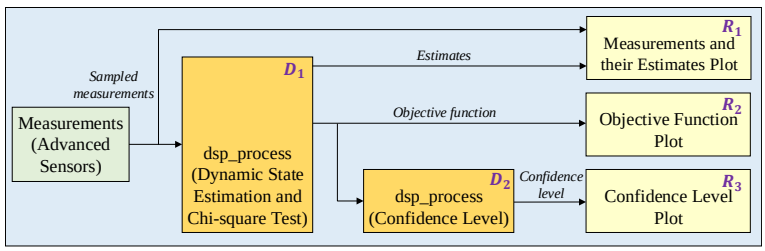

Figure 6.6: Data flow process diagram for the experimental setup at Chalmers power system laboratory.

6.2.6 Trip Signal Logic

The consistency of the objective function is used to obtain the confidence level which in turn is used to generate the trip signal. In order to generate the trip signal, the confidence level signal should be low. The objective function is observed for 40 consecutive samples (or any desired number of samples by the user) to be above a threshold value and then the confidence level signal goes low. The motivation to observe the objective function for 40 consecutive samples is to obtain enhanced reliability of the protection decision. Once the trip signal is generated, it is sent to the circuit breakers which isolate the transmission line from the rest of the network. All the confidence level results in the case studies performed with experimental validation are obtained by considering 40 consecutive samples. A USB latch device is used as an interface between the smart node and the circuit breaker. The trip signal setup is shown in Figure 6.7(b).

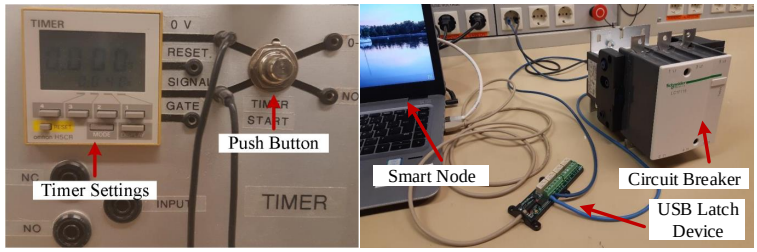

Figure 6.7: (a) A picture showing the timer settings, (b) Trip signal setup using the USB latch device and the circuit breaker.

6.3 Validation Results and Discussion

6.3.1 Balanced Three-phase Fault with Resistive Load

The single-line diagram of the experimental setup is presented in Figure 6.8. The validation results using the setup in terms of measurements and their estimated values are presented in Figure 6.9. The measurements, state estimates, objective function, and confidence level are continuously obtained and their values are updated and plotted in R_1, R_2, and R_3 plots, respectively.

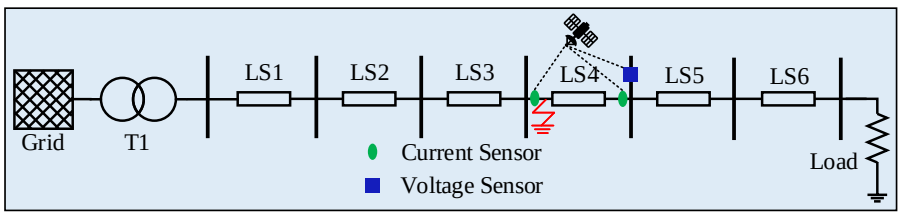

Figure 6.8: Single-line diagram of the experimental setup with the location of AdvSens and fault.

It can be seen from Figure 6.9, that during the normal operating conditions (until 2.795 seconds), the measurements and their estimated values (sending end currents (i_A, i_B, i_C), receiving end currents (i_a, i_b, i_c), and receiving end voltages (v_a, v_b, v_c)) conform with each other. Correspondingly, the objective function is low and the confidence level is high, as shown in Figure 6.10. The obtained results confirm that measurements and estimated values should be in conformity during the healthy operation, thanks to the correct dynamic modelling of the transmission line.

Thereafter, a three-phase short-circuit fault is created for 40 milliseconds at the sending end of the fourth π-section, as shown in Figure 6.8. The fault time settings could be set by using a timer and then a push button is pressed which creates the fault for a set time. This mechanism then auto clears the fault. The timer settings and the push button can be seen in

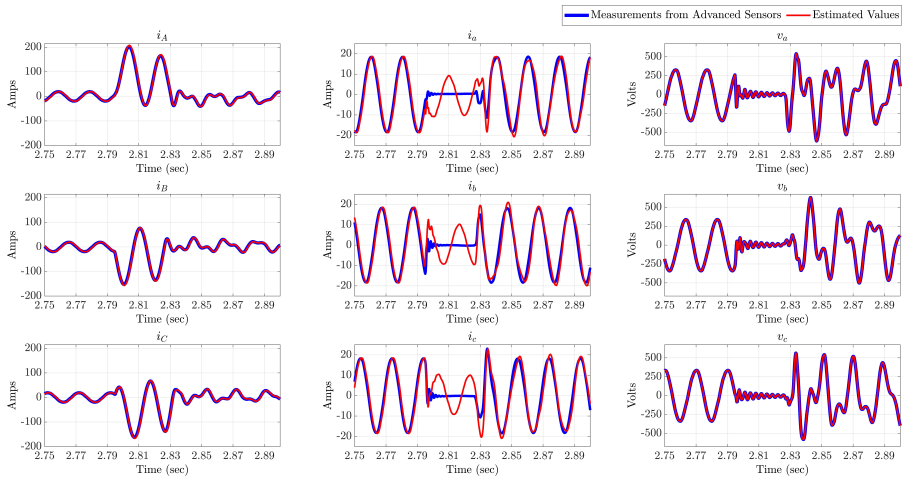

Figure 6.9: Validation results for a three-phase fault with resistive load in terms of measured and estimated values of the sending end currents (i_A, i_B, i_C), receiving end currents (i_a, i_b, i_c), and receiving end voltages (v_a, v_b, v_c).

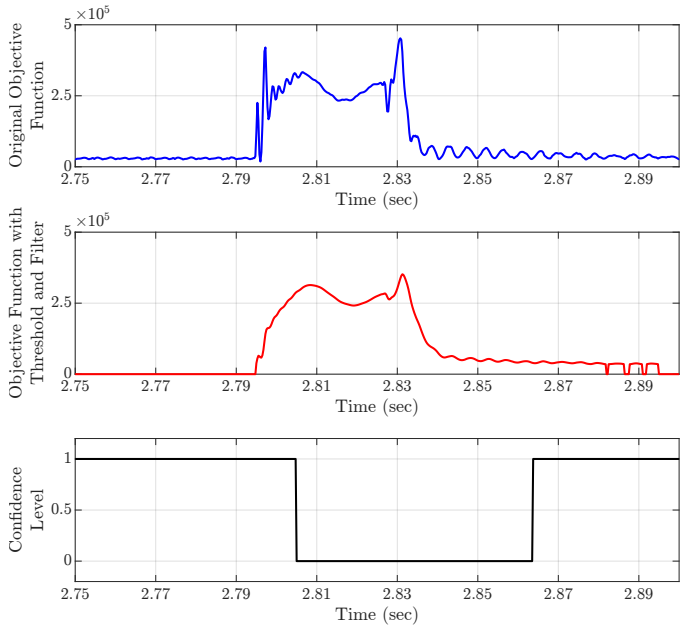

Figure 6.10: Validation results for a three-phase fault with resistive load in terms of objective function and confidence level.

Figure 6.7(a). As can be seen from Figure 6.9, that during the fault condition (approximately between 2.795 and 2.835 seconds), the sending end currents (i_A, i_B, i_C) becomes high, while the receiving end currents (i_a, i_b, i_c) and receiving end voltages (v_a, v_b, v_c) tends towards zero due to the short-circuit fault. The objective function goes higher than the threshold value of 35e3 and the confidence level goes low, during the fault condition (approximately between 2.795 and 2.835 seconds), as can be seen in Figure 6.10. The non-conformity between the measurements and their estimated values leads to a high value of the objective function.

6.3.2 Unbalanced Faults

This subsection presents the results of the unbalanced faults using the experimental setup which is explained in Section 6.2. The schematic of the experimental setup in case of an unbalanced fault is presented in Figure 6.11. In this section, the results for two unbalanced faults i.e., single-line-to-ground and double-line-to-ground faults, are presented.

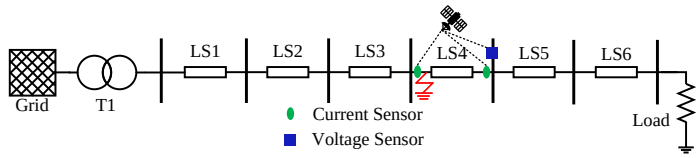

Figure 6.11: Schematic of the experimental setup for an unbalanced fault.

6.3.2.1 Single-line-to-ground Fault

A single-line-to-ground fault is the most common and frequently occurring fault type in transmission systems. The validation results in terms of measured and estimated values of sending end currents (i_A, i_B, i_C), receiving end currents (i_a, i_b, i_c), and receiving end voltages (v_a, v_b, v_c) are presented in Figure 6.12. The objective function and confidence level results are presented in Figure 6.13. The measurements, estimated values, objective function, and confidence level are obtained continuously and plotted in Figure 6.12 and Figure 6.13. As can be seen from Figure 6.12, during the normal operating conditions (until 4.95 seconds) the measured and estimated values are in concurrence with each other. The concurrency between the measured and their estimated values signify the correct modelling of the transmission line. Consequently, the objective function has lower values, and the confidence level remains high.

Thereafter, a single-line-to-ground fault is created in phase A (at sending end of the fourth π-section) for 40 milliseconds at around 4.95 seconds. It can be seen from Figure 6.12 that during the fault the sending end current in phase A (i_A) increases significantly and reaches a peak value up to 130 Amperes (as it is the faulted phase), while the sending end currents in other phases (i_B and i_C) see some distortions during the fault as they are healthy phases. The receiving end current in phase A (i_a) reduces during the fault as the short circuit fault occurs before the receiving end and part of the current is fed to the fault, while the receiving end currents in other phases (i_b and i_c) see a very small dip in currents as they are healthy

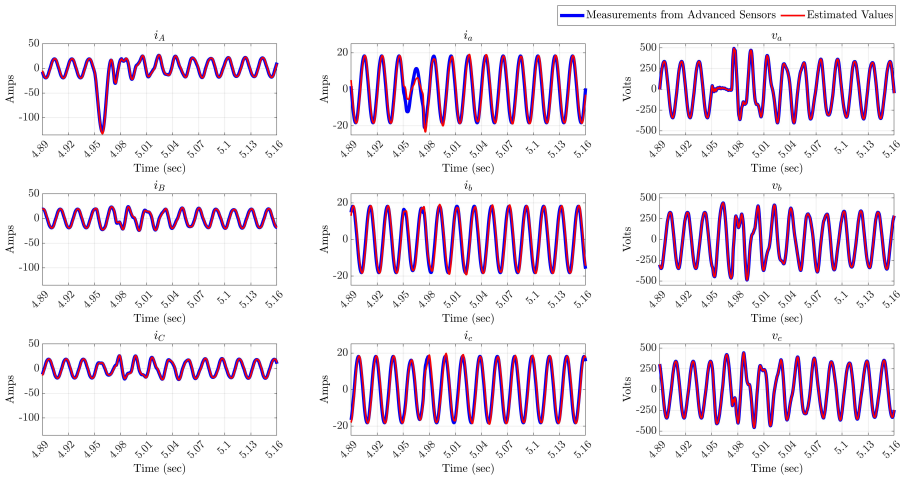

Figure 6.12: Validation results for a single line-to-ground fault in terms of measured and estimated values of the sending end currents (i_A, i_B, i_C), receiving end currents (i_a, i_b, i_c), and receiving end voltages (v_a, v_b, v_c).

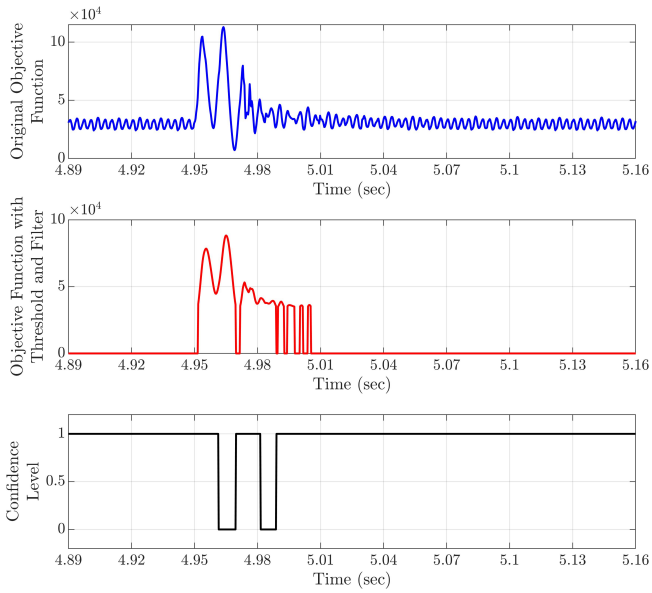

Figure 6.13: Validation results for a single line-to-ground fault in terms of objective function and confidence level.

phases. Conversely, the receiving end voltage in phase A (v_a) reduces to zero during the fault because the fault occurs with a zero impedance path, and hence the voltage becomes close to zero at the fault point, while the receiving end voltages in unfaulted phases (v_b and v_c) see an increase because the grid-end transformer in the lab setup has DYn11 winding connection with the neutral of the secondary side solidly grounded which gives a ground path to the zero-sequence current to flow and hence the voltages in unfaulted phases are affected. Further, it can be seen from Figure 6.13 that as soon as the single-line-to-ground fault occurs at around 4.95 seconds the objective function goes higher than the threshold value of 35e3, and subsequently, the confidence level goes low (i.e., 0) after 40 samples (10 milliseconds) at around 4.96 seconds. The low confidence level generates a trip signal to isolate the fault. The results obtained from the case study suggest that DSEBPS works as intended during a single-line-to-ground fault.

6.3.2.2 Double-line-to-ground fault

A double-line-to-ground fault involves any of the two phases and ground during the fault conditions. The validation results in terms of measured and estimated values of sending end currents (i_A, i_B, i_C), receiving end currents (i_a, i_b, i_c), and receiving end voltages (v_a, v_b, v_c) are presented in Figure 6.14. The objective function and confidence level results are presented in Figure 6.15. The measurements, estimated values, objective function, and confidence level are obtained continuously and plotted in Figure 6.14 and Figure 6.15. As can be seen from Figure 6.14, during the normal operating conditions (until 2.76 seconds) the measured and estimated values are in concurrence with each other. The concurrency between the measured and their estimated values proves the correct modelling of the transmission line.

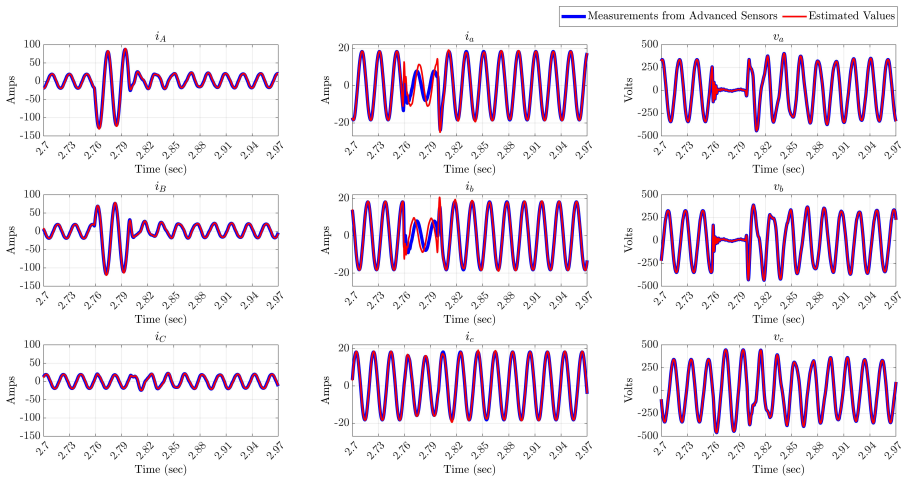

Figure 6.14: Validation results for a double line-to-ground fault in terms of measured and estimated values of the sending end currents (i_A, i_B, i_C), receiving end currents (i_a, i_b, i_c), and receiving end voltages (v_a, v_b, v_c).

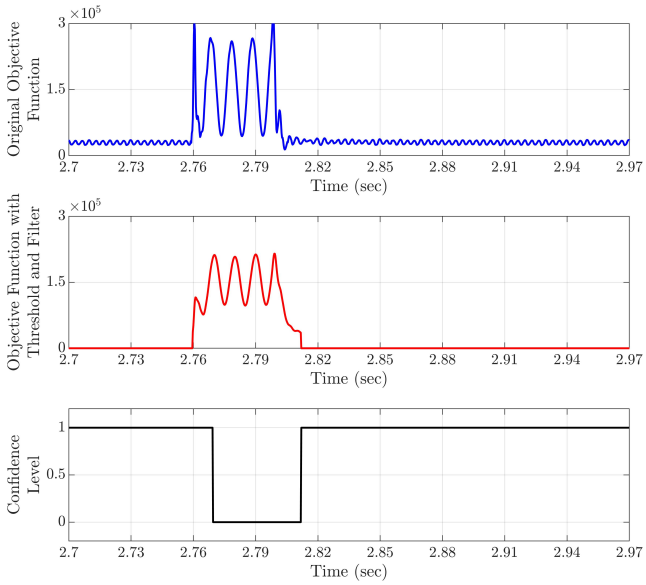

Figure 6.15: Validation results for a double line-to-ground fault in terms of objective function and confidence level.

Consequently, the objective function has lower values and the confidence level is high until 2.76 seconds.

Thereafter, a double-line-to-ground fault is created in phases A and B (at sending end of the fourth π-section) for 40 milliseconds at around 2.76 seconds. It can be seen from Figure 6.14 that during the fault the sending end currents in phases A and B (i_A and i_B) increase significantly and reaches a peak value up to 130 Amperes (as they are the faulted phases), while the sending end current in phase C (i_C) see some distortions during the fault as it is the healthy phase. The receiving end currents in phases A and B (i_a and i_b) reduce during the fault as the short circuit fault occurs before the receiving end and part of the current is fed to the fault, while the receiving end current in phase C (i_c) see a very small reduction in current as it is the healthy phase. Conversely, the receiving end voltages in phases A and B (v_a and v_b) reduce to zero during the fault because the fault occurs with a zero impedance path, and hence the voltage reaches close to zero at the fault point, while the receiving end voltage in unfaulted phase (v_c) see an increase because the grid-end transformer in the lab setup has DYn11 winding connection with the neutral of the secondary side solidly grounded which gives a ground path to the zero-sequence current to flow and hence the voltage in unfaulted phase is affected. Further, it can be seen from Figure 6.15 that as soon as the double-line-to-ground fault occurs at around 2.76 seconds the objective function goes higher than the threshold value of 35e3, and subsequently, the confidence level goes low after 40 samples at around 2.77 seconds. The low confidence level generates a trip signal to clear the fault. The results suggest that DSEBPS successfully detects the double-line-to-ground fault.

6.3.3 Unbalanced Fault with Inductive Conditions

Power systems mostly operate with the inductive power factor load conditions. The inductive load conditions not just make the system response to disturbances more sluggish due to increased time constant but also increases the phase difference between the voltage and current (compared to resistive load). Due to this different protection settings are required in some phasor-based protection methods such as distance and directional overcurrent, as the decision is based on both magnitude and angle of the phasor. In this regard, this case study is performed to validate the performance of DSEBPS under inductive load conditions. The picture showing the experimental setup for the inductive load conditions is presented in Figure 6.16. DSEBPS is validated with an inductive load of 0.78 power factor (2.2 kW and 1.7 kVAr) using the same experimental setup. The validation results in terms of measured and estimated values of sending end currents (i_A, i_B, i_C), receiving end currents (i_a, i_b, i_c), and receiving end voltages (v_a, v_b, v_c), are presented in Figure 6.17. The objective function and confidence level results are presented in Figure 6.18. The measurements, estimated values, objective function, and confidence level are obtained continuously and plotted in Figure 6.17 and Figure 6.18. As can be seen from Figure 6.17, during the normal operating conditions (until 2.47 seconds) the measured and estimated values are in concurrence with each other. The concurrency between the measured and their estimated values signify the correct modelling of the transmission line. Consequently, the objective function has lower values, and the confidence level is high until 2.47 seconds.

Thereafter, a single-line-to-ground fault is created in phase A (at sending end of the fourth π-section) for 40 milliseconds at around 2.47 seconds. It can be seen from Figure 6.17 that during the fault the sending end current in phase A (i_A) increases significantly and reaches

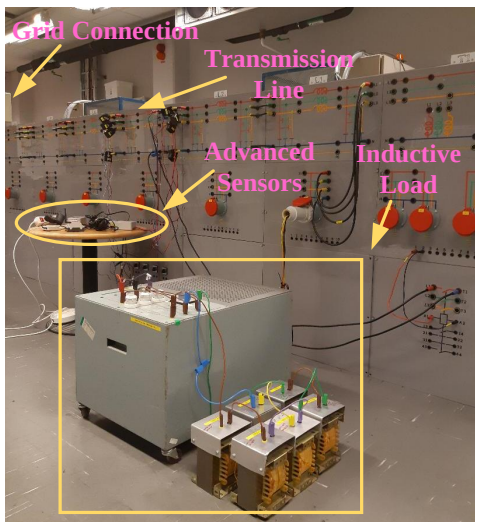

Figure 6.16: A picture showing the experimental setup of DSEBPS with R-L load.

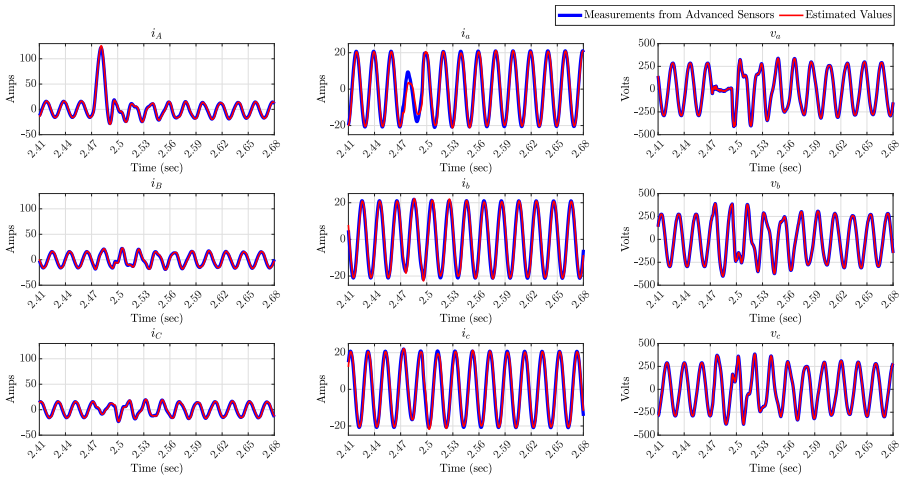

Figure 6.17: Validation results for a single line-to-ground fault with R-L load in terms of measured and estimated values of the sending end currents (i_A, i_B, i_C), receiving end currents (i_a, i_b, i_c), and receiving end voltages (v_a, v_b, v_c).

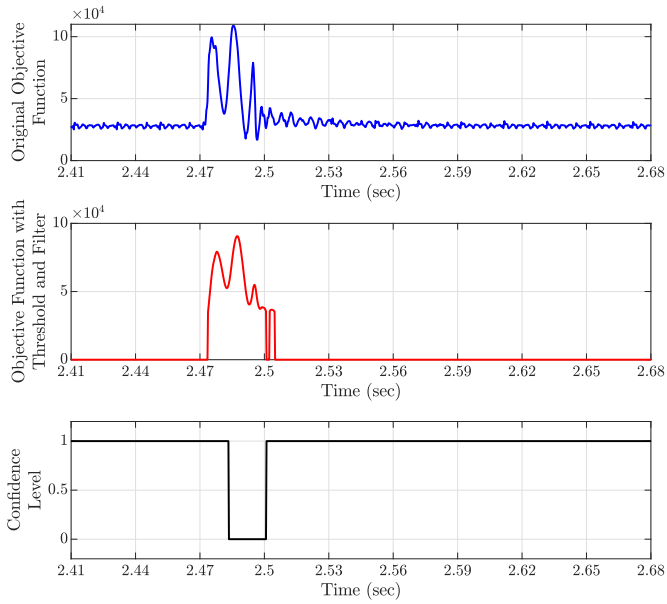

Figure 6.18: Objective function and confidence level results in case of a single line-to-ground fault with R-L load.

a peak value of 130 Amperes (as it is the faulted phase), while the sending end currents in other phases (i_B and i_C) see some distortions during the fault as they are healthy phases. The receiving end current in phase A (i_a) reduces during the fault as the short circuit fault occurs before the receiving end and part of the current is fed to the fault, while the receiving end currents in other phases (i_b and i_c) see a very small dip in currents as they are healthy phases. Conversely, the receiving end voltage in phase A (v_a) reduces to zero during the fault because the fault occurs with a zero impedance path and hence the voltage becomes close to zero at the fault point, while the receiving end voltages in unfaulted phases (v_b and v_c) see an increase because the grid-end transformer in the lab setup has DYn11 winding connection with the neutral of the secondary side solidly grounded which gives a ground path to the zero-sequence current to flow and hence the voltages in unfaulted phases are affected. Further, it can be seen from Figure 6.18 that immediately after the occurrence of a single-line-to-ground fault at around 2.47 seconds, the objective function goes higher than the threshold value of 35e3, and subsequently, the confidence level goes low (i.e., 0) after 40 samples at around 2.48 seconds. The low confidence level leads to the generation of a trip signal and hence the fault is successfully detected. It is important to highlight here that the transient response of the system to the fault with inductive load is a little sluggish when compared to the system with purely resistive load. However, the results affirmed that the difference in system response does not have any impact on the performance of DSEBPS. The fault is well detected and cleared within the standard fault clearing time and does not require any changes in this case. The results from the case study confirm the intended performance of DSEBPS with the inductive load as well.

6.3.4 High Impedance Fault

A high impedance fault can be classified as a fault that includes high impedance in the fault path. The high impedance fault path distinguishes it from the low impedance fault path as the fault current is reduced significantly, sometimes close to or less than the normal operating conditions. The reduced fault current makes it difficult to detect and clear the fault. The picture showing the experimental setup for a high impedance fault is presented in Figure 6.19. DSEBPS is validated for a high impedance (single-line-to-ground) fault using the same experimental setup. The validation results in terms of measured and estimated values of sending end currents (i_A, i_B, i_C), receiving end currents (i_a, i_b, i_c), and receiving end voltages (v_a, v_b, v_c) are presented in Figure 6.20. The objective function and confidence level results are presented in Figure 6.21. The measurements, estimated values, objective function, and confidence level are obtained continuously and plotted in Figure 6.20 and Figure 6.21. As can be seen from Figure 6.20, during the normal operating conditions (until 2.90 seconds) the measured and estimated values are in concurrence with each other. The concurrency between the measured and their estimated values indicates the correct modelling of the transmission line. Consequently, the objective function has lower values and the confidence level is high.

Thereafter, a single-line-to-ground fault with a fault impedance of 9 Ω is created in phase A (at sending end of the fourth π-section) for 40 milliseconds at around 2.90 seconds. It can be seen from Figure 6.20 that during the fault the sending end current in phase A (i_A) does not increase significantly (compared to a single-phase-to-ground fault with a low impedance fault path) as the fault path has increased impedance and reduced current is

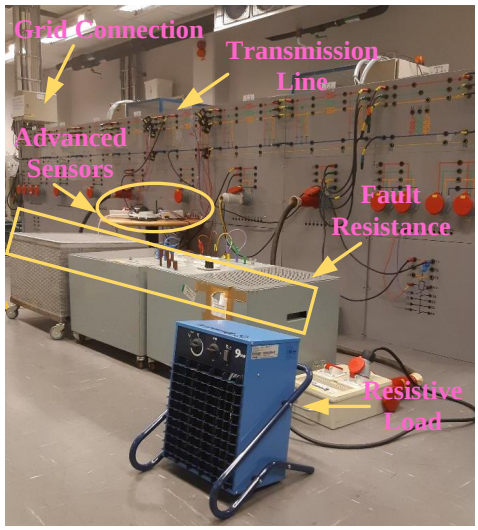

Figure 6.19: A picture showing the experimental setup of DSEBPS for a high impedance fault.

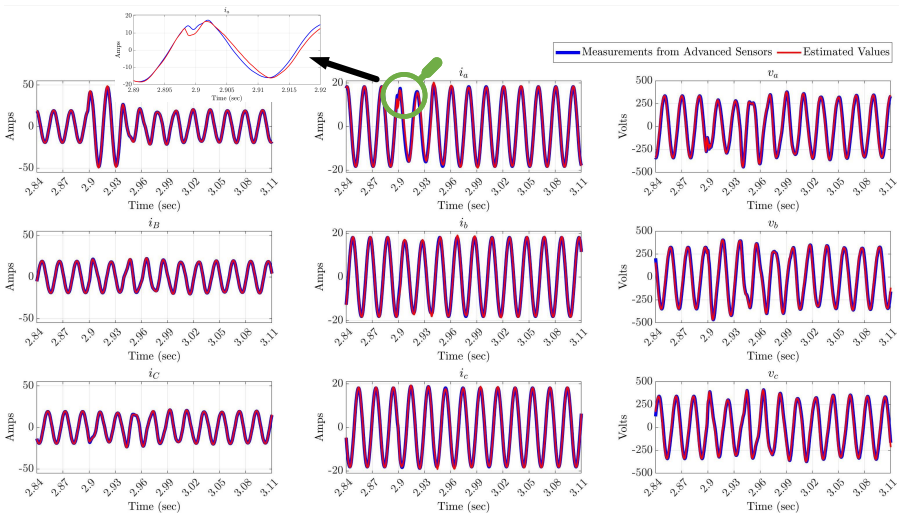

Figure 6.20: Validation results for a single line-to-ground fault with high impedance in terms of measured and estimated values of the sending end currents (i_A, i_B, i_C), receiving end currents (i_a, i_b, i_c), and receiving end voltages (v_a, v_b, v_c).

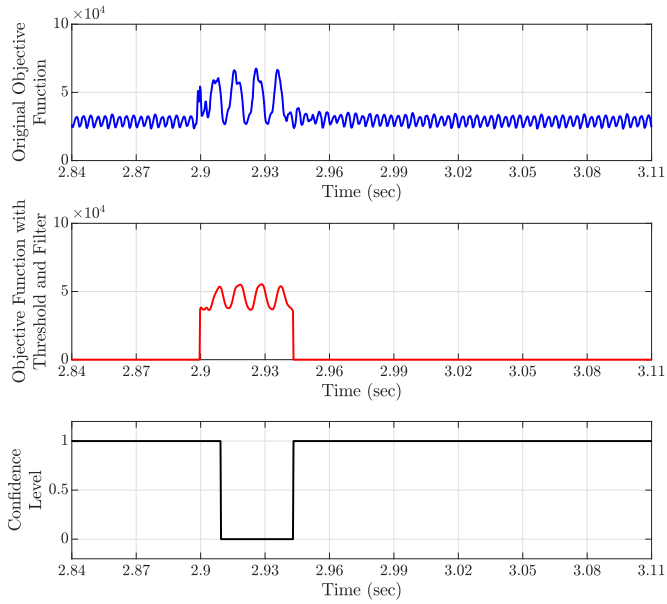

Figure 6.21: Objective function and confidence level results in the case of a single line-to-ground fault with high impedance.

fed to the fault and reaches a peak value of 50 Amperes (compared to 130 Amperes in a single-phase-to-ground fault with zero fault impedance), while the sending end currents in other phases (i_B and i_C) see some distortions during the fault as they are healthy phases. The receiving end current in phase A (i_a) sees a slight reduction during the fault as the fault current has reduced compared to a case with zero impedance fault, while the receiving end currents in other phases (i_b and i_c) remain close to normal operating value due to lesser fault effects on the faulted phase. Conversely, the receiving end voltage in phase A (v_a) does not reduce to zero during the fault (compared to a single-phase-to-ground fault with zero fault impedance), while the receiving end voltages in other phases (v_b and v_c) see a slight spike. Further, it can be seen from Figure 6.21 that as soon as the single-line-to-ground fault occurs at around 2.90 seconds the objective function (with threshold and filter) goes higher than the threshold value of 35e3, and subsequently, the confidence level goes low (i.e., 0) after 40 samples at around 2.91 seconds. However, it can be observed that the spike in the objective function is lower than the objective function obtained with a single-line-to-ground fault with zero fault impedance. But since the confidence level signal is based on the consistency of the objective function, thus when the objective function remains above (crosses) the threshold value for 40 samples, the confidence level goes low (i.e., 0). The low confidence level generates a trip signal and hence the fault is successfully detected. It is important to highlight here that DSEBPS performs as intended during a high impedance fault and hence affirms it is one of the significant features.

6.3.5 Fault Current Fed from Both Ends

Transmission systems are generally connected as meshed networks where the fault is fed from both ends of the transmission line. The schematic of the system with a fault current fed from both ends is presented in Figure 6.22, while the corresponding experimental setup is presented in Figure 6.23.

The validation results in terms of measured and estimated values of sending end currents (i_A, i_B, i_C), receiving end currents (i_a, i_b, i_c), and receiving end voltages (v_a, v_b, v_c) are presented in Figure 6.24. The objective function and confidence level results are presented in Figure 6.25. The measurements, estimated values, objective function, and confidence level are obtained continuously and plotted in Figure 6.24 and Figure 6.25. All the plots in Figure 6.24 show that during the normal operating conditions (until 1.03 seconds) the measured and estimated values are in concurrence with each other signifies the correct modelling of the transmission line. Consequently, the objective function has lower values, and the confidence level is high until 1.03 seconds in Figure 6.25.

Thereafter, a three-phase fault is created (at sending end of the fourth π-section) for 40 milliseconds at around 1.03 seconds. It can be seen from Figure 6.24 that during the fault the sending end currents (i_A, i_B, i_C) increase significantly and reach a peak value up

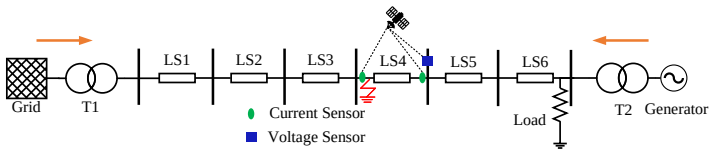

Figure 6.22: Schematic of the experimental setup for a fault current fed from both ends.

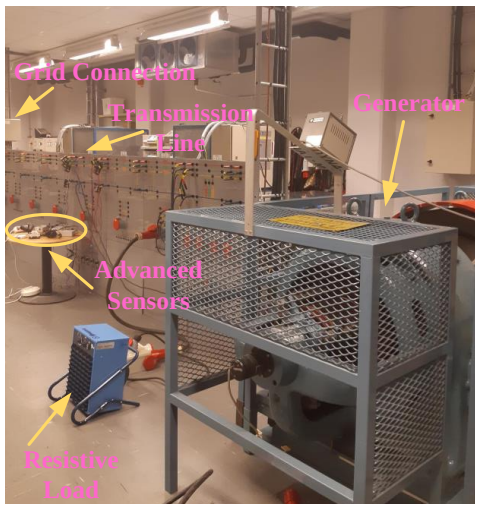

Figure 6.23: A picture showing the experimental setup of DSEBPS for a fault fed from both ends.

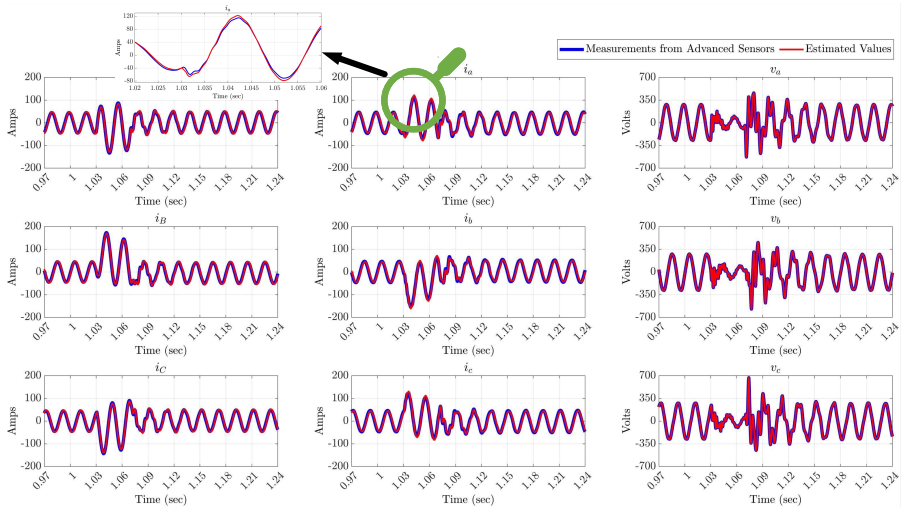

Figure 6.24: Validation results for a three-phase fault current fed from both ends in terms of measured and estimated values of the sending end currents (i_A, i_B, i_C), receiving end currents (i_a, i_b, i_c), and receiving end voltages (v_a, v_b, v_c).

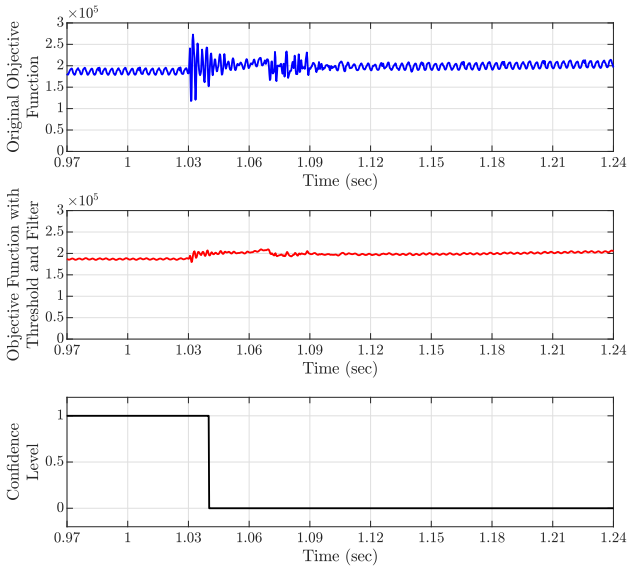

Figure 6.25: Objective function and confidence level results in case of a three-phase fault fed from both ends.

to 180 Amperes as the fault path has zero impedance which leads to high fault current. The receiving end currents (i_a, i_b, i_c) also increase during the fault (unlike the fault current fed from one end) as the fault current is fed from both ends and thus the generator also contributes to the fault current leading to the high current on the receiving end. In the case of the receiving end voltages, (v_a, v_b, v_c) a reduction can be seen during the fault but they are not reduced to zero unlike the fault current fed from one end as the corresponding receiving end current is not zero as fault current is fed from both ends. Further, it can be seen from Figure 6.25 that as soon as the three-phase fault occurs at around 1.03 seconds, the objective function goes higher than the threshold value, and subsequently, the confidence level goes low (i.e., 0) after 40 samples at around 1.04 seconds. The low confidence level generates a trip signal and hence the fault is successfully detected. However, a different value of the threshold value i.e., 189e3 is used in this case study as the network configuration is changed due to the addition of a generator. This case study demonstrated the expected performance of DSEBPS during the condition where the fault current is fed from both ends.

6.3.6 Hidden Failure or Instrumentation Error

Hidden failure can be described as one which could be caused due to failure of instrument transformers, human errors such as wrong connections, incorrect settings, etc. [146]. In this case study, DSEBPS is validated with the same experimental setup for a case of a hidden failure where a CT connected to sending end side of phase B is considered as failed. The validation results in terms of measured and estimated values of sending end currents (i_A, i_B, i_C), receiving end currents (i_a, i_b, i_c), and receiving end voltages (v_a, v_b, v_c) are presented in Figure 6.26. The objective function and confidence level results are presented

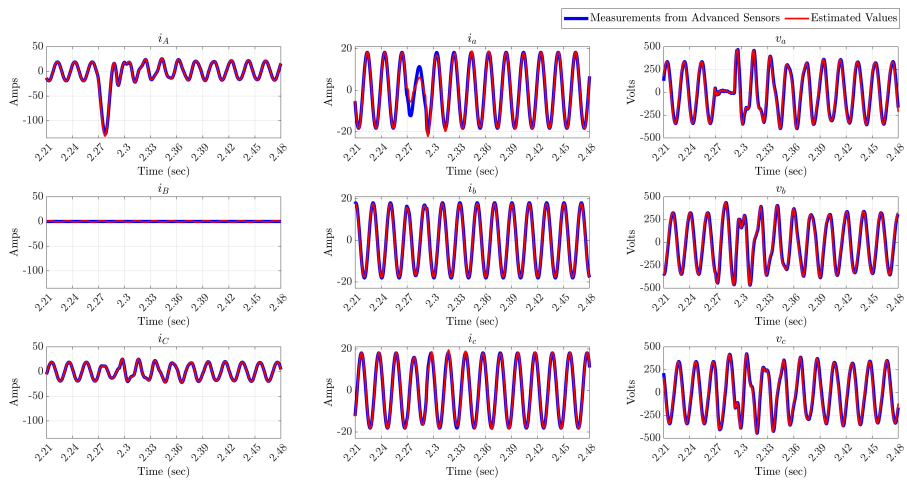

Figure 6.26: Validation results for a hidden failure in terms of measured and estimated values of the sending end currents (i_A, i_B, i_C), receiving end currents (i_a, i_b, i_c), and receiving end voltages (v_a, v_b, v_c).

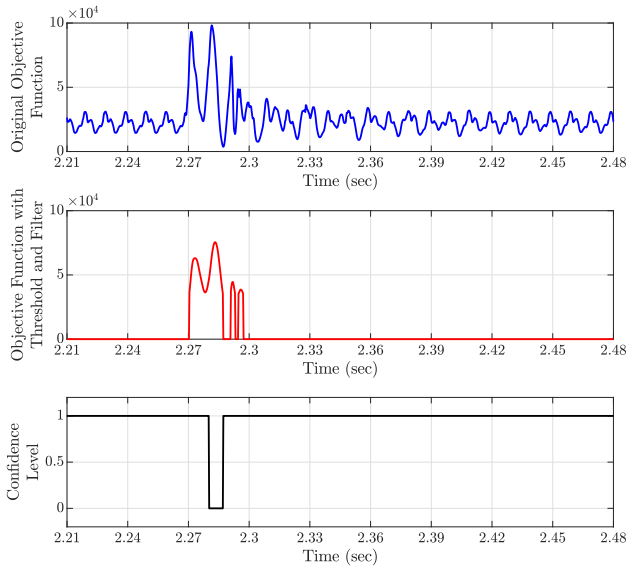

Figure 6.27: Validation results for a hidden failure in terms of objective function and confidence level.

in Figure 6.27. The measurements, estimated values, objective function, and confidence level are obtained continuously and plotted in Figure 6.26 and Figure 6.27.

As can be seen from Figure 6.26, due to consideration of CT failure connected to sending end of phase B, the measurements are not received, and consequently, the estimated values are also not obtained. However, the corresponding plot shows the noise values associated with that measurement. The other plots in Figure 6.26 show that during the normal operating conditions (until 2.27 seconds) the measured and estimated values are in concurrence with each other. However, the concurrency between the other measurements and their estimated values indicates the correct modelling of the transmission line. Consequently, the objective function has lower values, and the confidence level is high until 2.27 seconds.

Thereafter, a single-phase-to-ground fault is created (at sending end of the fourth π-section) for 40 milliseconds at around 2.27 seconds. It can be seen from Figure 6.27 that during the fault the sending end current in phase A (i_A) reaches a peak value of 130 Amperes (as it is the faulted phase), sending end current in phase C (i_C) slightly decreases, while sending end current in phase B (i_B) does not change. The receiving end currents in all the phases (i_a, i_b, i_c) see a slight reduction during the fault as the short circuit fault occurs before the receiving end and part of the current is fed to the fault. Also, the receiving end voltage in phase A (v_a) reduces to zero during the fault because the fault occurs with a zero impedance path, and hence the voltage becomes close to zero at the fault point, while the receiving end voltages in unfaulted phases (v_b and v_c) see an increase because the grid-end transformer in the lab setup has DYn11 winding connection with the neutral of the secondary side solidly grounded which gives a ground path to the zero-sequence current to flow and hence the

voltages in unfaulted phases are affected. Further, it can be seen from Figure 6.27 that as soon as the single-phase-to-ground fault occurs at around 2.27 seconds, the objective function goes higher than the threshold value of 35e3, and subsequently, the confidence level goes low (i.e., 0) after 40 samples at around 2.28 seconds. The low confidence level generates a trip signal and hence the fault is successfully detected and cleared. It is important to highlight here that despite the hidden failure (in CT of sending end side of phase B), the fault is detected and cleared within the standard fault clearing time. The results from the case study suggest that DSEBPS performed as expected in case of a hidden failure and thereby confirming its robustness.

6.3.7 External Fault

An external fault is one that does not occur inside the designated protection zone implying that it should not be detected as an internal fault and hence trip signal should not be generated. In this case study, DSEBPS is validated for a case of an external fault (at receiving end of the third π-section). The validation results in terms of measured and estimated values of sending end currents (i_A, i_B, i_C), receiving end currents (i_a, i_b, i_c), and receiving end voltages (v_a, v_b, v_c) are presented in Figure 6.28. The objective function and confidence level results are presented in Figure 6.29. The measurements, estimated values, objective function, and confidence level are obtained continuously and plotted in Figure 6.28 and Figure 6.29. As the external fault occurs at approximately 1.56 seconds, the transients in the currents and voltages can be seen in Figure 6.28. The origination of transients could be due to the radial structure of the transmission line set up which means the fault current is fed from one end only and hence whenever the fault occurs in any π-section its impact could

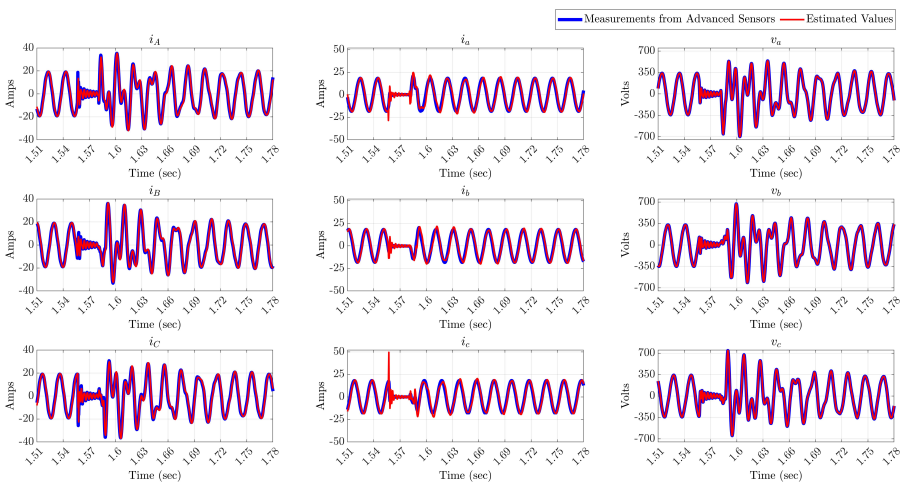

Figure 6.28: Validation results for an external fault in terms of measured and estimated values of the sending end currents (i_A, i_B, i_C), receiving end currents (i_a, i_b, i_c), and receiving end voltages (v_a, v_b, v_c).

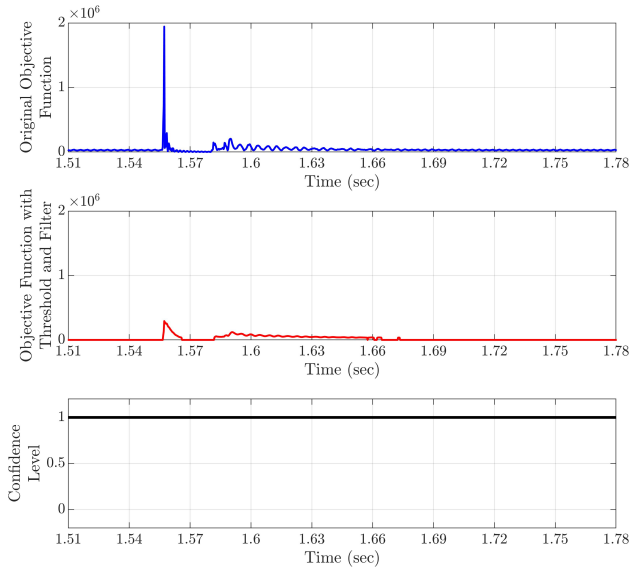

Figure 6.29: Validation results for an external fault in terms of objective function and confidence level.

be seen in the other π-sections. Also, the capacitive line charging currents could lead to the origination of transients. Despite the transients, the estimated values are in concurrency with the measured values. However, there is a sharp spike in the objective function when the fault starts but soon after (within 5 milliseconds) the objective function comes below the threshold value. Since the spike in the objective function is very impulsive and does not meet the criteria for lowering the confidence level i.e., remains above the threshold value for more than 40 samples, thus the confidence level remains high during this condition and hence the trip signal is not generated (which is desired). The results from this case study imply that DSEBPS clearly discriminates against the external fault and thus does not generate a trip signal.

6.3.8 Load Change Conditions

Load change is a frequent operation in power systems that might require changes in the protection settings (for example when load current contributes significantly to the fault current like in large induction motors) and failing to do so could lead to maloperation. In this case study, DSEBPS is validated for a case where a load change (in the form of load increment) occurs. The type of load employed in this case study is purely resistive. The initial load in the studied system is 0 kW, while it is increased up to 18 kW in four steps, each of 4.5 kW. The objective function corresponding to these load changes is obtained continuously and plotted in Figure 6.30. It can be seen from Figure 6.30 that as the first load change occurs (i.e., from 0 to 4.5 kW) at around 0.25 seconds, the objective function

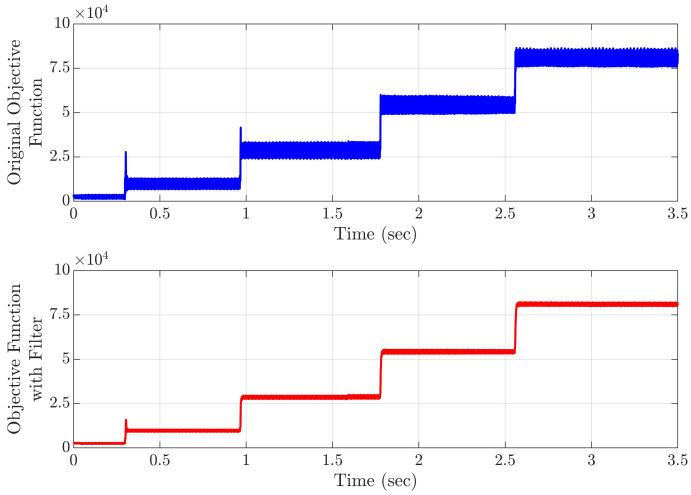

Figure 6.30: Validation results for a load change in terms of the objective function and confidence level.

increases and settles at a new higher value (approximately 1e4). Again, as the load increases further (i.e., from 4.5 to 9 kW) at around 1 second, the objective function further increases and settles at a new higher value (approximately 3e4). Similar changes could be seen for the further increments i.e., from 9 to 13.5 kW and 13.5 to 18 kW. The result from the case study suggests that the change in the loading conditions has an impact on the objective function and subsequently the threshold value is required to be changed for achieving the correct operation.

6.3.9 Lessons Learned from Experimental Validation of DSEBPS

This subsection presents the lessons learned from results obtained with the experimental validation of DSEBPS.

- In the case of a high impedance fault, the overshoot in the objective function during the fault conditions is lower compared to the fault with a low or zero fault impedance path. It is due to the fact that during a high impedance fault, the fault currents do not shoot to a high value, unlike the fault with a zero fault impedance path, which results in a reduced mismatch between the measured and estimated values and hence reduced overshoot in the objective function. This observation provides motivation to explore further the limit of the fault impedance path until which the high impedance faults could be detected. The physical limitations of the experimental setup are a barrier to determining this limit.

- Under the load change conditions, the steady-state values of the objective function vary with the variations in load. From the case study presented in this chapter, the general observation is that the increase in loading leads to an increase in the steady-state value of the objective function. This observation signifies the direct connection of the objective function with the loading conditions and suggests the objective function threshold value could be adaptive to the load changes. The application of machine learning techniques could be one of the potential solutions to determine the threshold value in real-time.

- In a case study with fault current fed from both ends, the objective function has higher values compared to the fault fed from one end, while the overshoot in the objective function values during the fault conditions is smaller compared to the fault fed from one end and also shows an oscillatory nature. Due to the smaller overshoot in the objective function, reduced leverage is available for distinguishing the normal and fault conditions. The threshold value for the objective function is required to be changed based on the values obtained during normal operating conditions. These changes mainly occur due to the change in the network configuration by the addition of a synchronous generator.

6.4 Analysis of State Estimation Algorithm

The following aspects related to the SE algorithm are discussed:

- *Robustness*: The WLS SE is robust in its performance and thus it is widely employed. WLS works well with missing measurements similar to other SE techniques assuming that the network observability is maintained. However, bad data detection in WLS SE becomes tedious in the case of multiple bad measurements. In the experimental validation presented in this work, the ratio of a number of measurements (9) to a number of state variables (6) is kept higher i.e., 1.5. The high ratio helps in maintaining the high redundancy and network observability intact in case of any loss of measurement.

- *Accuracy*: The WLS SE technique has shown good accuracy, as can be seen from Figure 5.5 and Figure 6.9. During normal operating conditions, the measurements match well with their estimated values and hence could be seen overlapping each other. One of the important factors for SE accuracy is the quality of measurements. In the experimental validation, the measurements are provided with high accuracy from AdvSens due to proper calibration and data conversion strategy. The accuracy of the estimator could be further enhanced with an increased sampling frequency of measurements such as 16 kHz or 32 kHz (currently at 4 kHz).

- *Speed*: A linear version of the WLS SE technique is employed which computes estimates much faster than the non-linear version. In the experimental validation, the average processing time of a sample block has come out to be 12.5 milliseconds. According to current standards related to fault detection and also considering the computational capability of the experimental setup, the estimation speed is in a reasonable range.

6.5 Comparison between Validation and Simulation Results

This subsection presents a comparison between the validation and simulation results obtained for a three-phase fault. The motivation for using the same test case in the simulation and validation studies is to perform a comparison between the two results. Overall, the simulation and validation results have matched very well including the peak values and waveforms during both normal and fault conditions. The following observations could be made using Figure 5.5 and Figure 6.9:

- *Voltage and Current Waveforms*: The measurements, as well as their estimated values from the simulation, have matched well with the validation results during the whole simulation time except for the post-fault condition. It can be seen from Figure 6.31 (for v_a) that the measurements from AdvSens and their estimated values remain in a transient state for the next few cycles after the clearing of the fault unlike the simulation, which could be due to the transient over-voltage in the L-C circuit of the transmission line.
- *Objective Function*: From Figure 5.6 and Figure 6.10, a higher peak for the objective function can be seen during the fault in the simulation results which is due to a larger mismatch between the measurements and the estimated values of receiving end currents and voltages.

It can be inferred from the comparison between the validation and simulation results that the results obtained from the simulation are accurate and closely match the real results

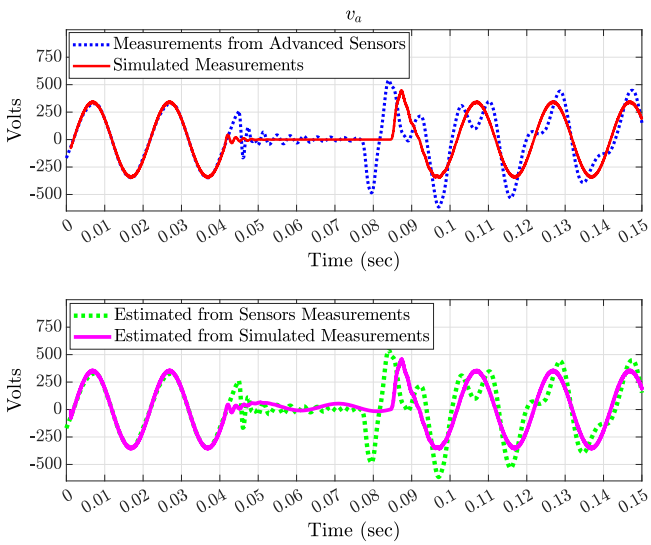

Figure 6.31: Comparison plot for measurements and estimated values of receiving end voltage v_a in case of simulation and experimental validation.

obtained from the validation, while the validation results prove that the scheme works as intended in this experimental setup, with the use of AdvSens in case of a particular type of fault. However, more tests would be needed including different types of faults and fault duration.

6.6 Fault Detection Time during Experimental Validation

The fault detection time is an important criterion to evaluate the performance of a protection scheme. For good performance, the scheme should be able to detect the fault within the standard fault detection time. Distance protection, one of the most widely employed protection schemes in transmission systems, takes around 1 to 2 cycles (20 to 40 milliseconds in a 50 Hz system) for fault detection depending on how close to the relay the fault has occurred. Therefore, a performance analysis is done with regard to the fault detection time of DSEBPS.

From the implementation diagram of DSEBPS as presented in Figure 6.5, the main components of the fault detection time include sample collection time, communication time for a sample block to reach smart node (c_1), model calculation time, communication time from model calculation step to confidence level step (c_2), confidence level calculation time, communication time from confidence level step to trip signal step (c_3), and trip signal generation time. To avoid missing any signal events, sample block streaming and processing calculations are done continuously. Further, processing time and communication delays must be less than the time required to capture a sample block in order to ensure processing in real-time. A block size of 40 samples is chosen in this work so that it is large enough to contain the fault frequency information and minimize the noise effects. Although the samples are sent in blocks, they are processed on a per-sample basis and keep the same timestamp. Therefore, any processing delay is not visible in the result plots as presented in Section 6.3.

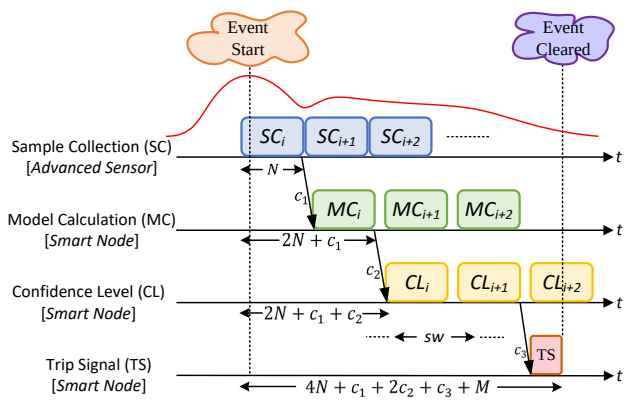

Figure 6.32: Timing diagram showing different steps such as sample collection, model calculation, confidence level and trip signal generation involved in DSEBPS.

The timing diagram showing different steps from the instant when the event started until the event is cleared is presented in Figure 6.32. The first step includes the sample collection (SC) step and requires time which is $N(= 40 \times 250$ microseconds $= 10$ milliseconds). The model calculation (MC) step is triggered by the reception of the sample block and requires time which is N to reach the confidence level calculation step. The confidence level (CL) step operates in a sliding window (SW) with 40 samples which slide over the results of the MC step. The logic of the trip signal is designed using the confidence level signal which is based on the consistency of the objective function. For increased reliability of DSEBPS, the confidence level goes low if the objective function remains above the threshold for 40 consecutive samples. It implies that the worst-case delay for the CL step could stretch over two sample blocks and hence two sample blocks are required for accurate calculation of confidence level. Thus, the confidence level step requires time which is $2N$ to reach the trip signal decision. Once the CL determination is done a trip signal is generated and requires time which is M and sent to the circuit breakers' for clearing the fault. The communication time required for a sample block to reach from SC step to MC step is c_1, MC step to CL step is c_2, and CL step to TS step is c_3. Thus, the fault detection time (in the worst case) using DSEBPS comes out as $4N + c_1 + 2c_2 + c_3 + M$. In practice, the communication delays $c_1, c_2,$ and c_3 are generally very small as compared to processing delays and thus neglected. Further, the time for the trip signal generation (M) is considered 2.5 milliseconds, and the circuit breaker operating time (mechanical device) is widely considered to be 2 cycles (40 milliseconds in the case of a 50 Hz system). Thus, the fault detection time (in the worst case) is 42.5 milliseconds, while the fault clearing time (in the worst case) is 82.5 milliseconds as tested in the lab.

6.7 Discussion on DSEBPS Performance Under Special Operating Conditions

This section discusses the possible performance of DSEBPS under various special operating conditions. In the future development process, they need to be further examined and tested.

6.7.1 CT Saturation Conditions

CT saturation is a common problem in power system protection studies. Many of the newly proposed and as well as existing protection schemes get impacted by this problem. However, there are many practical solutions available for mitigating the CT saturation issue which could also be incorporated into DSEBPS (after detailed investigations) so that it performs as intended even during CT saturation. Some of the solutions could be by employing a higher accuracy class CT [147], reducing CT burden by adding another set of CT cables in parallel, employing percentage differential relay to avoid CT saturation effect, incorporating CT saturation detection algorithms [148], and filtering of decaying DC component and effects of CT saturation using least error squares technique [149]. The recent research works in [150] and [151] employs DSE to detect the CT saturation. Since DSEBPS is also based on DSE, the concept of detecting CT saturation and estimating CT primary current could be easily incorporated in DSEBPS.

6.7.2 Power Swings

Due to power swings, a disturbance in one area could lead to oscillations in generators connected in another area (in the case of an interconnected power system). These oscillations might cause the voltage and currents to start fluctuating. In such conditions, all the measurements including the voltages and currents from local and remote ends of a transmission line would see the same degree of variations. Since the intensity and frequency of power swings are low, the estimated values of the measurements will not have high non-conformity with the measurements like the fault condition. However, during the power swing, the level of conformity will reduce if compared with the normal operating conditions. The non-conformity between the measurements and their estimated values during the power swings could be incorporated using the objective function threshold value and hence the confidence level will remain high and thus DSEBPS will not trigger the tripping.

6.7.3 Lightning Surge

Most of the transmission line substations are equipped with a surge arrester (SA) for lightning protection. SAs are installed at the end of the transmission line and between the instrumentation transformers (VTs/CCVTs and CTs) and transmission line [152]. The location of SA ensures that if the lighting occurs at any location of the transmission line then the surge gets arrested by the SA before it can enter VTs/CCVTs and CTs. The modern SA (such as ZnO-arrester) can react very fast, in the order of 10 nanoseconds. If the surge does not enter VTs/CCVTs and CTs, then the corresponding measurements remain unaffected and subsequently, objective function and confidence level also remains unaffected ensuring that DSEBPS works as intended. A typical substation diagram showing transmission line, surge arrester, current transformer, and voltage transformer is shown in Figure 6.33.

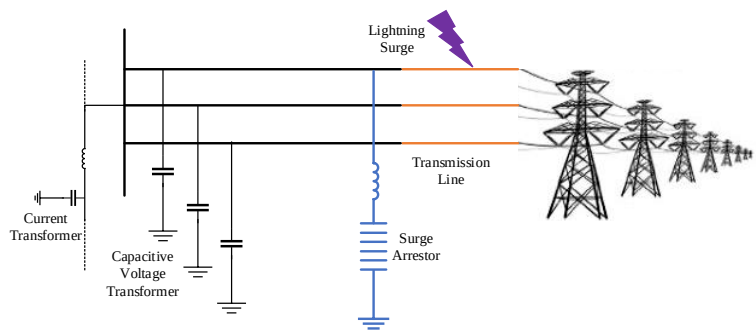

Figure 6.33: A typical substation diagram showing transmission line, surge arrester, current transformer and voltage transformer.

6.7.4 Switching Phenomenon

Switching phenomenons in power systems could be due to switching on of a transformer leading to inrush current or a large induction motor which could draw heavy currents, etc. Such a phenomenon could lead to the misoperation of protection schemes (e.g., overcurrent,

distance relays). Several solutions are proposed in the literature to handle and avoid false tripping, such as the one in [153]. A similar technique could also be tested and applied to DSEBPS. However, such a study is not carried out within the scope of this work but it is planned to be investigated as part of future studies.

6.7.5 Infeed or Outfeed Condition

Infeed or outfeed condition arises due to the line tappings leading to a condition where the distance relay could experience under-reach or over-reach issues and thus negatively impact the tripping decision. In order to investigate this issue, the dynamic model of the transmission line was modified to take into account the changes caused due to this condition in the original model and presented in Section 5.3.7 and Appendix A.4. The modifications include new model equations and matrices by incorporating the new branch and currents at the tapped point. Thereafter, a case study was performed with the same test setup but with the incorporation of a tapping point in the middle of the transmission line. This setup requires more measurements (including phase currents at the tapped point) as compared to the original case study. The results from the case study proved that DSEBPS works as intended during this condition and the trip signal was successfully generated as the fault was initiated.

6.7.6 External Fault with CT Saturation

A few external faults could include e.g., severe CT saturation. The main concern in such a condition is the saturation of only one of the CTs, which could lead to false tripping or sometimes even failure of operation for internal fault under specific conditions [154]. As mentioned previously, DSEBPS is inspired from differential protection which also faces this issue, thus a solution similar to the one proposed in [154] for differential protection could be tested and validated as part of future studies.

In addition to the above identified special operating conditions, asymmetrical operation of circuit breakers in the three-phase system and a single line to ground fault with an auto-reclosing mechanism leading to asymmetrical conditions during the dead-time followed by the single-phase tripping, also could have an impact on DSEBPS performance and are required to be further examined and validated in the future work.

6.8 Advantages of Open Platform and Real-World Application

6.8.1 AdvSens

This subsection discusses the advantages of the open platform from AdvSens perspective. Next to the provided hardware, AdvSens also provides an open platform, which allows third parties to develop their algorithms in common programming languages such as Python and C++. From an innovation perspective, AdvSens and an open platform can be harnessed to produce innovative solutions with a high technology readiness level (TRL).

6.8.2 Dynamic State Estimation based Protection Scheme

This subsection discusses the different aspects to be considered for the real-world application of DSEBPS. The implementation of DSEBPS is done using an open platform such as that of AdvSens. The code for DSEBPS is written in an open-source programming language, Python. The Python code of DSEBPS also helps in forming an easy interface to get access to the real-time measurements provided by AdvSens. The following aspects will be important to be considered for real-world application:

- *Communication*: A reliable communication infrastructure is one of the important aspects of DSEBPS implementation. A closed private communication network or wireless communication could be a few of the solutions which could address both communication failures and delay issues. However, the measurement redundancy and pseudo measurements in DSE could also be utilized in some cases of communication failures. A wide area monitoring system could also be used in some applications.
- *Smart Node*: The configuration and location of the smart node are also important aspects for consideration. The smart node should have enough computational power so that the trip signal can be calculated and sent within the standard fault detection time. The location of the smart code could be at one of the substations so that at least one end measurement is locally received.
- *CTs and VTs/CCVTs Calibration*: For the application of AdvSens in high voltage transmission lines, metering transformers (such as CTs and VTs/CCVTs) are needed to be installed for conversion of the high voltages and currents to the measurement level [155]. A secondary stage calibration procedure could also be used for correcting the phase and voltage displacement of the signals provided that the calibration parameters are known within AdvSens.
- *Primary or Backup Protection Scheme*: DSEBPS could first be used as a backup protection scheme and after satisfactory implementation and validation spanning over a few years, it could be employed as a primary protection scheme.

6.9 Summary

The chapter concludes that the application of DSE-based protection on a transmission line works satisfactorily in an experimental setup. It further suggests that the scheme performed adequately both in terms of selectivity and time. The experimental setup does not generate a trip signal during the normal operating conditions (avoids unwanted tripping), while the trip signal is successfully generated during the balanced fault, unbalanced faults, fault with inductive load conditions, high impedance fault, fault current fed from both ends, and hidden failure. The application of AdvSens has also been validated which worked as the key component in the scheme providing an opportunity to be rolled out as a commercial product. The DSE and AdvSens integration in the open platform works well and could contribute to more development in the future. The work conducted in this chapter has led to the identification of several new areas for development and validation within DSEBPS.

CHAPTER 7

Decentralized Dynamic State Estimation of Transmission Lines Using Unscented Kalman Filter

This chapter presents the work conducted on the development of a decentralized dynamic state estimation method for transmission lines using the unscented Kalman filter. Further, the simulation results for a case study with realistic transmission line parameters are presented.

7.1 Introduction

The objective of this chapter is to develop a new dynamic state estimation method for application in power systems monitoring. One of the advantages of this method is that the remote end state variables of a transmission line can be estimated using only the local end variables and, hence, the need for communication infrastructure is eliminated. The results obtained from the chapter shows that the method works satisfactorily for monitoring purposes and could have potential applications in dynamic state estimation based protection. The proposed method addresses some limitations associated with the dynamic state estimation method employed in Chapter 5 and 6 for protection applications. However, the implementation of the proposed method for the protection applications is not included in this chapter but is suggested for future work.

7.2 Transmission Line Modelling and the Discrete DAEs

A single-phase π-model representation of a transmission line is presented in Figure 7.1. This section presents the derivation of the discrete DAEs of a transmission line by using continuous DAEs. The resistance, reactance, and shunt capacitance of a transmission line are represented as R_J, L_J, and C_J, respectively. The sending and receiving end current are represented as i_J and i_j, respectively. Similarly, the sending and receiving end voltage are represented as v_J and v_j, respectively. For UKF-based DSE, the sending end currents are taken as the measurements $z = (i_A, i_B, i_C)$, while the sending end voltages are taken as the pseudo inputs $u = (v_A, v_B, v_C)$. The receiving end currents and receiving end voltages are the estimated quantities $x = (i_a, i_b, i_c, v_a, v_b, v_c)$ as presented in Figure 7.2.

The continuous DAEs for a transmission line model can be written as:

$$i_J = i_j + C_J \frac{dv_j}{dt} + C_J \frac{dv_J}{dt} \tag{7.1}$$

$$v_J = v_j + R_J \left[i_j + C_J \frac{dv_j}{dt} \right] + L_J \left[\frac{di_j}{dt} + C_J \frac{d^2 v_j}{dt^2} \right] \tag{7.2}$$

where subscript J represents the sending end side and subscript j represents the receiving end side.

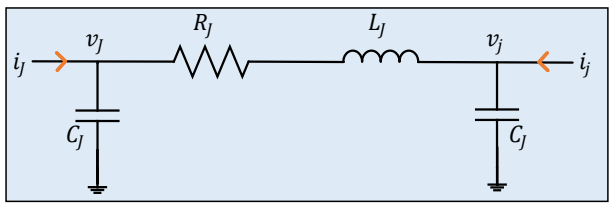

Figure 7.1: A single-phase π-model representation of a transmission line with designated variables.

The discrete DAEs of a transmission line are obtained using the continuous DAEs and are presented in (7.3)−(7.8). Among these equations, (7.13) corresponds to (7.7) and (7.8), while (7.14) corresponds to (7.4).

For the conversion of the continuous DAEs of a transmission line into the discrete DAEs, the following formulations are used:

$$\frac{d^2x}{dt^2} = \frac{x(k+1) - 2x(k) + x(k-1)}{T^2}, \frac{dx}{dt} = \frac{x(k+1) - x(k)}{T}, x = x(k+1) \tag{7.3}$$

Applying the above formulations to (7.1) leads to:

$$i_J(k+1) = i_j(k+1) + C_J \left[\frac{v_j(k+1) - v_j(k)}{T} \right] + C_J \left[\frac{v_J(k+1) - v_J(k)}{T} \right] + w(k+1) \tag{7.4}$$

$$i_j(k+1) = i_J(k+1) + v_j(k+1)\left[-\frac{C_J}{T}\right] + v_j(k)\left[\frac{C_J}{T}\right] + v_J(k+1)\left[-\frac{C_J}{T}\right] + v_J(k)\left[\frac{C_J}{T}\right] + w(k+1) \quad (7.5)$$

Restructuring (7.2) and applying the same formulations, leads to:

$$\frac{dv_j}{dt} = -\left(\frac{1}{R_J C_J}\right)v_j - \left(\frac{1}{C_J}\right)i_j + \left(\frac{1}{R_J C_J}\right)v_J - \left(\frac{L_J}{R_J C_J}\right)\frac{di_j}{dt} - \left(\frac{L_J}{R_J}\right)\frac{d^2 v_j}{dt^2}$$

$$\left[\frac{v_j(k+1) - v_j(k)}{T}\right] = -v_j(k+1)\left(\frac{1}{R_J C_J}\right) - i_j(k+1)\left(\frac{1}{C_J}\right) + v_J(k+1)\left(\frac{1}{R_J C_J}\right) - \left[\frac{i_j(k+1) - i_j(k)}{T}\right]\left(\frac{L_J}{R_J C_J}\right) - \left[\frac{v_j(k+1) - 2v_j(k) + v_j(k-1)}{T^2}\right]\left(\frac{L_J}{R_J}\right) + v(k+1)$$

$$v_j(k+1) = v_j(k)E_1 + v_j(k-1)E_2 + i_j(k)E_3 + i_j(k+1)E_4 + v_J(k+1)E_5 + v(k+1) \quad (7.6)$$

where $E_1 = \left[\frac{C_J(TR_J + 2L_J)}{D}\right]$, $E_2 = \left[\frac{-L_J C_J}{D}\right]$, $E_3 = \left[\frac{TL_J}{D}\right]$,

$E_4 = \left[\frac{-T(TR_J + L_J)}{D}\right]$, $E_5 = \left[\frac{T^2}{D}\right]$, $D = [TR_J C_J + T^2 + C_J L_J]$.

Substituting $i_j(k+1)$ from (7.5) into (7.6), leads to:

$$v_j(k+1) = v_j(k)E_1 + v_j(k-1)E_2 + i_j(k)E_3 + \left[i_J(k+1) + v_j(k+1)\left(-\frac{C_J}{T}\right) + v_j(k)\left(\frac{C_J}{T}\right) + v_J(k+1)\left(-\frac{C_J}{T}\right) + v_J(k)\left(\frac{C_J}{T}\right) + w(k+1)\right]E_4 + v_J(k+1)E_5 + v(k+1)$$

$$v_j(k+1) = F_1 v_j(k) - F_1 v_j(k-1) + F_2 i_j(k) + F_3 i_J(k+1) + F_4 v_J(k) + F_5 v_J(k+1) + w(k+1) + v(k+1) \quad (7.7)$$

where $F_1 = \left[\frac{TE_1 + E_4C_J}{T + E_4C_J}\right], F_2 = \left[\frac{TE_3}{T + E_4C_J}\right], F_3 = \left[\frac{TE_4}{T + E_4C_J}\right],$

$$F_4 = \left[\frac{E_4C_J}{T + E_4C_J}\right], F_5 = \left[\frac{T}{T + E_4C_J}\right]$$

Substituting $v_j(k+1)$ from (7.7) into (7.5), leads to:

$$\begin{aligned} i_j(k+1) = i_J(k+1) + v_j(k)\left[\frac{C_J}{T}\right] + v_J(k+1)\left[-\frac{C_J}{T}\right] + v_J(k)\left[\frac{C_J}{T}\right] \\ + [F_1v_j(k) - F_1v_j(k-1) + F_2i_j(k) + F_3i_J(k+1) + F_4v_J(k) + F_5v_J(k+1) \\ + w(k+1) + v(k+1)]\left[-\frac{C_J}{T}\right] + w(k+1) \end{aligned}$$

$$\begin{aligned} i_j(k+1) = M_1i_J(k+1) + M_2v_j(k) + M_3v_J(k+1) + M_4v_J(k) \\ + M_5v_j(k-1) + M_6i_j(k) + w(k+1) + v(k+1) \end{aligned} \tag{7.8}$$

where $M_1 = \left[1 - \frac{F_3C_J}{T}\right], M_2 = \left[(1-F_1)\frac{C_J}{T}\right], M_3 = \left[-(1+F_5)\frac{C_J}{T}\right],$

$$M_4 = \left[(1-F_4)\frac{C_J}{T}\right], M_5 = \left[F_1\frac{C_J}{T}\right], M_6 = \left[-F_2\frac{C_J}{T}\right]$$

7.3 Formulation of Decentralized Dynamic State Estimation Method

With appropriate assumptions, a transmission line can be represented using the following set of continuous-time nonlinear DAEs:

$$\dot{\boldsymbol{x}}(t) = \bar{\boldsymbol{g}}[\dot{\boldsymbol{x}}(t), \boldsymbol{x}(t), \dot{\boldsymbol{u}}(t), \boldsymbol{u}(t), \boldsymbol{y}(t), \boldsymbol{v}(t)] \tag{7.9}$$

$$\boldsymbol{y}(t) = \boldsymbol{h}[\dot{\boldsymbol{x}}(t), \boldsymbol{x}(t), \dot{\boldsymbol{u}}(t), \boldsymbol{v}(t)] + \boldsymbol{w}(t) \tag{7.10}$$

The sampling of (7.9) and (7.10) at a sampling time period T_0 results in (7.11) and (7.12). To represent (7.11) and (7.12) in the discrete form, $(k+1)T_0$ and kT_0 are rewritten as $(k+1)$ and k, respectively, resulting in (7.13) and (7.14).

$$\frac{\boldsymbol{x}((k+1)T_0) - 2\boldsymbol{x}(kT_0) + \boldsymbol{x}((k-1)T_0)}{{T_0}^2} = \bar{\boldsymbol{g}}\left[\left(\frac{\boldsymbol{x}((k+1)T_0) - \boldsymbol{x}(kT_0)}{T_0}\right), \boldsymbol{x}((k+1)T_0), \left(\frac{\boldsymbol{u}((k+1)T_0) - \boldsymbol{u}(kT_0)}{T_0}\right), \boldsymbol{u}((k+1)T_0), \boldsymbol{y}((k+1)T_0), \boldsymbol{v}((k+1)T_0)\right] \tag{7.11}$$

$$\boldsymbol{y}((k+1)T_0) = \boldsymbol{h}\left[\left(\frac{\boldsymbol{x}((k+1)T_0) - \boldsymbol{x}(kT_0)}{T_0}\right), \boldsymbol{x}((k+1)T_0), \left(\frac{\boldsymbol{u}((k+1)T_0) - \boldsymbol{u}(kT_0)}{T_0}\right), \boldsymbol{v}((k+1)T_0)\right] + \boldsymbol{w}((k+1)T_0) \tag{7.12}$$

$$\boldsymbol{x}(k+1) = \boldsymbol{g}[\boldsymbol{x}(k), \boldsymbol{x}(k-1), \boldsymbol{u}(k+1), \boldsymbol{u}(k), \boldsymbol{y}(k+1), \boldsymbol{v}(k+1)] \tag{7.13}$$

$$\boldsymbol{y}(k+1) = \boldsymbol{h}[\boldsymbol{x}(k+1), \boldsymbol{x}(k), \boldsymbol{u}(k+1), \boldsymbol{u}(k), \boldsymbol{v}(k+1)] + \boldsymbol{w}(k+1) \tag{7.14}$$

The state $\boldsymbol{x}(k+1)$ is treated as a random variable in the state estimation problem with an estimated mean and covariance as $\hat{\boldsymbol{x}}(k+1)$ and $\boldsymbol{P}_x(k+1)$, respectively. It can be deduced from (7.13) and (7.14) that the measurement noise $\boldsymbol{w}(k+1)$ is considered as additive, while the process noise $\boldsymbol{v}(k+1)$ is considered as non-additive. $\boldsymbol{v}(k+1)$ is nonlinearly related to the state and measurement. The covariance matrices for both measurement and process noise are assumed to be constant and denoted as $\boldsymbol{R}$ and $\boldsymbol{Q}$, respectively. The process noise $\boldsymbol{v}(k+1)$ is also considered as a state and, hence, augmented with the state $\boldsymbol{x}(k+1)$, resulting in augmented state random variable $\boldsymbol{X}(k+1) = [\boldsymbol{x}(k+1)^T, \boldsymbol{v}(k+1)^T]^T$ with estimated mean and covariance as $\hat{\boldsymbol{X}}(k+1)$ and $\boldsymbol{P}_X(k+1)$, respectively. Thus, (7.13) and (7.14) can be restructured as:

$$\boldsymbol{X}(k+1) = \boldsymbol{g}[\boldsymbol{X}(k), \boldsymbol{X}(k-1), \boldsymbol{u}(k+1), \boldsymbol{u}(k), \boldsymbol{y}(k+1), \boldsymbol{v}(k+1)] \tag{7.15}$$

$$\boldsymbol{y}(k+1) = \boldsymbol{h}[\boldsymbol{X}(k+1), \boldsymbol{X}(k), \boldsymbol{u}(k+1), \boldsymbol{u}(k)] + \boldsymbol{w}(k+1) \tag{7.16}$$

7.3.1 Problem Statement

Find $\hat{\boldsymbol{X}}(k+1)$ and $\boldsymbol{P}_X(k+1)$, given $\hat{\boldsymbol{X}}(k)$, $\hat{\boldsymbol{X}}(k-1)$, $\boldsymbol{P}_X(k)$, $\boldsymbol{P}_X(k-1)$, $\boldsymbol{g}$, $\boldsymbol{h}$, $\boldsymbol{u}(k+1)$, $\boldsymbol{u}(k)$, $\boldsymbol{y}(k+1)$, $\boldsymbol{R}$, and, $\boldsymbol{Q}$, such that the state estimation algorithm is decentralized, and uses only the local end measurements, which can be easily measured using PMUs/MUs.

The problem can be stated in other words as follows: To develop an iterative algorithm for evaluating the real-time estimates of the mean and covariance of the states, where the transmission line DAEs, inputs, local sampled measurements, and noise covariance matrices are given.

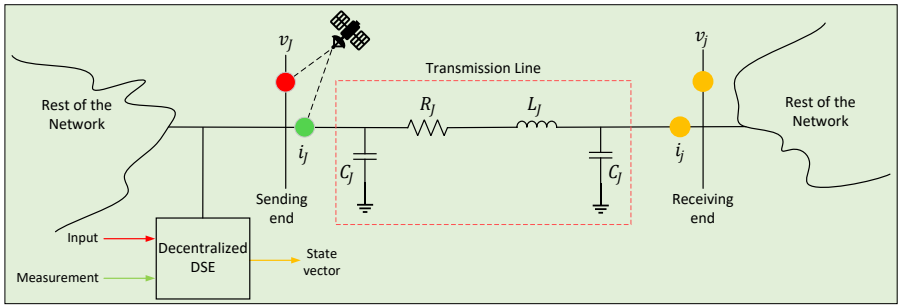

Figure 7.2: Conceptualization of the proposed methodology.

7.3.2 Methodology

The conceptualization of the overall methodology used for the decentralized dynamic state estimation in the transmission line is presented in Figure 7.2. The local end is equipped with measuring infrastructure for measuring the local voltage and current. This work uses the sampled (instantaneous) measurements of the voltage and current. The motivation to choose sampled measurements over phasors is that the phasors are updated at a lower frequency compared to sampled measurements. With a reduced update rate of phasors, the accuracy to capture any transient event reduces. The sampled measurements are provided at a sampling rate of 1.25 kHz in this work which is capable of preserving the signal information to be used in state estimation problems.

For a given measurement, the finite accuracy is modelled by superimposing the white-Gaussian noise over the true value of the measurement. The noise is assumed to have a zero mean, while the standard deviation is taken to be equal to the corresponding measurement's accuracy. The sampled measurements along with their noise variances are sent from the measurement units to the DSE block. Since this method utilizes only the local end measurements for estimation purposes, the communication requirements are easily qualified. The DSE block utilizes these sampled measurements and estimates the state vector (i.e., remote end voltage and current) using UKF in a decentralized manner. Thereafter, the estimates of the state vector could be sent to a local substation or central control center to be used in applications like monitoring, protection, and dynamic security assessment.

7.4 Unscented Kalman Filter

A UKF was proposed to overcome the limitations associated with an extended Kalman filter (EKF). UKF has higher accuracy and easier implementation as compared to EKF. The nonlinear transformations are used for the propagation of mean and covariance data in UKF. The basis of UKF is that it is easier to approximate a probability distribution than it is to approximate a nonlinear function. Based on the previous intuition, it can be implied that this method could be employed for obtaining consistent, efficient, and unbiased estimates of the mean and covariance of the function which is going through a nonlinear transformation [40], [156]–[158].

With the application of the nonlinear transformation presented in (7.15) to $\boldsymbol{X}(k)$, the estimated mean and covariance of the resultant state vector $\boldsymbol{X}(k+1)$ can be evaluated as explained in the following steps [159]:

1. *Sigma Points Generation*: This step generates a set of points, referred to as sigma points, with the same sample mean and covariance as that of $\boldsymbol{X}(k)$. If the dimension of $\boldsymbol{X}(k)$ is n, then exactly $2n$ sigma points $\boldsymbol{\chi}_l(k)$ are generated for capturing its distribution [158]. The sigma points can be generated using the following equations:

$$\boldsymbol{\chi}_l(k) = \hat{\boldsymbol{X}}(k) + (\sqrt{n\boldsymbol{P}_X(k)})_l \qquad l = 1, 2, \ldots, n$$

$$\boldsymbol{\chi}_l(k) = \hat{\boldsymbol{X}}(k) - (\sqrt{n\boldsymbol{P}_X(k)})_l \qquad l = n+1, n+2, \ldots, 2n$$

   where $(\sqrt{n\boldsymbol{P}_X(k)})_l$ represents the lth column of the lower triangular matrix $\sqrt{n\boldsymbol{P}_X(k)}$ which is calculated using Cholesky decomposition, given as

$$n\boldsymbol{P}_X(k) = \left(\sqrt{n\boldsymbol{P}_X(k)}\right)\left(\sqrt{n\boldsymbol{P}_X(k)}\right)^T$$

2. *Predict State*: In this step, the predicted state sigma points $\boldsymbol{\chi}_l^-(k+1)$ are generated using the sigma points. The estimated mean $\hat{\boldsymbol{X}}^-(k+1)$ and the estimated covariance $\boldsymbol{P}_X^-(k+1)$ of a predicted state random variable are equal to the sample mean and sample covariance of the predicted state sigma points, respectively, whose expressions are given as:

$$\boldsymbol{\chi}_l^-(k+1) = \boldsymbol{g}[\boldsymbol{\chi}_l(k), \boldsymbol{u}(k)] \qquad l = 1, 2, \ldots, 2n$$

$$\hat{\boldsymbol{X}}^-(k+1) = \frac{1}{2n}\sum_{l=1}^{2n} \boldsymbol{\chi}_l^-(k+1)$$

$$\boldsymbol{P}_X^-(k+1) = \frac{1}{2n}\sum_{l=1}^{2n} [\boldsymbol{\chi}_l^-(k+1) - \hat{\boldsymbol{X}}^-(k+1)] \times [\boldsymbol{\chi}_l^-(k+1) - \hat{\boldsymbol{X}}^-(k+1)]^T + \begin{bmatrix} \boldsymbol{P}_v & \boldsymbol{0}_{m\times 3} \\ \boldsymbol{0}_{3\times m} & \boldsymbol{0}_{3\times 3} \end{bmatrix}$$

   where m is the total number of states to be estimated and $\boldsymbol{P}_v$ is the process noise covariance matrix.

3. *Predict Measurement*: In this step, the predicted measurement sigma points $\boldsymbol{\gamma}_l^-(k+1)$ are generated. The estimated mean $\hat{\boldsymbol{y}}^-(k+1)$ of a predicted measurement random variable is equal to the sample mean of the predicted measurement sigma points and the estimated covariance $\boldsymbol{P}_y^-(k+1)$ is equal to the sum of $\boldsymbol{R}$ and sample covariance of the predicted measurement sigma points. The estimated cross-correlation covariance

between the predicted state sigma points and predicted measurement sigma points is $\boldsymbol{P}_{Xy}^{-}(k+1)$. These expressions are given as:

$$\boldsymbol{\gamma}_l^{-}(k+1) = \boldsymbol{h}[\boldsymbol{\chi}_l^{-}(k+1), \boldsymbol{u}(k+1)]$$
$$l = 1, 2, \ldots, 2n$$

$$\hat{\boldsymbol{y}}^{-}(k+1) = \frac{1}{2n}\sum_{l=1}^{2n}\boldsymbol{\gamma}_l^{-}(k+1)$$

$$\boldsymbol{P}_{y}^{-}(k+1) = \frac{1}{2n}\sum_{l=1}^{2n}[\boldsymbol{\gamma}_l^{-}(k+1) - \hat{\boldsymbol{y}}^{-}(k+1)][\boldsymbol{\gamma}_l^{-}(k+1) - \hat{\boldsymbol{y}}^{-}(k+1)]^T + \boldsymbol{P}_w$$

$$\boldsymbol{P}_{Xy}^{-}(k+1) = \frac{1}{2n}\sum_{l=1}^{2n}[\boldsymbol{\chi}_l^{-}(k+1) - \hat{\boldsymbol{X}}^{-}(k+1)][\boldsymbol{\gamma}_l^{-}(k+1) - \hat{\boldsymbol{y}}^{-}(k+1)]^T$$

where $\boldsymbol{P}_w$ is the measurement noise covariance matrix.

4. *Kalman Update*: In the final step, $\hat{\boldsymbol{X}}(k+1)$ and $\boldsymbol{P}_X(k+1)$ are found out using the normal Kalman filter as follows [160]:

$$\boldsymbol{K}(k+1) = \boldsymbol{P}_{Xy}^{-}(k+1)[\boldsymbol{P}_{y}^{-}(k+1)]^{-1}$$
$$\hat{\boldsymbol{X}}(k+1) = \hat{\boldsymbol{X}}^{-}(k+1) + \boldsymbol{K}(k+1)[\boldsymbol{y}(k+1) - \hat{\boldsymbol{y}}^{-}(k+1)]$$
$$\boldsymbol{P}_X(k+1) = \boldsymbol{P}_X^{-}(k+1) - \boldsymbol{K}(k+1)[\boldsymbol{P}_{Xy}^{-}(k+1)]^T$$

7.5 Pseudo Inputs

The consideration of sending end voltage V_J as the inputs need to be addressed as only the measured values of V_J are available (given as V_{yA}, V_{yB}, V_{yC}), not their actual values. Since the measurements are contaminated and have their associated noises (given as V_{wA}, V_{wB}, V_{wC}), they are required to be treated. One way to treat the associated noises in the DAEs is by modelling them as input noises [161], but it requires linearization which topples the advantages associated with the unscented transformation and nonlinear filtering. Interestingly, another way is to include the associated noises based on a reality that the actual inputs are equal to the difference between the measured values and their associated noises. Using this hypothesis, the inputs can be written as:

$$V_J = V_{yJ} - V_{wJ} \tag{7.17}$$

The application of this hypothesis to the state function presented in (7.13) makes $\boldsymbol{u}(k)$ act as a pseudo input vector and $\boldsymbol{v}(k)$ act as a pseudo-process noise vector, which can be expressed as:

$$\boldsymbol{u}(k) = [V_{yA}, V_{yB}, V_{yC}]^T$$
$$\boldsymbol{v}(k) = [V_{wA}, V_{wB}, V_{wC}]^T \tag{7.18}$$

The pseudo-process noise V_{wA}, V_{wB}, V_{wC} are white noises which has zero means and standard deviations as $\sigma_{V_{wA}}, \sigma_{V_{wB}}, \sigma_{V_{wC}}$. It can deduce from this explanation that the mean and covariance of $\boldsymbol{v}(k)$ remains constant for each sample and can be expressed as:

$$\begin{aligned} \hat{\boldsymbol{v}}(k) &= [\boldsymbol{0}_{3\times 1}] \\ \boldsymbol{P}_v(k) &= \boldsymbol{Q} = \text{diag}\left[\sigma^2_{V_{wA}}, \sigma^2_{V_{wB}}, \sigma^2_{V_{wC}}\right] \end{aligned} \tag{7.19}$$

Further, the estimates of the mean and covariance of $\boldsymbol{x}(k)$ are given by $\hat{\boldsymbol{x}}(k)$ and $\boldsymbol{P}_x(k)$, respectively, while the cross-correlation between the $\boldsymbol{x}(k)$ and $\boldsymbol{v}(k)$ is given by $\boldsymbol{P}_{xv}(k)$. The augmentation of $\boldsymbol{x}(k)$ with $\boldsymbol{v}(k)$ gives $\boldsymbol{X}(k)$ which can be expressed as:

$$\boldsymbol{X}(k) = [\boldsymbol{x}(k)^T, \boldsymbol{v}(k)^T]^T$$

The mean and covariance of the estimates of $\boldsymbol{X}(k)$ can be given as follows:

$$\hat{\boldsymbol{X}}(k) = \begin{bmatrix} \hat{\boldsymbol{x}}(k) \\ \hat{\boldsymbol{v}}(k) \end{bmatrix}; \boldsymbol{P}_X(k) = \begin{bmatrix} \boldsymbol{P}_x(k) & \boldsymbol{P}_{xv}(k)^T \\ \boldsymbol{P}_{xv}(k) & \boldsymbol{P}_v(k) \end{bmatrix} \tag{7.20}$$

Similarly, the mean and covariance of measurement noise $\boldsymbol{w}(k)$ can be given as follows:

$$\begin{aligned} \hat{\boldsymbol{w}}(k) &= [\boldsymbol{0}_{3\times 1}] \\ \boldsymbol{P}_w(k) &= \boldsymbol{R} = \text{diag}\left[\sigma^2_{I_{wA}}, \sigma^2_{I_{wB}}, \sigma^2_{I_{wC}}\right] \end{aligned} \tag{7.21}$$

7.6 Choosing Adequate Sampling Rate of DSE

The sampling rate of DSE is the rate at which state estimates are updated. The selection of sampling rate is one of the important parameters in UKF-based DSE of a transmission line if a detailed non-linear model is used for estimation. This is because a higher sampling rate ensures the proper capturing of any dynamic event, while at the same time it leads to a higher discretization error as can be seen from (7.7). The discretization error depends mainly on the $1/(1 + E_4 C_J/T)$ term in (7.7), which is equal to $(R_J C_J/T + C_J L_J/T^2 + 1)$. This term becomes too large for very small T, mainly because $C_J L_J/T^2$ becomes too large. To keep this term small, $C_J L_J/T^2$ should be close to 1 which means T should be close to $\sqrt{C_J L_J}$. Thus, T also shouldn't be too large as then UKF performance will get affected. Therefore, the sampling rate (F) in the case of transmission line DSE is a trade-off between the event capturing accuracy and the discretization error, and a value of $F = 1/T \approx 1/\sqrt{C_J L_J}$ is a good balance between the two.

It should be noted that i_j has higher discretization error as compared to v_j, because the d^2/dt^2 term first appears in v_j, which gives rise to $1/(1 + E_4 C_J/T)$ terms in (7.7), and introduces error in v_j. This error accumulates and becomes enhanced when v_j is again substituted in the expression of i_j, as i_j already has its own errors due to the d/dt terms (that is, the C_J/T term). Hence, making $1/(1+E_4 C_J/T)$ small has such a significant impact on the accuracy of i_j and, therefore, on the accuracy of transmission line DSE itself.

7.7 Case Study

7.7.1 Description

The case study considered in this work is a three-phase long overhead transmission line with a nominal voltage of 345 kV. The considered parameters and their values in this simulation are presented in Table 7.1 and are taken from [162]. The single-line diagram of the simulation setup is presented in Figure 7.3.

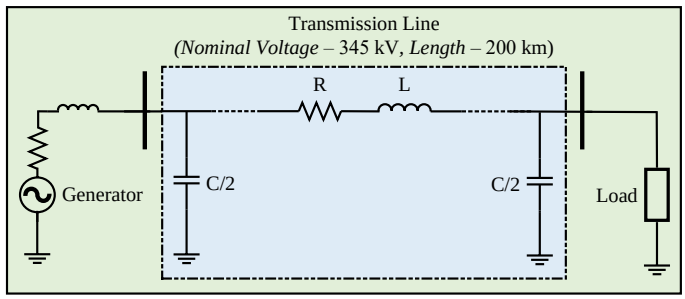

Figure 7.3: Single-line diagram of the simulation setup used.

Table 7.1: Parameters and the Values of the Transmission Line (per-phase)

Parameter	**Value**
Nominal voltage	345 kV
Rated frequency	60 Hz
Resistance (R)	0.037 Ω/km
Inductive Reactance ($x_L = \omega L$)	0.367 Ω/km
Susceptance ($b_C = \omega C$)	4.518 μs/km
Line length	200 km
Rated load	400 MVA
Considered load	350 MVA

7.7.2 Simulation Setup

The simulation for the case study is performed in MATLAB Simulink (R2020b version) using a personal computer with Intel(R) Core(TM) i7-7700K, 4.20 GHz CPU, and 48.0 GB of RAM. The simulation network consists of a long transmission line and is connected to an infinite grid at one end and a load at the other end. The transmission model is developed in Simulink and the voltages and currents of both sending and receiving ends are taken out as variables. The sending end currents as considered as measurements, while the sending end

voltages are considered as inputs. The receiving end currents and receiving end voltages are also taken out to be compared with their estimated values obtained from the UKF-based DSE proposed in this paper.

7.7.3 Sampling Rate Setup

Based on the line parameters used in the case study, the sampling rate is taken as 8E-4, which is close to $\sqrt{C_J L_J}$, as explained in Section 7.6. A sampling rate of 8E-4 translates to a sampling frequency of 1.25 kHz.

7.7.4 Other Parameters used in the Simulation

7.7.4.1 Measurements

In the time-domain simulation, the actual values of local end voltages and currents were sampled at 1.25 kHz ($T_0 = 800$ μs) and white Gaussian noises were added to these samples to obtain the measurements.

7.7.4.2 Process Noise

The process noise has the variance $\boldsymbol{Q} = \text{diag}\{6.6 \times 10^{-6}, 6.6 \times 10^{-6}\}$.

7.7.4.3 Measurement Noise

The measurement noise has the variance $\boldsymbol{R} = \text{diag}\{6.6 \times 10^{-6}, 6.6 \times 10^{-6}\}$.

7.7.4.4 Initial Values

The initial values for all the variables are taken as zero. The zero initial values are an advantage as the proposed method is independent of the initial conditions and works as intended without the availability of this information.

7.8 Results and Discussion

This section presents the results obtained from the different case studies and is followed by subsequent discussions. All the case studies are performed using the test setup presented in Section 7.7 and parameters presented in Table 7.1. The UKF-based DSE algorithm was running simultaneously with the simulation of the transmission line under the given load conditions. The generated measurements were given as input to the UKF-based DSE. Each simulation was run for 0.15 seconds, while the sampling frequency of 1.25 kHz is used in simulation. The results presented in the plots show per unit values, where the nominal voltage is 345 kV and the nominal current is calculated using the nominal voltage (345 kV) and rated load which is 400 MW.

7.8.1 With Resistive Load

This subsection presents the results from UKF-based DSE when the considered load is purely resistive. The considered load is $S = 350$ MVA and as the load is purely resistive so $P = 350$ MW and $Q = 0$ MVAr. The simulated values (obtained from Simulink) along with the estimated values obtained from the UKF-based DSE are presented in Figure 7.4.

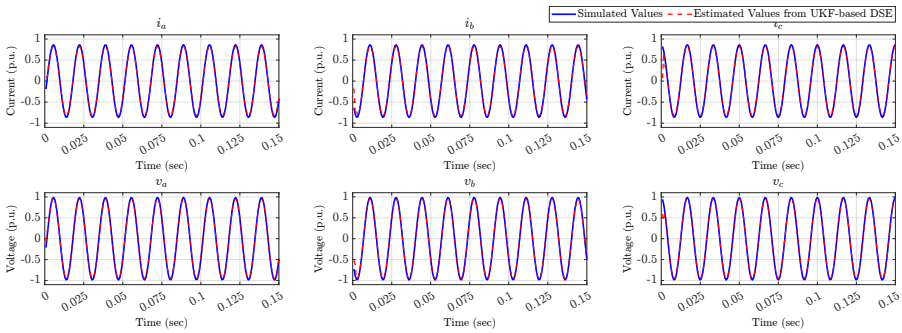

Figure 7.4: Simulated measurements and the estimated values from UKF-based DSE for the receiving end currents (i_a, i_b, i_c) and receiving end voltages (v_a, v_b, v_c) for resistive load.

Estimation Performance

It can be seen from Figure 7.4 that the estimated values obtained from the UKF-based DSE are concurrent with the simulated values obtained from Simulink. A small mismatch can be seen at the beginning of the simulation which is due to the flat start of the guess values for the UKF-based DSE. Thus, it is evident from the results presented in Figure 7.4 that the UKF-based DSE accurately estimates the dynamic states of the transmission line (i.e., receiving end voltages and receiving end currents). It should be noted here that the dynamic states are estimated using the local end signals only. The estimation with high accuracy once again underlines that the proposed UKF-based DSE can be employed reliably for further control and security applications.

7.8.2 With Inductive Load

The loading conditions in power systems are mostly inductive which could make the system response to disturbances more sluggish due to the increase in the time constant and also leads to an increased phase difference between the voltages and currents. These factors could also impact the performance of any DSE method and thus forms an interesting case to be investigated. In this regard, this subsection presents the results from UKF-based DSE when the considered load is inductive with a p.f. of 0.85. The considered load is $S = 350$ MVA and as the load is inductive with a p.f. of 0.85 so $P = 297.5$ MW and $Q = 184.4$ MVAr. The simulated values (obtained from Simulink) along with the estimated values obtained from the UKF-based DSE are presented in Figure 7.5.

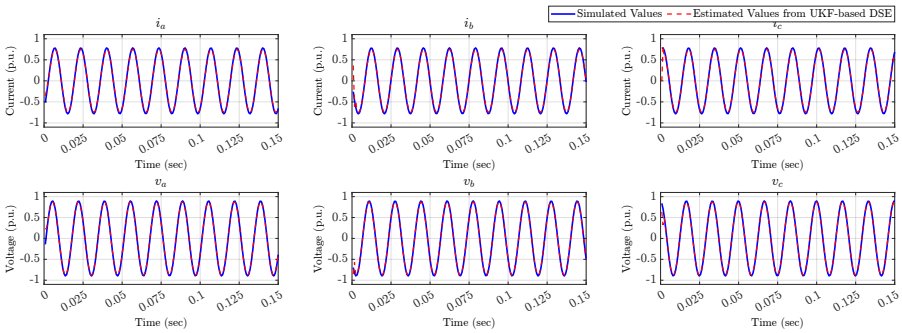

Figure 7.5: Simulated measurements and the estimated values from UKF-based DSE for the receiving end currents (i_a, i_b, i_c) and receiving end voltages (v_a, v_b, v_c) for R-L load with pf of 0.85.

Estimation Performance

It can be seen from Figure 7.5 that the estimated values obtained from the UKF-based DSE are concurrent with the simulated values obtained from Simulink with the inductive load conditions as well. A phase difference between the voltage and current could be seen in Figure 7.5 which is due to inductive load. Therefore, the results presented in Figure 7.5 confirm that the dynamic states of the transmission line (i.e., receiving end voltages and receiving end currents) are accurately estimated by the UKF-based DSE despite the phase difference between the voltages and currents due to the inductive load.

7.8.3 Under Load Change Conditions

Power systems operate in the quasi-static state which means that the system operates at an operating point with small changes around this point. These small changes could be in the form of load changes which could adversely impact the performance of a DSE method. Therefore, in order to validate the performance of the proposed UKF-based DSE method during the load change conditions, this case study is performed. The base load (corresponding to 1 p.u.) is $S = 350$ MVA with a p.f. of 0.85, so $P = 297.5$ MW and $Q = 184.4$ MVAr. Thereafter, the load is increased by 10% to 1.1 p.u. at 0.05 seconds and subsequently decreased to 0.9 p.u. at 0.1 seconds. The variation of this load change is presented in Figure 7.6. The simulated values (obtained from Simulink) along with the estimated values obtained from the UKF-based DSE corresponding to this load change are presented in Figure 7.7.

Estimation Performance

Figure 7.7 shows that the estimated values obtained from the UKF-based DSE correctly follow the simulated values obtained from Simulink during the load change conditions as well. As load increases at 0.05 seconds, correspondingly the current in all the phases increases,

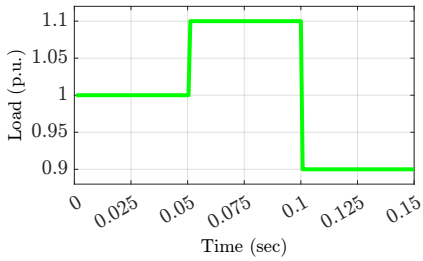

Figure 7.6: A plot showing the load change in per unit.

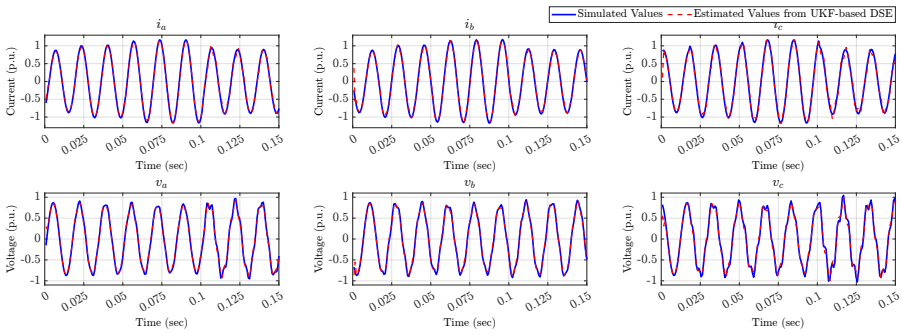

Figure 7.7: Simulated measurements and the estimated values from UKF-based DSE for the receiving end currents (i_a, i_b, i_c) and receiving end voltages (v_a, v_b, v_c) with load change conditions.

while the voltage in all the phases decreases as can be seen in Figure 7.7. The currents and voltages settle at a new steady state until another load change occurs at 0.1 seconds. This change decreases the load to 0.9 p.u. which leads to decreased current in all the phases, while the voltage increases. Interestingly, the estimated values from the UKF-based DSE strictly match the simulated values obtained from Simulink even during the small transients that occurred due to steep load changes. It can be concluded from the results presented in Figure 7.7 and subsequent discussion that the dynamic states of the transmission line (i.e., receiving end voltages and receiving end currents) can be accurately estimated from the UKF-based DSE.

7.8.4 Under Fault Conditions

Transmission lines are also subjected to different fault conditions and satisfactory performance of a DSE method during and after the fault conditions is an important performance indicator. In this regard, this case study is performed to validate the performance of the proposed UKF-based DSE under a three-phase fault. The fault is created in the middle of the transmission line and initiated at 0.04 seconds and cleared at 0.08 seconds. A fault impedance of 1 Ω is used in the simulation. The simulated values (obtained from Simulink) along with the

estimated values obtained from the UKF-based DSE corresponding to this load change are presented in Figure 7.8.

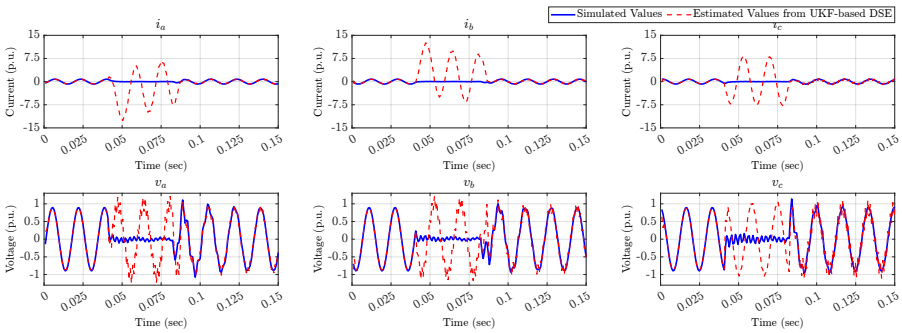

Figure 7.8: Simulated measurements and the estimated values from UKF-based DSE for the receiving end currents (i_a, i_b, i_c) and receiving end voltages (v_a, v_b, v_c) with a three-phase fault.

Estimation Performance

Figure 7.8 shows that before the fault is initiated (i.e., between 0 and 0.04 seconds), the estimated values obtained from the UKF-based DSE match with the simulated values obtained from Simulink. However, when the fault is initiated at 0.04 seconds, the simulated values go to zero because as the fault occurs in the middle of the line and is fed from the local end, thus the remote end voltages and currents go to zero. However, the estimated values from the UKF-based DSE during the fault show a high value for both currents (peak value of 12 p.u.) and voltages (peak value of 1.2 p.u.) which are different from the simulated values. The main reason behind the mismatch is that the UKF-based DSE is using only the local end variables (i.e., voltages and currents) in the estimation process which goes high during the fault and thus it predicts the remote end variables as high. After the fault is cleared at 0.08 seconds, the estimated values from the UKF-based DSE again match well with the simulated values.

It is important to highlight here that the performance of the proposed UKF-based DSE method during the fault is associated with the idea of the DSE-based protection scheme. This protection scheme identifies a fault based on the mismatch of simulated and estimated values during the fault. Experimental validation of one such version of the DSE-based protection scheme is presented in [114].

7.9 Summary

The chapter concludes the proposed decentralized dynamic state estimation method for real-time estimation of the dynamic states of a transmission line has worked satisfactorily. The proposition of the method preserves the nonlinearity in the transmission line modelling

and therefore improved results can be achieved with an unscented Kalman filter as compared to other nonlinear filters. The method works in a decentralized manner which is achieved by treating one set of measured quantities as pseudo inputs. The feasibility of the method is evaluated by carrying out various case studies with resistive load, inductive load, load change, and fault conditions. The results obtained from these case studies highlight the intended performance of the proposed method in terms of accuracy, speed, and feasibility over other existing methods.

CHAPTER 8

Conclusions, Recommendations for Utilization of Research Results, and Future Work

This chapter presents the main conclusions from the work carried out in the thesis. The key findings from the work provide answers to the research questions identified in Chapter 1 of the thesis. The recommendations for the utilization of research results obtained from the developed tools and methods are given. Further, the plausible ideas for future work in continuation to the work done in this thesis are presented.

8.1 Conclusions

This thesis presents the development and validation of advanced support tools for system operators contextual to their transition toward future power systems. First, the thesis proposed a comprehensive future-readiness assessment framework which is developed based on the identification of key technical, market, and policy indicators, to help the DSOs in evaluating their current status and preparedness for a future transition. Second, the thesis developed an advanced congestion forecast tool that is based on a probabilistic approach and employs the BFS power flow method. This tool will assist DSOs by forecasting congestion levels in their network through interactive visualization of different congestion indicators. Third, a dynamic state estimation-based protection scheme is implemented and validated at Chalmers power system laboratory for transmission line protection by employing an experimental setup in the thesis. Finally, a decentralized dynamic state estimation method for transmission lines is developed based on the unscented Kalman filter which could be

used for real-time monitoring, protection, and dynamic security assessment.

In Section 1.2 of this thesis, four different research questions were formulated based on the challenges identified in future power systems.

With regards to **RSQ-1**, a *future-readiness assessment framework* with a list of technical, market, and policy indicators for DSOs were developed in the thesis. From the assessment of three DSOs (from France, The Netherlands, and Sweden) using this proposed framework, the following conclusions can be made:

- Generally, the key focus for evaluating the future-readiness remains on the technical aspects such as level of DERs, monitoring, and control, etc., while the policy and market aspects are not much emphasized, which might not provide the correct evaluation of future-readiness. In this framework, policy aspects such as level of unbundling, network codes, etc., and market aspects such as business models, tariffs, etc. have been considered and evaluated, since they would have great impacts on the actions required by the DSOs in the future.
- The proposed indicators have played a central role in scenario description of intelligent distribution systems, policy recommendations, end-user acceptance, and the development of the pathways for future development.
- The assessment results from the three DSOs have shown that the current level of connected DERs is limited in their networks but DSOs need to be prepared for the increased level of DERs.
- The increased level of DERs would require investment in flexibilities, advanced forecasting and monitoring, advanced system automation and protection schemes, incentives schemes, and business models to promote end-user engagement, and changes in the roles of DSO in which it can own and/or procure certain resources and services to support distribution grid operations.

Concerning **RSQ-2**, *an advanced congestion forecast tool* was developed in the thesis to assist the DSO to forecast the congestion levels in their networks as per the preferences specified by the DSO. The tool is implemented using the probabilistic power flow model which employs the backward-forward sweep algorithm. The tool can present the cumulative probability-based contour plots and colour-maps of the network which visualize the network loading conditions for the DSO and make it easy for the DSO to take necessary preventive or corrective actions. The tool has also incorporated various important factors such as PV production and load forecasts accuracy, load models, and PV-inverter operating modes, which can impact the accuracy of network congestion, and their simulation results are presented. From the case studies carried out with the congestion forecast tool, the following conclusions can be made:

- The results from the case studies for visualization of congestion forecast over a day have shown that the network congestion varies considerably due to the different PV production levels and load consumption during a day. The networks have higher congestion problems, especially during the noon hours when the PV production is quite high and the load consumption is small.
- The case study with the 141-bus distribution system shows the impact of load models on congestion forecast results under different load compositions. The results also

show that the explicit inclusion of load-voltage dependency models would improve the accuracy of the congestion forecast. For a 141-bus distribution system, the constant power load leads to the highest network congestion while the constant impedance leads to the lowest.

- The case study with the 141-bus distribution system to examine the impact of operating modes of PV-inverters on congestion forecast results shows that operating modes have a substantial impact on the network congestion. In constant-V mode, the CP for node voltage reduces drastically as compared to constant-pf mode, however, this reduction occurs at the cost of increased branches and transformers loading level.

Concerning **RSQ-3** related to the *development and validation of a reliable and fast protection scheme* based on advanced measurement technologies and dynamic state estimation to address the challenges and limitations associated with existing schemes for the protection of transmission lines, DSEBPS could be one of the potential solutions. The simulation results have shown that DSEBPS successfully detects the fault conditions and produces a trip signal under various types of faults and conditions. The obtained results affirm that the scheme does not require any relay settings (except the threshold value required for the objective function) which is one of the main reasons for mis-operations.

The thesis further performs the *implementation and experimental validation of* a dynamic state estimation-based protection scheme at Chalmers power system laboratory. The protection scheme utilizes real-time high frequency sampled measurements from advanced sensors and evaluates the operating condition of the transmission line based on which a tripping signal is generated in case a fault occurs. The validation is performed using a physical scaled-down model of a power system, consisting of a transmission line, transformer, synchronous generator, and loads. The scheme has been validated successfully with different fault types and conditions and the following inferences could be made from the validation of the protection scheme:

- The scheme performs as intended and thus proves its efficacy in correctly detecting various types of faults.
- The maximum fault detection time is calculated to be 42.5 milliseconds, while the maximum fault clearing time comes out to be 82.5 milliseconds, on par with currently employed protection methods.
- The obtained results demonstrate the ability of the scheme to detect fault under varying conditions and avoid potential issues with relay coordination.

Regarding **RSQ-4**, a *decentralized dynamic state estimation method for transmission lines* was developed that considers the nonlinear dynamics of the transmission lines and does not require any approximations. The development of the proposed DSE method is done using the unscented Kalman filter which overcomes the limitations of the static state estimation such as adequate capture of system dynamics, etc. The simulation results are obtained using the realistic transmission line parameters with a nominal voltage of 345 kV. The following inferences could be made from the results obtained with the case study:

- The method works in a decentralized way and accurately estimates the remote end state variables (voltages and currents) by using only the local end measurements.
- The method estimates two remote end variables (voltage and current) using only two local end variables (voltage and current) which means it is a balanced determined

system and not an over-determined system, unlike a conventional state estimation.

- The simulation results obtained with the case study prove the efficacy of the proposed method in terms of speed, robustness, and accuracy.

8.2 Recommendations for Utilization of Research Results

The following are the recommendations for the utilization of research results obtained from the developed tools and methods in this thesis:

- *Future-readiness Assessment Framework*: The proposed framework can be used by DSOs to assess their current status and future-readiness. The assessment results obtained from this framework will serve as input for developing a transition plan for the DSOs to facilitate a smoother transition towards the future. The assessment results would also help in identifying plausible scenarios, policy recommendations, and pathways development, all of which also serve as inputs for a transition plan for the DSOs.
- *Advanced Congestion Forecast Tool*: The tool will assist DSO in the operation of distribution systems by supporting in daily congestion management and network planning, depending on the forecast horizons. In short forecast horizons, the DSO will be enabled with timely congestion management by employing market and tariff-based flexibility solutions [163]. It would result in enhancement of the system's resiliency, mitigation of equipment ageing due to overloading, reducing the high additional congestion cost, and other economic benefits, while long-term forecast horizons (e.g., several months or years ahead) will allow the DSO to procure flexibility for avoiding costly grid reinforcement.
- *Dynamic State Estimation based Protection Scheme*: The implementation and validation of DSEBPS will support the transmission system operators in the protection of their network. The experimental validation of the scheme has increased the TRL of the scheme and brought it closer to real-world applications. The efficacy of the scheme is validated for the transmission lines in the thesis but it can also be extended to other elements in power systems and protection of distribution systems (including microgrids) where new protection challenges have risen recently.
- *Decentralized Dynamic State Estimation for Transmission Lines*: The development of the decentralized DSE of transmission lines will assist the transmission system operators in the time-critical operation of their network. Further, the proposed DSE method is envisioned to have potential applications in transmission line monitoring, control, and protection.

8.3 Future Work

The following ideas concerning the *future-readiness assessment framework* are identified for future work:

- *Evaluate Development Gaps*: The assessment results from the framework about the current status and future-readiness will provide the DSOs with specific details for the scope of development in terms of technical, market, and policy indicators. These details in conjunction with the plausible future scenarios would help the DSOs to evaluate the development gaps in the network.

In the context of the *advanced congestion forecast tool*, the following ideas could be considered for future work:

- *Linkage with Flexibility Market*: The congestion forecast tool can be expanded to be linked with local flexibility market structures. The output of the congestion forecast tool concerning the location, severity, and probability of the congestion incidents could be provided to the DSO which can then initiate the local flexibility market to procure the required flexibility for mitigation of these incidents. Depending on the time horizon of the congestion forecast i.e., long-term or real-time, the DSO can procure the required reservation or activate flexibility, respectively.
- *Enhancing Performance*: Currently, the proposed congestion forecast tool uses the Monte-Carlo simulation approach to run the scenarios. However, this approach could require high computational power in the case of large-size distribution systems. In this regard, new approaches for scenario reduction could be employed to reduce the computational demand. Although, the accuracy of the congestion forecast could be compromised with such enhancements and that needs to be investigated properly.

Concerning the experimental validation of *dynamic state estimation based protection scheme*, the following could be considered as an extension of this work:

- *Performance Evaluation of Advanced Sensors*: The performance of advanced sensors in terms of accuracy, latency, etc., could be evaluated when they are connected with a protection class instrumentation transformer in a real high voltage transmission line.
- *More In-depth Investigations*: In order to evaluate the robustness and accuracy of the scheme under all possible conditions, further investigations could be carried out under CT saturation, power swings, lightning surge, switching phenomenons, external fault with CT saturation, asymmetrical operation of circuit breakers in the three-phase system, and a single line to ground fault with an auto-reclosing mechanism leading to asymmetrical conditions during the dead-time followed by the single-phase tripping.
- *Optimising Performance*: Some programming tweaks could be investigated in Python coding to further enhance the processing time requirements which could make the scheme, even more, faster in terms of fault detection time.
- *Centralised Protection Scheme*: The experimental validation could be extended to other power system components such as transformers, alternators, inverters, etc. The validation of each of these components could lay the foundation for the development, implementation, and validation of a dynamic state estimation-based centralized protection scheme for a power system.
- *GPS Synchronization Error*: The measurements required for DSEBPS should have GPS time tag in order to be synchronized. However, GPS synchronization itself could have errors which in turn have an impact on the performance of the scheme. Some of the common errors are loss of GPS signal, loss of data packets, loss of communication

link, etc. The loss of GPS signal can be addressed by using a second-time reference such as computer clocks, etc. Regarding data packet loss, buffering of last data packets or averaging data packets over last instants could be used as an alternative.

Regarding the development of a *decentralized dynamic state estimation method for transmission lines*, the following points could be taken into consideration in the future:

- *Application in Transmission Line Protection*: UKF-based DSE is an accurate method for predicting the operating states of a transmission line without using linearization techniques and approximations. Therefore, in the future, it could be used as an alternative to WLS-based DSE which is employed in the DSEBPS presented in this thesis. However, the accuracy and speed of UKF-based DSE need to be investigated for proper applicability.
- *Limitations with Sampling Rate*: The sampling rate of the measurements gets limited due to its directly proportional relationship with the discretization error i.e., the discretization error increases with the increased sampling rate. At a point, the error becomes so high that it leads to divergence of the algorithm. Further investigations related to this aspect could be taken up in the future to extend the work presented in this thesis.
- *Performance Evaluation under Special Operating Conditions*: Although the performance of the proposed method is tested under different conditions but still validating the performance of the proposed method under special operating conditions such as CT saturation, switching phenomenons, power swings, etc., will further increase the maturity of the proposed method.

References

[1] J. A. P. Lopes, A. G. Madureira, M. Matos, *et al.*, "The future of power systems: Challenges, trends, and upcoming paradigms," *Wiley Interdisciplinary Reviews: Energy and Environment*, vol. 9, no. 3, e368, 2020.

[2] Swedish Energy Agency, *Energy in Sweden 2020 – An overview*, [Online] Available: `https://energimyndigheten.a-w2m.se/Home.mvc?ResourceId=174155`.

[3] Swedish Energy Agency, *Energy in Sweden 2021 – An overview*, [Online] Available: `https://energimyndigheten.a-w2m.se/Home.mvc?ResourceId=198022`.

[4] S. Vindenergi, *Statistics and forecast*, [Online] Available: `https://svenskvindenergi.org/statistik/2017-3`.

[5] *Systemutvecklingsplan 2020–2029*, Statnett, Fingrid, Energinet, Svenska Kraftnät, Tech. Rep., [Online] Available: `www.svk.se/om-oss/rapporter-och-remissvar`, Dec. 2019.

[6] International Energy Agency, *Global EV Outlook 2018*, [Online] Available: `https://www.iea.org/gevo2018`.

[7] International Energy Agency, *Global EV Outlook 2019*, [Online] Available: `https://iea.blob.core.windows.net/assets/7d7e049e-ce64-4c3f-8f23-6e2f529f31a8/Global_EV_Outlook_2019.pdf`.

[8] International Energy Agency, *Global EV Outlook 2021*, [Online] Avail-

able: https://iea.blob.core.windows.net/assets/ed5f4484-f556-4110-8c5c-4ede8bcba637/GlobalEVOutlook2021.pdf.

[9] International Energy Agency, *Global EV Outlook 2022*, [Online] Available: https://iea.blob.core.windows.net/assets/ad8fb04c-4f75-42fc-973a-6e54c8a4449a/GlobalElectricVehicleOutlook2022.pdf.

[10] ETIP SNET, *Vision 2050 - Integrating Smart Networks for the Energy Transition: Serving Society and Protecting the Environment*, [Online] Available: https://smart-networks-energy-transition.ec.europa.eu/sites/default/files/documents/vision/VISION2050-DIGITALupdated.pdf.

[11] IRENA, "Renewable power generation costs in 2018," *International Renewable Energy Agency, Abu Dhabi, Tech. Rep.*, 2019.

[12] GWEC, *Global wind report 2018*, [Online] Available: https://gwec.net/global-wind-report-2018/, Apr. 2018.

[13] International Energy Agency, *Photovoltaic Power Systems Programme Annual Report 2017*, [Online] Available: https://www.iea-pvps.org/index.php?id=6.

[14] International Energy Agency, *Photovoltaic Power Systems Programme Snapshot of Global PV Markets 2022*, [Online] Available: https://iea-pvps.org/wp-content/uploads/2022/04/IEA_PVPS_Snapshot_2022-vF.pdf.

[15] European Commission, *A European Green Deal*, [Online] Available: https://ec.europa.eu/info/strategy/priorities-2019-2024/european-green-deal_en, 2019.

[16] IRENA and European Commission, *Renewable energy prospects for the European Union*, [Online] Available: https://www.irena.org/publications/2018/Feb/Renewable-energy-prospects-for-the-EU, 2018.

[17] Peter Fairley, *Hawaii's solar push strains the grid*, MIT Technology Review, [Online] Available: https://www.technologyreview.com/s/534266/hawaiis-solar-push-strains-the-grid/, Jan. 2015.

[18] Pamela M. Prah, *Utility companies have a solar power problem*, [Online] Available: `https://www.governing.com/news/headlines/utility-companies-have-a-.html`, Feb. 2014.

[19] Liz Hobday, *Electricity distributors warn excess solar power in network could cause blackouts, damage infrastructure*, Australian Broadcasting Corporation, [Online] Available: `https://www.abc.net.au/news/2018-10-11/electricity-distributors-warn-excess-solar-could-damage-grid/10365622`, Oct. 2018.

[20] H. Schermeyer, M. Studer, M. Ruppert, and W. Fichtner, "Understanding distribution grid congestion caused by electricity generation from renewables," in *Proc. Smart Energy Research. At the Crossroads of Engineering, Economics, and Computer Science*, Springer, 2017, pp. 78–89.

[21] U. R. Nair, M. Sandelic, A. Sangwongwanich, T. Dragičević, R. Costa-Castelló, and F. Blaabjerg, "Grid congestion mitigation and battery degradation minimisation using model predictive control in PV-based microgrid," *IEEE Transactions on Energy Conversion*, vol. 36, no. 2, pp. 1500–1509, 2020.

[22] J. Widén, M. Shepero, and J. Munkhammar, "Probabilistic load flow for power grids with high PV penetrations using copula-based modeling of spatially correlated solar irradiance," *IEEE Journal of Photovoltaics*, vol. 7, no. 6, pp. 1740–1745, 2017.

[23] Reddy, S.S., "Optimal scheduling of thermal-wind-solar power system with storage," *Renewable energy*, vol. 101, 1357–1368, 2017.

[24] Reddy, S.S. and Momoh, J.A., "Realistic and transparent optimum scheduling strategy for hybrid power system," *IEEE Transactions on Smart Grid*, vol. 6, no. 6, 3114–3125, 2015.

[25] E. Hartvigsson *et al.*, "Estimating national and local low-voltage grid capacity for residential solar photovoltaic in Sweden, UK and Germany," *Renewable Energy*, vol. 171, pp. 915–926, 2021.

[26] S. M. Brahma *et al.*, "Development of adaptive protection scheme for distribution systems with high penetration of distributed generation," *IEEE Transactions on Power Delivery*, vol. 19, no. 1, pp. 56–63, Jan. 2004.

[27] O. Vasios, S. Kampezidou, and A. S. Meliopoulos, "A dynamic state estimation based centralized scheme for microgrid protection," in *Proc. North American Power Symposium (NAPS)*, 2018, pp. 1–6.

[28] V. A. Papaspiliotopoulos *et al.*, "Hardware-in-the-loop design and optimal setting of adaptive protection schemes for distribution systems with distributed generation," *IEEE Transactions on Power Delivery*, vol. 32, no. 1, pp. 393–400, Feb. 2017.

[29] V. Telukunta, J. Pradhan, A. Agrawal, M. Singh, and S. G. Srivani, "Protection challenges under bulk penetration of renewable energy resources in power systems: A review," *CSEE Journal of Power and Energy Systems*, vol. 3, no. 4, pp. 365–379, 2017.

[30] S. M. Brahma *et al.*, "Insight into microgrid protection," in *Proc. IEEE PES Innovative Smart Grid Technologies Europe*, 2014, pp. 1–6.

[31] P. Naveen and P. Jena, "A review on issues and coordination strategies for over current protection in microgrid," in *Proc. 14th IEEE India Council International Conference (INDICON)*, 2017, pp. 1–6.

[32] A. Khademlahashy *et al.*, "A review on protection issues in microgrids embedded with distribution generations," in *Proc. 12th IEEE Conference on Industrial Electronics and Applications (ICIEA)*, 2017, pp. 913–918.

[33] North American Electric Reliability Corporation, [Online] Available: `https://www.nerc.com/Pages/default.aspx`.

[34] A. Srivastava, R. Mohanty, M. A. F. Ghazvini, L. A. Tuan, D. Steen, and O. Carlson, "A review on challenges and solutions in microgrid protection," in *Proc. IEEE Madrid PowerTech*, 2021, pp. 1–6.

[35] European Network of Transmission System Operators for Electricity (ENTSO-E), *Best protection practices for HV and EHV AC-transmission systems of ENTSO-E electrical grids*, [Online] Available: `https://eepublicdownloads.entsoe.eu/clean-documents/SOC%20documents/Best_protection_practices_for_HV_EHV_AC_transmission_system.pdf`, 2018.

[36] A. S. Meliopoulos, G. J. Cokkinides, *et al.*, "Dynamic state estimation-based protection: Status and promise," *IEEE Transactions on Power Delivery*, vol. 32, no. 1, pp. 320–330, 2016.

[37] Z. Y. Xu, Z. Q. Du, L. Ran, Y. K. Wu, Q. X. Yang, and J. L. He, "A current differential relay for a 1000-kV UHV transmission line," *IEEE Transactions on Power Delivery*, vol. 22, no. 3, pp. 1392–1399, 2007.

[38] J. Zhao, M. Netto, Z. Huang, S. S. Yu, *et al.*, "Roles of dynamic state estimation in power system modeling, monitoring and operation," *IEEE Transactions on Power Systems*, vol. 36, no. 3, pp. 2462–2472, 2020.

[39] Y. Liu, A. P. S. Meliopoulos, R. Fan, L. Sun, and Z. Tan, "Dynamic state estimation based protection on series compensated transmission lines," *IEEE Trans. on Power Delivery*, vol. 32, no. 5, pp. 2199–2209, 2016.

[40] A. K. Singh and B. C. Pal, "Decentralized dynamic state estimation in power systems using unscented transformation," *IEEE Transactions on Power Systems*, vol. 29, no. 2, pp. 794–804, 2013.

[41] Y. Xu, Z. Y. Dong, J. H. Zhao, *et al.*, "A reliable intelligent system for real-time dynamic security assessment of power systems," *IEEE Transactions on Power Systems*, vol. 27, no. 3, pp. 1253–1263, 2012.

[42] Y. Liu, A. K. Singh, J. Zhao, *et al.*, "Dynamic state estimation for power system control and protection," *IEEE Transactions on Power Systems*, vol. 36, no. 6, pp. 5909–5921, 2021.

[43] S. M. Joshi, S. B. Bhattacharjee, V. C. Deshpande, and M. Tadvalkar, "Developing key performance indicators framework for evaluating performance of engineering faculty," in *Proc. IEEE Eighth International Conference on Technology for Education (T4E)*, 2016, pp. 220–223.

[44] F. Folino, M. Guarascio, and L. Pontieri, "A prediction framework for proactively monitoring aggregate process-performance indicators," in *Proc. IEEE 19th International Enterprise Distributed Object Computing Conference*, 2015, pp. 128–133.

[45] H. A. Zheng *et al.*, "Designing a key performance indicator system for technological innovation audit at firm's level: A framework and an empirical study," in *Proc. IEEE International Conference on Industrial Engineering and Engineering Management*, 2009, pp. 1–5.

[46] R. Carli, M. Dotoli, R. Pellegrino, and L. Ranieri, "Measuring and managing the smartness of cities: A framework for classifying performance indicators," in *Proc. IEEE International Conference on Systems, Man, and Cybernetics*, 2013, pp. 1288–1293.

[47] H. Liu, F. Huang, H. Li, W. Liu, and T. Wang, "A big data framework for electric power data quality assessment," in *Proc. 14th Web Information Systems and Applications Conference (WISA)*, 2017, pp. 289–292.

[48] S. Moazeni and B. Defourny, "Distribution system controls assessment in a nonbinding transactive energy market," in *Proc. North American Power Symposium (NAPS)*, 2017, pp. 1–6.

[49] C. Dumbs, G. Jarry, D. Laffaille, *et al.*, "Flexibility for DSOs on a local scale: Business models and associated regulatory questions raised in the Interflex project," AIM, 2018.

[50] S. Huang and Q. Wu, "Real-time congestion management in distribution networks by flexible demand swap," *IEEE Transactions on Smart Grid*, vol. 9, no. 5, pp. 4346–4355, 2017.

[51] G. Prettico, M. Flammini, N. Andreadou, S. Vitello, G. Fulli, and M. Masera, "Distribution system operators observatory 2018," *Publications Office of the European Union*, 2019.

[52] S. Huang, Q. Wu, H. Zhao, and C. Li, "Distributed optimization-based dynamic tariff for congestion management in distribution networks," *IEEE Transactions on Smart Grid*, vol. 10, no. 1, pp. 184–192, 2017.

[53] Reddy, S.S., "Multi-objective based congestion management using generation rescheduling and load shedding," *IEEE Transactions on Power Systems*, vol. 32, no. 2, 852–863, 2016.

[54] T. M. Masaud, R. D. Mistry, and P. K. Sen, "Placement of large-scale utility-owned wind distributed generation based on probabilistic forecasting of line congestion," *IET Renewable Power Generation*, vol. 11, no. 7, pp. 979–986, 2017.

[55] A. Srivastava, D. Steen, L. A. Tuan, and O. Carlson, "A congestion forecast framework for distribution systems with high penetration of PVs and PEVs," in *Proc. IEEE PowerTech Milano*, 2019, pp. 1–6.

[56] M. Fan and L. Huang, "Probabilistic power reserve evaluation algorithm for power systems considering high solar energy penetration," in *Proc. IEEE Power and Energy Society General Meeting*, 2018, pp. 1–5.

[57] M. S. S. Abad, J. Ma, D. Zhang, A. S. Ahmadyar, and H. Marzooghi, "Probabilistic assessment of hosting capacity in radial distribution systems," *IEEE Transactions on Sustainable Energy*, vol. 9, no. 4, pp. 1935–1947, 2018.

[58] M. Nijhuis, M. Gibescu, and S. Cobben, "Gaussian mixture based probabilistic load flow for LV-network planning," *IEEE Transactions on Power Systems*, vol. 32, no. 4, pp. 2878–2886, 2016.

[59] J. M. Lujano-Rojas, R. Dufo-Lopez, J. L. Bernal-Agustin, J. A. D. Navarro, and J. P. S. Catalao, "Probabilistic methodology for estimating the optimal photovoltaic capacity in distribution systems to avoid power flow reversals," *IET Renewable Power Generation*, vol. 12, no. 9, pp. 1045–1064, 2018.

[60] G. E. Constante-Flores and M. S. Illindala, "Data-driven probabilistic power flow analysis for a distribution system with renewable energy sources using Monte Carlo simulation," *IEEE Transactions on Industry Applications*, vol. 55, no. 1, pp. 174–181, 2018.

[61] Hitachi ABB Power Grids, *"Network Manager ADMS"*, [Online] Available: `https://www.hitachiabb-powergrids.com/offering/product-and-system/scada/network-management/network-manager-adms`, 2020.

[62] Siemens, *"Spectrum Power^{TM} ADMS"*, [Online] Available: `https://new.siemens.com/global/en/products/energy/energy-automation-and-smart-grid/grid-control/advanced-distribution-management.html`, 2021.

[63] Schneider Electric, *"EcoStruxure^{TM}"*, [Online] Available: `https://www.se.com/ww/en/work/solutions/for-business/electric-utilities/advanced-distribution-management-system-adms/`, 2021.

[64] J. Shiles *et al.*, "Microgrid protection: An overview of protection strategies in North American microgrid projects," in *Proc. IEEE Power & Energy Society General Meeting (PESGM)*, 2017, pp. 1–5.

[65] X. Kang, C. E. Nuworklo, B. S. Tekpeti, and M. Kheshti, "Protection of micro-grid systems: A comprehensive survey," *The Journal of Engineering*, vol. 2017, no. 13, pp. 1515–1518, 2017.

[66] B. Hadzi-Kostova, Z. Styczynski, and R. Krebs, "New protection concepts for distribution systems with dispersed generation," in *Proc. IEEE Russia PowerTech*, 2005, pp. 1–6.

[67] A. Hooshyar and R. Iravani, "Microgrid protection," *Proceedings of the IEEE*, vol. 105, no. 7, pp. 1332–1353, 2017.

[68] S. F. Zarei and M. Parniani, "A comprehensive digital protection scheme for low-voltage microgrids with inverter-based and conventional distributed generations," *IEEE Transactions on Power Delivery*, vol. 32, no. 1, pp. 441–452, Feb. 2017.

[69] R. Jain, D. L. Lubkeman, and S. M. Lukic, "Dynamic adaptive protection for distribution systems in grid-connected and islanded modes," *IEEE Transactions on Power Delivery*, vol. 34, no. 1, pp. 281–289, Feb. 2019.

[70] S. Mirsaeidi *et al.*, "A protection strategy for micro-grids based on positive-sequence component," *IET Renewable Power Generation*, vol. 9, no. 6, pp. 600–609, 2015.

[71] N. K. Sharma and S. R. Samantaray, "PMU assisted integrated impedance angle based microgrid protection scheme," *IEEE Transactions on Power Delivery*, vol. 35, no. 1, pp. 183–193, Feb. 2020.

[72] N. K. Sharma and S. R. Samantaray, "Assessment of PMU-based wide-area angle criterion for fault detection in microgrid," *IET Generation, Transmission & Distribution*, vol. 13, no. 19, pp. 4301–4310, 2019.

[73] H. Nikkhajoei and R. H. Lasseter, "Microgrid protection," in *Proc. IEEE Power Engineering Society General Meeting (PESGM)*, 2007, pp. 1–6.

[74] Z. Chen *et al.*, "A novel protection scheme for inverter-interfaced microgrid (IIM) operated in islanded mode," *IEEE Transactions on Power Electronics*, vol. 33, no. 9, pp. 7684–7697, 2017.

[75] K. Lai, M. S. Illindala, and M. A. Haj-Ahmed, "Comprehensive protection strategy for an islanded microgrid using intelligent relays," in *Proc. IEEE Industry Applications Society Annual Meeting*, 2015, pp. 1–11.

[76] A. Soleimanisardoo, H. K. Karegar, and H. H. Zeineldin, "Differential frequency protection scheme based on off-nominal frequency injections for inverter-based islanded microgrids," *IEEE Transactions on Smart Grid*, vol. 10, no. 2, pp. 2107–2114, 2018.

[77] S. Brahma, N. Pragallapati, and M. Nagpal, "Protection of islanded microgrid fed by inverters," in *Proc. IEEE Power & Energy Society General Meeting (PESGM)*, 2018, pp. 1–5.

[78] S. Brahma, "Protection of distribution system islands fed by inverter-interfaced sources," in *Proc. IEEE Milan PowerTech*, 2019, pp. 1–6.

[79] F. Blaabjerg *et al.*, "Distributed power-generation systems and protection," *Proceedings of the IEEE*, vol. 105, no. 7, pp. 1311–1331, 2017.

[80] D. Pal and B. K. Panigrahi, "Analysis and mitigation of the impact of ancillary services on anti-islanding protection of distributed generators," *IEEE Transactions on Sustainable Energy*, vol. 11, no. 4, pp. 2950–2961, 2020.

[81] Y. Liu, A. P. S. Meliopoulos, R. Fan, and L. Sun, "Dynamic state estimation based protection of microgrid circuits," in *Proc. IEEE Power & Energy Society General Meeting (PESGM)*, 2015, pp. 1–5.

[82] S. Choi *et al.*, "Effective real-time operation and protection scheme of microgrids using distributed dynamic state estimation," *IEEE Transactions on Power Delivery*, vol. 32, no. 1, pp. 504–514, 2016.

[83] X. Dong *et al.*, "Traveling wave based single-phase-to-ground protection method for power distribution system," *CSEE Journal of power and Energy Systems*, vol. 1, no. 2, pp. 75–82, 2015.

[84] X. Li *et al.*, "Traveling wave-based protection scheme for inverter-dominated microgrid using mathematical morphology," *IEEE Transactions on Smart Grid*, vol. 5, no. 5, pp. 2211–2218, 2014.

[85] N. Davydova and G. Hug, "Traveling wave based protection for medium voltage grids with distributed generation," in *Proc. IEEE Manchester PowerTech*, 2017, pp. 1–6.

[86] N. Davydova and G. Hug, "Travelling wave protection with disturbance classification for distribution grids with distributed generation," *The Journal of Engineering*, vol. 2018, no. 15, pp. 830–835, 2018.

[87] H. Lin *et al.*, "Adaptive protection combined with machine learning for microgrids," *IET Generation, Transmission & Distribution*, vol. 13, no. 6, pp. 770–779, 2019.

[88] T. S. Abdelgayed *et al.*, "Fault detection and classification based on co-training of semisupervised machine learning," *IEEE Transactions on Industrial Electronics*, vol. 65, no. 2, pp. 1595–1605, 2017.

[89] M. Mishra and P. K. Rout, "Detection and classification of micro-grid faults based on HHT and machine learning techniques," *IET Generation, Transmission & Distribution*, vol. 12, no. 2, pp. 388–397, 2017.

[90] M. Manohar, E. Koley, and S. Ghosh, "Enhancing the reliability of protection scheme for PV integrated microgrid by discriminating between array faults and symmetrical line faults using sparse auto encoder," *IET Renewable Power Generation*, vol. 13, no. 2, pp. 308–317, 2018.

[91] Q. Cui and S. Li, "A microgrid protection scheme with conventional relay measurements," in *Proc. IEEE Power & Energy Society General Meeting (PESGM)*, 2018, pp. 1–5.

[92] M. Uzair, L. Li, and J. G. Zhu, "Identifying line-to-ground faulted phase in low and medium voltage AC microgrid using principal component analysis and supervised machine-learning," in *Proc. Australasian Universities Power Engineering Conference (AUPEC)*, 2018, pp. 1–6.

[93] J. James, Y. Hou, A. Y. Lam, and V. O. Li, "Intelligent fault detection scheme for microgrids with wavelet-based deep neural networks," *IEEE Transactions on Smart Grid*, vol. 10, no. 2, pp. 1694–1703, 2017.

[94] D. P. Mishra, S. R. Samantaray, and G. Joos, "A combined wavelet and data-mining based intelligent protection scheme for microgrid," *IEEE Transactions on Smart Grid*, vol. 7, no. 5, pp. 2295–2304, 2015.

[95] M. Manohar *et al.*, "A reliable fault detection and classification scheme based on wavelet transform and ensemble of SVM for microgrid protection," in *Proc. 3rd Intl. Conf. on Applied and Theoretical Computing and Communication Technology (iCATccT)*, 2017, pp. 24–28.

[96] L. Jin *et al.*, "Fault analysis of microgrid and adaptive distance protection based on complex wavelet transform," in *Proc. International Power Electronics and Application Conf. and Exposition*, 2014, pp. 360–364.

[97] T. S. Aghdam, H. K. Karegar, and H. H. Zeineldin, "Variable tripping time differential protection for microgrids considering DG stability," *IEEE Transactions on Smart Grid*, vol. 10, no. 3, pp. 2407–2415, 2018.

[98] B. Satuyeva *et al.*, "Q-learning based protection scheme for microgrid using multi-agent system," in *Proc. International Conference on Smart Energy Systems and Technologies (SEST)*, 2019, pp. 1–6.

[99] H. S. Samkari and B. K. Johnson, "Multi-agent protection scheme for resilient microgrid systems with aggregated electronically coupled distributed energy resources," in *Proc. 44th Annual Conference of the IEEE Industrial Electronics Society (IECON)*, 2018, pp. 752–757.

[100] M. J. Daryani, A. E. Karkevandi, and O. Usta, "Multi-agent approach to wide-area integrated adaptive protection system of microgrid for pre-and post-contingency conditions," in *Proc. IEEE PES Innovative Smart Grid Technologies Conference Europe*, 2018, pp. 1–6.

[101] H. F. Habib *et al.*, "Decentralized multi-agent system for protection and the power restoration process in microgrids," in *Proc. 9th Annual IEEE Green Technologies Conference (GreenTech)*, 2017, pp. 358–364.

[102] H. F. Habib *et al.*, "A multiagent system for simple overcurrent protection of microgrids with distributed generation," in *Proc. IEEE Industry Applications Society Annual Meeting (IAS)*, 2018, pp. 1–8.

[103] S. Ranjbar *et al.*, "Fault detection in microgrids using combined classification algorithms and feature selection methods," in *Proc. Intl. Conf. on Protection and Automation of Power System (IPAPS)*, 2019, pp. 17–21.

[104] S. Kar, S. Samantaray, and M. D. Zadeh, "Data-mining model based intelligent differential microgrid protection scheme," *IEEE Systems Journal*, vol. 11, no. 2, pp. 1161–1169, 2015.

[105] J. Zhao *et al.*, "Power system dynamic state estimation: Motivations, definitions, methodologies, and future work," *IEEE Transactions on Power Systems*, vol. 34, no. 4, pp. 3188–3198, 2019.

[106] A. S. Meliopoulos, G. J. Cokkinides, Z. Tan, S. Choi, Y. Lee, and P. Myrda, "Setting-less protection: Feasibility study," in *Proc. 46th IEEE Hawaii International Conference on System Sciences*, 2013, pp. 2345–2353.

[107] J. Xie, A. P. S. Meliopoulos, and B. Xie, "Transmission line fault classification based on dynamic state estimation and support vector machine," in *Proc. IEEE North American Power Symposium (NAPS)*, 2018, pp. 1–5.

[108] H. F. Albinali and A. P. S. Meliopoulos, "Resilient protection system through centralized substation protection," *IEEE Transactions on Power Delivery*, vol. 33, no. 3, pp. 1418–1427, 2018.

[109] D. Rimorov, Y. Brissette, I. Kamwa, and G. Joós, "Synchrophasor-based state estimation for microgrid protection," in *Proc. IEEE Power & Energy Society General Meeting*, 2018, pp. 1–5.

[110] Y. Cui, R. Kavasseri, and S. Brahma, "Dynamic state estimation assisted posturing for generator out-of-step protection," in *Proc. IEEE Power and Energy Society General Meeting*, 2016, pp. 1–5.

[111] B. Wang, Y. Liu, D. Lu, K. Yue, and R. Fan, "Transmission line fault location in MMC-HVDC grids based on dynamic state estimation and gradient descent," *IEEE Transactions on Power Delivery*, vol. 36, no. 3, pp. 1714–1725, 2020.

[112] Shalini *et al.*, "Enhancing performance of wide-area back-up protection scheme using PMU assisted dynamic state estimator," *IEEE Transctions on Smart Grid*, vol. 10, no. 5, pp. 5066–5074, 2018.

[113] Y. Liu *et al.*, "Dynamic state estimation for power system control and protection," *IEEE Transactions on Power Systems*, vol. 36, no. 6, pp. 5909–5921, 2021.

[114] A. Srivastava, D. Steen, O. Carlson, O. Mansour, D. Bijwaard, *et al.*, "Transmission line protection using dynamic state estimation and advanced sensors: Experimental validation," *in Early Access IEEE Transactions on Power Delivery*, 2022.

[115] B. Wang, Y. Liu, K. Yue, D. Lu, and J. Zhao, "Improved dynamic state estimation based protection on transmission lines in MMC-HVDC grids," *in Early Access IEEE Transactions on Power Delivery*, 2021.

[116] Y. Liu, A. P. S. Meliopoulos, L. Sun, and R. Fan, "Dynamic state estimation based protection of mutually coupled transmission lines," *CSEE Journal of Power and Energy Systems*, vol. 2, no. 4, pp. 6–14, 2016.

[117] Y. Liu, A. P. S. Meliopoulos, Z. Tan, L. Sun, and R. Fan, "Dynamic state estimation-based fault locating on transmission lines," *IET Generation, Transmission & Distribution*, vol. 11, no. 17, pp. 4184–4192, 2017.

[118] R. Fan, Y. Liu, R. Huang, R. Diao, and S. Wang, "Precise fault location on transmission lines using ensemble Kalman filter," *IEEE Transactions on Power Delivery*, vol. 33, no. 6, pp. 3252–3255, 2018.

[119] A. Srivastava, D. Steen, L. A. Tuan, *et al.*, "A DSO support framework for assessment of future-readiness of distribution systems: Technical, market, and policy perspectives," in *Proc. 25th International Conference and Exhibition on Electricity Distribution (CIRED)*, AIM, 2019.

[120] D. Steen, A. Srivastava, L. A. Tuan, *et al.*, "UNITED-GRID D2.1 Baseline description of distribution grid management," 2018.

[121] SmartGrids SRA 2035, *Smartgrids strategic research agenda for RD&D needs towards 2035*.

[122] Energy European Commission, *Market legislation*, [Online] Available: `https://ec.europa.eu/energy/en/topics/markets-and-consumers/marketlegislation`.

[123] Energy European Commission, *Clean energy for all Europeans*, [Online] Available: `https://ec.europa.eu/energy/en/news/clean-energy-package-topagenda-eu-energy-council`.

[124] IVA, "Sweden's future electricity production – a project report," 2017.

[125] T. Tran, M. Damaj, M. Guemri, *et al.*, "UNITED-GRID D2.2 Scenario descriptions for active distribution grid developments," 2019.

[126] Research Institutes of Sweden (RISE), [Online] Available: `https://www.ri.se/en`.

[127] J. Rossi, A. Srivastava, D. Steen, and L. A. Tuan, "Study of the European regulatory framework for smart grid solutions in future distribution systems," in *Proc. CIRED Berlin Workshop*, AIM, 2020.

[128] J. Rossi, A. Srivastava, T. T. Hoang, Q. T. Tran, and M. Warneryd, "Pathways for the development of future intelligent distribution grids," *Energy Policy*, vol. 169, Oct. 2022.

[129] A. Srivastava, D. Steen, L. A. Tuan, *et al.*, "Development of a DSO support tool for congestion forecast," *IET Generation, Transmission & Distribution*, vol. 15, no. 23, pp. 3345–3359, 2021.

[130] The French Alternative Energies and Atomic Energy Commission (CEA), [Online] Available: `http://www.cea.fr/english`.

[131] M. Haque, "Load flow solution of distribution systems with voltage dependent load models," *Electric Power Systems Research*, vol. 36, no. 3, pp. 151–156, 1996.

[132] "IEEE Standard 1547-2018," *IEEE Standard for Interconnection and Interoperability of Distributed Energy Resources with Associated Electric Power Systems Interfaces*, Feb. 2018.

[133] C. S. Cheng and D. Shirmohammadi, "A three-phase power flow method for real-time distribution system analysis," *IEEE Transactions on Power Systems*, vol. 10, no. 2, pp. 671–679, 1995.

[134] UNITED-GRID, [Online] Available: `https://united-grid.eu/`.

[135] H. Khodr *et al.*, "Maximum savings approach for location and sizing of capacitors in distribution systems," *Electric Power Systems Research*, vol. 78, no. 7, pp. 1192–1203, 2008.

[136] P. Balram, L. A. Tuan, and O. Carlson, "Predictive voltage control of batteries and tap changers in distribution system with photovoltaics," in *Proc. IEEE Power Systems Computation Conference*, 2016, pp. 1–7.

[137] Animated Colour-map, [Online] Available: `http://publications.lib.chalmers.se/img/srivastava/`.

[138] Atos, [Online] Available: `https://atos.net/en/`.

[139] Y. H. Lee, "A comprehensive protection scheme for distribution systems," Ph.D. dissertation, Georgia Institute of Technology, Atlanta, USA, 2014.

[140] A. P. Meliopoulos, G. J. Cokkinides, and G. K. Stefopoulos, "Quadratic integration method," in *Proc. Citeseer International Power System Transients Conference (IPST)*, 2005, pp. 19–23.

[141] A. Srivastava, "Towards intelligent distribution systems: Solutions for congestion forecast and dynamic state estimation based protection," Licentiate Thesis, Chalmers University of Technology, 2021.

[142] F. A. M. Vásquez and K. M. Silva, "Instantaneous-power-based busbar numerical differential protection," *IEEE Transactions on Power Delivery*, vol. 34, no. 2, pp. 616–626, 2019.

[143] D. Ritzmann, P. S. Wright, *et al.*, "A method for accurate transmission line impedance parameter estimation," *IEEE Transactions on Instrumentation and Measurement*, vol. 65, no. 10, pp. 2204–2213, 2016.

[144] Smart State Technology, The Netherlands, [Online] Available: `https://www.smartstatetechnology.nl/`.

[145] P. Hintjens, *ZeroMQ: Messaging for Many Applications*. "O'Reilly Media, Inc.", 2013.

[146] H. F. Albinali, A. Meliopoulos, and C. Vournas, "Dynamic state estimation based centralized protection scheme," in *Proc. IEEE Manchester PowerTech*, 2017, pp. 1–6.

[147] A. Hargrave, M. J. Thompson, and B. Heilman, "Beyond the knee point: A practical guide to CT saturation," in *Proc. IEEE 71st Annual Conference for Protective Relay Engineers (CPRE)*, 2018, 1–23.

[148] Y.-C. Kang, S.-H. Ok, and S.-H. Kang, "A CT saturation detection algorithm," *IEEE Transactions on Power Delivery*, vol. 19, no. 1, pp. 78–85, 2004.

[149] A. Hooshyar and M. Sanaye-Pasand, "Accurate measurement of fault currents contaminated with decaying DC offset and CT saturation," *IEEE Transactions on Power Delivery*, vol. 27, no. 2, pp. 773–783, 2012.

[150] P. E. Obikwelu and A. P. S. Meliopoulos, "VT instrumentation channel error correction using dynamic state estimation," in *Proc. IEEE 52nd North American Power Symposium (NAPS)*, 2021, pp. 1–6.

[151] P. E. Obikwelu and A. P. S. Meliopoulos, "CT saturation error correction within merging units using dynamic state estimation," in *Proc. IEEE 3rd International Conference on Renewable Energy and Power Engineering (REPE)*, 2020, pp. 45–50.

[152] S. A. Hosseini, M. Mirzaie, and T. Barforoshi, "Impact of surge arrester number and placement on reliability and lightning overvoltage level in high voltage substations," *International Journal of Electrical Power & Energy Systems*, vol. 65, pp. 146–158, 2015.

[153] B. Kasztenny, "Impact of transformer inrush currents on sensitive protection functions," in *Proc. IEEE Transmission and Distribution Conference and Exhibition*, 2006, pp. 820–823.

[154] S. AsghariGovar and H. Seyedi, "Adaptive CWT-based transmission line differential protection scheme considering cross-country faults and CT saturation," *IET Generation, Transmission & Distribution*, vol. 10, no. 9, pp. 2035–2041, 2016.

[155] H. E. V. Brom *et al.*, "Voltage dependence of the reference system in medium-and high-voltage current transformer calibrations," *IEEE Transactions on Instrumentation and Measurement*, vol. 70, pp. 1–8, 2021.

[156] S. J. Julier and J. K. Uhlmann, "New extension of the Kalman filter to nonlinear systems," in *Proc. ISOP Signal processing, sensor fusion, and target recognition VI*, vol. 3068, 1997, pp. 182–193.

[157] S. Julier and J. K. Uhlmann, "Unscented filtering and nonlinear estimation," *Proceedings of the IEEE*, vol. 92, no. 3, pp. 401–422, 2004.

[158] J. K. Uhlmann, "Simultaneous map building and localization for real time applications," Transfer Thesis, University of Oxford, Oxford, UK, 1994.

[159] A. K. Singh and B. Pal, *Dynamic estimation and control of power systems*. Academic Press, 2018.

[160] R. E. Kalman, "A new approach to linear filtering and prediction problems," *Journal of Fluids Engineering*, vol. 82, no. 1, pp. 35–45, 1960.

[161] I. Markovsky and B. De Moor, "Linear dynamic filtering with noisy input and output," *Automatica*, vol. 41, no. 1, pp. 167–171, 2005.

[162] P. S. Kundur and O. P. Malik, *Power system stability and control*. McGraw-Hill Education, 2022.

[163] C. Zhang *et al.*, "FLECH: A Danish market solution for DSO congestion management through DER flexibility services," *Journal of Modern Power Systems and Clean Energy*, vol. 2, no. 2, pp. 126–133, 2014.

APPENDIX A

Transmission Line Modelling for Dynamic State Estimation based Protection Scheme

The model development of a transmission line (adapted from the model of distribution line developed in [139]) for DSEBPS is explained as follows:

A.1 Quadratic Integration Method

The quadratic integration method is used to reduce the complexity of the component's dynamic model by simplification of the involved differential equations. In this method, the considered function is treated to vary as a quadratic function in comparison to the trapezoidal method where it is considered to vary as a linear function. This method helps in increasing the accuracy of the integration technique [140].

The concept of the quadratic integration method is shown in Figure A.1. Here, an integration time step is taken of length k, between two-time instants $(t-k)$ and t. The corresponding function values are $y(t-k)$ and $y(t)$. Additionally, a time instant $(t-k/2)$ is taken between the above two instants and corresponding function is $y(t-k/2)$. These three-time instants define the quadratic function in the time step of $[t-k, t]$.

The following example will be useful for a better understanding of the quadratic integration method:

$$\frac{dy\,(t)}{dx} = Fy\,(t) \tag{A.1}$$

when the quadratic integration method is applied to (A.1), over the time interval $[t-k, t]$, it yields the following equation:

$$\begin{bmatrix} \frac{k}{24}F & I-\frac{k}{3}F \\ I-\frac{k}{6}F & -\frac{2k}{3}F \end{bmatrix} \begin{bmatrix} y\,(t) \\ y\,(t-k/2) \end{bmatrix} = \begin{bmatrix} I+\frac{5k}{24}F \\ I-\frac{k}{3}F \end{bmatrix} [y\,(t-k)] \tag{A.2}$$

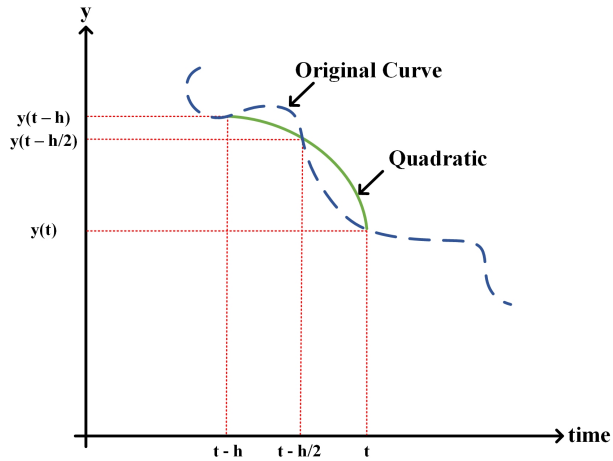

Figure A.1: Quadratic integration method.

A.2 Algebraic Quadratic Companion Form Model

This section presents the AQCF model for a transmission line which is based on the quadratic integration method. The presented model is for a three-phase line and represents one π- section [139].

The schematic of the π-representation of a three-phase transmission line is presented in Figure A.2. In the presented schematic, the line has three phases A, B, and C. The resistances

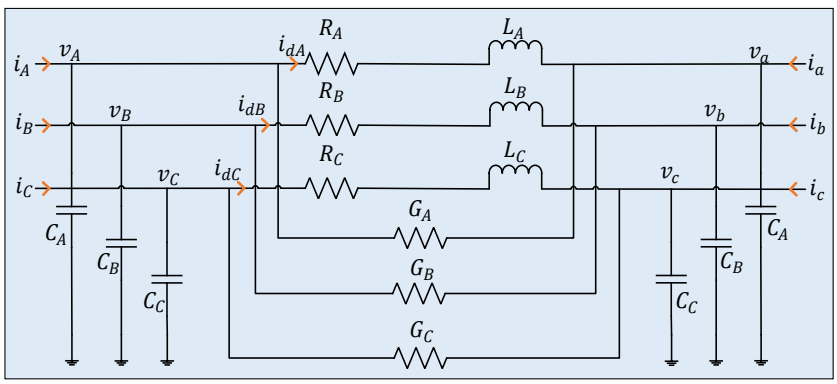

Figure A.2: Schematic of a three-phase transmission line.

and reactances of each phase are represented as (R_A, R_B, R_C) and (L_A, L_B, L_C), respectively. The shunt capacitances for each phase are represented as (C_A, C_B, C_C). Also, (G_A, G_B, G_C) are considered for the numerical stabilization purpose and may not be essentially part of actual system. The sending end voltages and currents are represented as (v_A, v_B, v_C) and (i_A, i_B, i_C), respectively, while the receiving end voltages and currents are represented as (v_a, v_b, v_c) and (i_a, i_b, i_c), respectively. Also, (i_{dA}, i_{dB}, i_{dC}) are the currents in the series branch of the three phases of the transmission line. The model equations using the KVL and KCL for the network diagram shown above can be written as:

$$i_A + G_A v_a = i_{dA} + G_A v_A + C_A \frac{dv_A}{dt} \tag{A.3}$$

$$i_B + G_B v_b = i_{dB} + G_B v_B + C_B \frac{dv_B}{dt} \tag{A.4}$$

$$i_C + G_C v_c = i_{dC} + G_C v_C + C_C \frac{dv_C}{dt} \tag{A.5}$$

$$i_a - G_A v_a - C_A \frac{dv_a}{dt} = -i_{dA} - G_A v_A \tag{A.6}$$

$$i_b - G_B v_b - C_B \frac{dv_b}{dt} = -i_{dB} - G_B v_B \tag{A.7}$$

$$i_c - G_C v_c - C_C \frac{dv_c}{dt} = -i_{dC} - G_C v_C \tag{A.8}$$

$$v_a = v_A - R_A i_{dA} - L_A \frac{di_{dA}}{dt} \tag{A.9}$$

$$v_b = v_B - R_B i_{dB} - L_B \frac{di_{dB}}{dt} \tag{A.10}$$

$$v_c = v_C - R_C i_{dC} - L_C \frac{di_{dC}}{dt} \tag{A.11}$$

The above equations (A.3)−(A.11), can be further written as:

$$R_1 z + R_2 \frac{dz}{dt} = S_1 x + S_2 \frac{dx}{dt} \tag{A.12}$$

where z is the measurement vector which is a function of time and can be expressed as:

$$z = [i_A \quad i_B \quad i_C \quad i_a \quad i_b \quad i_c \quad v_a \quad v_b \quad v_c] \tag{A.13}$$

x is the estimation vector which is a function of time and can be expressed as:

$$x = [v_A \quad v_B \quad v_C \quad i_{dA} \quad i_{dB} \quad i_{dC}] \tag{A.14}$$

and matrices R_1, R_2, S_1 and S_2 can be expressed as:

$$R_1 = \begin{bmatrix} 1&0&0&0&0&0 & G_A & 0 & 0 \\ 0&1&0&0&0&0 & 0 & G_B & 0 \\ 0&0&1&0&0&0 & 0 & 0 & G_C \\ 0&0&0&1&0&0 & -G_A & 0 & 0 \\ 0&0&0&0&1&0 & 0 & -G_B & 0 \\ 0&0&0&0&0&1 & 0 & 0 & -G_C \\ 0&0&0&0&0&0 & 1 & 0 & 0 \\ 0&0&0&0&0&0 & 0 & 1 & 0 \\ 0&0&0&0&0&0 & 0 & 0 & 1 \end{bmatrix}, \; R_2 = \begin{bmatrix} 0&0&0&0&0&0 & 0 & 0 & 0 \\ 0&0&0&0&0&0 & 0 & 0 & 0 \\ 0&0&0&0&0&0 & 0 & 0 & 0 \\ 0&0&0&0&0&0 & -C_A & 0 & 0 \\ 0&0&0&0&0&0 & 0 & -C_B & 0 \\ 0&0&0&0&0&0 & 0 & 0 & -C_C \\ 0&0&0&0&0&0 & 0 & 0 & 0 \\ 0&0&0&0&0&0 & 0 & 0 & 0 \\ 0&0&0&0&0&0 & 0 & 0 & 0 \end{bmatrix}$$

$$S_1 = \begin{bmatrix} G_A & 0 & 0 & 1 & 0 & 0 \\ 0 & G_B & 0 & 0 & 1 & 0 \\ 0 & 0 & G_C & 0 & 0 & 1 \\ -G_A & 0 & 0 & -1 & 0 & 0 \\ 0 & -G_B & 0 & 0 & -1 & 0 \\ 0 & 0 & -G_C & 0 & 0 & -1 \\ 1 & 0 & 0 & -R_A & 0 & 0 \\ 0 & 1 & 0 & 0 & -R_B & 0 \\ 0 & 0 & 1 & 0 & 0 & -R_C \end{bmatrix}, S_2 = \begin{bmatrix} C_A & 0 & 0 & 0 & 0 & 0 \\ 0 & C_B & 0 & 0 & 0 & 0 \\ 0 & 0 & C_C & 0 & 0 & 0 \\ 0 & 0 & 0 & 0 & 0 & 0 \\ 0 & 0 & 0 & 0 & 0 & 0 \\ 0 & 0 & 0 & 0 & 0 & 0 \\ 0 & 0 & 0 & -L_A & 0 & 0 \\ 0 & 0 & 0 & 0 & -L_B & 0 \\ 0 & 0 & 0 & 0 & 0 & -L_C \end{bmatrix}$$

Subsequently, quadratic integration method as derived in (A.1) and (A.2) is used for the equation derived in (A.12), which results in the following equations:

Over the time interval $[t-k, t]$

$$R_1\left[\frac{k}{6}z(t-k)+\frac{2k}{3}z\left(t-\frac{k}{2}\right)+\frac{k}{6}z(t)\right]+R_2\left[z(t)-z(t-k)\right] = S_1\left[\frac{k}{6}x(t-k)+\frac{2k}{3}x\left(t-\frac{k}{2}\right)+\frac{k}{6}x(t)\right]+S_2\left[x(t)-x(t-k)\right] \quad \text{(A.15)}$$

Over the time interval $[t-k, t-k/2]$

$$R_1\left[\frac{5k}{24}z(t-k)+\frac{k}{3}z\left(t-\frac{k}{2}\right)-\frac{k}{24}z(t)\right]+R_2\left[z\left(t-\frac{k}{2}\right)-z(t-k)\right] = S_1\left[\frac{5k}{24}x(t-k)+\frac{k}{3}x\left(t-\frac{k}{2}\right)-\frac{k}{24}x(t)\right]+S_2\left[x\left(t-\frac{k}{2}\right)-x(t-k)\right] \quad \text{(A.16)}$$

The above equations (A.15) and (A.16) can be written down in condensed form as follows:

$$\begin{bmatrix} \frac{k}{6}R_1+R_2 & \frac{2k}{3}R_1 \\ -\frac{k}{24}R_1 & \frac{k}{3}R_1+R_2 \end{bmatrix}\begin{bmatrix} z(t) \\ z\left(t-\frac{k}{2}\right) \end{bmatrix} = \begin{bmatrix} \frac{k}{6}S_1+S_2 & \frac{2k}{3}S_1 \\ -\frac{k}{24}S_1 & \frac{k}{3}S_1+S_2 \end{bmatrix}\begin{bmatrix} x(t) \\ x\left(t-\frac{k}{2}\right) \end{bmatrix} - \begin{bmatrix} \frac{k}{6}R_1-R_2 \\ \frac{5k}{24}R_1-R_2 \end{bmatrix}\left[z(t-k)\right] - \begin{bmatrix} -\frac{k}{6}S_1+S_2 \\ -\frac{5k}{24}S_1+S_2 \end{bmatrix}\left[x(t-k)\right] \quad \text{(A.17)}$$

$$H_1\begin{bmatrix} z(t) \\ z\left(t-\frac{k}{2}\right) \end{bmatrix} = H_2\begin{bmatrix} x(t) \\ x\left(t-\frac{k}{2}\right) \end{bmatrix} - H_3\left[z(t-k)\right] - H_4\left[x(t-k)\right] \quad \text{(A.18)}$$

where H_1, H_2, H_3, and H_4 are the coefficient matrices defined as follows.

$$H_1 = \begin{bmatrix} \frac{k}{6}R_1+R_2 & \frac{2k}{3}R_1 \\ -\frac{k}{24}R_1 & \frac{k}{3}R_1+R_2 \end{bmatrix}, H_2 = \begin{bmatrix} \frac{k}{6}S_1+S_2 & \frac{2k}{3}S_1 \\ -\frac{k}{24}S_1 & \frac{k}{3}S_1+S_2 \end{bmatrix}$$

$$H_3 = \begin{bmatrix} \frac{k}{6}R_1 - R_2 \\ \frac{5k}{24}R_1 - R_2 \end{bmatrix}, H_4 = \begin{bmatrix} -\frac{k}{6}S_1 + S_2 \\ -\frac{5k}{24}S_1 + S_2 \end{bmatrix}$$

A.3 Algebraic Quadratic Companion Form Model with Consideration of Inter-phase Mutual Coupling

Consider the schematic of a π-section for a three-phase transmission line with inter-phase mutual coupling as presented in Figure A.3. In the presented schematic, the line has three phases A, B, and C. The self-resistances and self-reactances of each phase are represented as R_{AA}, R_{BB}, R_{CC} and L_{AA}, L_{BB}, L_{CC}, respectively. The shunt self-capacitances for each phase are represented as C_{AA}, C_{BB}, C_{CC}. However, G_A, G_B, G_C are not considered for the purpose of simplicity as they are mainly used for numerical stabilization purposes. The mutual resistances, reactances, and shunt capacitance between the different phases are also taken into consideration and are represented by the subscript with the name of the connected phases.

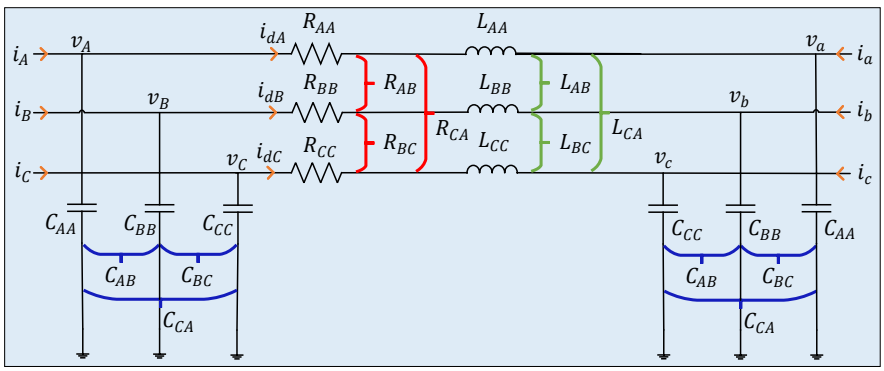

Figure A.3: Schematic of a three-phase transmission line with inter-phase mutual coupling.

The sending end voltages and currents are represented as v_A, v_B, v_C, and i_A, i_B, i_C, respectively, while the receiving end voltages and currents are represented as v_a, v_b, v_c and i_a, i_b, i_c, respectively. Also, i_{dA}, i_{dB}, i_{dC} are the currents in the series branch of the three phases of the line. The model equations using the KVL and KCL for the network diagram shown in Figure A.3 can be written as:

$$i_A = i_{dA} + C_{AA}\frac{dv_A}{dt} + C_{AB}\frac{dv_B}{dt} + C_{AC}\frac{dv_C}{dt} \tag{A.19}$$

$$i_B = i_{dB} + C_{BA}\frac{dv_A}{dt} + C_{BB}\frac{dv_B}{dt} + C_{BC}\frac{dv_C}{dt} \tag{A.20}$$

$$i_C = i_{dC} + C_{CA}\frac{dv_A}{dt} + C_{CB}\frac{dv_B}{dt} + C_{CC}\frac{dv_C}{dt} \tag{A.21}$$

$$i_a - C_{AA}\frac{dv_a}{dt} - C_{AB}\frac{dv_b}{dt} - C_{AC}\frac{dv_c}{dt} = -i_{dA} \tag{A.22}$$

$$i_b - C_{BA}\frac{dv_a}{dt} - C_{BB}\frac{dv_b}{dt} - C_{BC}\frac{dv_c}{dt} = -i_{dB} \tag{A.23}$$

$$i_c - C_{CA}\frac{dv_a}{dt} - C_{CB}\frac{dv_b}{dt} - C_{CC}\frac{dv_c}{dt} = -i_{dC} \tag{A.24}$$

$$v_a = v_A - R_{AA}i_{dA} - L_{AA}\frac{di_{dA}}{dt} - R_{AB}i_{dB} - L_{AB}\frac{di_{dB}}{dt} - R_{AC}i_{dC} - L_{AC}\frac{di_{dC}}{dt} \tag{A.25}$$

$$v_b = v_B - R_{BA}i_{dA} - L_{BA}\frac{di_{dA}}{dt} - R_{BB}i_{dB} - L_{BB}\frac{di_{dB}}{dt} - R_{BC}i_{dC} - L_{BC}\frac{di_{dC}}{dt} \tag{A.26}$$

$$v_c = v_C - R_{CA}i_{dA} - L_{CA}\frac{di_{dA}}{dt} - R_{CB}i_{dB} - L_{CB}\frac{di_{dB}}{dt} - R_{CC}i_{dC} - L_{CC}\frac{di_{dC}}{dt} \tag{A.27}$$

The above equations (A.19)−(A.27), can be further written as:

$$R_1 z + R_2\frac{dz}{dt} = S_1 x + S_2\frac{dx}{dt} \tag{A.28}$$

where z is the measurement vector which is a function of time and can be expressed as:

$$z = [i_A \quad i_B \quad i_C \quad i_a \quad i_b \quad i_c \quad v_a \quad v_b \quad v_c]$$

x is the estimation vector which is a function of time and can be expressed as:

$$x = [v_A \quad v_B \quad v_C \quad i_{dA} \quad i_{dB} \quad i_{dC}]$$

and matrices R_1, R_2, S_1 and S_2 can be expressed as:

$$R_1 = \begin{bmatrix} 1&0&0&0&0&0&0&0&0&0\\ 0&1&0&0&0&0&0&0&0&0\\ 0&0&1&0&0&0&0&0&0&0\\ 0&0&0&1&0&0&0&0&0&0\\ 0&0&0&0&1&0&0&0&0&0\\ 0&0&0&0&0&1&0&0&0&0\\ 0&0&0&0&0&0&1&0&0&0\\ 0&0&0&0&0&0&0&1&0&0\\ 0&0&0&0&0&0&0&0&1&0\\ 0&0&0&0&0&0&0&0&0&1 \end{bmatrix}, \; R_2 = \begin{bmatrix} 0&0&0&0&0&0 & 0 & 0 & 0\\ 0&0&0&0&0&0 & 0 & 0 & 0\\ 0&0&0&0&0&0 & 0 & 0 & 0\\ 0&0&0&0&0&0 & -C_{AA} & -C_{AB} & -C_{AC}\\ 0&0&0&0&0&0 & -C_{BA} & -C_{BB} & -C_{BC}\\ 0&0&0&0&0&0 & -C_{CA} & -C_{CB} & -C_{CC}\\ 0&0&0&0&0&0 & 0 & 0 & 0\\ 0&0&0&0&0&0 & 0 & 0 & 0\\ 0&0&0&0&0&0 & 0 & 0 & 0 \end{bmatrix}$$

$$S_1 = \begin{bmatrix} 0&0&0 & 1 & 0 & 0\\ 0&0&0 & 0 & 1 & 0\\ 0&0&0 & 0 & 0 & 1\\ 0&0&0 & -1 & 0 & 0\\ 0&0&0 & 0 & -1 & 0\\ 0&0&0 & 0 & 0 & -1\\ 1&0&0 & -R_{AA} & -R_{AB} & -R_{AC}\\ 0&1&0 & -R_{BA} & -R_{BB} & -R_{BC}\\ 0&0&1 & -R_{CA} & -R_{CB} & -R_{CC} \end{bmatrix}, \; S_2 = \begin{bmatrix} C_{AA} & C_{AB} & C_{AC} & 0 & 0 & 0\\ C_{BA} & C_{BB} & C_{BC} & 0 & 0 & 0\\ C_{CA} & C_{CB} & C_{CC} & 0 & 0 & 0\\ 0 & 0 & 0 & 0 & 0 & 0\\ 0 & 0 & 0 & 0 & 0 & 0\\ 0 & 0 & 0 & 0 & 0 & 0\\ 0 & 0 & 0 & -L_{AA} & -L_{AB} & -L_{AC}\\ 0 & 0 & 0 & -L_{BA} & -L_{BB} & -L_{BC}\\ 0 & 0 & 0 & -L_{CA} & -L_{CB} & -L_{CC} \end{bmatrix}$$

Subsequently, the quadratic integration method is applied and the rest of the procedure for DSEBPS remains the same as mentioned in Section A.2. The above procedure is followed for the consideration of inter-phase mutual coupling in a transmission line.

A.4 Algebraic Quadratic Companion Form Model during Infeed Condition

Consider a single phase representation of the transmission line in the case of the infeed condition as presented in Figure A.4. The transmission line has three phases A, B, and C. The resistances and reactances of the transmission line before the tapping point are represented as R_A, R_B, R_C, and L_A, L_B, L_C, respectively. The shunt capacitances of the transmission line before the tapping point are represented as C_A, C_B, C_C, while, the resistances and reactances of the transmission line after the tapping point are represented as R_{A1}, R_{B1}, R_{C1}, and L_{A1}, L_{B1}, L_{C1}, respectively. The shunt capacitances of the transmission line before the tapping point are represented as C_{A1}, C_{B1}, C_{C1}. Also, G_A, G_B, G_C, G_{A1}, G_{B1}, G_{C1} are considered for the numerical stabilization purpose and may not be essentially part of actual system. The sending end voltages and currents before the tapping point are represented as v_A, v_B, v_C, and i_A, i_B, i_C, respectively. The receiving end voltages and currents before the tapping point are represented as v_a, v_b, v_c, and i_a, i_b, i_c, respectively. Also, i_{dA}, i_{dB}, i_{dC}, are the currents in the series branch before the tapping point. While, the sending end voltages and currents after the tapping point are represented as v_{A1}, v_{B1}, v_{C1}, and i_{A1}, i_{B1}, i_{C1}, respectively. The receiving end voltages and currents after the tapping point are represented as v_{a1}, v_{b1}, v_{c1}, and i_{a1}, i_{b1}, i_{c1}, respectively. Also, i_{dA1}, i_{dB1}, i_{dC1}, are the currents in the series branch after the tapping point. The model equations using the KVL and KCL for the network diagram shown above can be written as:

$$i_A + G_A v_a = i_{dA} + G_A v_A + C_A \frac{dv_A}{dt} \tag{A.29}$$

$$i_B + G_B v_b = i_{dB} + G_B v_B + C_B \frac{dv_B}{dt} \tag{A.30}$$

$$i_C + G_C v_c = i_{dC} + G_C v_C + C_C \frac{dv_C}{dt} \tag{A.31}$$

$$i_a - G_A v_a - C_A \frac{dv_a}{dt} = -i_{dA} - G_A v_A \tag{A.32}$$

$$i_b - G_B v_b - C_B \frac{dv_b}{dt} = -i_{dB} - G_B v_B \tag{A.33}$$

$$i_c - G_C v_c - C_C \frac{dv_c}{dt} = -i_{dC} - G_C v_C \tag{A.34}$$

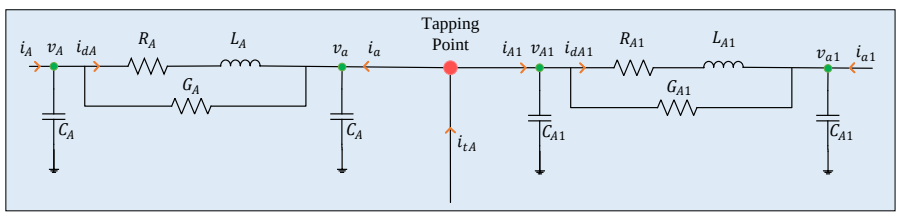

Figure A.4: Single phase representation of the transmission line in the case of the infeed condition.

$$v_a = v_A - R_A i_{dA} - L_A \frac{di_{dA}}{dt} \tag{A.35}$$

$$v_b = v_B - R_B i_{dB} - L_B \frac{di_{dB}}{dt} \tag{A.36}$$

$$v_c = v_C - R_C i_{dC} - L_C \frac{di_{dC}}{dt} \tag{A.37}$$

$$i_{A1} + G_{A1} v_{a1} = i_{dA1} + G_{A1} v_{A1} + C_{A1} \frac{dv_{A1}}{dt} \tag{A.38}$$

$$i_{B1} + G_{B1} v_{b1} = i_{dB1} + G_{B1} v_{B1} + C_{B1} \frac{dv_{B1}}{dt} \tag{A.39}$$

$$i_{C1} + G_{C1} v_{c1} = i_{dC1} + G_{C1} v_{C1} + C_{C1} \frac{dv_{C1}}{dt} \tag{A.40}$$

$$i_{a1} - G_{A1} v_{a1} - C_{A1} \frac{dv_{a1}}{dt} = -i_{dA1} - G_{A1} v_{A1} \tag{A.41}$$

$$i_{b1} - G_{B1} v_{b1} - C_{B1} \frac{dv_{b1}}{dt} = -i_{dB1} - G_{B1} v_{B1} \tag{A.42}$$

$$i_{c1} - G_{C1} v_{c1} - C_{C1} \frac{dv_{c1}}{dt} = -i_{dC1} - G_{C1} v_{C1} \tag{A.43}$$

$$v_{a1} = v_{A1} - R_{A1} i_{dA1} - L_{A1} \frac{di_{dA1}}{dt} \tag{A.44}$$

$$v_{b1} = v_{B1} - R_{B1} i_{dB1} - L_{B1} \frac{di_{dB1}}{dt} \tag{A.45}$$

$$v_{c1} = v_{C1} - R_{C1} i_{dC1} - L_{C1} \frac{di_{dC1}}{dt} \tag{A.46}$$

$$-i_{tA} + i_a + i_{A1} = 0 \tag{A.47}$$

$$-i_{tB} + i_b + i_{B1} = 0 \tag{A.48}$$

$$-i_{tC} + i_c + i_{C1} = 0 \tag{A.49}$$

The above equations (A.29)−(A.49), can be further written as:

$$R_1 z + R_2 \frac{dz}{dt} = S_1 x + S_2 \frac{dx}{dt} \tag{A.50}$$

where, z is the measurement vector which is a function of time and can be expressed as:

$$z = [i_A \;\; i_B \;\; i_C \;\; i_a \;\; i_b \;\; i_c \;\; v_a \;\; v_b \;\; v_c \;\; i_{A1} \;\; i_{B1} \;\; i_{C1} \;\; i_{a1} \;\; i_{b1} \;\; i_{c1} \;\; v_{a1} \;\; v_{b1} \;\; v_{c1}] \tag{A.51}$$

x is the estimation vector which is a function of time and can be expressed as:

$$x = [v_A \;\; v_B \;\; v_C \;\; i_{dA} \;\; i_{dB} \;\; i_{dC} \;\; v_{A1} \;\; v_{B1} \;\; v_{C1} \;\; i_{dA1} \;\; i_{dB1} \;\; i_{dC1}] \tag{A.52}$$

and matrices R_1, R_2, S_1 and S_2 can be expressed as:

$$R_1 = \begin{bmatrix}
1&0&0&0&0&0&G_A&0&0&0&0&0&0&0&0&0&0&0&0\\
0&1&0&0&0&0&0&G_B&0&0&0&0&0&0&0&0&0&0&0\\
0&0&1&0&0&0&0&0&G_C&0&0&0&0&0&0&0&0&0&0\\
0&0&0&1&0&0&-G_A&0&0&0&0&0&0&0&0&0&0&0&0\\
0&0&0&0&1&0&0&-G_B&0&0&0&0&0&0&0&0&0&0&0\\
0&0&0&0&0&1&0&0&-G_C&0&0&0&0&0&0&0&0&0&0\\
0&0&0&0&0&0&1&0&0&0&0&0&0&0&0&0&0&0&0\\
0&0&0&0&0&0&0&1&0&0&0&0&0&0&0&0&0&0&0\\
0&0&0&0&0&0&0&0&1&0&0&0&0&0&0&0&0&0&0\\
0&0&0&0&0&0&0&0&0&1&0&0&0&0&G_{A1}&0&0&0&0\\
0&0&0&0&0&0&0&0&0&0&1&0&0&0&0&G_{B1}&0&0&0\\
0&0&0&0&0&0&0&0&0&0&0&1&0&0&0&0&G_{C1}&0&0\\
0&0&0&0&0&0&0&0&0&0&0&0&1&0&-G_{A1}&0&0&0&0\\
0&0&0&0&0&0&0&0&0&0&0&0&0&1&0&-G_{B1}&0&0&0\\
0&0&0&0&0&0&0&0&0&0&0&0&0&0&1&0&-G_{C1}&0&0\\
0&0&0&0&0&0&0&0&0&0&0&0&0&0&0&1&0&0&0\\
0&0&0&0&0&0&0&0&0&0&0&0&0&0&0&0&1&0&0\\
0&0&0&0&0&0&0&0&0&0&0&0&0&0&0&0&0&1&0\\
0&0&0&0&0&0&0&0&0&0&0&0&0&0&0&0&0&0&1
\end{bmatrix}$$

$$R_2 = \begin{bmatrix}
0&0&0&0&0&0&0&0&0&0&0&0&0&0&0&0&0&0&0\\
0&0&0&0&0&0&0&0&0&0&0&0&0&0&0&0&0&0&0\\
0&0&0&0&0&0&0&0&0&0&0&0&0&0&0&0&0&0&0\\
0&0&0&0&0&0&-C_A&0&0&0&0&0&0&0&0&0&0&0&0\\
0&0&0&0&0&0&0&-C_B&0&0&0&0&0&0&0&0&0&0&0\\
0&0&0&0&0&0&0&0&-C_C&0&0&0&0&0&0&0&0&0&0\\
0&0&0&0&0&0&0&0&0&0&0&0&0&0&0&0&0&0&0\\
0&0&0&0&0&0&0&0&0&0&0&0&0&0&0&0&0&0&0\\
0&0&0&0&0&0&0&0&0&0&0&0&0&0&0&0&0&0&0\\
0&0&0&0&0&0&0&0&0&0&0&0&0&0&0&0&0&0&0\\
0&0&0&0&0&0&0&0&0&0&0&0&0&0&0&0&0&0&0\\
0&0&0&0&0&0&0&0&0&0&0&0&0&0&0&0&0&0&0\\
0&0&0&0&0&0&0&0&0&0&0&0&0&0&-C_{A1}&0&0&0&0\\
0&0&0&0&0&0&0&0&0&0&0&0&0&0&0&-C_{B1}&0&0&0\\
0&0&0&0&0&0&0&0&0&0&0&0&0&0&0&0&-C_{C1}&0&0\\
0&0&0&0&0&0&0&0&0&0&0&0&0&0&0&0&0&0&0\\
0&0&0&0&0&0&0&0&0&0&0&0&0&0&0&0&0&0&0\\
0&0&0&0&0&0&0&0&0&0&0&0&0&0&0&0&0&0&0\\
0&0&0&0&0&0&0&0&0&0&0&0&0&0&0&0&0&0&0\\
0&0&0&0&0&0&0&0&0&0&0&0&0&0&0&0&0&0&0
\end{bmatrix}$$

$$S_1 = \begin{bmatrix}
G_A&0&0&1&0&0&0&0&0&0&0&0\\
0&G_B&0&0&1&0&0&0&0&0&0&0\\
0&0&G_C&0&0&1&0&0&0&0&0&0\\
-G_A&0&0&-1&0&0&0&0&0&0&0&0\\
0&-G_B&0&0&-1&0&0&0&0&0&0&0\\
0&0&-G_C&0&0&-1&0&0&0&0&0&0\\
1&0&0&-R_A&0&0&0&0&0&0&0&0\\
0&1&0&0&-R_B&0&0&0&0&0&0&0\\
0&0&1&0&0&-R_C&0&0&0&0&0&0\\
0&0&0&0&0&0&G_{A1}&0&0&1&0&0\\
0&0&0&0&0&0&0&G_{B1}&0&0&1&0\\
0&0&0&0&0&0&0&0&G_{C1}&0&0&1\\
0&0&0&0&0&0&-G_{A1}&0&0&-1&0&0\\
0&0&0&0&0&0&0&-G_{B1}&0&0&-1&0\\
0&0&0&0&0&0&0&0&-G_{C1}&0&0&-1\\
0&0&0&0&0&0&1&0&0&-R_{A1}&0&0\\
0&0&0&0&0&0&0&1&0&0&-R_{B1}&0\\
0&0&0&0&0&0&0&0&1&0&0&-R_{C1}\\
0&0&0&0&0&0&0&0&0&0&0&0\\
0&0&0&0&0&0&0&0&0&0&0&0\\
0&0&0&0&0&0&0&0&0&0&0&0
\end{bmatrix}$$

$$S_2 = \begin{bmatrix}
C_A & 0 & 0 & 0 & 0 & 0 & 0 & 0 & 0 & 0 & 0 & 0 \\
0 & C_B & 0 & 0 & 0 & 0 & 0 & 0 & 0 & 0 & 0 & 0 \\
0 & 0 & C_C & 0 & 0 & 0 & 0 & 0 & 0 & 0 & 0 & 0 \\
0 & 0 & 0 & 0 & 0 & 0 & 0 & 0 & 0 & 0 & 0 & 0 \\
0 & 0 & 0 & 0 & 0 & 0 & 0 & 0 & 0 & 0 & 0 & 0 \\
0 & 0 & 0 & 0 & 0 & 0 & 0 & 0 & 0 & 0 & 0 & 0 \\
0 & 0 & 0 & -L_A & 0 & 0 & 0 & 0 & 0 & 0 & 0 & 0 \\
0 & 0 & 0 & 0 & -L_B & 0 & 0 & 0 & 0 & 0 & 0 & 0 \\
0 & 0 & 0 & 0 & 0 & -L_C & 0 & 0 & 0 & 0 & 0 & 0 \\
0 & 0 & 0 & 0 & 0 & 0 & C_{A1} & 0 & 0 & 0 & 0 & 0 \\
0 & 0 & 0 & 0 & 0 & 0 & 0 & C_{B1} & 0 & 0 & 0 & 0 \\
0 & 0 & 0 & 0 & 0 & 0 & 0 & 0 & C_{C1} & 0 & 0 & 0 \\
0 & 0 & 0 & 0 & 0 & 0 & 0 & 0 & 0 & 0 & 0 & 0 \\
0 & 0 & 0 & 0 & 0 & 0 & 0 & 0 & 0 & 0 & 0 & 0 \\
0 & 0 & 0 & 0 & 0 & 0 & 0 & 0 & 0 & 0 & 0 & 0 \\
0 & 0 & 0 & 0 & 0 & 0 & 0 & 0 & 0 & -L_{A1} & 0 & 0 \\
0 & 0 & 0 & 0 & 0 & 0 & 0 & 0 & 0 & 0 & -L_{B1} & 0 \\
0 & 0 & 0 & 0 & 0 & 0 & 0 & 0 & 0 & 0 & 0 & -L_{C1} \\
0 & 0 & 0 & 0 & 0 & 0 & 0 & 0 & 0 & 0 & 0 & 0 \\
0 & 0 & 0 & 0 & 0 & 0 & 0 & 0 & 0 & 0 & 0 & 0 \\
0 & 0 & 0 & 0 & 0 & 0 & 0 & 0 & 0 & 0 & 0 & 0
\end{bmatrix}$$

Subsequently, the quadratic integration method is applied and the rest of the procedure for DSEBPS remains the same as mentioned in Section A.2. The above procedure is followed during the infeed condition in a transmission line.

APPENDIX B

Network Parameters of 7-bus Feeder in Sorea's Distribution System

The branches and transformers data for the part of Sorea's system are presented in Table B.1. The branches have different lengths with the same per unit-length parameters. The branches' ampacity and the transformer rating are also given.

Table B.1: Branches and Transformer Parameters for Sorea's Grid

Sl. No.	**Location**	**Resistance** (mΩ)	**Reactance** (mΩ)	**Susceptance** (μS)	**Capacity** (kVA/Amp)
		Transformer (LV-side)			
1	1-2	3.0637	14.9269	-	250
		Branches			
2	2-3	9.4350	13.2418	0.1319	350
3	3-4	21.6376	30.3679	0.3026	350
4	4-5	23.2679	5.0894	0.1847	350
5	4-6	27.2495	4.4271	0	350
6	4-7	7.5420	4.1469	0.1150	350

APPENDIX C

Abstracts of Published/Submitted Papers

The abstracts of all the published/submitted papers which are listed in Section 1.6 are presented here.

[A] **A. Srivastava**, L. A. Tuan, D. Steen, O. Carlson, O. Mansour, D. Bijwaard, "Transmission line protection using dynamic state estimation and advanced sensors: Experimental validation," *in Early Access, IEEE Transactions on Power Delivery*, 2022. **DOI**: https://doi.org/10.1109/tpwrd.2022.3184479.

This paper presents the experimental validation of a protection scheme for a transmission line based on dynamic state estimation along with the practical application of advanced sensors in this protection scheme. The scheme performs dynamic state estimation with high-frequency measurements provided by the sensors, assesses the operating condition (i.e., health) of the transmission line in real-time, and thereby determines the tripping signal whenever a fault is detected. The validation was carried out in two steps, first with simulation studies for a three-phase fault and then with the experimental implementation using a physical scaled-down model of a power system consisting of transmission lines, transformers, and loads. The simulation and validation results have shown that the scheme performs adequately in both normal and fault conditions. In the fault case with the experimental setup, the scheme could correctly detect the fault and send the trip signal to the line's circuit breakers with a total fault clearing time of approximately 65 milliseconds which is comparable to conventional protection methods. The average processing time for a measurement sample block is 12.5 milliseconds. The results demonstrate that this scheme and the sensors would work for transmission line protection which can avoid relay coordination and settings issues.

[B] **A. Srivastava**, D. Steen, L. A. Tuan, O. Carlson, I. Bouloumpasis, Q. T. Tran, L. Lemius, "Development of a DSO support tool for congestion forecast," *IET Generation, Transmission & Distribution*, vol. 15, no. 23, pp. 3345-3359, Aug. 2021. **DOI**: https://doi.org/10.1049/gtd2.12266.

This paper presents a novel DSO support tool with visualisation capability for forecasting network congestion in distribution systems with a high level of renewables. To incorporate the uncertainties in the distribution systems, the probabilistic power flow framework has been utilised. An advanced photovoltaic production forecast based on sky images and a load forecast using an artificial neural network is used as the input to the tool. In addition, advanced load models and operating modes of photovoltaic inverters have been incorporated into the tool. The tool has been applied in case studies to perform congestion forecasts for two real distribution systems to validate its usability and scalability. The results from case studies demonstrated that the tool performs satisfactorily for both small and large networks and is able to visualise the cumulative probabilities of nodes voltage deviation and network components (branches and transformers) congestion for a variety of forecast horizons as desired by the DSO. The results have also shown that explicit inclusion of load-voltage dependency models would improve the accuracy of the congestion forecast. For demonstrating the applicability of the tool, it has been integrated into an existing distribution management system via the IoT platform of a DMS vendor, Atos Worldgrid.

[C] J. Rossi, **A. Srivastava**, T. T. Hoang, Q. T. Tran, M. Warneryd, "Pathways for the development of future intelligent distribution grids," *Energy Policy*, vol. 169, Oct. 2022. **DOI**: https://doi.org/10.1016/j.enpol.2022.113140.

The next decade will bring several technical and organisational challenges to the electrical distribution grids, which are becoming an important pillar of the energy transition. Distribution system operators will play a crucial role and thus need to find innovative solutions that will prepare them for these changes. Acknowledging large differences between European distribution grids, this paper presents pathways for distribution system operators developed within the scope of the UNITED-GRID project, in close cooperation with distribution grids in the Netherlands, France and Sweden. Investment decision tools based on future scenarios and future-readiness assessment form the first step to steer the distribution system operators towards the necessary technical and digital innovations that increase the observability and controllability of the grid. Secondly, new types of business models are introduced that can be integrated into the operators' portfolios. Thirdly, a workshop methodology is proposed to define the new internal requirements that make distribution system operators more agile to face the fast impacts of the energy transition. Case studies from the demonstration sites in the three countries are used as examples in the paper.

[D] **A. Srivastava**, L. A. Tuan, D. Steen, O. Carlson, O. Mansour, D. Bijwaard, "Dynamic State Estimation based Transmission Line Protection Scheme: Extended Experimental Validation with Different Fault Types and Conditions," *in Revision, International Journal of Electrical Power & Energy Systems*, June 2022.

This paper presents the experimental validation of a transmission line protection scheme based on dynamic state estimation for different fault types and conditions. The protection scheme utilizes real-time high frequency sampled measurements from

advanced sensors and evaluates the operating condition of the transmission line based on which a tripping signal is generated in case a fault occurs. The validation is performed using a physical scaled-down model of a power system, consisting of a transmission line, transformer, synchronous generator, and loads. The following faults are examined during the validation: unbalanced faults under different load conditions, high impedance fault, fault current fed from both ends, hidden failure, external fault, and load change conditions. The results show that the scheme performs as intended and thus proves its efficacy to detect various types of faults. The maximum fault detection time is calculated to be 42.5 milliseconds, while the maximum fault clearing time comes out to be 82.5 milliseconds, on par with currently employed protection methods. The obtained results demonstrate the ability of the scheme to detect different fault types under varying conditions and avoid potential issues with relay coordination.

[E] **A. Srivastava**, D. Steen, L. A. Tuan, O. Carlson, "A congestion forecast framework for distribution systems with high penetration of PVs and PEVs," in *Proc. IEEE Milan PowerTech*, Milan, 2019, pp. 1–6. **DOI**: https://doi.org/10.1109/PTC.2019.8810871.

This paper presents a congestion forecast framework based on probabilistic power flow for electrical distribution systems with high penetration of solar photovoltaic and plug-in electric vehicles. The proposed framework is tested using data of the real distribution grid of Chalmers campus for case studies to analyze the impact of different local production levels and operating modes of solar photovoltaic inverters. The results have shown that cumulative probability for network congestion in branches and transformers would increase by 30% and 20%, respectively, in the case when level of local solar photovoltaic production, demand, and number of plug-in electric vehicles is increased by 100%, 95%, and 100%, respectively. It has also been shown that network congestion in branches and transformers is 4% and 8%, respectively, more likely to occur in constant-V mode as compared to constant-pf mode. This framework could be used by distribution system operators to predict network congestion.

[F] **A. Srivastava**, D. Steen, L. A. Tuan, O. Carlson, et. al., "A DSO support framework for assessment of future-readiness of distribution systems: technical, market, and policy perspectives," in *Proc. CIRED 25th International Conference and Exhibition on Electricity Distribution*, Madrid, 2019. **DOI**: http://dx.doi.org/10.34890/832.

This paper proposes a framework to support the distribution system operators for assessing current status of network infrastructures, market/business models, and policies applicable to distribution systems, and thus identify future-readiness of their network. The assessment framework consists of two steps as the identification of the key indicators associated with this transition and assessing the current status by evaluation of these indicators based on inputs from distribution system operators. Case studies have been carried out for distribution system operators in three European countries, i.e., Göteborg Energi (Sweden), SOREA (France), and ENEXIS (The Netherlands). The key results have shown that presently the three distribution system operators have a small proportion of renewable power generation in their grids, but it is going to increase in the future. Hence, they need investments in flexibilities, generation and load forecasting, advanced network control, and protection strategies, etc. The results also suggest needs for development of novel business models for customers

and changes in the policy and regulations. Finally, a comparative assessment of three distribution system operators is presented in the paper.

[G] K. A. Plytaria, **A. Srivastava**, M. A. F. Ghazvini, L. A. Tuan, D. Steen, O. Carlson, "Chalmers campus as a testbed for intelligent grids and local energy systems," in *Proc. IEEE International Conference on Smart Energy Systems and Technologies (SEST)*, Porto, 2019, pp. 1-6. **DOI**: https://doi.org/10.1109/SEST.2019.8849014.

This paper presents an overview of a testbed for intelligent distribution grids, local energy systems, and energy flexible buildings, which is being developed at the campus of Chalmers University of Technology in Gothenburg, Sweden. It describes the test sites, the functionalities, and the planned demonstration activities within the scope of on-going research projects. The proposed demonstrations include a local energy market platform, energy management solutions for microgrids and smart buildings, as well as voltage control in distribution grids. The paper aims to show how the physical energy supply systems of the university are being adapted to integrate the communication and control set-ups that provide the technical requirements for smart grid interoperability. As an example, the on-site implementation of remote battery control is presented, where initial results show the feasibility and potential benefits of the external control. Finally, challenges and lessons learned during the development of the testbed are highlighted.

[H] J. Rossi, **A. Srivastava**, D. Steen, L. A. Tuan, "Study of the European regulatory framework for smart grid solutions in future distribution systems," in *Proc. CIRED 2020 Workshop*, Berlin, 2020. **DOI**: https://doi.org/10.1049/oap-cired.2021.0230.

Electric distribution systems in Europe are facing significant challenges due to climate change goals, changing market frameworks and technological innovations, which will significantly impact the role of the distribution system operators. The nature and scale of these challenges are strongly driven by the European vision and strategies on climate and energy. This study identifies which policies can become barriers for distribution grid innovation and the implementation of advanced smart grid solutions developed within the UNITED-GRID project. After an extensive review of new policy priority areas within the energy and climate framework and electricity market design, and subsequent discussions with three partner distribution system operators, five priority barriers are identified. The results show that ambitious decarbonisation targets and changing expectations on the distribution system operators' role in the energy system would require more flexible and efficient network management. However, binding income frameworks, lacking incentives for innovation and regulatory uncertainties hinder modernisation in distribution systems. It can be concluded that these concerns increase the risks for distribution system operators and have to be considered by research projects and developers of smart grid solutions in order to implement and achieve market uptake of the developed solutions within the next 5–10 years.

[I] **A. Srivastava**, R. Mohanty, M. A. F. Ghazvini, L. A. Tuan, D. Steen, O. Carlson, "A review on challenges and solutions in microgrid protection," in *Proc. IEEE Madrid PowerTech, 2021*, Madrid, pp. 1–6. **DOI**: `https://doi.org/10.1109/PowerTech46648.2021.9495090`.

Protection of microgrid has become challenging due to the hosting of various actors such as distributed generation, energy storage systems, information and commu-

nication technologies, etc. The main protection challenges in the microgrid are the bi-directional power flow, protection blinding, sympathetic tripping, change in short-circuit level due to different modes of operation, and limited fault current contribution by converter-interfaced sources. This paper presents a comprehensive review of the available microgrid protection schemes which are based on traditional protection principles and emerging techniques such as machine learning, data-mining, wavelet transform, etc. A categorical assessment of the reviewed protection schemes is also presented. The key findings of the paper suggest that the time-domain and communication-assisted protection schemes could be suitable solutions to address the identified protection challenges in the microgrid.